Particulate Matter Deposition in Indoor Heritage

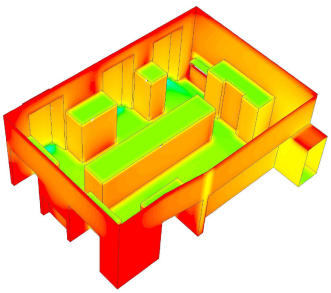

Josep Grau-Bové
UCL
Doctoral Thesis

Declaration

I, Josep Grau Bové, confirm that the work presented in this Thesis is my own. Where information has been derived from other sources, I confirm that this has been indicated in the Thesis.

Abstract

This Thesis describes the simulation of particulate matter transport and deposition in indoor heritage spaces using Computational Fluid Dynamics (CFD). The mathematical model follows an Eulerian approach, i.e. particles are simulated as a continuous scalar. Deposition fluxes are implemented as a boundary condition in all the walls, and the diffusive and convective terms are modified to account for gravitational settling, near-wall turbulent diffusivity and thermophoresis. We [1] validate this model experimentally using a test tunnel and most importantly, using data collected in real heritage buildings (Apsley House, Wellington Arch, Wellcome Collection and Hampton Court Palaces). This is the first time a CFD model of indoor deposition is validated against direct measurements of deposition fluxes in actual indoor spaces. We compare the model predictions against measurements of deposited and suspended PM, and we obtain suitable boundary conditions using thermal images, wind data and indoor air velocities. The model successfully predicts deposition of particles from 0.1 to 100 μm under different conditions: natural and mechanical ventilation, filtration through leaks or emission by visitors. We also investigate the effects of deposited PM on organic materials, and show how the model can be combined with chemical information and conservation know-how in order to be used as a powerful tool for risk assessment.

[1] As we embark together in this journey of discovery, I will use the plural form "we", thus including the reader, even though I often refer to work I have carried out on my own. When the plural form refers to the work of collaborators and colleagues, it is appropriately specified. Very occasionally I will use the singular form "I", in the instances, such as this footnote, where it is the most fitting solution.

To Gemma and my parents.

Acknowledgements

My supervisors Matija Strlic and Luca Mazzei deserve the greatest of thanks, I'll just say that I've spent my PhD telling everyone how good my supervisors are. I also want to thank May Cassar, for making this adventure possible. And of course, this work is also indebted to Mark, Katherine, Tiphaine, and everyone with whom I have shared the Heritage Science Lab, my second home for three years.

I must thank those who have opened doors and held ladders for me -sometimes literally and sometimes metaphorically: Dave Thickett, Stefania Signorello, Constantina Vlachou-Moigre, Josephine Oxley and the Staff of Apsley House: Helen Swan, Lydia Rousseau, Tony Page, Chris Small, Rachel Goreing, Jennifer Watling and of the Wellington Arch: Martin Stiles, Clive Philips and Max Duerden. Of course, also Leslie and Rebecca, for their help in my experiments.

This Thesis was enriched enormously through helpful discussions with Dave Thickett, Liora Malki-Epshtein, Dejan Mumovic, and even Josep Bonet, who may not remember it.

And I want to thank Josep Bové, the wisest and strongest, and Carme Grau, Xavi Grau and Carme Bové, for their unconditional support. My last thanks go to the people of La Masó, who believe in me.

This thesis has been written in a good many desks, of which I should mention two: I completed the first chapter in Wittgenstein House, Vienna, and wrote the last lines in a cabin near Walden Pond in Concord, Massachusetts.

La Masó, September 11, 2014

Contents

1

Introduction: Particulate matter indoors

"The National Gallery as it now stands, is thoroughly exposed to all that can exist in the atmosphere of a great city like London, both the inorganic fumes from the chimneys and the organic miasma from the crowds that are in the town."

Michael Faraday, 1850.

1.1 Introduction

Particulate matter is nothing but a vague way of referring to the size of pieces of matter. The quote that opens this Thesis is not here to provide a patina of historical significance, but as a provocation. I believe that speaking of particulate matter (PM) in a heritage context may be as imprecise as speaking of "miasmas from the crowds" was in the early XIX century. It is a concept that is insufficient to describe the problems and challenges that we associate with it. PM deposition causes a loss of value and for this reason, surfaces are wiped and vacuum cleaned, protected and covered, windows are sealed and filters are installed, and for the same reason PM is monitored, photographed, counted and weighted in museums worldwide. And yet our understanding of the processes that lead PM to surfaces is still vague: our measurements are difficult to interpret, and once interpreted, it is difficult to take appropriate action. There is great interest in PM indoors, but theory must stand up to the challenge.

In this thesis we present a mathematical description of the behaviour of PM in indoor heritage environments, and we validate it experimentally in various case studies. By doing so, new concepts and terminology naturally arise. This Thesis unfolds a way of describing and referring to indoor deposition phenomena, a framework for the interpretation of deposition. The reader

will find in this pages a mathematical model, evidence supporting it and ways of using it, as well as abundant information on the trends, the behaviour and the consequences of deposition. But hopefully we also will be able to contribute with a language -and a logic- of speaking and thinking about deposition.

1.2 Particulate matter in indoor heritage environments

PM can be an elusive subject of study. Different sizes display different properties, typical sources and even different behaviours. The great variation in composition adds more complexity. Studies of PM in indoor heritage environments have generally focused on dust, which is one of the characteristic size modes -the largest- of PM. This bias towards coarse particles is evident if we look at the minimum diameter of the particles collected in different monitoring campaigns in the field of heritage science. A survey of 25 scientific papers [1–25], most of them reviewed here, with the keywords "heritage" and "particulate matter" reveal that 32% of them analyse only particles up to 10 μm and 16% include particles up to 2.5 μm, i.e. more than half of the studies did not look into submicron particles. If a study did take into account particles $\sim$0.5 - 1 μm, it is generally the lowest size mode considered (36% of cases) and no particles are studied under this value. Finally, in 92% of the cases, particles are studied in only two or one size modes (usually 2.5 and 10 μm). However, two size fractions are not enough to reflect the actual size distribution, which is only analysed in a minority (8%) of the studies.

It seems that in the cultural heritage field researchers are more interested in medium sized and large particles (d_p>2.5 μm) than fine PM. I would argue that this bias is not only due to the specific properties of these particles but also, to some extent, due to instrumental limitation. After all in aerosol monitoring outside the heritage field it is common practice to obtain complete size distributions than include submicron particles, and more recently, including particles smaller than 0.1 μm. It is true that coarse particles exhibit characteristics of great interest to conservators: they are significant carriers of mass to surfaces, and, being bigger, are more likely to alter the visual appearance of objects. But their number concentrations are orders of magnitude smaller than the concentrations of fine particles, especially in urban environments. Additionally, the composition of coarse and ultrafine particles is also different, and while small particles might carry less mass, they may carry components of different reactivity. Small particles may also require different strategies of removal.

This review chapter serves a double purpose. Firstly, it aims to provide a guide to the properties of particulate pollutants, and also to find areas that require further research that will be addressed in this thesis. Secondly, it attempts to identify if fine and ultrafine particles can be regarded as a relevant risk to cultural heritage indoors. Since not many investigations deal directly with fine and ultrafine particles in heritage environments, this review will make use of work produced in other fields -aerosol science, environmental science, computational modelling- which can be applied to heritage at least partly.

1.3 Sources, trends, and projections

The term PM identifies all the particles that can be found in the atmosphere, in other words, those that can be suspended in air and transported by it before they deposit. This includes particles composed only of several molecules, with diameters around 0.01 μm, up to coarse dust with diameters around 100 μm. Samples of atmospheric PM usually display a very characteristic size distribution, clearly separated in three different size modes (Figure 1.1). These modes are referred to as the nucleation, ultrafine, or Aitken mode ($<$0.1 μm), coagulation or accumulation mode (0.1 - 1 μm) and coarse mode ($>$1 μm) [26]. An alternative and common nomenclature is using PM_x for all the particles smaller than x in μm, the usual values being 10, 2.5 μm or, less commonly, 5 and 1 μm. Although the use of this notation is widely spread, it makes an artificial division between the actual size modes. E.g., $PM_{2.5}$ is in the middle of the coarse mode, but is generally taken as a good indication of the amount of anthropogenic particulate pollutants in urban environments. This nomenclature is useful from the health perspective as it approximately denotes the fractions which can penetrate to different depths of the human respiratory system [27]. It is not, as we shall see, particularly suited for heritage purposes. However, its status of a standard makes its use unavoidable.

Given such a broad definition, it is natural that there are a variety of origins, sources and compositions of PM. Nonetheless, not all sources are equally important. The majority are related to energy production, and natural sources (such as sea-spray) are often negligible in comparison with the anthropogenic ones [28]. Among them, the combustion of fossil fuels, especially in road transportation, has a prominent role.

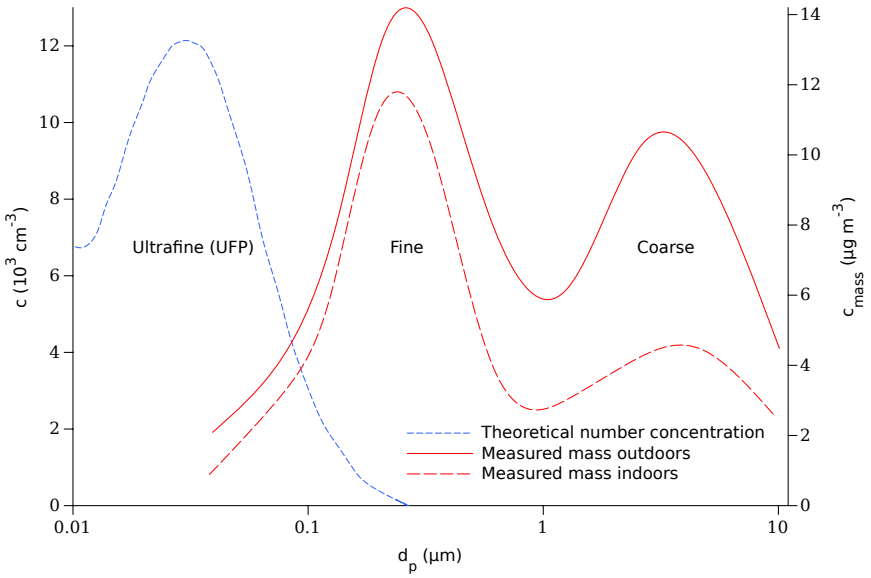

Figure 1.1: An example of distribution of atmospheric particles showing the relevant and typical properties of DPM. Mass concentrations adapted from measurements taken in the National Library in Prague [24]. Theoretical number concentration of ultrafine particles taken from [29]

In the UK, road transport is responsible for more than half of the particles of the smaller size ranges and around 20% of the larger [30]. This relative contribution is even greater in urban areas. At Marylebone Road, arguably one of the most polluted streets in London [31], traffic-generated particles make up to 27% of the PM_{10} mass concentration and 42% of the $PM_{2.5}$ [32]. Most road transport particles are due to diesel vehicles (e.g. 72% of USA road transport PM) [33]. Even though this picture varies between regions, similar particle source apportionments have been reported by different studies carried out elsewhere [34, 35].

Emissions of all types of PM are predicted to decrease in the decades to come, including emissions of the smallest particles [36] due to the implementation of mitigation strategies such as diesel soot filters and the substitution of fossil fuels with alternative energy sources. Analysis of global emission trends under different scenarios reveal that emissions of traffic-generated PM will reduce in all the continents except in Africa, where they are predicted to increase 1.3 - 3.1% per year, depending on the scenario, due to economic development and an ageing car fleet. Global emissions from vehicles will reduce 1.3 - 2% on average per year in the following 40 years [37]. China will achieve a reduction in emissions of black carbon of 9% by 2020 [38].

The PM concentration limit suggested by the World Health Organisation (WHO) [39] and the European Commission [40] for $PM_{2.5}$ is 25 $\mu\mathrm{gm}^{-3}$, and the US Environmental Protection Agency has suggested a value of 13 $\mu\mathrm{gm}^{-3}$ [41]. Even though these limits are exceeded in some regions, it is likely that they will be satisfied in the near future. However, WHO states "as no threshold for PM has been identified below which no damage to health is observed,

the recommended value should represent an acceptable and achievable objective to minimize health effects in the context of local constraints, capabilities and public health priorities." [39] The same logic may be applicable to heritage materials. It can be concluded that, even though emissions are gradually decreasing, traffic-generated pollutants will remain an important part of urban atmospheres for decades, especially in developing economies.

1.4 Particles derived from combustion

The laser-cleaning literature abounds with uses of the word "soot", referring to dark deposits on indoor and outdoor materials. However, no standard description or characterisation of soot exists. The concept of "black carbon", extensively used in aerosol and environmental science, suffers from a similar imprecision, sometimes used interchangeably with soot [42].

What is clear is that fine particles (PM_1) mostly originate from combustion processes. Morphology and composition of these particles varies with the source to some degree: burning of candles, coal, tobacco or diesel fuel. These particles also have common features: a high content of inorganic carbon that will display high light absorbance, combined or coated with traces of other elements, and an aggregate-like shape [43].

1.4.1 Diesel particulates

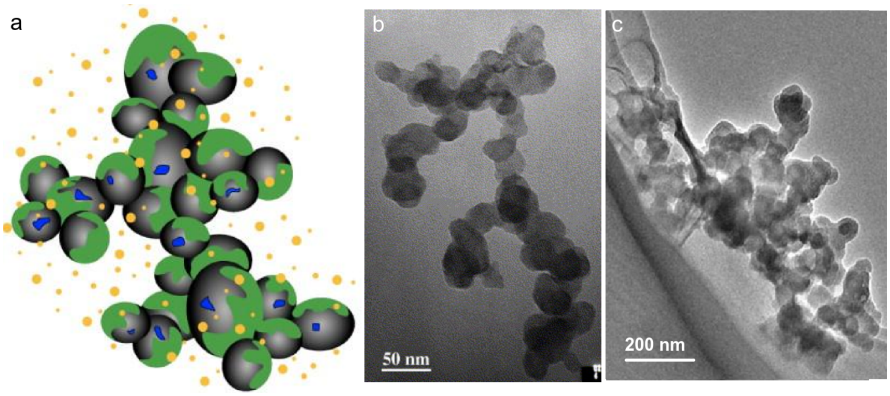

Figure 1.2: a) Graphic representation of a typical diesel particle containing all its components: EC substrate, OC coating, metal traces and nucleation particles, taken from [44]. b) TEM image of a diesel exhaust particle with a magnification of 230000x, taken from [45]. c) A candle soot particulate displaying a similar morphology to that of DPM [46]

A typical diesel particulate is shown in its graphic representation in Figure 1.2a and a TEM photograph in Figure 1.2b. Diesel particulates in the accumulation mode have a distinct morphology consisting of a self-similar agglomeration of primary particles, which has led some researchers to use fractality as a characterisation factor [47]. These primary particles are mainly composed

of elemental carbon with metallic traces, and are coated with a layer of organic carbon and sulfates. This composition is subject to some variability as it depends on the engine type, the engine load and the fuel used. Total carbon usually accounts for 75 - 90% of the overall mass [48], and the metal traces can include, in the order of relative abundance: Ca, Fe, Mg, Zn, Cr, Ni, Ba, Pb [44, 49]. Elemental carbon (EC) is a characteristic component of DPM, which is typically the source of 90% of the EC in urban environments [50]. Organic Carbon (OC) may be emitted directly into the atmosphere or can be formed in gas-to-particle atmospheric processes (secondary aerosol). EC, on the other hand, emerges primarily from the combustion of carbonaceous matter, and its presence is generally regarded as a good indicator of the fossil fuel combustion origin of PM, especially in urban areas. Recently, however, it has been claimed that atmospheric EC can originate from sources other than diesel exhausts [35, 51], which makes source apportionment difficult. Polycyclic aromatic hydrocarbons (PAHs) and n-alkanes have also been suggested as possible tracers for different particulate pollutants generated by road traffic [52].

1.4.2 Other combustion particulates

Even though most of the PM mentioned in this review are from outdoor origin, mention should be made of indoor sources of fine and ultrafine particles which may be of interest. Candle-burning soot, for example, is commonly associated with indoor deposits in temples and churches. It has been found that the amount and composition of particles emitted from candles depends on the burning mode. If the flame is in steady state, it emits a relatively high number of ultrafine particles dominated by either phosfates or alkali nitrates originated from additives. Sooting burn, in addition, emits larger particles mainly consisting of agglomerated elemental carbon, with a morphology which is similar to DPM [53] (Figure 1.2c. Particles with the same morphology and similar composition can be emitted during cooking [54], an activity not unusual in large heritage sites and museums. A “black deposit” or “soot deposit”, must, therefore, be assessed with care in order to identify the most likely origin of the particles.

1.5 Concentration patterns indoors

The indoor PM concentration is generally a reflection of the outdoor concentration. Certain indoor activities cause exceptions to this rule. It has long been established that different activities, such as cooking, housework, or simply any physical activity, result in concentration peaks over the baseline set by the outdoor concentration [55]. The frequency of these activities in heritage environments combined with the rates of infiltration and removal define the daily PM pattern.

Fine PM such as DPM originate from outdoor sources, and events that can cause a drop or a sudden increase in its concentration are rare. Figure 1.3 shows the variation of fine particle (d <1 μm) concentration in a roadside house. It can be clearly appreciated that the indoor concentration reflects the outdoor concentration, except when particles are emitted during cooking activities.

In heritage environments, indoor events that lead to emission of fine particles are uncommon.

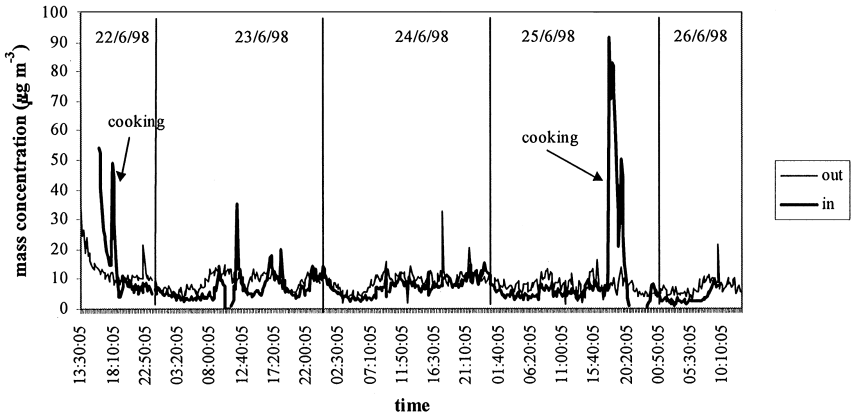

Figure 1.3: Outdoor and indoor variations of PM concentration in a roadside house, taken from [55]

Actions such as cleaning, or physical activity cause variations in the concentration of the larger particles, but generally leave the smaller size modes unaltered. Figure 1.4 shows the variation of airborne particle concentration in the Correr Museum, Italy [17]. It can be appreciated that the peaks of 10, 5, 2, and 1 μm particles, which correspond with the opening hours of the museum, as well as their high variability, are not reflected in the concentration pattern of the finer particles, which varies smoothly. Very similar temporal evolutions have been reported in the Anatomy Theatre of Padua [7] and in the Chiericati Municipal Museum of Vicenza, Italy [56]. As a general rule, while physical movement increases the number of coarse particles, actions involving heating tend to increase the concentration of the smallest particles. Air heaters, electrical radiators and stoves have been found to increase concentrations of particles between 0.02 - 0.1 μm up to 100,000 - 200,000 cm^{-3}, while leaving larger particles unaltered. This increase is not necessarily related to PM emission, but it has been hypothesised to be related to the thermal degradation of deposited coarse dust [57].

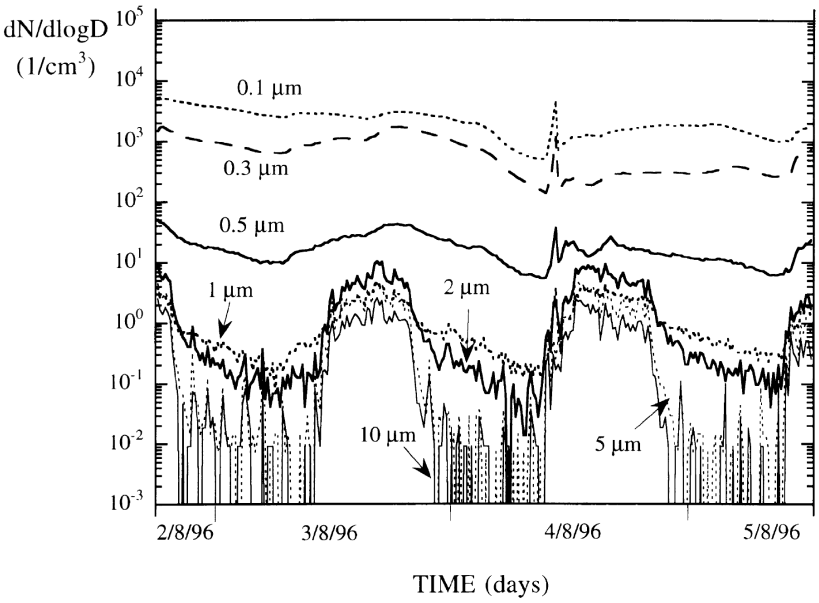

Figure 1.4: Variation of particulate matter concentrations in the Correr Museum, Italy, taken from [17]

The mass and number concentrations seen in Figures 3 and 4 are representative of the typical concentrations in indoor environments. The average concentration of PM_1 inside the Alhambra, Spain, was 17 $\mu\mathrm{gm}^{-3}$ in the summer and 8 $\mu\mathrm{gm}^{-3}$ in the winter [2], and its most abundant component was black carbon. Traffic was found to be the major source of fine particles. Between 20 and 10 $\mu\mathrm{gm}^{-3}$ of $PM_{2.5}$ were detected in display rooms in the Plantin-Moretus museum in Belgium [19], and 40 $\mu\mathrm{gm}^{-3}$ in the archaeological museum of Thessaloniki [12]. If total suspended particles are measured, higher values should be expected, e.g. 60 - 70 $\mu\mathrm{gm}^{-3}$ inside the Wawel Castle Museum in Cracow [13]. At this site, particles containing elemental and organic carbon were found to be the ones that penetrate more easily into the museum. Even though particle concentrations in heritage locations are commonly measured in this manner, it tells us little about the fraction of fine particles that penetrate from the outdoor environment. The concentration of suspended PM is typically complemented with an analysis of the bulk chemical composition of the collected particles. In only a few studies we also find more detailed measurements of the size distribution including fine particles. A good example are the detailed measurements taken in the Czech National Library in Prague [24], or in some Californian museums [25] which display a clear bimodal size distribution (Figure 1.1).

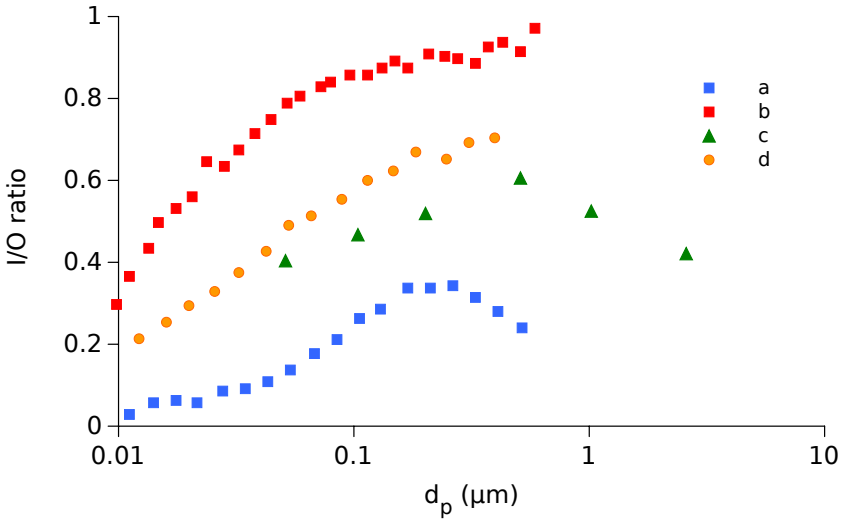

Figure 1.5: Experimental I/O ratios as a function of particle size. Values taken from [58] (a) [59] (b) [60] (c) [61] (d).

The indoor/outdoor ratio (I/O ratio) is widely used to describe the differences between the indoor and the outdoor environments. There is a great variability in the measured PM I/O ratios in particular cases, but in general, some rules of thumb can be extracted from experience. Firstly, as shown in Figure 1.5, the I/O will be higher for particles of size between 0.1 - 1 µm. An explanation for this phenomenon is given by the aerodynamics of these particles, and will be further explored in the next sections. Secondly, I/O ratios for particles containing EC (which in urban atmospheres can be understood as DPM), the I/O ratio are typically 0.5 - 0.9 [55, 61, 62].

1.6 The life-cycle of fine particles indoors

Fine particulates penetrate into buildings not only through large openings but also through cracks and filter inlets [63]. At the end of its indoor life, PM deposits on surfaces or is removed by mechanical or natural ventilation. Some particles, especially the larger ones [64], may be re-suspended and re-deposited. This set of inlets and outlets of PM summarizes all the steps that ultimately determine the amount of particles that reaches the surfaces. They have been extensively studied as separate phenomena, and considerable literature exists describing each process experimentally, or with empirical or semi-empirical correlations. The work of Nazaroff [65] presents a comprehensive summary of all the possible particle flows in any given building. Figure 1.6 summarizes, in an approach similar to Nazaroff's, the main particulate matter fluxes in a room of one of our case-studies, Apsley House. The equations that describe these fluxes will be explained in detail in Section 2.2.2.

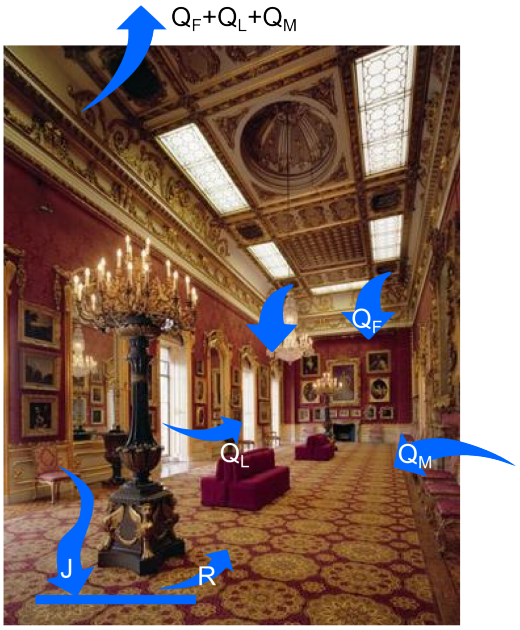

Figure 1.6: The possible inlets and outlets of particles. Q_M is the main inlet, such as an open door, Q_L the leakage, Q_F the filtered inlet, R the re-suspension, J the deposition to walls, floor, and ceiling, Both Q_F and Q_L are subject to certain efficiency.

1.6.1 Penetration

First and foremost, particles enter through the following main inlets: windows, doors, and any openings that connect the indoor and outdoor environments, such as gaps under doors. The use of windows for ventilation can quickly increase the particle concentration indoors to match outdoor levels [66] for all particle sizes. For example, a study of PM in Californian museums [67], such as Sepulveda house, which lacks an air filtration system, showed I/O rates equal to 1. This implied that the risk of deposition indoors was equal to the one outdoors. Leakage, or the penetration of particles through cracks or gaps in building envelopes, has also been extensively studied both experimentally and theoretically. It is the major particle source in buildings that rely on mechanical ventilation [68]. The fundamental difference between a crack and a large opening is that a significant fraction of particles will deposit on the internal surfaces of the crack, and therefore leakage has a certain penetration efficiency which depends on particle size. Ultrafine particles led by Brownian motion will tend to deposit on crack walls, and coarse particles will also deposit quickly on upward facing surfaces [65]. Only the accumulation mode (0.1 - 1 μm) will cross the crack efficiently. Liu and Nazaroff [69] developed a simple mathematical model to estimate the penetration efficiency of particles, and it has been successfully used in several experimental studies since then [70, 71]. Figure 1.7 shows a solution of the Nazaroff equation along with an estimation of particle deposition velocities. Note that the particles between 0.1 - 1 μm penetrate with almost 100% efficiency through the crack. Although generally regarded

as a minor source, crack infiltration has been found to account for 73% of the PM_1 indoors in a poorly ventilated building [63]. Leakage can lead particles to the interior of showcases. The comparison of particle size distribution inside and outside a display case in a Museum in Padova revealed that the I/O ratio was 1 for all particle sizes, except for particles larger than 1 μm[72], which is in accordance with the theory.

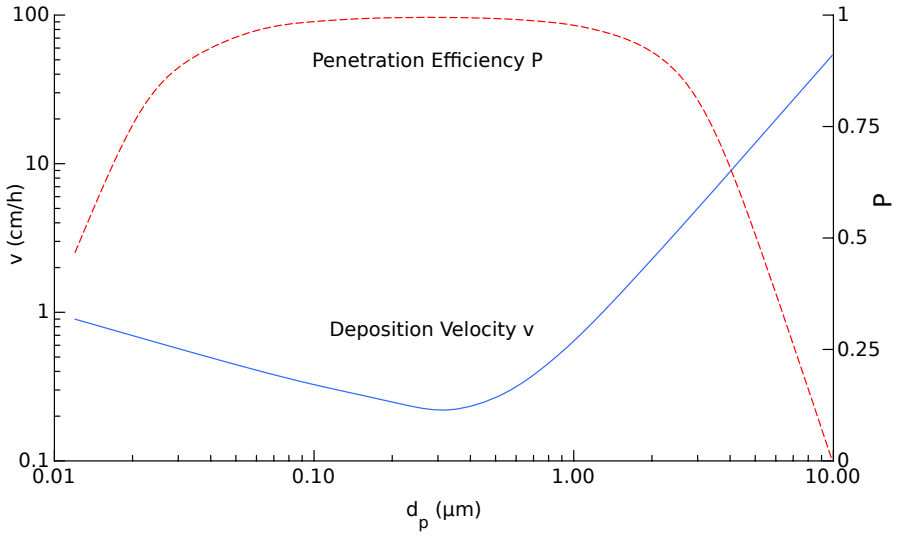

Figure 1.7: Comparison of deposition and penetration through cracks and leaks obtained with Nazaroff's equations for deposition and leakage. Note that the particles with smaller deposition rates also penetrate through cracks more efficiently. Crack dimensions: Width=0.20 mm, Length=4 cm, Pressure difference = 4 Pa, Air flow conditions: K=0.5, Cubic room (3x3x3 m). All values taken as representative of realistic cracks by [69].

1.6.2 Indoor emission

Indoor sources of fine particles are found in some specific heritage environments, such as in-use churches where incense and candles are burned. An increase for a factor of 9.1 in the concentration of PM_1 has been found after services that involved incense burning in Ruhr, Germany. In this case, the concentration inside the church remained above the outdoor levels for $\sim$24 h approximately [73]. These findings are consistent with values found during services in medieval churches in Cyprus, where indoor $PM_{0.5-1}$ concentration was found to be up to 10.7 times larger than the outdoor concentration.

A relatively unknown indoor source is the thermal desorption of organic compounds and emission of submicron particles from household dust [74, 75]. At temperatures above 50 °C, which are often present in indoor environments, concentrations around 2500 cm^{-3} can be generated [75]. Investigation of this phenomenon, which to the best of our knowledge has not been researched in heritage sites, should be considered when introducing new heating points into an environment.

1.6.3 Movement

Air transport

PM is largely transported by movement of air. The airflow in an indoor space, isolated from the outdoor climate, is governed predominantly by three factors: mechanical mixing, pressure differences and to a lesser extent, temperature gradients. In a totally isolated room, only the temperature profile will define the air velocity pattern. However, as we will see, in the presence of strong air currents he effects of temperature are generally negligible. Studies of indoor micro-climates show that temperature gradients are the consequence of a number of factors such as presence of heating points, proximity to windows, temperature of the surrounding spaces, human presence, lighting or similar [76]. Heat sources induce vertical convective flows that displace contaminants upwards in an enclosed space. Cool vertical surfaces, such as windows, induce downward flows, which results in a circular movement of air around the room. A typically observed air movement pattern is the upward flow from radiators or air circulation behind furniture or paintings due to the difference of temperature between the wall and the air [77].

However, the velocity field of particles does not coincide completely with the velocity field of air. Particles have a certain mass, and therefore their velocity has a vertical component due to gravitational settling. Coarse particles settle down gravitationally much faster than fine particles, and this creates a certain stratification of the concentration. Measurements in indoor domestic environments have revealed a higher proportion of $PM_{2.5}$ on the upper parts of rooms, and more abundance of PM_{10} towards the floor [57]. Measurements of particle deposition on ceiling, walls and floor reveal that almost no coarse particles deposit on the ceiling, while all the deposited mass on the floor is due to coarse particles [25].

Other transport mechanisms

The smallest particles are largely affected by Brownian diffusion (also called "random walk"), which is a result of collisions between particles and air molecules and occurs in all directions. In any given room, coarse particles will be found in areas with the highest air flow, while fine particles will tend to diffuse around all the available space. Thermophoresis, the displacement of particles from high to low temperatures, is a phenomenon also common indoors. The balance between air transport, diffusion and thermophoresis has been studied in detail by Camuffo [78] in the case of the soiling of murals. It was pointed out that when a vertical fresco is colder than the surrounding air, the temperature gradient forces thermophoresis towards the wall, and at the same time a downward free-convection flow develops, resulting in an overall increase of deposition rates. When a fresco is warmer than the air thermophoresis takes fine particles away from the wall, but this effect may be counteracted by an upwards convective flow that increases deposition of coarse particles. The best situation for conservation purposes is, therefore, a thermal equilibrium between wall and air, whereas cold walls are the less desirable scenario.

1.6.4 Deposition

The deposition velocity of PM varies with particle diameter. This dependence is well known, and several authors have suggested mathematical expressions to estimate deposition velocities under different conditions. Perhaps the most used is the model derived by Nazaroff et al. [79, 80], which has been successfully applied to museum environments [81]. Figure 1.7 has been obtained by solving this model, and shows the range of values of deposition velocity that can be expected under different flow conditions and for different diameters. This model is further explained in Section 2.2.

Dependence on particle diameter

The highest deposition rates are found for the largest particles (1 - 10 μm), which are governed mostly by gravity and tend to deposit on horizontal surfaces, and for the smallest particles (0.01 - 0.1 μm), which are mostly governed by Brownian motion and tend to diffuse and collide against floor, walls or ceiling. The particle flux due to gravitational settling should be proportional to the gravitational settling velocity, which as we know from Stoke's law depends on the density of the fluid, ρ, the density of the particle, ρ_p and the square of the particle radius, r:

$$v = \frac{2(\rho_p - \rho_f)g}{9\mu} r^2 \tag{1.1}$$

And the particle flux due to diffusion should be proportional to the Brownian diffusivity of the particles, which we know from the Einstein equation that is proportional to the inverse of r:

$$\mathscr{D} = \frac{k_B T}{6\pi\,\eta} \frac{1}{r} \tag{1.2}$$

where k_B is the Boltzmann constant and T is the temperature in K. The combination of these two transport mechanisms results in the typical curve of particle deposition, as seen Figure 1.8. This curve is very similar to the actual deposition velocities (Figure 1.7)

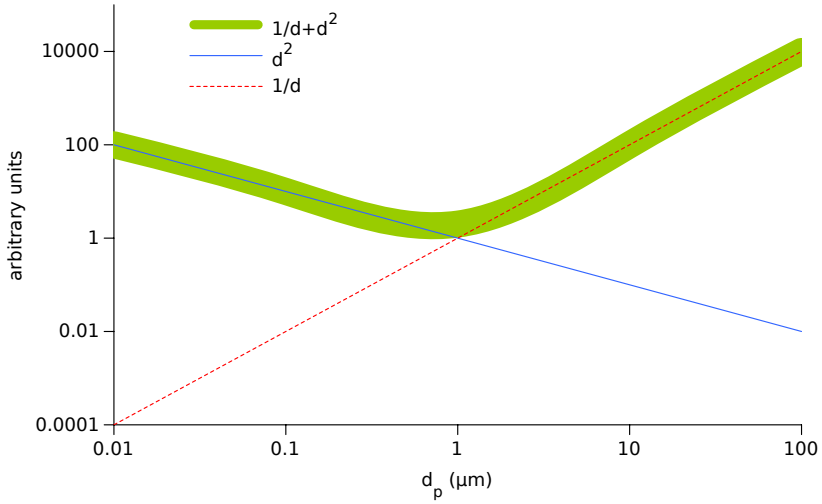

Figure 1.8: The shape of the deposition rate curve as can be expected from a simple analysis of the influencing factors. In the legend, the particle diameter is represented by d.

The mass of particles is only relevant in the larger size fraction, in which larger densities mean larger deposition velocities. Between these two size modes, the accumulation mode (0.1 - 1 μm) shows the slower deposition rates, which are up to 2 orders of magnitude smaller than that of the coarse particles [65]. These lower deposition rates imply that particles in the accumulation mode tend to remain in suspension for longer, and therefore travel longer distances. In other words, while the coarse particles will deposit shortly after penetration indoors, near the source, the accumulation particles will distribute more evenly around the available space [82].

Dependence on air flow

The deposition rates for all diameters increase with higher air velocities, which can be produced by wind or mechanical ventilation [65]. The dependence of deposition on turbulence and other characteristics of the flow is complex and non-linear. It is one of the major topics of this work, and it will be described in detail in the next sections.

Deposition rates are also smaller when the surface to volume ratio of the room is small, i.e. when the room has a small surface in relation to its volume . As a general rule, small volumes such as display cases and boxes will have larger S/V ratios than large galleries, but one should bear in mind that the number of objects (e.g. furnishings and exhibits) present in the room will also increase the S/V ratio, and thus increase deposition. Similarly, the roughness of surfaces favours deposition [82].

1.6.5 Re-suspension

Once deposited, PM is adhered to surfaces by adhesion forces that can be orders of magnitude higher than gravity [83], and of which Van der Waals adhesion is the most relevant [84]. Changes in air flow conditions can eventually compensate these adhesion forces and re-suspend the deposited particles. Re-suspension rates are strongly dependant on particle diameter. Larger particles are re-suspended more easily. In some museum environments, particles of >1 μm appear only during museum opening hours due to re-suspension caused by visitors. These particles redeposit gravitationally as soon as the museum is closed [17]. This type of behaviour has been studied for a long time, and common indoor activities such as walking and vacuum cleaning have been associated with re-suspension of particles >1 μm [64], and have been found to increase particle concentrations up to 7 times the background concentration [85]. Re-suspension due to inappropriate cleaning habits has been found to account for the spatial distribution of particles in a monastery which displayed an otherwise very stable indoor environment [86].

This mechanism is very dependent on particle size, and <1 μm particles are rarely affected. Furthermore, re-suspension affects only those particles that are deposited on the floor or the objects involved in the human activity that causes it, such as furniture. The fraction of fine particles involved in the deposition and re-suspension cycle could be expected to be negligible, although there appears to be no relevant experimental research about re-suspension of the accumulation size mode. Nonetheless, re-suspension is a phenomenon that has been extensively modelled [87–89], and it is possible to assess the re-suspension rates of fine particles mathematically.

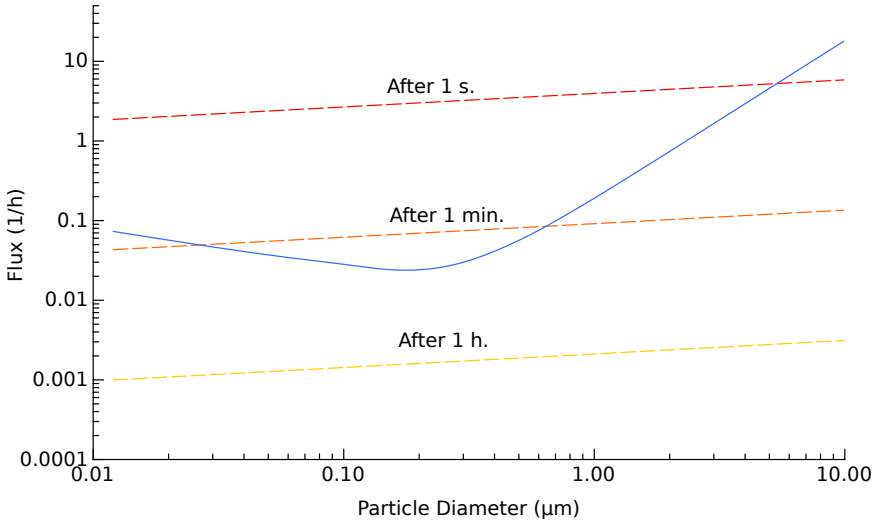

Figure 1.9: Re-suspension rates obtained with the empirical correlation recommended in [90]. Friction velocity = 1 m/s, same flow conditions as Figure 7

Figure 1.9 shows the solution of one of these models, the empirical correlation recommended by [90], along with deposition rates calculated with the Nazaroff equation. A friction velocity

of 1 $\mathrm{m/s}$ has been used, a relatively high air velocity for an indoor environment which may represent an extreme situation, e.g. a draft from an open window. Note that particle re-suspension decays exponentially with time since the moment in which the re-suspending event begins. Consequently, even though re-suspension might exceed deposition when air starts moving, the re-suspension rate rapidly decreases below the deposition rate. The overall particle flux is positive towards surfaces. It can be concluded that as an approximate guideline, re-suspension rates for submicron particles indoors will be orders of magnitude smaller than deposition rates, unless air speed is subject to frequent fluctuations due to wind or mechanical ventilation.

1.6.6 Coagulation

Some authors attribute the measured particle decay in experimental conditions exclusively to deposition while others do to coagulation as well [91]. Naturally, the fraction of particles in a given size fraction that collide or deposit depends largely on the number of particles and on the proportions of the room, specifically on the surface/volume ratio. In some cases either the former or the latter process may be negligible. But in broader terms, it is clear that the temporal evolution of particle number concentration cannot be fully understood without taking both processes into account. In a small chamber with a high concentration of diesel particles (from 8.11×10^5 to 84.3×10^5 $\mathrm{cm^{-3}}$, which compares to the range of 1×10^5 to 7×10^5, a concentration which can be found in street canyons in Stockholm [92]), with diameters from 15 to 670 nm, particle size increased up to a factor of 2.6 during the experiment due to coagulation [93]. An increase of particle size up to 60% has been also found in the case of tobacco smoke during the first 30 min. after smoking a cigarette [94].

However, it is rare to find such high concentrations in indoor environments. It has been experimentally demonstrated that coagulation can be neglected in comparison to deposition when total suspended particles (TSP) concentration is under 1×10^3 $\mathrm{cm^{-3}}$, and for ultrafine particles ($<$0.1 $\mu\mathrm{m}$) it is only relevant above 1×10^4 $\mathrm{cm^{-3}}$ [93] .

In some cases particle coagulation can be visually detected in a plot of the decay of concentration in time. While particle deposition occurs at a constant rate directly proportional to the particle number, i.e.:

$$\frac{\delta c}{\delta t} = -Kc \tag{1.3}$$

coagulation is a second order process that depends on the square of particle number concentration. This is described by the following equation [95]:

$$\frac{\delta c}{\delta t} = -Kc^2 \tag{1.4}$$

where c is the particle number concentration and K are constants. The difference in behaviour (linear for deposition and quadratic for coagulation) allows us to appreciate the effect of both processes on particle decay. If we plot a decay of $log(c)$ against time, we will obtain a straight

line if we have only deposition, and a curve if coagulation is present to some degree (Figure 1.10).

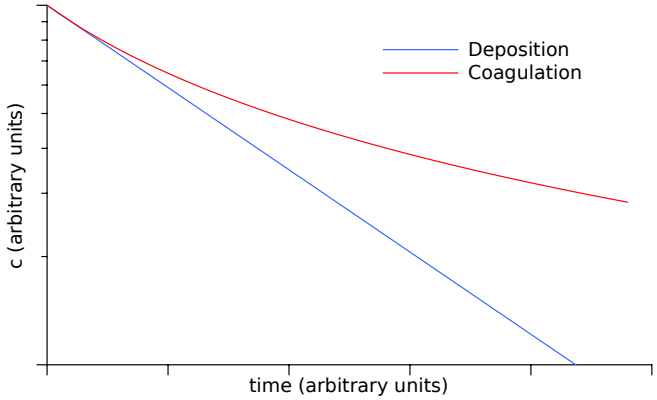

Figure 1.10: Semi-log plot showing the shape of the decay of c in the presence and absence of coagulation.

Other authors have acknowledged the importance of coagulation as a relevant removal process. It has been found to account for up to 80% of particle loss in a small chamber (1.6 m^3) with steady air, with deposition removing only 10 to 15% of paper ash particles used (average particle diameter of 0.069 μm). This situation changes with stirring, in which case deposition may account for 50% of the removal in the beginning of the experiment and up to 90% at the end [91], as coagulation rate gradually reduces as particle number decays. These results are in agreement with [96], where it was estimated that coagulation could remove from 40% to 70% of the environmental particles in a street canyon with a low wind speed (2 m/s) and around 20% at higher wind speeds (8 m/s), and with the experimental results of [97], who found high coagulation rates in rooms with low air exchange rates. All the mentioned studies focus on particles smaller than 1 μm, since the smallest particles are more likely to coagulate, not only because of their higher mobility, but because they are typically present in higher number concentrations [79]. Coagulation is known to be fairly independent of particle composition and air relative humidity [98]. There is little doubt that coagulation is a relevant removal process in enclosed or semi-enclosed and highly polluted environments [99], but it is also true that it may be negligible in most heritage environments.

1.6.7 Filtered removal

In some cases PM is removed using a filtration system. There are a number of filter configurations. Air inlet and outlet can be both filtered, or air can be filtered and recirculated into the room in a closed system. The efficiency of such filters is well known and its calculation as a function of particle size is standardised throughout the industry. Commonly, efficiency is expressed using the Minimum Efficiency Reporting Value (MERV) ranging from 1 - 20, 1 - 4 being common values for domestic filters capable of retaining only the largest particles ($>$10 μm) and 17 - 20

are typical values for fine filters used in pharmaceutical or electronic applications, capable of retaining submicron sized particles (<0.3 μm), Figure 1.11 shows the efficiency of some American Society of Heating, Refrigerating and Air-Conditioning Engineers (ASHRAE) rated filters. The ASHRAE recommends museums using filters with a MERV from 7 - 11 [100], aiming to compromise between filtering efficiency and energy use.

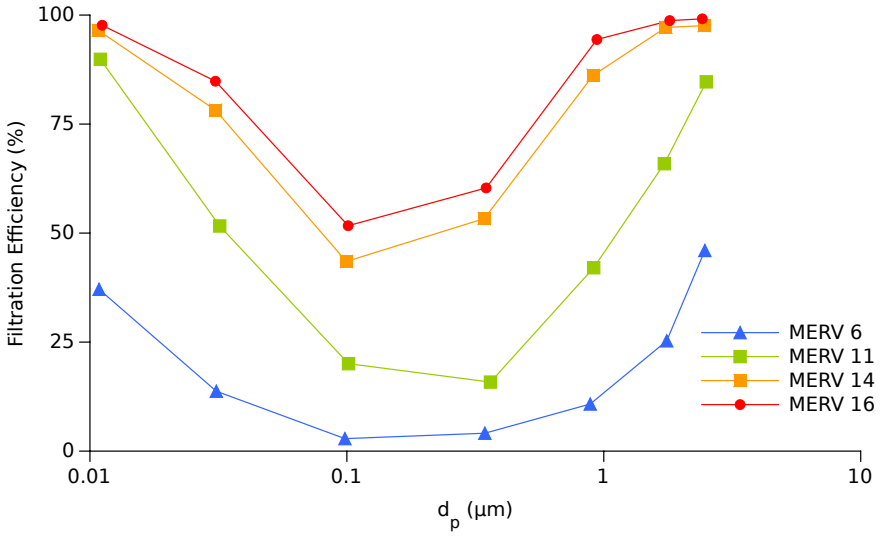

Figure 1.11: Filtration efficiency of some commercial ASHRAE-rated filters operating at 1.3 $\mathrm{m/s}$ as a function of particle diameter (adapted from [101]).

Particle filtration is governed by the same physical mechanisms as infiltration through cracks, thus the expected removal efficiency for each particle size will be inversely proportional to the particle penetration factor. Once more, fine particles deposit through Brownian diffusion and coarse particles are easily intercepted by impaction, while the accumulation mode exhibits the lowest removal efficiency. It is also worth remarking that an increase of air flow rate will improve the removal of fine particles, but would be less effective as particle size increases, as larger particles are less affected by airflow. The accumulation mode of DPM are the particles, which are removed less efficiently by ventilation systems.

1.7 The consequences of deposition

The deposition of PM on heritage surfaces can lead to a loss of value, which is not necessarily related directly with a material loss. This loss may be of aesthetic, artistic, architectural or evidential value [102], which are intricately related with economic value [103]. PM deposition can reduce the value of a surface through four mechanisms:

$$\textbf{Loss of value} \begin{cases} \text{Visual impact} \\ \text{Chemical degradation} \\ \text{Cleaning and handling} \\ \text{Biological growth} \end{cases}$$

Which can be briefly described as follows:

1. PM can merely cause area coverage and have a visual effect on the soiled object, a "visual nuisance", as it has been qualified in some of the most relevant investigations [104, 105].
2. The deposited particles might interact chemically with the surface, leading to irreversible degradation. This interaction is explored experimentally in this thesis.
3. Frequent or intense cleaning might have a negative effect on the underlying surface, as well as being a cost-intensive process. For example, the National Trust's Manual of Housekeeping states that dry cleaning methods, such as brushing, vacuum cleaning, or even the use of erasers, might be insufficient, and that the deposition of soot can produce "disfiguring, virtually indelible staining" [106].
4. Accumulation of PM can favour biological growth or the appearance of pests. This has not been studied in depth in the heritage field, but evidence exists from other areas of knowledge.

Even though evidence exists of all these phenomena having been observed indoors, research has prioritized soiling on outdoor surfaces and particularly damage layers produced on outdoor historical stone, which has been exposed to much higher doses of PM than indoor materials. The following section attempts to assess these four processes in indoor environments based on the understanding that evidence is scarce, and in some cases conclusions must be extracted from evidence obtained in outdoor experiments.

1.7.1 Soiling indoors

Figure 11 may convey a sense of the time-scale of soiling processes. It shows experimental values of the percentage of reflectance lost during environmental exposure from different publications [4, 107–111]. Due to the lack of experimental data on soiling indoors, some sheltered locations are included. The time needed to achieve a 10% loss of reflectance , which corresponds

approximately to a change visible with the naked eye[112], is highly variable and ranges from a month to a year. Note also that all soiling processes occur at a varying rate, which tends to be higher during the first weeks of exposure. This non-linear behaviour is what equations (2), (3) and (4) attempt to reflect.

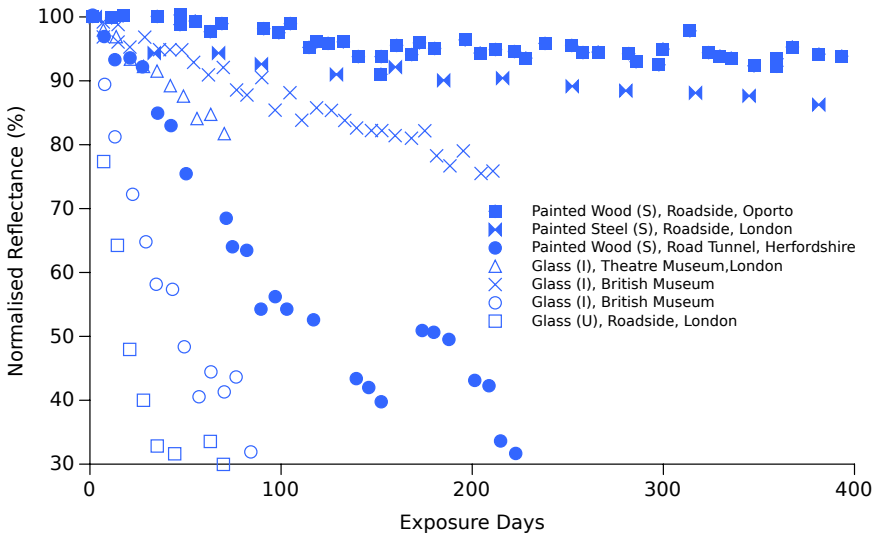

Figure 1.12: Experimental values of loss of reflectance. S=Sheltered, I=Indoors, U=Unsheltered. Data adapted from [107] (Oporto), [4] (Roadside, London), [108] (Road Tunnel, Hertfordshire), [109] (Theatre Museum, London), [110] (British Museum, London) and [111] (Unsheltered Roadside, London).

Soiling is generally assumed to be directly proportional to the loss of reflectance and lightness (or increase in haze) of a material. Several models for soiling are currently under discussion. Historically, the first dose-response functions were developed under the assumption that soiling is proportional to the square root of the concentration of total suspended PM.

$$\frac{\Omega}{\Omega_0} = k\sqrt{ct} \tag{1.5}$$

where Ω is an optical property and Ω_0 its initial value, k is a "soiling constant", t is the elapsed time and c is the concentration of PM in the surrounding air. This model was first proposed by Beloin and Haynie in 1975[113] and has been significantly endorsed by several researchers [10, 107, 114]. A second model, also widely used, follows an exponential relation in the form:

$$\frac{\Omega}{\Omega_0} = exp(kct) \tag{1.6}$$

which was firstly suggested by Mansfield and Hamilton in 1989 [115] and has also been extensively used [4, 116, 117]. The previous two models have been compared with experimental data

in [107, 110]. Lastly, the most recent research suggested the use of the Hill equation for the development of dose-response functions:

$$\Omega_t = B + \frac{K}{1 + (M/t)^H} \tag{1.7}$$

where B, K, M and H are constants that define the varying response of soiling with time (see [118] for a detailed explanation). This model has been fitted to experimental data by Lombardo and Ionescu at different occasions[119, 120] and has been tested with data collected during the MULTI-ASSESS project [121] in different European locations.

Of these models, only the bounded exponential describes area coverage in a way which is physically understandable (at least for particles larger than the wavelength of light), while the Hill equation lacks a strong phyisical basis. As can be seen in Figure 1.13 each of them can display a very different trend. In fact, any of these equations, with the appropriate constants, could fit well with any of the data series reported in Figure 1.12.

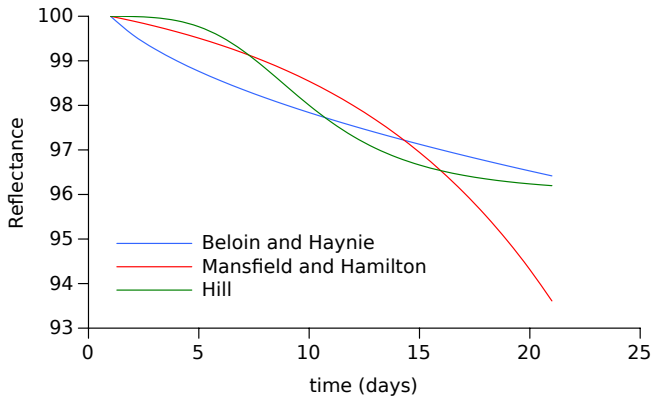

Figure 1.13: Comparison of different models describing loss of reflectance on particle deposition.

A second discussion relates to which concentration should be used as c. Some authors have suggested total suspended particles, while others have used $PM_{2.5}$, PM_{10}, DPM or particulate elemental carbon (PEC), given that most of soiling is due to traffic-generated particulates [115].

Cases of soiling indoors

Soiling outdoors is popularly associated with black stains on façades, while soiling indoors is mostly associated with the deposition of household dust, i.e. coarse particles. In effect, experimental and observational studies are markedly biased towards outdoor blackening and indoor dust, perhaps due to the experimental difficulties of discerning different particle sizes of indoor deposits, especially the smallest. However, it is not difficult to find examples of well visible deposition of fine combustion particles. Some notable examples are found at ventilation outlets

[122] or on the murals, such as those in the Carrera Palace in Padova, where inconveniently placed radiators were causing heavy soiling by dust and soot [123]. The darkening in the centre of the murals in Michelozzo's Courtyard, Florence, has been attributed to deposition of traffic-generated particles, since measurements of $PM_{2.5}$ display a high proportion of organic and elemental carbon [18]. In some occasions, the damage layers related to the deposition of combustion particles are related to the past use of the building, and not to modern traffic emissions e.g. in the Buddhist statues of the Yunguang Grottoes [124].

"Ghosting": a particular type of deposition

A specific indoor discolouration process related to heating points and the presence of semi volatile organic compounds (SVOCs) has been repeatedly reported in the literature under various names, which include "Ghosting" [125] , "Black Magic Dust" [126] and "Fogging" [127]. Even though there have been no specific mentions of the phenomenon in a heritage context, it is clearly not exclusively found in dwellings. "Ghosting" deposits differ from dry deposition by the presence of droplet-like particles, and a layer of condensed SVOCs [128]. The phenomenon is triggered only under certain conditions: emission of SVOCs (e.g. from refurbished materials), low ventilation rates, high temperature gradients (e.g. above lamps or radiators), and, naturally, the presence of PM. The dark appearance of stains is caused by the presence of elemental and organic carbon agglomerates, but coarse dust particles rich in Ca and Fe can be present as well [128]. Even though efforts have been made to isolate the causes that can initiate this type soiling, all attempts to reproduce it in experimental conditions have been unsuccessful [129].

1.7.2 Visual impact

Different kinds of particles have different visual effects. Firstly, not all particles are visible to the human eye. An important fraction of fine PM is smaller than the wavelength of light visible to humans ($\sim$390 - 750 nm). This, however, does not mean that particles smaller than $0.5\ \mu\mathrm{m}$ cannot be seen when they accumulate on a surface. Firstly, if enough particles are deposited, the deposit will become visible even if a single particle would not be seen. For example, candle soot deposits are common, even if the size of particles emitted from burning candle ranges from 10 - 100 nm [130]. Secondly, fine particles do not deposit alone, and all analyses of deposits have found a certain size distribution. Beyond that remark, it can be added that particles with diameters below the visible range can still scatter light when in suspension or when deposited on transparent materials through scattering in the Rayleigh regime. Several investigations report refractive indexes for particles or soot small in comparison with wavelength [131, 132]. These aspects; however, have not been researched in the context of heritage science.

While perceivable visually, the effects of soiling are quite difficult to quantify. Recently, attempts have been made to identify threshold of unacceptable levels of soiling on building façades. However, the relations between perception and soiling are complex, as the reaction of the public is not simply proportional to the amount of matter deposited. Soiling can be perceived in some cases as patina, and to a certain degree, it can enhance the appearance of a building [133]. The

perceived degree of soiling is also influenced by the cleanliness of the surrounding environment. Despite these issues, Brimblecombe et al. [104] used on-site questionnaires to identify soiling levels that are publicly unacceptable. Their results show that the public perception measured in terms of perceived lightness is fairly consistent with the perceived need for cleaning and could be used to define thresholds in terms of environmental particle concentration. Another study [134] shows that soiling is perceived as negative when it interferes with architectural shapes. However, these studies are focused on the darkening of building features outdoors, and it could be argued that they have a limited applicability to indoor deposition.

Some researchers have left aside the complexities of aesthetic judgement, and have concentrated on the limits on the perception of soiling. Bellan et al. [67] have measured the human eye ability to detect soot deposition on flat, plain colour surfaces using printed dots (60 - 160 μm) on white and coloured matte surfaces. Their results show that some observers are able to discern a soiled surface from a clean one when the covered area is just a bit higher than 1% of the total, and that deposition becomes obvious to all at around 9% coverage. The perceptive ability is improved if the soiled surface is observed alongside a clean one, in which case all observers identify soiling when just 3.5% of the area is covered. Experiments with larger dots (0.5 - 1 mm) have led to a threshold of 0.2% area coverage [112]. These results have been of great use for the establishment of guidelines and recommendations, e.g. by [135], since they provide a threshold value in terms of area coverage. Values between 3 and 6 % are normally taken as thresholds of unacceptable deposition, for example, Historic Royal Palaces aims to reduce deposition an 3% monthly area coverage [136]. But it must be noted that the diameters used in the experiments correspond with the coarser dust rather than with "soot" or fine particles, for which no direct account of their thresholds for visibility has been published. Recently, Druzik and Cass claimed that some specific paintings were under special risk of soiling [137]. Particularly paintings with large colour fields, such as those by Mark Rothko or Franz Kline, were assessed as being more vulnerable to the aesthetic damage due to soiling.

1.7.3 Chemical degradation

It has long been established that particulate pollution from road traffic contributes greatly to the degradation of stone outdoors. The presence of DPM has been related to the decay of carbonaceous [138] and silicate stones [139]. Also outdoors, several corrosion products of copper were identified on statues where soot was also present [140], but no formal relation was established. Although the effects on materials other than stone are less investigated, it can be expected that the reactive components of DPM also interact with organic materials that are typically displayed and used indoors, such as paper, paint and varnishes, or textiles.

There is an important lack of literature about the effects of particulate deposition on the surface of paper, leather, textiles, paintings, varnishes and any material typically found indoors, perhaps due to the complexity of the problem and the great variety of materials involved. A brief list of potential degradation pathways related to particle deposition is available in the literature [17]: (i) S-rich material (such as DPM, which contains oxidised sulfur compounds[44]) can cause discolouration of paintings. (ii) Ammonium sulfate can induce bloom on varnish. Ammonium

sulfate is a "secondary aerosol" (that is, formed in the atmosphere), but it often coexists (and even aggregates) with carbonaceous particles [141]. (iii) The presence of $CaSO_4$ favours the adsorption of soot. (iv) and Fe-Rich particles can catalyse the oxidation of SO_2 to H_2SO_4. Aged diesel particulate matter is hygroscopic [142], and therefore can favour the adsorption of water that accelerates oxidative processes, leading to fading of pigments, and damage in paper and textiles [11]. Despite the lack of systematic investigations, the effects of fine PM deposition have been repeatedly noted by conservators. Damage layers related to black carbon deposition have been detected on indoor murals and wall paintings [143], and on polychromy [144]. The word "black crust" is sometimes used to describe these damage layers found indoors, but it is a macroscopic term that gives very little information about the origin of degradation.

Conclusions may be extracted from studies carried out with particles of similar composition. Corrosion of zinc and steel has been studied in relation to the presence of deposited particles derived from the combustion of oil (which may be comparable to diesel fuel) and coal [145]. The authors concluded that in relatively unpolluted atmospheres inert particulates can induce corrosion in zinc and mild steel due to differential aeration, an effect which is masked when the overall corrosion rates increase. Oil-ash particles were also found to be much more corrosive than coal-ash particles. Although far from the heritage field in terms of temperature and concentration, some investigations have demonstrated that DPM leads to severe degradation of ceramic filters used in engine exhaust tubes [146].

1.7.4 Biological growth

Accumulated coarse particles (or dust) can become a breeding ground for pests and insects. A well researched species which breed in indoor dust are house dust mites. It is well-known that their presence requires high humidity as well as dust deposition [147]. A recommendation to avoid their presence is to keep less than 50% humidity in air and clean frequently [148].

In the field of HVAC research the role of deposited PM in fungal growth has been mentioned. PM accumulated inside ventilation systems has been found to provide the required nutrients that would not be available without soiling [149]. There is also a link with humidity. In this respect, two effects have been observed: when surfaces are heavily soiled, organisms grow at RHs considerably lower than those required for growth in clean surfaces, and moderate growth is observed in soiled materials that do not support growth in the absence of dust [149]. Research on the fungal deterioration in indoor heritage environments has revealed that dust deposited recently can have a higher potential to support fungal growth [150]. However all this evidence is merely based in field observations, and this issues have not been investigated experimentally in controlled conditions.

1.7.5 Cleaning and handling

Cleaning of soiled surfaces can induce undesired degradation. The POPART project has studied the damage caused by different cleaning methods on historic plastics [151]. It is well known that cementation of coarse dust increases the difficulty of removal [152]. DPM behaves in a

similar way, due to its ability to penetrate into pores and its potential chemical interaction with the surface. As mentioned above, the National Trust's Manual of Housekeeping warns that many common dry cleaning methods are insufficient for the removal of soot [106]. In cases of extreme soiling, it has been reported that vacuum cleaning removes only the loose deposits of smoke particulates, and that wiping may further attach particles to porous surfaces [153]. These difficulties have prompted the use of laser cleaning methods; however, laser removal of particles from organic materials have been found to result in yellowing of the underlying surface [154, 155]. Lastly, some activities related with cleaning, for example, the removal of dust from tapestries, are between the most resource-intensive tasks in heritage institutions [156].

1.8 Conclusions

In the past, there has been considerable discussion on of the terminology of staining of façades (black crust formation, staining, darkening, blackening, soiling...) [104, 157]; however, such discussion has not taken place for indoor heritage. For example, it is not clear what the word "soot" refers to in some cases. It can refer to carbon-based agglomerates in suspension, or the same particles deposited on a surface, or a black stain of unknown composition but of "carbonaceous" appearance, which might also be only superficial deposition. There is a need for terminology that makes a clear distinction between suspended fine particles (DPM, combustion-derived or even soot), dry deposition of fine or coarse particles without further effects and removable with cleaning (which could be called darkening, or soiling), and the degradation layer formed due to the interaction of the deposit with the underlying surface.

The formation of black stains in the presence of SVOCs ("ghosting"), or the emission of fine and ultrafine particles when indoor dust is in contact with warm surfaces are phenomena that have been repeatedly observed in indoor environments. It is unknown what the impact of this type of soling is, and whether in some cases they are wrongly attributed to outdoor sources.

PM monitoring in heritage sites is generally focused on coarse dust, and the two most frequently measured particle types are PM_{10} and $PM_{2.5}$, which include particles up to 10 and 2.5 μm respectively. This standard has limitations. Measurements of $PM_{2.5}$ sum up some particles from the coarse mode (>1 μm) and some from the fine mode (<1 μm) and therefore these values do not help to identify the fine and coarse fractions, which could be used to assess the outdoor or indoor origin of the particles. Size-resolved measurements of particle concentration would provide more information on the likely source and typology of particles; however, size distributions require costly equipment. A much more informative and cost-effective measurement would be PM_{10} and PM_1, or PM_{10-1} and PM_1. In a heritage site located in an urban environment, for example, these values would provide a useful estimate of particles as a consequence of traffic emissions that penetrate into a building.

When reporting number concentrations, the notation of PM_x can be misleading, because small particles can be very numerous and dominate the measurement. It could be, for example, that in a number concentration of $PM_{2.5}$, 90% of the particles were below 0.1 μm. For this reason, in this thesis we will always report a lower and upper bound to our concentration measurements.

Very little is known about what occurs after soiling. There is a significant disproportion between the detailed knowledge of the aerodynamics of fine particles, and what is currently known about the chemical effects of the most common particle types and the potential degradation of soiled (heritage) surfaces due to cleaning or biological growth. The scarce evidence available is just enough to assess that fine particles derived from combustion can have an active role in the degradation of materials. Furthermore, considering the costs associated with cleaning, it is important to know if removal of deposited fine particles of different properties should be a priority. Risk assessment cannot be based solely on the concentration of fine particles. There is a need for research into chemical interactions between the most common fine particulates and different materials that represent indoor heritage surfaces.

In contrast, the aerodynamics of fine PM is well known. As explained above, the accumulation mode (0.1 - 1 μm), displays low deposition rates due to its size, low re-suspension rates, and a high penetration efficiency through cracks and filters. Low deposition rates have different implications. Deposition will be a slow process, but it will occur eventually if particles are not removed. They will distribute evenly around the space, depositing far from the source, and will reach areas in walls and ceiling that are difficult to access. Low re-suspension rates, in combination with a small size that favours penetration into porous surfaces, will lead to difficulties with cleaning.

Despite the solidity of the knowledge on the physics of aerosols, we find there is still a long way to go before we are able to produce risk assessments that are site-specific, accurate, and that can trigger action. There are two main needs that are not met by the current knowledge:

1. We need to be able to manage deposition. Our predictions have to involve factors that can be modified (e.g. room layout, location of sources, numbers of visitors, ventilation and heating operation) and have to reveal the consequences of a change in these factors.

2. We need to be able to assess the loss of value. We need to understand the relation between composition, diameter, number and mass with cleaning, biological growth, visual impact and chemical degradation in order to judge which amount (of which type) of PM constitutes unacceptable deposition.

To fill the corresponding knowledge gaps, I think that the first step should be the production of a computational model that provides a satisfactory understanding of deposition. This chapter included some simple equations and general principles describing the aerodynamic behaviour of PM. But in order to develop a predictive model we need to dwell deeper into the underlying physics. As explained above, particles are transported by air. This simple statement masks a complex reality: air movement often implies turbulence, and therefore a set of non-linear phenomena that require complex simulations.

References

[1] N. Ghedini et al. “Atmospheric aerosol monitoring as a strategy for the preventive conservation of urban monumental heritage: The Florence Baptistery”. *Atmospheric Environment* 45:33 (2011), pp. 5979–5987.

[2] B. Horemans et al. “Evaluation of airborne particles at the Alhambra monument in Granada , Spain”. *Microchemical Journal* 99:2 (2011), pp. 429–438.

[3] F. Monforti et al. “An evaluation of particle deposition fluxes to cultural heritage sites in Florence, Italy.” *The Science of the Total Environment* 334-335 (2004), pp. 61–72.

[4] J. Watt, D. Jarrett, and R. Hamilton. “Dose-response functions for the soiling of heritage materials due to air pollution exposure”. *Science of the Total Environment* 400:1-3 (2008), pp. 415–424.

[5] F. Karaca. “Mapping the corrosion impact of air pollution on the historical peninsula of Istanbul”. *Journal of Cultural Heritage* Article in press (2012).

[6] D. de la Fuente et al. “City scale assessment model for air pollution effects on the cultural heritage”. *Atmospheric Environment* 45:6 (2011), pp. 1242–1250.

[7] D. Camuffo and A. Bernardi. “Controlling the microclimate and particulate matter inside the historic anatomy theatre, Padua”. *Museum Management and Curatorship* 15:3 (1996), pp. 285–298.

[8] Z. Spolnik et al. “Influence of different types of heating systems on particulate air pollutant deposition: The case of churches situated in a cold climate”. *Journal of Cultural Heritage* 8:1 (2007), pp. 7–12.

[9] L. Samek et al. “The impact of electric overhead radiant heating on the indoor environment of historic churches”. *Journal of Cultural Heritage* 8:4 (2007), pp. 361–369.

[10] M. Urosevic et al. “Black soiling of an architectural limestone during two-year term exposure to urban air in the city of Granada (Spain)”. *Science of the Total Environment* 414 (2011), pp. 564–75.

[11] K. Gysels, F. Deutsch, and R. Van Grieken. “Characterisation of particulate matter in the Royal Museum of Fine Arts, Antwerp, Belgium”. *Atmospheric Environment* 36:25 (2002), pp. 4103–4113.

[12] T. Mouratidou and C. Samara. “PM2.5 and associated ionic component concentrations inside the archaeological museum of Thessaloniki, N. Greece”. *Atmospheric Environment* 38:27 (2004), pp. 4593–4598.

[13] A. Worobiec et al. “Transport and deposition of airborne pollutants in exhibition areas located in historical buildings–study in Wawel Castle Museum in Cracow, Poland”. *Journal of Cultural Heritage* 11:3 (2010), pp. 354–359.

[14] T. Hu et al. “Characterization of winter airborne particles at Emperor Qin’s Terracotta Museum, China”. *Science of the Total Environment* 407:20 (2009), pp. 5319–5327.

[15] K. Gysels et al. “Indoor environment and conservation in the Royal Museum of Fine Arts, Antwerp, Belgium”. *Journal of Cultural Heritage* 5:2 (2004), pp. 221–230.

[16] A. Verney-Carron et al. “Predicting changes of glass optical properties in polluted atmospheric environment by a neural network model”. *Atmospheric Environment* 54 (2012), pp. 141–148.

[17] D. Camuffo et al. “Indoor air quality at the Correr Museum, Venice, Italy.” *The Science of the Total Environment* 236:1-3 (1999), pp. 135–52.

[18] S. Nava et al. “An integrated approach to assess air pollution threats to cultural heritage in a semi-confined environment: The case study of Michelozzo’s Courtyard in Florence (Italy)”. *Science of the Total Environment* 408:6 (2010), pp. 1403–1413.

[19] B. Krupinska et al. “Assessment of the air quality (NO2, SO2, O3 and particulate matter) in the Plantin-Moretus Museum/Print Room in Antwerp, Belgium, in different seasons of the year”. *Microchemical Journal* 102 (2012), pp. 49–53.

[20] N. Hanapi and S. Din. “A Study on the airborne particulate matter in selected museums of peninsular Malaysia”. *Procedia - Social and Behavioral Sciences* 50 (2012), pp. 602–613.

[21] A. Bonazza et al. “Mapping the impact of climate change on surface recession of carbonate buildings in Europe.” *The Science of the Total Environment* 407:6 (2009), pp. 2039–2050.

[22] Y. H. Yoon and P. Brimblecombe. “The distribution of soiling by coarse particulate matter in the museum environment.” *Indoor air* 11:4 (2001), pp. 232–40.

[23] M. Ferm et al. “Deposition measurement of particulate matter in connection with corrosion studies”. *Analytical and Bioanalytical Chemistry* 384:6 (2006), pp. 1320–30.

[24] L. Andelova et al. “Characterization of airborne particles in the Baroque Hall of the National Library in Prague”. *E-Preservation Science* 7 (2010), pp. 141–146.

[25] W. W. Nazaroff. *Airborne particles in museums*. Getty Conservation Institute, Marina del Rey, Calif. : 1993.

[26] P. Gehr and J. Heyder. *Particle-Lung Interactions*. Lung Biology in Health and Disease. Taylor & Francis, 2000.

[27] M. Jantunen and J. Jaakkola. *Assessment of Exposure to Indoor Air Pollutants*. WHO regional publications / European series: European series / WHO, Regional Office for Europe. World Health Organization, Regional Office for Europe, 1997.

[28] R. M. Harrison. “Key pollutants—airborne particles”. *Science of The Total Environment* 334–335 (2004), pp. 3–8.

[29] P. McMurry, M. Shepherd, and J. Vickery. *Particulate matter science for policy makers: a NARSTO assessment*. EPRI Report 1007735. Cambridge University Press, 2004.

[30] AQEG. *Particulate matter in the UK*. London: Defra, 2005.

[31] A. Namdeo and M. Bell. “Characteristics and health implications of fine and coarse particulates at roadside, urban background and rural sites in {UK}”. *Environment International* 31:4 (2005), pp. 565–573.

[32] D. Butterfield et al. *2011 Annual report for the UK black carbon network*. Tech. rep. Hampton Road, Teddington, Middlesex, TW11 0LW: National Physical Laboratory, 2012.

[33] *National air quality and emissions trends report*. Tech. rep. Research Triangle Park NC 27711: United States Environmental Protection Agency, Office of Air Quality, Planning and Standards, 2001.

[34] X. Querol et al. “PM10 and PM2.5 source apportionment in the Barcelona Metropolitan area, Catalonia, Spain”. *Atmospheric Environment* 35:36 (2001), pp. 6407–6419.

[35] L. Díaz-Robles, J. Fu, and G. Reed. “Modeling and source apportionment of diesel particulate matter”. *Environment International* 34:1 (2008), pp. 1–11.

[36] AQEG. *Fine particulate matter (PM2.5) in the United Kingdom*. London: Defra, 2012.

[37] F. Yan et al. “Global emission projections of particulate matter (PM): I. Exhaust emissions from on-road vehicles”. *Atmospheric Environment* 45:28 (2011), pp. 4830–4844.

[38] D. G. Streets et al. “Black carbon emissions in China”. *Atmospheric Environment* 35:25 (2001), pp. 4281–4296.

[39] *Air quality guidelines for Europe*. Tech. rep. Copenhagen: World Health Organization Regional Office for Europe, WHO Regional Publications, 2000.

[40] *European Comission air quality standards*. 2008. URL: http://ec.europa.eu/environment/air/quality/standards.htm (visited on 08/06/2014).

[41] *National Ambient Air Quality Standards for Particulate Matter; Final Rule*. Tech. rep. Environmental Protection Agency, 2013.

[42] P. R. Buseck et al. "Are black carbon and soot the same?" *Atmospheric Chemistry and Physics Discussions* 12:9 (2012), pp. 24821–24846.

[43] M. Sharma, A. K. Agarwal, and K. Bharathi. "Characterization of exhaust particulates from diesel engine". *Atmospheric Environment* 39:17 (2005), pp. 3023–3028.

[44] M. Mattimaricq. "Chemical characterization of particulate emissions from diesel engines: A review". *Journal of Aerosol Science* 38:11 (2007), pp. 1079–1118.

[45] J. Song, J. Wang, and A. L. Boehman. "The role of fuel-born catalysts in diesel particulate oxidation behavior". *Combustion and Flame* 146:1– 2 (2006), pp. 73–84.

[46] Z. Su, W. Zhou, and Y. Zhang. "New insight into the soot nanoparticles in a candle flame". *Chemical Communications* 47:16 (2011), pp. 4700–4702.

[47] K. O. Lee et al. "Morphological investigation of the microstructure, dimensions, and fractal geometry of diesel particulates". *Proceedings of the Combustion Institute* 29:1 (2002), pp. 647–653.

[48] D. Williams et al. "Particulate emissions from in-use motor vehicles: Spark and ignition vehicles". *Atmospheric Environment* 23:12 (1989), pp. 2639–2645.

[49] A. Sarvi et al. "Particulate emissions from large-scale medium-speed diesel engines: 2. Chemical composition". *Fuel Processing Technology* 92:10 (2011), pp. 2116–2122.

[50] E. Sahan, H. Brink, and E. Weijers. *Carbon in Atmospheric Particulate Matter*. Tech. rep. ECN Energy Research Centre of the Netherlands, 2008.

[51] J. J. Schauer. "Evaluation of elemental carbon as a marker for diesel particulate matter". *Journal of Exposure Analysis and Environmental Epidemiology* 13:6 (2003), pp. 443–53.

[52] M. Kendall et al. "Characterisation of selected speciated organic compounds associated with particulate matter in London". *Atmospheric Environment* 35:14 (2001), pp. 2483–2495.

[53] J. Pagels et al. "Chemical composition and mass emission factors of candle smoke particles". *Journal of Aerosol Science* 40:3 (2009), pp. 193–208.

[54] G. Buonanno, L. Morawska, and L. Stabile. "Particle emission factors during cooking activities". *Atmospheric Environment* 43:20 (2009), pp. 3235–3242.

[55] N. Jones et al. "Indoor/outdoor relationships of particulate matter in domestic homes with roadside, urban and rural locations". *Atmospheric Environment* 34:16 (2000), pp. 2603–2612.

[56] A. Bernardi and D. Camuffo. "Microclimate in the Chiericati Palace Municipal Museum, Vicenza". *Museum Management and Curatorship* 14:1 (1995), pp. 5–18.

[57] A. Afshari, U. Matson, and L. E. Ekberg. "Characterization of indoor sources of fine and ultrafine particles: a study conducted in a full-scale chamber". *Indoor Air* 15:2 (2005), pp. 141–150.

[58] I. K. Koponen et al. "Indoor air measurement campaign in Helsinki, Finland 1999 – the effect of outdoor air pollution on indoor air". *Atmospheric Environment* 35:8 (2001), pp. 1465–1477.

[59] T. Hussein et al. "Indoor and outdoor particle size characterization at a family house in Espoo–Finland". *Atmospheric Environment* 39:20 (2005), pp. 3697–3709.

[60] J. Thornburg et al. “Penetration of particles into buildings and associated physical factors. Part I: Model development and computer simulations”. *Aerosol Science and Technology* 34:3 (2001), pp. 284–296.

[61] K. Na and D. Cocker. “Organic and elemental carbon concentrations in fine particulate matter in residences, schoolrooms, and outdoor air in Mira Loma, California”. *Atmospheric Environment* 39:18 (2005), pp. 3325–3333.

[62] T. Gotschi et al. “Comparison of black smoke and PM2.5 levels in indoor and outdoor environments of four European cities”. *Environmental Science & Technology* 36:6 (2002), pp. 1191–7.

[63] M. Viana, S. Díez, and C. Reche. “Indoor and outdoor sources and infiltration processes of PM1 and black carbon in an urban environment”. *Atmospheric Environment* 45:35 (2011), pp. 6359–6367.

[64] T. L. Thatcher and D. W. Layton. “Deposition, resuspension, and penetration of particles within a residence”. *Atmospheric Environment* 29:13 (1995), pp. 1487–1497.

[65] W. W. Nazaroff. “Indoor particle dynamics”. *Indoor Air* 14:Suppl 7 (2004), pp. 175–83.

[66] Y. Zhu et al. “Penetration of freeway ultrafine particles into indoor environments”. *Journal of Aerosol Science* 36:3 (2005), pp. 303–322.

[67] M. P. Ligocki et al. “Characteristics of airborne particles inside southern California museums”. *Atmospheric Environment* 27:5 (1993), pp. 697–711.

[68] D.-L. Liu and W. W. Nazaroff. “Particle penetration through building cracks”. *Aerosol Science and Technology* 37:October 2011 (2010), pp. 37–41.

[69] D.-L. Liu and W. W. Nazaroff. “Modeling pollutant penetration across building envelopes”. *Atmospheric Environment* 35:26 (2001), pp. 4451–4462.

[70] L. Tian et al. “Mathematical model of particle penetration through smooth/rough building envelop leakages”. *Building and Environment* 44:6 (2009), pp. 1144–1149.

[71] T. Hussein et al. “Particle size characterization and emission rates during indoor activities in a house”. *Atmospheric Environment* 40:23 (2006), pp. 4285–4307.

[72] D. Camuffo, G. Sturaro, and A. Valentino. “Showcases: a really effective mean for protecting artworks?” *Thermochimica Acta* 365:1–2 (2000), pp. 65–77.

[73] S. Weber. “Exposure of churchgoers to airborne particles”. *Environmental Science & Technology* 40:17 (2006), pp. 5251–5256.

[74] A. Hirvonen et al. “Thermal desorption of organic compounds associated with settled household dust”. *Indoor Air* 4:4 (1994), pp. 255–264.

[75] E. K. Pedersen et al. “Physical changes of indoor dust caused by hot surface contact”. *Atmospheric Environment* 35:24 (2001), pp. 4149–4157.

[76] D. Mumovic and M. Santamouris. *A Handbok of Sustainable Building Design and Engineering*. 1st. London, Sterling, VA: Earthscan, 2009, p. 328.

[77] L. H. Mortensen, C. Rode, and R. Peuhkuri. “Investigation of airflow patterns in a microclimate by particle image velocimetry (PIV)”. *Building and Environment* 43:11 (2008), pp. 1929–1938.

[78] D. Camuffo. “Wall temperature and the soiling of murals”. *Museum Management and Curatorship* 10:4 (1991), pp. 373–383.

[79] W. W. Nazaroff and G. R. Cass. “Mathematical modeling of indoor aerosol dynamics”. *Environmental Science and Technology* 23:2 (1989), pp. 157–166.

[80] A. C. K. Lai and W. W. Nazaroff. “Modeling indoor particle deposition from turbulent flow onto smooth surfaces”. *Journal of Aerosol Science* 31:4 (2000), pp. 463–476.

[81] W. W. Nazaroff et al. “Particle deposition in museums: comparison of modeling and measurement results”. *Aerosol Science and Technology* 13:3 (1990), pp. 332–348.

[82] T. Hussein et al. “Deposition rates on smooth surfaces and coagulation of aerosol particles inside a test chamber”. *Atmospheric Environment* 43:4 (2009), pp. 905–914.

[83] W. C. Hinds. *Aerosol technology: properties, behavior, and measurement of airborne particles*. Wiley-Interscience. Wiley, 1999.

[84] M. Guingo and J.-P. Minier. “A new model for the simulation of particle resuspension by turbulent flows based on a stochastic description of wall roughness and adhesion forces”. *Journal of Aerosol Science* 39:11 (2008), pp. 957–973.

[85] A. R. Ferro, R. J. Kopperud, and L. M. Hildemann. “Source strengths for indoor human activities that resuspend particulate matter”. *Environmental Science & Technology* 38:6 (2004), pp. 1759–64.

[86] V. Kontozova-Deutsch et al. “Characterization of indoor and outdoor atmospheric pollutants impacting architectural monuments: the case of San Jerónimo Monastery (Granada, Spain)”. *Environmental Earth Sciences* 63 (7-8 2011), pp. 1433–1445.

[87] M. Lazaridis and Y. Drossinos. “Multilayer resuspension of small identical particles by turbulent flow”. *Aerosol Science and Technology* 28:June 2012 (1998), pp. 37–41.

[88] M. Lazaridis, Y. Drossinos, and P. Georgopoulos. “Turbulent resuspension of small nondeformable particles”. *Journal of Colloid and Interface Science* 204:1 (1998), pp. 24–32.

[89] L. Biasi et al. “Use of a simple model for the interpretation of experimental data on particle resuspension in turbulent flows”. *Journal of Aerosol Science* 32 (2001).

[90] G. A. Loosmore. “Evaluation and development of models for resuspension of aerosols at short times after deposition”. *Atmospheric Environment* 37:1352 (2003), pp. 639–647.

[91] M. Schnell, C. Cheung, and C. Leung. “Investigation on the coagulation and deposition of combustion particles in an enclosed chamber with and without stirring”. *Journal of Aerosol Science* 37:11 (2006), pp. 1581–1595.

[92] L. Gidhagen et al. “Urban scale modeling of particle number concentration in Stockholm”. *Atmospheric Environment* 39 (2005), pp. 1711–1725.

[93] M. Schnell, C. Cheung, and C. Leung. “Coagulation of diesel particles in an enclosed chamber”. *Journal of Aerosol Science* 35:10 (2004), pp. 1289–1293.

[94] L. Morawska, M. Jamriska, and N. D. Bofinger. “Size characteristics and ageing of the environmental tobacco smoke”. *Science of the Total Environment* 196:1 (1997), pp. 43–55.

[95] P. Eastwood. *Particulate emissions from vehicles*. Wiley-professional engineering publishing series. John Wiley & Sons, 2008.

[96] L. Gidhagen et al. “Simulation of NOx and ultrafine particles in a street canyon in Stockholm, Sweden”. *Atmospheric Environment* 38:14 (2004), pp. 2029–2044.

[97] M. Jamriska and L. Morawska. “Quantitative assessment of the effect of surface deposition andcoagulation on the dynamics of submicrometer particles indoors”. *Aerosol Science and Technology* 37:5 (2003), pp. 425–436.

[98] L. Gidhagen et al. “Model simulation of ultrafine particles inside a road tunnel”. *Atmospheric Environment* 37:15 (2003), pp. 2023–2036.

[99] M. Ketzel and R. Berkowicz. “Modelling the fate of ultrafine particles from exhaust pipe to rural background: an analysis of time scales for dilution, coagulation and deposition”. *Atmospheric Environment* 38:17 (2004), pp. 2639–2652.

[100] ASHRAE. “Museums, libraries and archives”. *Heating, Ventilating and Air-Conditioning: Applications. ASHRAE Handbook.* Atlanta, Ga.: ASHRAE, 2003. Chap. 21.

[101] W. Kowalski and W. Bahnfleth. *MERV Filter Models for Aerobiological Applications*. Tech. rep. The Pennsylvania State University, 1999.

[102] R. Lefèvre and C. Sabbioni. *Climate change and cultural heritage*. CUEBC. Scienze e materia del patrim. cult. Edipuglia, 2010.

[103] P. Lehtovuori. *Economics and Built Heritage: Seminar Proceedings : Built Heritage–value Adding Sector*. Nordic Council of Ministers, 2007.

[104] P. Brimblecombe and C. M. Grossi. “Aesthetic thresholds and blackening of stone buildings.” *The Science of the Total Environment* 349:1-3 (2005), pp. 175–89.

[105] R. Hamilton and T. Mansfield. “The soiling of materials in the ambient atmosphere”. *Atmospheric Environment* 26:18 (1992), pp. 3291–3296.

[106] *The National Trust manual of housekeeping: the care of collections in historic houses open to the public*. Henry Ford Estate collection. National Trust, Elsevier, 2006.

[107] C. A. Pio, M. M. Ramos, and A. C. Duarte. “Atmospheric aerosol and soiling of external surfaces in an urban environment”. *Atmospheric Environment* 32:11 (1998), pp. 1979–1989.

[108] T. Mansfield et al. “Diesel particulate emissions and the implications for the soiling of buildings”. *The Environmentalist* 11:4 (1991), pp. 243–254.

[109] D. Ford. “Deposition rates of particulate matter in the internal environment of two London museums”. *Atmospheric Environment* 33:29 (1999), pp. 4901–4907.

[110] S. Adams. “A particle accumulation study during the reconstruction of The Great Court, British Museum”. *Journal of Cultural Heritage* 3:4 (2002), pp. 283–287.

[111] M. J. R. Schwar. “Nuisance dust deposition and soiling rate measurements”. *Environmental Technology* 19:2 (1998), pp. 223–229.

[112] L. M. Bellan, L. G. Salmon, and G. R. Cass. “A Study on the human ability to detect soot deposition onto works of art”. *Environmental Science & Technology* 34:10 (2000), pp. 1946–1952.

[113] N. J. Beloin and F. H. Haynie. “Soiling of building materials”. *Journal of the Air Pollution Control Association* 25:4 (1975), pp. 399–403.

[114] C. Grossi. “Soiling of building stones in urban environments”. *Building and Environment* 38:1 (2003), pp. 147–159.

[115] J. Watt et al. *The effects of air pollution on cultural heritage*. Springer, 2009.

[116] P. Brimblecombe and C. M. Grossi. “Millennium-long damage to building materials in London.” *The Science of the Total Environment* 407:4 (2009), pp. 1354–61.

[117] P. Pesava et al. “Dry deposition of particles to building surfaces and soiling”. *Science of the Total Environment* 235:1-3 (1999), pp. 25–35.

[118] A. Ionescu et al. “Modeling of soiling based on silica-soda-lime glass exposure at six European sites”. *The Science of the Total Environment* 369:1-3 (2006), pp. 246–55.

[119] T. Lombardo et al. “Dose-response function for the soiling of silica-soda-lime glass due to dry deposition”. *The Science of the Total Environment* 408:4 (2010), pp. 976–84.

[120] T. Lombardo et al. “Soiling of silica-soda-lime float glass in urban environment: measurements and modelling”. *Atmospheric Environment* 39:6 (2005), pp. 989–997.

[121] J. Tidblad et al. *Multi Assess report (Model for multi-pollutant impact andd assessment of threshold levels for cultural heritage)*. Tech. rep. Stockholm, Sweden: Swedish Corrosion Institute (SCI), 2005.

[122] H. Timmer and M. Zeller. “Particle deposition near ceiling induction outlets”. *International Journal of Refrigeration* 27:3 (2004), pp. 248–254.

[123] D. Camuffo et al. “The impact of heating, lighting and people in re-using historical buildings: a case study”. *Journal of Cultural Heritage* 5:4 (2004), pp. 409–416.

[124] H. Zhang et al. “Damage or protection? The role of smoked crust on sandstones from Yungang Grottoes”. *Journal of Archaeological Science* 40:2 (2013), pp. 935–942.

[125] F. Vigil. *Black stains in houses: soot, dust, or ghosts?* 1998. URL: http://www.homeenergy.org/show/article/nav/refrigerators/id/1360/magazine/107 (visited on 08/06/2014).

[126] L. Morawska and T. Salthammer. *Indoor Environment*. Wiley, 2006.

[127] T. Salthammer and E. Uhde. *Organic indoor air pollutants*. Wiley, 2009.

[128] U. E. A. Fittschen et al. “Indoor aerosol determination with respect to a soiling phenomenon in private residences”. *Environmental Science & Technology* 47:1 (2013), pp. 608–615.

[129] T. Salthammer et al. “Effect of particle concentration and semi-volatile organic compounds on the phenomenon of "black magic dust" in dwellings”. *Building and Environment* 46:10 (2011), pp. 1880–1890.

[130] S. Zai, H. Zhen, and W. Jia-song. “Studies on the size distribution, number and mass emission factors of candle particles characterized by modes of burning”. *Journal of Aerosol Science* 37:11 (2006), pp. 1484–1496.

[131] T. C. Bond and R. W. Bergstrom. “Light absorption by carbonaceous articles: an investigative review”. *Aerosol Science and Technology* 40:1 (2006), pp. 27–67.

[132] Q. Zhang and P. Rubini. “Modelling of light extinction by soot particles”. *Fire Safety Journal* 46:3 (2011), pp. 96–103.

[133] C. M. Grossi et al. “Color changes in architectural limestones from pollution and cleaning”. *Color Research & Application* 32:4 (2007), pp. 320–331.

[134] C. M. Grossi and P. Brimblecombe. “Aesthetics of simulated soiling patterns on architecture”. *Environmental Science & Technology* 38:14 (2004), pp. 3971–6.

[135] J. Tétreault. *Airborne pollutants in museums, galleries and archives: risk assessment, control strategies and preservation management*. Canadian Heritage. Canadian Conservation Institute, 2003.

[136] F. K. “Creative conservation risk management: evolving a collection risk management strategy at a major heritage attraction.” *Collections* 9:1 (2013), pp. 103–114.

[137] J. R. Druzik and G. R. Cass. “A new look at soiling of contemporary paintings by soot in art museums”. *The Indoor Air Quality Meeting for Museums Conference Report, Oxford Brookes University*. Oxford Brookes University, 2000, pp. 22–27.

[138] C. Rodriguez-Navarro and E. Sebastian. “Role of particulate matter from vehicle exhaust on porous building stones (limestone) sulfation”. *Science of the Total Environment* 187:2 (1996), pp. 79–91.

[139] J. Simão, E. Ruiz-Agudo, and C. Rodriguez-Navarro. “Effects of particulate matter from gasoline and diesel vehicle exhaust emissions on silicate stones sul-

fation". *Atmospheric Environment* 40:36 (2006), pp. 6905–6917.

[140] H. Strandberg. "Reactions of copper patina compounds—I. Influence of some air pollutants". *Atmospheric Environment* 32:20 (1998), pp. 3511–3520.

[141] M. Jacobson. *Atmospheric pollution: history, science, and regulation*. Cambridge University Press, 2002.

[142] O. B. Popovicheva et al. "Quantification of the hygroscopic effect of soot aging in the atmosphere: laboratory simulations". *The Journal of Physical Chemistry A* 115:3 (2011), pp. 298–306.

[143] M. Perez-Alonso et al. "Analysis of bulk and inorganic degradation products of stones, mortars and wall paintings by portable Raman microprobe spectroscopy". *Analytical and Bioanalytical Chemistry* 379:1 (2004), pp. 42–50.

[144] A. Duran et al. "Degradation of gold and false golds used as gildings in the cultural heritage of Andalusia, Spain". *Journal of Cultural Heritage* 9:2 (2008), pp. 184–188.

[145] A. Askey et al. "The effect of fly-ash particulates on the atmospheric corrosion of zinc and mild steel". *Corrosion Science* 34:7 (1993), pp. 1055–1081.

[146] L. Montanaro. "Durability of ceramic filters in the presence of some diesel soot oxidation additives". *Ceramics International* 25 (1999), pp. 437–445.

[147] J. Korsgaard. "House-Dust Mites and Absolute Indoor Humidity". *Allergy* 38:2 (1983), pp. 85–92.

[148] H. Harving et al. "House dust mite allergy and anti-mite measures in the indoor environment". *Allergy* 46 (1991), pp. 33–38.

[149] K. K. Foarde, D. W. VanOsdell, and J. C. S. Chang. "Evaluation of Fungal Growth on Fiberglass Duct Materials for Various Moisture, Soil, Use, and Temperature Conditions". *Indoor Air* 6:2 (1996), pp. 83–92.

[150] N. B. F. Pinzari V. Cialei. "Measurement of the fungal deteriorating potential in the dust of indoor environments" (2010).

[151] B. Lavédrine, A. Fournier, and G. Martin. *POPART*. Comité Des Travaux Historiques Et Scientifiques, 2012.

[152] P. Brimblecombe, D. Thickett, and Y. H. Yoon. "The cementation of coarse dust to indoor surfaces". *Journal of Cultural Heritage* 10:3 (2009), pp. 410–414.

[153] S. Spafford-Ricci and F. Graham. "The fire at the Royal Saskatchewan Museum, Part 2: removal of soot from artifacts and recovery of the building". *Journal of the American Institute for Conservation* 39:1 (2000), pages.

[154] M. Strlič et al. "Surface modification during Nd:YAG (1064 nm) pulsed laser cleaning of organic fibrous materials". *Applied Surface Science* 207:1–4 (2003), pp. 236–245.

[155] M. Strlič et al. "Optimisation and on-line acoustic monitoring of laser cleaning of soiled paper". *Applied Physics A: Materials Science & Processing* 81:5 (2005), pp. 943–951.

[156] F. Lennard and M. Hayward. *Tapestry Conservation: Principles and Practice*. Butterworth-Heinemann series in conservation and museology. Butterworth-Heinemann, 2006.

[157] L. Toniolo, C. Zerbi, and R. Bugini. "Black layers on historical architecture". *Environmental Science and Pollution Research* 16 (2 2009), pp. 218–226.

2
Simulation strategies

2.1 Introduction

This section describes the different approaches to the simulation of transport deposition of indoor particulate matter. There are many simulation approaches of different complexity. The simplest models involve only a few equations, and are useful in some contexts such as the prediction of deposition rates in well-mixed environments and uncomplicated environments. The most complex models can simulate many physical phenomena and their solution requires numerical methods. Every model answers different questions, in other words, they require different inputs and offer different outputs. This section classifies the many solutions available in the literature in their main families. It also looks into the detail of more complex Computational Fluid Dynamics (CFD) models, which we will use later in this work.

2.2 Well-mixed models

Well-mixed models are based in the assumption that the behaviour of a room is homogeneous: we consider that a space can be represented by the behaviour of a point in its centre, or we consider that a room is well characterised by its average behaviour. The well-mixed assumption is valid in many situations, because it is very common for indoor spaces to have a relatively homogeneous concentration of pollutants, distribution of temperature or relative humidity. The reader will see some good examples of this in our own experiments in real buildings in the next chapters.

2.2.1 Single-box models

The first and most influential model to describe deposition of particulate matter in a box of homogeneous concentration was derived by Crump and Seinfield [1] based on earlier work by Corner and Pendlebury [2]. Their intention was to simulate the sedimentation of particles in vessels of "arbitrary shape" for industrial applications, and they probably did not suspect the many applications that their research would have in indoor air problems. Here we report the model as described by [3]. Their approach predicts the rate of change of concentration c:

$$\frac{dc}{dt} = -\beta c \tag{2.1}$$

where t is the decay time and β is a deposition coefficient, which is calculated with a different expression for walls (β_w), floor (β_f) and ceiling (β_c):

$$\beta_w = \frac{2S_w}{\pi V}\sqrt{\mathscr{D}K_e} \tag{2.2}$$

$$\beta_c = \frac{S_c}{V}\frac{v_s}{\exp\left(\frac{\pi}{2}\frac{v_s}{\sqrt{\mathscr{D}K_e}}\right) - 1} \tag{2.3}$$

$$\beta_f = \frac{S_f}{V}\frac{v_s}{1 - \exp\left(-\frac{\pi}{2}\frac{v_s}{\sqrt{\mathscr{D}K_e}}\right)} \tag{2.4}$$

where v_s is the settling velocity of the particles, $\mathscr{D}$ is the Brownian diffusivity of the particles and K_e is the turbulence intensity of the fluid. The deposition coefficient is also a function of the surface of the area under examination (S) and the volume of the room (V). Consequently, deposition depends on the surface-to-volume ratio. If a room has a lot of surface for a very small volume (for example, due to abundant furniture), β increases. It may be tempting to consider that this dependence describes as well the effect of surface roughness, which we could interpret as an increase of S/V. However, this is only partly true. Surface roughness, as we will see in Section 7.3.4 alters deposition through other physical processes on a smaller scale.

This model also involves the Brownian diffusivity of the particles, $\mathscr{D}$ and the turbulence intensity K_e. Note that these two parameters appear together in the model. This has an interesting implication: an increase in turbulence intensity increases β in the same way of an increase in diffusivity. In other words, the consequences of a change in K_e or $\mathscr{D}$ are mathematically equivalent. We shall see more about the relationship between turbulence and particle diffusivity in the following sections. Figure 2.1 shows a solution of the Crump and Seinfield model taken directly from their article, which is a classical result:

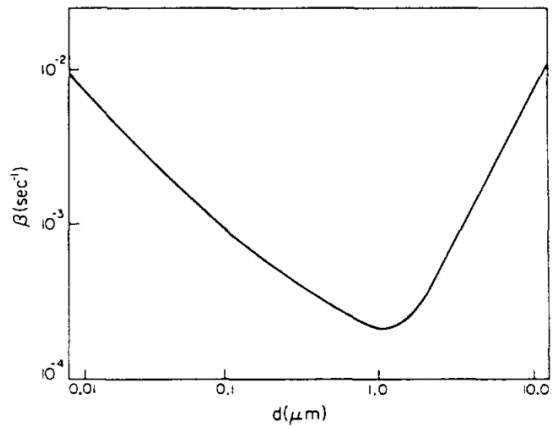

Figure 2.1: Solution of the Crump and Seinfield model, taken from [1], in a vessel with $K_e = 36^{-1}$.

The shape of the dependence of β on d_p shown in Figure 2.1 is perhaps the most influential and persistent result in the field of aerosol deposition. Note that it coincides well with our rough approximation displayed in Section 1.6.4: very small particles deposit due to diffusion, large particles settle due to gravity, while middle-sized particles exhibit deposition rates lower by 10 to 100 times. This model has been validated exhaustively and extended by many authors. Its popularity in the the indoor air field is due largely to the work of William Nazaroff, who modified it to include thermophoresis [4] and extended it to different flow regimes, such as natural convection [5]. It has been successfully used to describe experimental data in many situations until very recently, in environmental test chamber experiments [6], in furnished and unfurnished rooms [7], and also museums [8].

2.2.2 Multi-compartment models

Multi-compartment or multi zone-models arise when we apply the notion of single-box models to a series of connected boxes and we consider that some particles travel from box to box. A multi compartment model can become complex and include many phenomena, but is based on a simple idea: the rate of change of the amount of particles in a volume, N, depends on the sum of fluxes, J, that remove and add particles:

$$\frac{d}{dt}N = \sum J \tag{2.5}$$

Our task is now reduced to finding the relevant fluxes and estimating them. There are many examples in the literature that follow this mass balance approach. For example, Nazaroff himself listed the fluxes of particles in museums in this manner [9]. Multi zone models continue to be used and produced nowadays for all kinds of indoor environments: pesticides in residential areas [10], PM in schools [11], entire apartments [12] or a few connected rooms [13]. Here we will follow the exhaustive list of sinks and sources presented by [14]. In this model particles penetrate

from the outdoor environment through each existing inlet (e.g. a leak, a window or a ventilation inlet) with the following flux:

$$J_{penetration} = \frac{1}{V_r} \sum QPN_{out} \tag{2.6}$$

where V_r is the volume of the room, N_{out} is the concentration outside and Q is the air flow rate of the inlet. P is the penetration factor, which depends on particle size and the properties of the leak. There are some published models and correlations to calculate P [15], and we will make use of this concept in the simulations described in Chapter 5. It is likely that if air infiltrates into a room there will also be some exfiltration and the pressure will be in equilibrium with the outdoor environment. The flux of particles removed through exfiltration of air is:

$$J_{removal} = \frac{1}{V_r} \sum QN \tag{2.7}$$

where Q represents the exfiltration air flow. The exchange of particles with the neighbouring rooms is expressed with the following equation:

$$J_{exchange} = \frac{1}{V_r} \sum (Q_{a-b}N_a - Q_{b-a}N_b) \tag{2.8}$$

where the subindexes a and b refer to the two adjacent rooms. Some particles are also removed by deposition:

$$J_{deposition} = \frac{1}{V_r} \sum (AvN) \tag{2.9}$$

where A is the area of the surface that receives the particles and v_s is the deposition velocity, which may be calculated with the model as per Equations 2.2 - 2.4 for each well-mixed volume. Resuspension can also be represented with a flux, which in this case would contribute to increase N:

$$J_{resuspension} = \frac{1}{V_r} \sum fA\lambda B \tag{2.10}$$

where B is the amount of particles deposited, f is the fraction of particles available for resuspension, A is the area of the surface where particles are deposited and λ is the rate of resuspension. Calculating this rate is not trivial, and there are no simple models that can provide this information in a form comparable to the deposition rate. The reason is that particle resuspension is inherently time-dependant and it defies the notion of a well-mixed and time-averaged volume. We will explore this issue in Section 7.3.3. For now, let us assume that a value for λ exists. Therefore we can obtain the net flux towards the surfaces of the room by balancing equations 2.9 and 2.10:

$$A\frac{d}{dt}B = J_{deposition} - J_{resuspension} \tag{2.11}$$

This simple balance expresses an interesting idea: the amount of particles on the surface depends on the balance between deposition and resuspension. This may sound trivial, but in practice these concepts are frequently misunderstood. There are factors, such as humidity, that attach particles to the walls (reducing resuspension), and others, such as temperature gradients, that bring particles to the walls (increasing deposition). In Chapter 7, when we explain the role of particles on surfaces, we will explore in more detail the consequences of this distinction. Finally, the model presented by [14] also contains terms for the change in size of the particles either by coagulation or by vapour condensation on their surface. When particles coagulate the coagulation flux reduces the concentration of certain size bins, N_j, and enlarges the concentration of the size bin of larger particles, N_i. It is calculated with:

$$J_{coagulation} = \frac{1}{2}\sum_{j=1}^{i-1} K_{j,i-j}N_jN_{i-j} - N_{k,i}\sum_{j=1}^{\inf} K_{i,j}N_j \tag{2.12}$$

where K is the coagulation Kernel between size fractions i and j. Condensation has similar consequences, some particles are enlarged, and therefore become part of another size bin:

$$J_{condensation} = \frac{\dot{V}_{i-1}}{V_i - V_{i-1}}N_{i-1} - \frac{\dot{V}_i}{V_{i+1} - V_i}N_i \tag{2.13}$$

here $\dot{V}$ is the rate of change of the volume and V is the volume of a particle. Expressions for K and V can be found in [14].

2.3 CFD approaches

The next level of complexity involves abandoning the well-mixed assumption. Instead, we need to divide the volume into many sub-volumes, as small as necessary to capture the phenomena of interest. Then the equations that describe air movement and the transport of species are solved in every sub-volume or computational node. This procedure involves an iterative solution of large systems of equations, which require the use of numerical methods and computational tools. The equations and algorithms used to predict the motion of fluids and its interaction with solid boundaries constitute the field known as Computational Fluid Dynamics. In this section we will describe the CFD methods that have been successfully used to simulate indoor aerosols and we will show some of their applications.

This reivew does not include parametric CFD models. This subset of CFD models are based on the simulation of a simplified model problem which includes the relevant parameters that can be modified. For example, it could include the location of a painting, its inclination, the dimensions

of the room where it hangs, the position of the ventilation inlets, etc... The results of the simulations are later post-processed statistically, and used to build a parametric model that relates all the input parameters with the simulation output. These models are faster and simpler, and are very useful in many engineering applications. However, they have a fundamental shortcoming which is crucial for our application: they are not site-specific. The CFD simulations that we review in this chapter are based on specific room geometries, and allow the exploration of detailed changes in these rooms, case by case. Parametric modelling would be an ideal method if we could speak of a "typical" indoor heritage room. And insomuch as this room does not exist, we must resort to studying each geometry, and its possible modifications, individually.

2.3.1 Modelling the particle field

The distribution of particles indoors involves a gaseous flow with suspended solid matter, and is therefore a two-phase problem. As such, it can be modelled using two different approaches: The Eulerian-Eulerian model (normally referred to as Eulerian) or the Eulerian-Lagrangian model (or simply Lagrangian) [16]. The Eulerian model considers both the fluid and the solid particles as a continuum. It models particles using averaged properties on a control volume basis, in other words, it solves the discrete phase similarly to the fluid phase. For this reason the Eulerian methods is also known as the single fluid model [17]. Lagrangian models, on the other hand, trace the movement of each particle independently, and are based on a force balance for each individual particle. They are sometimes called "particle tracking" models.

Lagrangian models

The output of Lagrangian models is the position of any individual particle at any time, which could be expressed as: $x(particle,\, t)$ [18]. To calculate x we need to know the velocity of the particles, u_p, which depends on the balance of all the forces acting on each particle:

$$\frac{du_p}{dt} = \sum F \tag{2.14}$$

$$\frac{dx}{dt} = u_p \tag{2.15}$$

As in the case of the multi-compartment method, to build a Lagrangian model we only have to list all the forces we are interested in, in the same way that we listed fluxes before. There are many published lists of forces that are relevant to the problem of particle dispersion and deposition indoors. Here we will follow the exhaustive list provided by [19]. We may start by the simplest force, the gravitational force:

$$F_{gravitational} = \left(1 - \frac{\rho}{\rho_p}\right) g \tag{2.16}$$

where ρ is the density of the air and ρ_p the density of the particle. The interaction between air motion and particle movement is described by the drag-force. For small spherical particles the magnitude of the drag force is given by the Stokes law:

$$F_{drag} = 6\pi r\mu(u - u_p)/m \tag{2.17}$$

where r is the radius of the particle and m its mass. A relatively smaller aerodynamic force is the Staffman or shear force, the lift force induced by shear flow:

$$F_{shear} = 1.542\frac{\rho}{\rho_p}\nu\frac{1}{r}\sqrt{\frac{1}{\nu}\left|\frac{\mathrm{d}u}{\mathrm{d}y}\right|}(u - u_p) \tag{2.18}$$

where u is the air velocity and ν the air viscosity. We can also add the effects of thermophoresis if there are important temperature gradients:

$$F_{thermophoretic} = -(\eta/m)\nabla lnT \tag{2.19}$$

where T is the temperature the value of η is the turbophoretic force coefficient, for which an expression is provided in [20]. If the particles are significantly charged, we can also include the effect of electrical forces:

$$F_{electrical} = \frac{qE}{m} - \frac{3q^2}{64\pi^2\epsilon_0\rho_p r^3 y^2} \tag{2.20}$$

where q is the charge of a particle, E is the strength of the electrical field, y is the distance from the wall and ϵ_0 is the electric permittivity of the medium.

In Lagrangian models the fate of the particles that collide with a wall is described by very simple boundary conditions. The boundary condition which is almost universally used is a "trap" condition (i.e. when a particle touches the wall, it stays in the wall).

Eulerian Drift-Flux models

Instead of the position of each particle, the output of Eulerian models is the velocity of the simulated fluid at every position and time, $u(x, t)$ [18]. In a multiphase model, we describe both the air motion and the suspended particles as an Eulerian field, and for this reason such models are known as Eulerian-Eulerian. If our model describes the mixture motion instead of the motion of the individual phases, we are using a "drift-flux-model" [21].

The concept of drift-flux model was introduced in 1965 by Zuber and Findlay [22] who developed, "a general expression which can be used for predicting the average volumetric concentration" [sic]. The philosophy behind drift-flux models can be illustrated as follows: consider a mixture of two components A and B, each with a volume fraction α so that $\alpha_A = 1 - \alpha_B$. The

flux of each of them, J_A and J_B depends on the total flux, J, but also on the relative motion, J_{AB} (Figure 2.2). As explained in [23], the flux of each component can be expressed as:

$$J_A = \alpha_A J + J_{AB} \quad \text{and} \quad J_B = (1 - \alpha_A)J - J_{AB} \tag{2.21}$$

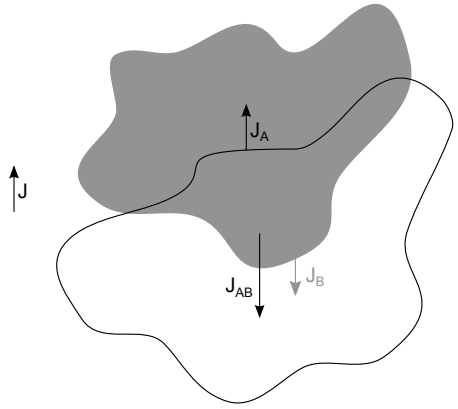

Figure 2.2: A mixture of two fluids, each with a certain mass flux and mixture flux.

There are some problems in which the relative motion, or drift-flux, is caused by an external force. Consider for example that fluid B is very heavy and A is light. Both are affected by a force, gravity, which is a function of the properties of the fluids. The drift-flux models were designed for these types of problems. A drift-flux velocity, u_{AB} can be defined as a function of α and the fluid properties, and thus J_{AB} can be defined as:

$$J_{AB} = \alpha(1 - \alpha)u_{AB} \tag{2.22}$$

and Equations 2.21 can now be solved. These models have been applied to sedimentation, fluidized beds and also the problem that we deal with in this work: fine particles suspended in air [23]. The transport equation for particles used in Eulerian drift-flux models is based on the convection-diffusion equation and has this general form:

$$\frac{\partial c}{\partial t} = \overbrace{-\boldsymbol{\nabla} c(\boldsymbol{u} + \boldsymbol{v})}^{\text{Convection}} \overbrace{+\boldsymbol{\nabla}(\Gamma \boldsymbol{\nabla} c)}^{\text{Diffusion}} \overbrace{+\boldsymbol{S_c}}^{\text{Source term}} \tag{2.23}$$

where c is the particle concentration, u is the velocity of the air, v is the settling velocity of the particles and Γ is their diffusivity. We will demonstrate the derivation of this equation in Section 3.2. Equation 2.23 is reported in the literature with some variations and its solution implies some problems that different authors solve differently:

1. As a second-order differential equation, 2.23 requires boundary conditions in all the boundaries of the domain. This implies that, unlike in the Lagrangian approach, we need to provide expressions that describe accurately the value of c on inlets, outlets, and walls. The

wall boundary condition has to accurately describe deposition. There are several possible solutions, discussed below.

2. The estimation of the diffusivity of particles is also problematic. It is generally accepted that Γ, in wall-bounded flows should account for more than Brownian diffusivity, because particles also diffuse through anisotropic turbulence. But the estimation of the turbulent diffusivity of particles as a function of particle and flow properties is a problem currently under research [24–26].

3. The number of velocities in the convective term and how are they calculated is also a matter for discussion. Some authors use the convective term to add other effects, such as electrical drift [27] or thermophoresis [28].

The first authors who developed Eulerian models of particle transport already noted that in order to describe deposition accurately we need a good prediction of near-wall phenomena. Reeks and Skyrme observed that deposition is determined by turbulence in the core and in the boundary layer, big particles being more influenced by the core and small particles by the turbulent boundary layer [29]. In their words: "inertia allows a particle to retain some memory of the vigorous turbulent fluctuations from the homogeneous core as it travels into the suddenly quiescent wall region. This nonequilibrium situation precludes the use of simple gradient-diffusion ideas (i.e. Fick's law) since these are based upon local equilibrium theory. Therefore, some recognition of the inhomogeneity of boundary layer turbulence must be made in Eulerian-type particle flow models in order to properly describe the deposition process." Many solutions have been proposed, starting by Corner and Pandelbury, who suggested that turbulent diffusivity of the particles near the wall (ε) follows a quadratic relationship with the distance to the wall, y:

$$\varepsilon = K_e y^2 \tag{2.24}$$

where K_e is a turbulence intensity parameter defined as $K_e = \kappa^2 \frac{du}{dy}$ where κ is a constant. This expression is reviewed along with many others in [30]. Another influential result is the two-layer near-wall model for ε proposed by [31]. Lai and Nazaroff suggested another correction of near-wall turbulent diffusivity based on a correlation with a direct numerical simulation of the boundary layer [32]. We will use their solution, which is described in Section 3.3. Other authors apply a correction to the velocity of the particles instead of their diffusivity. It has been shown that even a simple linear decay of particle velocity towards the wall results in some improvement in the accuracy of predictions [33].

Eulerian vs. Lagrangian

The theoretical differences between Eulerian and Lagrangian specifications of the particle field are well known:

1. Lagrangian models are based on a force balance on a moving particle, while Eulerian models are based on a mass balance on a fixed volume.

2. Lagrangian models simulate the trajectory of each particle, while Eulerian models treat particles as a continuous field.

3. Consequently, the number of equations to solve in Lagrangian models depends on the number of particles, while in Eulerian models it is independent of the number of particles.

4. The implementation of deposition boundary conditions in Lagrangian models is trivial (when a particle touches a wall, it is eliminated from the particle count), but in Eulerian models it is a matter currently under research, and there are many solutions available.

If we look at the implementation of these modelling philosophies, we encounter other technical differeces. Traditionally, the Lagrangian method has been regarded as more computationally intensive because the trajectory of every particle has to be modelled separately, but this shortcoming is quickly becoming insignificant thanks to the fast evolution of computing capacity. Still, the Eulerian method needs less computing time than the Lagrangian method. For example, in [34] it is found that an Eulerian model can compute in 0.2 h what a common Lagrangian approach coupled with any anisotropic turbulence model would solve in 10 to 100 h (these calculations were carried out in 2008). Eulerian models are recommended in situations where particles behave like a continuous field [17]. However, the continuous field hypothesis becomes less applicable as particle size increases, in which case the discrepancy between the two models is also higher [16].

It has been found that the accuracy of the predictions of the two approaches differs at very small particle concentrations, the Lagrangian method being better when the number of tracked particles is under 10^5 [35]. This makes Lagrangian models very well suited to small geometries that require precise simulations, such as the simulation of deposition in the respiratory tract. But how does this number of particles compare with our system of interest? In Apsley House, one of the buildings simulated in this work, a representative concentration of $PM_{0.02-1}$ would be, precisely, $10^5\ \mathrm{particles/cm^3}$. Apsley House has an approximate volume of 12000 m^3, which results in 12^{14} particles to track. With such a number of particles to simulate, we should expect the Eulerian approach to be more computationally efficient, and to provide very similar results to the Lagrangian approach.

Eulerian models require relatively complex boundary conditions to describe the interaction of particles with all types of boundaries, while most Lagrangian particle tracking is done with straightforward "trap" conditions. Both approaches require near-wall corrections to account for particle inertia and for the inhomogeneity of turbulence in the boundary layer, be it corrections in turbulent diffusivity in the case of Eulerian approaches or particle velocity in the case of Lagrangian approaches [33, 36].

Simulation of the population balance

The Population Balance Equations (PBEs) are models describing how the number of entities in a particular state changes with time [37]. In aerosol engineering, the population balance describes all the processes that can alter the particle size distribution: collisions, coagulation,

aggregation and breakage. As has been discussed in section 1.6.6, coagulation of particulate matter is sometimes an important removal process in indoor environments. Population balance equations can be incorporated to CFD models and solved alongside equations for airflow and particle dispersion. Only a few simulations of environmental diesel particulate matter include a population balance, some good examples are the work by Gidhagen et. al. [38] who modelled particle decay inside a road tunnel, or Sartelet et.al. [39] who studied the number distribution of aerosols in a vehicle exhaust. Both studies consider only Brownian coagulation, which is the main driving force for collisions in the size fraction of interest.

The most advanced PBE model is the direct quadrature method of moments and its variations, a novel and efficient approach based on a quadrature approximation of the size distribution of particles [40], which has been used in a number of applications. The concentration of diesel particulate matter indoors is relatively small in comparison with concentrations in the vehicle exhaust, and it can be expected that coagulation is not going to be prominent in our case studies.

2.3.2 Applications and validations

The concepts of experimental validation and verification appear very often in this thesis. With this term, I refer to the comparison of simulations with experimental measurements. It is evident that a CFD model will never be totally validated in all its possible applications: there is no definitive way of guaranteeing its viability. Comparison with experiments should always be part of the assesment of deposition using CFD. However, we can aim at testing the performance of the model in cases that are within its expected range of application, as a means of assessing its accuracy. This section reviews the applications of CFD in indoor PM problems found in the literature. Table 2.1 summarizes the turbulence models, geometries, particle modelling approaches and deposition boundary conditions used in the reviewed simulations.

One of the largest fields of application of CFD aerosol deposition models is the simulation of deposition in lungs or the respiratory tract. This problem is of great interests to the fields of allergology, toxicology, drug delivery and the tobacco industry. The lung system has been simulated hundreds of times, and has driven the development of new models in the recent years (some of the works cited in the above sections are from this area of research). In this section we omit this part of the deposition literature and we focus exclusively on the CFD simulations of PM deposition in indoor environments, which are generally motivated by indoor air quality and human health concerns.

Table 2.1: Published applications of CFD models to the simulation of indoor particulate matter. L = Lagrangian, E = Eulerian. Models that use the Lai and Nazaroff near-wall functions and deposition model [32] are labelled "Lai", c = suspended particulate matter concentration, N = not validated.

System	Turbulence	Particles	Wall	Deposition	Validation	Ref.
Ducts	$k-\epsilon$, DNS, LES		Two layer wall function	-	N	[41]
Ducts	DNS		Corrected drag force	-	N	[42]
Simplified cubic room	LES		none	t	N	[43]
2 rooms separated by a wall	LES		none	t	N	[44]
Store rooms	$k-\epsilon$, RNG $k-\epsilon$, $k-\omega$		none	t	Temperature	[45]
2 rooms separated by a wall	LES	L	Lai		c	[46]
Large office	$k-\epsilon$		Lai		c	[47]
Office room with steady occupants	$k-\epsilon$		none	-	N	[48]
Road tunnel (1	RNG $k-\epsilon$	E	none	Own model	c	[38]
Room	$k-\epsilon$	L	none	-	c (laboratory)	[49]
Small rooms with steady occupants	$k-\epsilon$	E	-	Fixed concentration	c (literature)	[50]
Small scaled room	$k-\epsilon$	L	Lai		N	[51]
Kitchen	RNG $k-\epsilon$		-	t	c	[52]
Dormitory with steady occupants	RNG $k-\epsilon$		-	t	c	[53]
Simple rooms	Realizable $k-\epsilon$		none	t	c	[54]
Multi zone room	LES and RNG $k-\epsilon$		none	t	N	[55]
Simple rooms	$k-\epsilon$		-	t	N	[56]
Simple rooms	ke plus lag		none	t	c	[57]
	v^2-f		none	t	c (literature)	[58]
Airliner cabin	RNG $k-\epsilon$		none	t	c	[59]
Office	$k-\epsilon$	E	none	not specified	c (laboratory)	[60]
Ducts	RNG $k-\epsilon$		Lai		N	[61]
Two ventilated	RNG $k-\epsilon$		No			[62]

The interest of all these simulations is to know the concentration of suspended particulate matter, c, and its decay rates. This is consistent with their motivation, which is human well-being, and

which is only related to c, not the deposition fluxes or the amount of particles in the walls. This preference is also reflected in the experimental validation of simulations. Only a minority of the simulations are experimentally validated, but those which are use measurements of suspended PM [38, 46, 47, 52, 53, 57, 59]. Some validate the model on a laboratory scale before using it in a real building [49, 60] while some others use validation cases obtained from the literature [50, 58].

Most of these simulations involve the simulation of small indoor spaces, generally one or two rooms with a cubic geometry. We have included some simulations of spaces with comparable geometries and flow regimes, such as a road tunnel [38] or ventilation ducts [41, 42, 61]. The geometries are smaller than a house, and are always simple and symmetrical, frequently allowing the use of structured meshes. In some occasions the simulations include occupants, which are steady and function simply as a source of heat [48, 50, 53], human movement is included only in [63] , where humans are simplified as geometrical mannequins with a constant velocity.

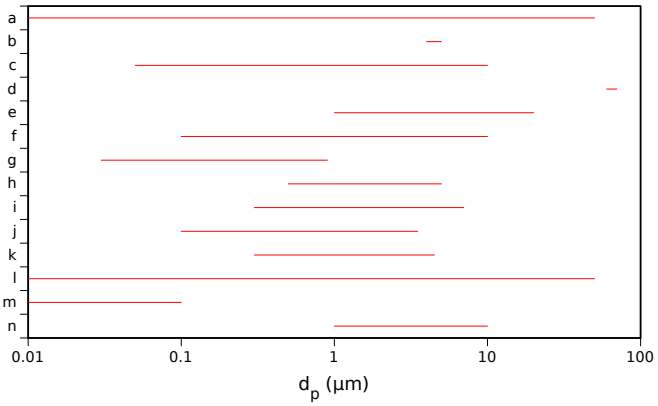

Figure 2.3: Range of d_p used in the simulations reported in Table 2.1. a-[41], b-[42], c-[44], d-[44], e-[46], f-[47], g-[38], h-[50], i-[51], j-[52], k-[57], l-[58], m-[60] and n-[62]

Common to all the reviewed works is the treatment of the relevant physical phenomena: coagulation is deemed insignificant and particles are considered not to alter the air flow (one-way coupling). Particle properties vary greatly. Figure 2.3 shows the ranges of particle diameter used in some of the reviewed papers (the ones that use a range instead of a single size). The range of possible diameters spans over 4 orders of magnitude, from 0.01 μm to 100 μm. Most of the simulations involve particles between 0.1 and 10 μm. The largest particles tend to be simulated using Lagrangian models [44, 47, 58].

Most of the simulations use the Lagrangian approach without any correction and with a simple trap condition, probably because it is readily available in some commercial codes (Such as ANSYS Fluent). Most of the simulations are coupled with RANS models, namely $k-\epsilon$. When Large Eddy Simulations (LES) or Direct Numerical Simulations (DNS) are used, they are found to be preferable to RANS [41], particularly for Lagrangian models. Authors who use an Eulerian drift-flux model tend to develop their own models and deposition boundary conditions ([38,

50]), or to use the model by Lai and Nazaroff ([46, 47, 62]). In the case of [50] they define deposition at the wall boundaries by setting a value of c which is corrected with an experimental factor.

With the only exception of [64], where particles are initially in suspension indoors and their evolution is simulated, all the reviewed articles assume a uniform inlet of particles, i.e. an opening in the walls with a constant and unidirectional inflow. The assumption of a uniform inlet inevitably leads the authors towards setting an air outlet in order to close the mass balance: otherwise, the room pressure would increase, which is clearly an unrealistic situation. This is an important simplification that must be assessed with care, as such an inlet-outlet system is not something that can be easily found in real-life situations.

An alternative solution is to extend the computational domain beyond the limits of the room of interest, thus including part of the external environment, where the airflow contour conditions can be set. If this procedure is followed, the flow through openings will be a consequence of the outdoor conditions. This solution has been claimed as indispensable by Fracastoro et. al. [65], who wrote: "As a first issue, the importance of a correct choice of the model geometrical domain should be emphasized. In fact, excluding the outdoor space from the calculation domain leads to physically meaningless results, even when the numerical indicators assume satisfactory values".

2.3.3 Air movement and turbulence

In the previous section we have already observed that deposition of PM interacts very closely with turbulence. The scale in which PM responds to turbulent fluctuations could be said to be mesoscopic. The mesoscopic scale may be described as being between the size of an atom and the size of micrometric particles. Modelling the mesoscales of atmospheric boundary layers has received growing interest in recent years [66], mostly because of the challenges associated with turbulence modelling, currently a laborious undertaking that usually pushes researchers to find the balance between computing costs and the precision of their results [66]. This section reviews several simulations of different kinds of environments in order to explore how turbulence modelling relates to PM modelling.

Reynolds-Averaged Navier-Stokes (RANS) equations were one of the first turbulence models to be developed, and are some of the most popular ones. Perhaps the most widely used is the $k-\epsilon$ model (where k stands for turbulent kinetic energy and ϵ for turbulent dissipation of this energy). The standard forms of this model have some well-known shortcomings, including poor performance in cases with large pressure differences or not fully developed flows. When modelling particle deposition, isotropic models (i.e. models that cannot discern a preferential spatial direction in turbulence) such as standard $k-\epsilon$, RNG $k-\epsilon$, or $k-\omega$ tend to overestimate the deposition velocity of the smallest particles (d$<$1 μm) [67–69].

The main reason for this overestimation is in the high estimates of the wall-normal stresses. As already mentioned, deposition of particles in the coarse mode (d_p $>$10 μm) is inertia and gravitation-governed, and in the accumulation mode (0.1-1 μm) the importance of diffusion

increases. Therefore, the overestimation of near-wall stresses for small diameters tends to blur the distinction between the behaviour of those two modes. In contrast, anisotropic turbulence models can correctly capture the behaviour of the smaller particles [67]. The Reynolds Stress Model (RSM), the Large Eddy Simulation (LES) or the Detached Eddy Simulation (DES) are higher level turbulence models. RSM introduces transport equations for all Reynolds stresses that account for the directional effects of the turbulence fields, while LES and DES use grid refinement to solve the smaller scales of flow. In particular, LES has shown a great agreement with experimental data in different practical applications [70, 71], and its use is common in complex geometries such as the deposition of particles in the human respiratory system [72].

Table 2.2: Computational times (in h, measured in 2007) and model performance comparison. A = good, B = acceptable, C = marginal, D = poor, n/a = not applicable. Adapted from [17]

	0-eq.	**RNG** $k-\epsilon$	**SST** $k-\omega$	**LRN-LS**	$\overline{v^2}-f$	**RSM-IP**	**DES**	**LES**
Mean Temp.	B	A	A	C	A	A	C	A
Mean Vel.	D	B	A	B	A	B	D	B
Turbulence	n/a	C	C	C	A	C	C	A
Computing time (unit)	1	2-4	2-4	4-8	4-8	10-20	$10^2 - 10^3$	$10^2 - 10^3$

However, not all turbulence models have the same computing requirements. Typically, isotropic models are less computationally demanding than anisotropic models, with computation times that may vary within three orders of magnitude. Table 2.2 shows the usual computation times for some of the models mentioned above, along with a performance rating defined by the authors that reflects the accuracy solving the temperature, velocity and turbulence profiles in a room with natural convection [17]. This comparison was carried out in 2007. In order to avoid using the computationally expensive DES and LES models, some authors have implemented corrections to isotropic models for achieving more accuracy in the small particle ranges. Some well known corrections are those of Matida et. al. [36] and Wang and James [73], both in a Lagrangian particle framework. Corrections by Matida have proven to be effective in reducing the deposition velocities for the smaller size fractions in RSM, RNG $k-\epsilon$ and SST $k-\omega$ modes, and mainly affects the deposition velocity of particles in the nucleation mode [74].

Table 2.3: Computational times (in h) measured in 2012 for several models using an eight core cluster, with two 2.5 GHz AMD quad-core processors and 32GB of memory. Case 1: Steady state room without ventilation. Case 2: Steady state with ventilation. Case 3: Transient state . A = good, B = acceptable, C = marginal, D = poor, n/a = not applicable. Grid with 273160 nodes. [75]

Method	**Case 1**	**Case 2**	**Case 3**
RANS + euler	1.0	3.7	N/A
URANS + euler	15.4	74.2	62.2
LES + euler	28.8	75	323.3
DES1 + euler	29.2	73.3	367.0
DES2 + euler	34.1	98.3	396.6
RANS + lagrange	2.4	5.3	N/A
URANS + lagrange	17.9	81.5	84.9
LES + lagrange	32.4	93.3	360.5
DES1 + lagrange	33.1	83.3	389.2
DES2 + lagrange	39.1	118.3	434.3

Even after applying these near-wall corrections, the RANS turbulence models still slightly overestimate the deposition velocity, while there is a good agreement with data in the coarse mode. In Table 2.2 it can also be appreciated that the $\overline{v^2} - f$ model shows an outstanding behaviour in all the studied parameters, and it is clearly the model with a better performance/computing time ratio. $\overline{v^2} - f$ is actually similar to the Standard $k - \epsilon$, but it includes near-wall anisotropic effects, which makes it a valuable option when modelling low Rayleigh (low convection) and low Reynolds (low turbulence) situations, in which case its results are comparable to those obtained with LES [17]. Other authors have used $\overline{v^2} - f$ specifically to model particulate matter in closed spaces, with good results [58, 76, 77].

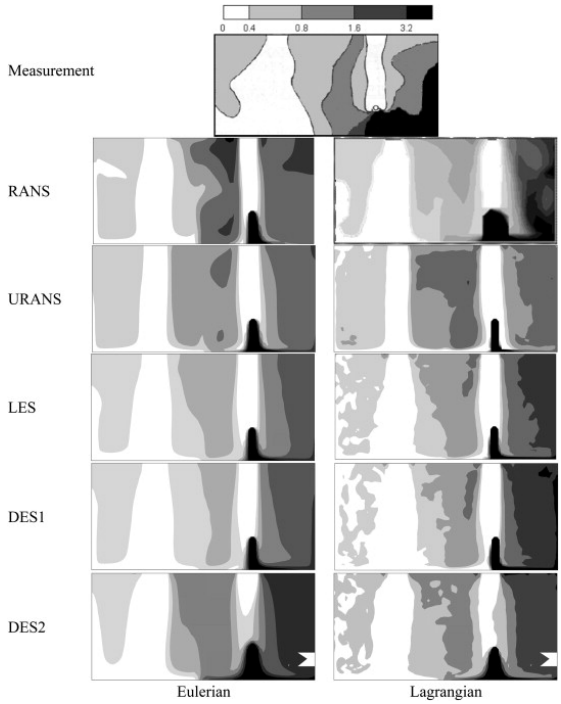

Figure 2.4: Distribution of particles around a room using various combinations of models. The first figure corresponds to experimental measurements. Taken from [75]

As the relation between particle velocity and air velocity is normally assumed as a one-way coupling (i.e. air affects particles but particles do not affect air), the particle tracking stage, which is usually resource intensive, should be independent from the turbulence model [67]. However, it may be interesting to observe how the combination of Eulerian or Lagrangian tracking with different turbulence models would affect the overall performance and computing time. A comparison of different combinations [75] can be seen in figure 2.4 and table 2.3.

The factor that most increases the calculation time is the steady or unsteady condition, followed by the choice of the turbulence model. Lagrange performs poorly when coupled with basic turbulence models. The particle tracking stage, although it can double the time needed for a RANS simulation, has a relatively small effect on anisotropic models. A general recommendation could be to use Euler with RANS for steady-state cases, and Lagrange with DES or LES for unsteady cases [75].

2.3.4 Towards a model for heritage applications

Model choice

Given the information collected in this Chapter and our objectives, we decided to use the drift-flux approach coupled with a RANS turbulence model. Our justification is:

1. The effect on heritage materials, either exhibited or stored, either hanging on walls or arranged in a space, is dependent not only on the absolute amount of particles present in the space, but also on the spatial distribution of these particles. A mass balance that takes the room as a whole, or which at best divides it between ceiling, floor and walls, cannot account for variations of particle concentration around the volume of the room. Well-mixed models, either in a single volume or in a multi-compartment framework are useful to describe the evolution of c, but not to simulate the distribution of deposition on every wall. We are particularly interested in knowing which surfaces receive the particles, and therefore we need to resort to a 3D, spatially-resolved simulation.

2. Our simulations will involve concentrations between 1000 and 10000 cm^{-3} in very large volumes, and simulating these particle numbers with a Lagrangian approach would be unaffordable. But independently of the particle number, our interest is not in the fate and trajectories of individual particles, but in the gas-like behaviour of the bulk of the particles. Finally, a desirable output would be to develop a simulation workflow that could allow us to run fast simulations on a personal computer. This would facilitate the use of the model outside scientific installations. It would also open the door to its future use by non-technical end-users, or its eventual implementation into user-friendly applications. Eulerian models are more suited to these requirements.

3. The literature review revealed that, while using a Lagrangian approach with a RANS model could undermine the accuracy of the predictions, Eulerian models work well with RANS models, particularly in steady-state simulations. Furthermore, the use of the $k-\epsilon$ model seems to be ubiquitous in simulations of indoor environments. Nonetheless, in the following sections we will attempt to select the best RANS model for our application.

Areas of improvement

The review has revealed that several of our major interests are not met by the current state of indoor PM simulation. Namely:

1. The output of the simulations is tipically in terms of c or the bulk deposition velocity, but very occasionally the profile of PM deposition on surfaces.

2. Simulations generally involve one or various rooms, but full buildings are rarely simulated.

3. As far as we know, the simulations of indoor deposition have seldom been compared with data from real buildings, and never with deposition data.

The modelling approach we have chosen needs to be validated experimentally, i.e., it needs to be compared with experimental data obtained in relevant cases, which are representative of the situations in which we intend to use the model. This validation must be based in deposition data, partly because it is easy to obtain, but mainly because deposition rates are our main interest.

While concentration is useful for assessing health-risks, the output of our model should use other metrics that are useful to assess the risk to heritage surfaces. These limitations stem from an essential difference in perspective: simulations of indoor PM have been so far focused on the volume, and we are concerned with particles on surfaces.

References

[1] J. G. Crump and J. H. Seinfeld. "Turbulent deposition and gravitational sedimentation of an aerosol in a vessel of arbitrary shape". *Journal of Aerosol Science* 12:5 (1981), pp. 405–415.

[2] J. Corner and E. D. Pendlebury. "The Coagulation and Deposition of a Stirred Aerosol". *Proceedings of the Physical Society. Section B* 64:8 (1951), p. 645.

[3] M. Xu et al. "Deposition of Tobacco Smoke Particles in a Low Ventilation Room". *Aerosol Science and Technology* 20:2 (1994), pp. 194–206.

[4] W. W. Nazaroff and G. R. Cass. "Mass-transport aspects of pollutant removal at indoor surfaces". *Environment International* 15:1–6 (1989), pp. 567–584.

[5] W. W. Nazaroff and G. R. Cass. "Mathematical modeling of indoor aerosol dynamics". *Environmental Science & Technology* 23:2 (1989), pp. 157–166.

[6] T. Hussein et al. "Deposition rates on smooth surfaces and coagulation of aerosol particles inside a test chamber". *Atmospheric Environment* 43:4 (2009), pp. 905–914.

[7] T. L. Thatcher et al. "Effects of room furnishings and air speed on particle deposition rates indoors". *Atmospheric Environment* 36:11 (2002), pp. 1811–1819.

[8] W. W. Nazaroff et al. "Particle deposition in museums: comparison of modeling and measurement results". *Aerosol Science and Technology* 13:3 (1990), pp. 332–348.

[9] W. Nazaroff and G. Cass. "Protecting museum collections from soiling due to the deposition of airborne particles". *Atmospheric Environment. Part A. General Topics* 25:5-6 (1991), pp. 841–852.

[10] D. H. Bennett and E. J. Furtaw. "Fugacity-Based Indoor Residential Pesticide Fate Model". *Environmental Science & Technology* 38:7 (2004), pp. 2142–2152.

[11] R. Goyal and M. Khare. "Indoor air quality modeling for PM10, PM2.5, and PM1.0 in naturally ventilated classrooms of an urban Indian school building". *Environmental Monitoring and Assessment* 176:1-4 (2011), pp. 501–516.

[12] B. Mølgaard et al. "Migration of Aerosol Particles inside a Two-Zone Apartment with Natural Ventilation: A multi-zone validation of the multi-compartment and size-resolved indoor aerosol model". *Indoor and Built Environment* (2013).

[13] T. Schneider, J. Kildes, and N. Breum. "A two compartment model for determining the contribution of sources, surface deposition and resuspension to air and surface dust concentration levels in occupied rooms". *Building and Environment* 34:5 (1999), pp. 583–595.

[14] T. Hussein et al. "Emission Rates Due to Indoor Activities: Indoor Aerosol Model Development, Evaluation, and Applications". *Aerosol Science and Technology* 39:11 (2005), pp. 1111–1127.

[15] D.-L. Liu and W. W. Nazaroff. "Particle Penetration Through Building Cracks". *Aerosol Science and Technology* 37:7 (2003), pp. 565–573.

[16] A. C. Lai and F. Chen. "Comparison of a new Eulerian model with a modified Lagrangian approach for particle distribution and deposition indoors". *Atmospheric Environment* 41:25 (2007), pp. 5249–5256.

[17] Z. Zhang and Q. Chen. "Comparison of the Eulerian and Lagrangian methods for predicting particle transport in enclosed spaces". *Atmospheric Environment* 41:25 (2007), pp. 5236–5248.

[18] I. Herrera and G. Pinder. *Mathematical Modeling in Science and Engineering: An Axiomatic Approach*. Wiley, 2012.

[19] A. Guha. "Transport and Deposition of Particles in Turbulent and Laminar Flow". *Annual Review of Fluid Mechanics* 40:1 (2008), pp. 311–341.

[20] L. Talbot et al. “Thermophoresis of particles in a heated boundary layer”. *Journal of Fluid Mechanics* 101 (04 1980), pp. 737–758.

[21] I. Mamoru and H. Takashi. “Thermo-Fluid Dynamics of Two-Phase Flow”. Springer US, 2006, pp. 381–418.

[22] N. Zuber and J. A. Findlay. “Average Volumetric Concentration in Two-Phase Flow Systems”. *Journal of Heat Transfer* 87:453-468 (1965), pp. 501–516.

[23] C. Brennen. *Fundamentals of Multiphase Flow*. Cambridge University Press, 2005.

[24] S. Parker et al. “Refinement and testing of the drift-flux model for indoor aerosol dispersion and deposition modelling”. *Journal of Aerosol Science* 41:10 (2010), pp. 921–934.

[25] L. Zaichik et al. “A diffusion-inertia model for predicting dispersion and deposition of low-inertia particles in turbulent flows”. *International Journal of Heat and Mass Transfer* 53:1–3 (2010), pp. 154–162.

[26] P. Nerisson et al. “Improved CFD transport and boundary conditions models for low-inertia particles”. *Computers and Fluids* 40:1 (2011), pp. 79–91.

[27] S. Ramechecandane, C. Beghein, and F. Allard. “Modeling fine particle dispersion in an inhomogeneous electric field with a modified drift flux model”. *Building and Environment* 45:6 (2010), pp. 1536–1549.

[28] M. Abdolzadeh et al. “Effect of thermophoresis and other parameters on the particle deposition on a tilted surface”. *International Journal of Heat and Fluid Flow* 32:3 (2011), pp. 670–679.

[29] M. Reeks and G. Skyrme. “The dependence of particle deposition velocity on particle inertia in turbulent pipe flow”. *Journal of Aerosol Science* 7:6 (1976), pp. 485–495.

[30] A. C. K. Lai. “Particle deposition indoors: a review”. *Indoor Air* 12:4 (2002), pp. 211–214.

[31] H. Chen and V. Patel. “Near-wall turbulence models for complex flows including separation”. *AIAA journal* 26:6 (1988), pp. 641–648.

[32] A. C. K. Lai and W. W. Nazaroff. “Modeling indoor particle deposition from turbulent flow onto smooth surfaces”. *Journal of Aerosol Science* 31:4 (2000), pp. 463–476.

[33] P. W. Longest and M. J. Oldham. “Numerical and experimental deposition of fine respiratory aerosols: Development of a two-phase drift flux model with near-wall velocity corrections”. *Journal of Aerosol Science* 39:1 (2008), pp. 48–70.

[34] J. Xi and P. W. Longest. “Numerical predictions of submicrometer aerosol deposition in the nasal cavity using a novel drift flux approach”. *International Journal of Heat and Mass Transfer* 51:23–24 (2008), pp. 5562–5577.

[35] M. Saidi et al. “Comparison between Lagrangian and Eulerian approaches in predicting motion of micron-sized particles in laminar flows”. *Atmospheric Environment* 89 (2014), pp. 199–206.

[36] E. A. Matida et al. “Improved numerical simulation of aerosol deposition in an idealized mouth–throat”. *Journal of Aerosol Science* 35:1 (2004), pp. 1–19.

[37] D. Marchisio and R. Fox. *Computational Models for Polydisperse Particulate and Multiphase Systems*. Cambridge Series in Chemical Engineering. Cambridge University Press, 2013.

[38] L. Gidhagen et al. “Model simulation of ultrafine particles inside a road tunnel”. *Atmospheric Environment* 37:15 (2003), pp. 2023–2036.

[39] B. Albriet et al. “Modelling aerosol number distributions from a vehicle exhaust with an aerosol CFD model”. *Atmospheric Environment* 44:8 (2010), pp. 1126–1137.

[40] A. Zucca et al. “Implementation of the population balance equation in CFD codes for modelling soot formation in turbulent flames”. *Chemical Engineering Science* 61:1 (2006), pp. 87–95.

[41] L. Tian and G. Ahmadi. “Particle deposition in turbulent duct flows—comparisons of different model predictions”. *Journal of Aerosol Science* 38:4 (2007), pp. 377–397.

[42] B. Arcen, A. Tanière, and B. Oesterlé. “On the influence of near-wall forces in particle-laden channel flows”. *International Journal of Multiphase Flow* 32:12 (2006), pp. 1326–1339.

[43] C. Béghein, Y. Jiang, and Q. Y. Chen. “Using large eddy simulation to study particle motions in a room”. *Indoor Air* 15:4 (2005), pp. 281–290.

[44] T.-J. Chang and T.-S. Hu. “Transport mechanisms of airborne particulate matters in partitioned indoor environment”. *Building and Environment* 43:5 (2008), pp. 886–895.

[45] M. Delele et al. “Optimization of the humidification of cold stores by pressurized water atomizers based on a multiscale CFD model”. *Journal of Food Engineering* 91:2 (2009), pp. 228–239.

[46] N. Gao et al. “The airborne transmission of infection between flats in high-rise residential buildings: Particle simulation”. *Building and Environment* 44:2 (2009), pp. 402–410.

[47] A. C. Lai and F. Chen. “Modeling particle deposition and distribution in a chamber with a two-equation Reynolds-averaged Navier–Stokes model”. *Journal of Aerosol Science* 37:12 (2006), pp. 1770–1780.

[48] N. Gao and J. Niu. “Transient CFD simulation of the respiration process and interperson exposure assessment”. *Building and Environment* 41:9 (2006), pp. 1214–1222.

[49] E. Hathway et al. “CFD simulation of airborne pathogen transport due to human activities”. *Building and Environment* 46:12 (2011), pp. 2500–2511.

[50] S. Holmberg and Y. Li. “Modelling of the Indoor Environment – Particle Dispersion and Deposition”. *Indoor Air* 8:2 (1998), pp. 113–122.

[51] A. C. Lai and F. Chen. “Comparison of a new Eulerian model with a modified Lagrangian approach for particle distribution and deposition indoors”. *Atmospheric Environment* 41:25 (2007), pp. 5249–5256.

[52] A. Lai and Y. Ho. “Spatial concentration variation of cooking-emitted particles in a residential kitchen”. *Building and Environment* 43:5 (2008), pp. 871–876.

[53] H. Qian and Y. Li. “Removal of exhaled particles by ventilation and deposition in a multibed airborne infection isolation room”. *Indoor Air* 20:4 (2010), pp. 284–297.

[54] Z. F. Tian, J. Y. Tu, and G. H. Yeoh. “CFD Studies of Indoor Airflow and Contaminant Particle Transportation”. *Particulate Science and Technology* 25:6 (2007), pp. 555–570.

[55] Z. Tian et al. “Numerical studies of indoor airflow and particle dispersion by large Eddy simulation”. *Building and Environment* 42:10 (2007), pp. 3483–3492.

[56] Z. Zhang and Q. Chen. “Comparison of the Eulerian and Lagrangian methods for predicting particle transport in enclosed spaces”. *Atmospheric Environment* 41:25 (2007), pp. 5236–5248.

[57] Z. Zhang and Q. Chen. “Experimental measurements and numerical simulations of particle transport and distribution in ventilated rooms”. *Atmospheric Environment* 40:18 (2006), pp. 3396–3408.

[58] Z. Zhang and Q. Chen. “Prediction of particle deposition onto indoor surfaces by CFD with a modified Lagrangian method”. *Atmospheric Environment* 43:2 (2009), pp. 319–328.

[59] Z. Zhang et al. “Experimental and numerical investigation of airflow and contaminant transport in an airliner cabin mockup”. *Building and Environment* 44:1 (2009), pp. 85–94.

[60] B. Zhao, C. Chen, and Z. Tan. “Modeling of ultrafine particle dispersion in indoor environments with an improved drift flux model”. *Journal of Aerosol Science* 40:1 (2009), pp. 29–43.

[61] B. Zhao and J. Chen. “Numerical analysis of particle deposition in ventilation duct”. *Building and Environment* 41:6 (2006), pp. 710–718.

[62] B. Zhao, X. Li, and Z. Zhang. “Numerical Study of Particle Deposition in Two Differently Ventilated Rooms”. *Indoor and Built Environment* 13:6 (2004), pp. 443–451.

[63] J. Wang and T. Chow. “Numerical investigation of influence of human walking on dispersion and deposition of expiratory droplets in airborne infection isolation room”. *Building and Environment* 46:10 (2011), pp. 1993–2002.

[64] Z. Zhang and Q. Chen. “Prediction of particle deposition onto indoor surfaces by CFD with a modified Lagrangian method”. *Atmospheric Environment* 43:2 (2009), pp. 319–328.

[65] G. Fracastoro. “Experimental and theoretical analysis of natural ventilation by windows opening”. *Energy and Buildings* 34:8 (2002), pp. 817–827.

[66] D. Mumovic and M. Santamouris. *A Handbok of Sustainable Building Design and Engineering*. 1st. London, Sterling, VA: Earthscan, 2009, p. 328.

[67] S. Parker, T. Foat, and S. Preston. “Towards quantitative prediction of aerosol deposition from turbulent flows”. *Journal of Aerosol Science* 39:2 (2008), pp. 99–112.

[68] Y. Liu et al. “Numerical simulation of aerosol deposition in a 3-D human nasal cavity using RANS, RANS/EIM, and LES”. *Journal of Aerosol Science* 38:7 (2007), pp. 683–700.

[69] M. Horn and H.-J. Schmid. “A comprehensive approach in modeling Lagrangian particle deposition in turbulent boundary layers”. *Powder Technology* 186:3 (2008), pp. 189–198.

[70] M. Breuer, H. Baytekin, and E. Matida. “Prediction of aerosol deposition in bends using LES and an efficient Lagrangian tracking method”. *Journal of Aerosol Science* 37:11 (2006), pp. 1407–1428.

[71] G. L. Iacono, P. Tucker, and A. Reynolds. “Predictions for particle deposition from LES of ribbed channel flow”. *International Journal of Heat and Fluid Flow* 26:4 (2005), pp. 558–568.

[72] H. Jin et al. “Large eddy simulation of inhaled particle deposition within the human upper respiratory tract”. *Journal of Aerosol Science* 38:3 (2007), pp. 257–268.

[73] Y. Wang and P. James. “On the effect of anisotropy on the turbulent dispersion and deposition of small particles”. *International Journal of Multiphase Flow* 25:3 (1999), pp. 551–558.

[74] N. Gao et al. “Using RANS turbulence models and Lagrangian approach to predict particle deposition in turbulent channel flows”. *Building and Environment* 48 (2012), pp. 206–214.

[75] M. Wang, C.-h. Lin, and Q. Chen. “Advanced Turbulence Models for Predicting Particle Transport in Enclosed Environments”. *Building* (2012), pp. 40–49.

[76] M. Abdolzadeh, M. Mehrabian, and A. Akbarinia. “Application of a modified Eulerian model to study the particle deposition on a vertical surface in turbulent flow”. *Powder Technology* 214:1 (2011), pp. 83–88.

[77] K. Li and G. Gong. “Numerical simulation of indoor suspension particles based on v2-f model”. *Applied Mathematical Modelling* (2011).

3
Mathematical model

3.1 Definition of the system

The system we are modelling is a multiphase flow in which air transports very diluted small particles. In the previous section we have outlined the ranges of concentrations and particle sizes that we are dealing with. We have seen that particulate matter can have hydraulic diameters ranging from 0.01 to 50 μm, and that we can expect concentrations to be between 1×10^3 cm^{-3} to 1×10^6 cm^{-3}. This information is sufficient to obtain the order of magnitude of the volume fraction of the particles, Φ. In our case, clearly Φ will be always much smaller than 1, and in most of the cases, $\Phi < 1 \times 10^{-3}$. According to [1] this is the threshold below which we can consider a multiphase system to be very diluted. In systems classified as very diluted, collisions between particles are very rare, and consequently particle coagulation is negligible.

Φ is the first non-dimensional number that we use to characterize our system. With some more information, we can also provide an estimation of another non-dimensional parameter: the Stokes number, St, which describes the behaviour of particles suspended in a flow. For very small values of St, particles can be considered to move at the same velocity than air. It is defined as follows:

$$\mathrm{St} = \frac{\tau u}{L} \tag{3.1}$$

where u is the free stream velocity of the fluid, L is the characteristic length of an obstacle, and τ is the relaxation time of the particles, given by:

$$\tau = \frac{\rho_p d_p^2}{18\mu} \tag{3.2}$$

where ρ_p is the particle density, d_p the particle diameter, and μ the fluid kinematic viscosity. Since we are interested in the simulation of indoor environments, we can easily imagine the likely dimensions and velocities of air motion. Most obstacles will have sizes ranging from 10 cm (decoration, stair steps, frames) to 10 m (walls). Indoor air will move around 1 $\mathrm{cm/s}$ due to natural convection or pressure differences, and up to 1 $\mathrm{m/s}$ in doors or ventilation outlets. Given these ranges, we can easily see that, in most of the cases, St will be vanishingly small. Therefore, we can assume one-way coupling between the fluid and solid phases (i.e. air influences the movement of particles, but particles do not affect air motion). We also assume that coagulation is negligible. Since particles do not interact with each other the third assumption, different sizes can be simulated independently. For this reason, when necessary, we solve a transport equation for each size mode.

These three considerations are the basis of the model described in the following sections. This Chapter begins with the development of the transport equation for the particle phase, its constitutive equations and boundary conditions, including the development of the deposition boundary condition. It continues with the description of the turbulence models we use, and finally it explains in detail the implementation of the model in Fluent.

3.2 Derivation of the transport equation

Let us consider particulate matter as a continuous scalar. This scalar is generally carried by air, both by convection and by diffusion. Additionally, since the particles have certain non-negligible mass, the scalar is also subject to gravitational settling. In any arbitrary volume the sum of these fluxes can be summarised with a simple mass balance, as illustrated in Figure 1 and Equation 3.3

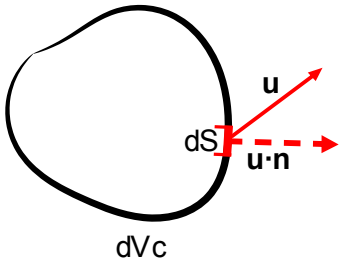

Figure 3.1: Schematic representation of the mass balance in an arbitrary volume.

$$ACC = IN - OUT + GEN \tag{3.3}$$

where ACC is the accumulation, GEN is the generation, and IN and OUT are the inlet and outlet fluxes. These fluxes are the sum of the convective (c) and diffusive (d) fluxes:

$$IN - OUT = (IN - OUT)_c + (IN - OUT)_d \tag{3.4}$$

Accumulation can be expressed as the change in time of the concentration within the volume:

$$ACC = \frac{d}{dt}\int_V c\mathrm{d}V = \int_V \frac{\partial c}{\partial t}\mathrm{d}V \tag{3.5}$$

and generation is simply a source term:

$$GEN = \int_V S_c\mathrm{d}V \tag{3.6}$$

where c is the scalar concentration and V is the volume. The following equations express the convective and diffusive balances. The change from surface (S) integrals to volume integrals is done by using the divergence theorem [1].

$$(IN - OUT)_c = -\int_S c\boldsymbol{u}\cdot\boldsymbol{n}\mathrm{d}S = \int_V \boldsymbol{\nabla}(c\boldsymbol{u})\mathrm{d}V \tag{3.7}$$

$$(IN - OUT)_d = -\int_S c(\boldsymbol{u} - \boldsymbol{u_{drift}})\cdot\boldsymbol{n}\mathrm{d}S = -\int_S J\boldsymbol{n}\mathrm{d}S = \int_V \boldsymbol{\nabla}J\mathrm{d}V \tag{3.8}$$

where u is the air velocity and u_{drift} is a velocity representing any movement of the particles which is not necessarily in the same direction than air. This is the reason why this approach is commonly referred to as drift-flux model [2]. The flux resulting from the combination of these two velocities is J. S is the surface through which the particles flow, and $\boldsymbol{n}$ is the vector perpendicular to S. By inserting Equations 3.5-3.8 into Equation 3.3, we obtain the following mass balance:

$$\int_V \frac{\partial c}{\partial t}\mathrm{d}V = -\int_V \boldsymbol{\nabla}(c\boldsymbol{u})\mathrm{d}V - \int_V \boldsymbol{\nabla}J\mathrm{d}V + \int_V S_c\mathrm{d}V \tag{3.9}$$

which can be arranged as:

$$\int_V \left[\frac{\partial c}{\partial t} + \boldsymbol{\nabla}(c\boldsymbol{u}) + \boldsymbol{\nabla}J - S_c\right]\mathrm{d}V = 0 \tag{3.10}$$

which, since the integral must be zero for all volumes, implies that:

$$\frac{\partial c}{\partial t} + \boldsymbol{\nabla}(c\boldsymbol{u}) = -\boldsymbol{\nabla}J + S_c \tag{3.11}$$

[1] The divergence or Ostrogradsky's theorem states that $\int_S (F\cdot n)dS = \int_V (\boldsymbol{\nabla}F)dV$

Finally, we can replace J with any appropriate definition of the diffusive flux. In our case, since particles are subject to diffusivity, as well as the effects of gravity, we can define J as:

$$J = -\Gamma \boldsymbol{\nabla} c + \boldsymbol{v} c \tag{3.12}$$

where Γ is the diffusivity of the particles and $\boldsymbol{v}$ is the settling velocity. The estimation of Γ is discussed in Section 3.2.1. Inserting Equation 3.12 into Equation 3.11 we obtain:

$$\frac{\partial c}{\partial t} = -\boldsymbol{\nabla}(c\boldsymbol{u}) + \boldsymbol{\nabla}[\Gamma \boldsymbol{\nabla} c - c\boldsymbol{v}] + \boldsymbol{S_c} \tag{3.13}$$

We can calculate the magnitude v of the settling velocity from the calculation of the Reynolds (Re) and Archimedes (Ar) numbers of a single particle suspended in the fluid [3]:

$$\text{Ar} = \frac{g d_p^3 \rho_f (\rho_p - \rho_f)}{\mu^2} \tag{3.14}$$

$$\text{Re} = [-3.809 + (3.809^2 + 1.832 Ar^{0.5})^{0.5}]^2 \tag{3.15}$$

$$v = \frac{\mu Re}{d_p \rho_f} \tag{3.16}$$

where g is the gravity and ρ_f is the density of the fluid.

3.2.1 Calculation of diffusivity

We simulate aerosol dispersion in a scale which is much larger than the smallest scales of the flow, which is turbulent. Since a full numerical resolution of all scales is unaffordable (the ratio between the bigger and smaller scales is >10), the effect of turbulence in the transport of particles has to be modelled. Here, we will use the concept of turbulent diffusivity to introduce in our model the movement of particles through isotropic turbulence. Consequently, we define Γ as the sum of two diffusivities:

$$\Gamma = \varepsilon + \mathscr{D} \tag{3.17}$$

where ε is the turbulent diffusivity and $\mathscr{D}$ is the Brownian diffusivity of the aerosol, which is given by [4]:

$$\mathscr{D} = CkT / 2\pi d_p \mu \tag{3.18}$$

where T is the temperature, k is the Boltzmann constant and C is the Cunningham slip correction factor [4]:

$$C = 1 + \frac{2\lambda}{d_p}\left[A_1 + A_2 exp\left(\frac{-A_3 d_p}{\lambda}\right)\right] \tag{3.19}$$

where $A_1 = 1.257$, $A_2 = 0.400$, $A_3 = 0.55$ and λ is the mean free path, given by:

$$\lambda = \frac{kT}{\sqrt{2}\pi d_p^2 p} \tag{3.20}$$

where p is the pressure.

Estimation of the turbulent diffusivity

The estimation of ε requires some further assumptions. Consider an inertia-less particle. We can imagine that it will be transported by all the scales of turbulent motion, as if it were another molecule of gas, and therefore will have a turbulent diffusivity identical to that of the fluid. This simplification is not uncommon. The order of magnitude of the turbulent diffusivity of atmospheric aerosols is generally considered to be approximately equal to that of the carrier fluid [5], thus assuming that aerosols have no inertia. However, this idea does not hold for all particle sizes and flow regimes.

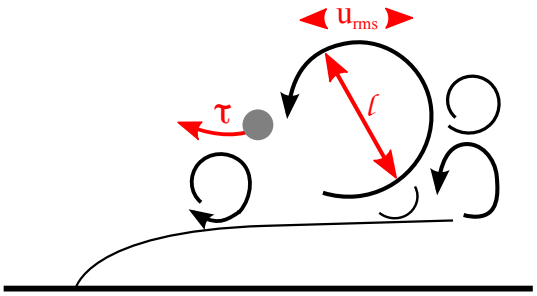

Figure 3.2: Schematic representation of a turbulent eddy with the relevant features used to calculate K_{pt}

.

In order to determine if this assumption is reasonable in a given scenario, we can define an inertial parameter similar to the Stokes number that describes a the ability of a particle to respond to the motion of an individual eddy. Let us consider a single particle being transported by a single turbulent eddy, as in Figure 3.2. Following [6], this parameter may be defined from the relaxation time τ, the characteristic turbulence root mean square of the fluctuating velocity, u_{rms}, and the integral length scale of the turbulent flow, l. τ is the time that a particle needs to react to a change in the velocity of the surrounding fluid, and l/u_{rms} is a good approximation of the characteristic time in which the turbulent eddy changes direction. We can deduce that if $\tau < l/u_{rms}$, when

the velocity and direction of a turbulent eddy change, the particle will respond immediately. Therefore we can define:

$$K_{pt} = \frac{\tau u_{rms}}{l} \tag{3.21}$$

So that, for very small values of K_{pt}, we can write that $\varepsilon/\mu_t \simeq 1$. We calculate τ using the following expression [4]:

$$\tau = \frac{\rho_d d_p^2}{18\mu_f} \tag{3.22}$$

An estimation of u_{rms} can be obtained from statistical sampling of a transient simulation of the turbulent flow. The integral length scale, l, can be obtained in a number of ways. It is generally accepted that its order of magnitude is given by [7]:

$$l \sim C_\mu^{3/4} \frac{k^{3/2}}{\epsilon} \tag{3.23}$$

where C_μ is a constant (usually 0.09), k is the turbulent kinetic energy and ϵ is its rate of diffusion. The estimation of this parameters is discussed in Section 3.5. It should be noted that Equation 3.23 provides only an estimation of the integral scale, which can actually be determined from experimentally observable fluctuations of the flow. Some authors usually refer to l as a *pseudo-integral scale* in order to avoid confusion with the actual integral scale [8]. In wall-bounded flows, and only as a rule of thumb, l can also be considered to be of the same order as the hydraulic diameter [9].

Some authors take the relaxation time as a sole indicator of the validity of the $\varepsilon/\mu_t \simeq 1$ assumption. For example, it has been suggested it is a valid assumption for relaxation times $\tau < 0.1$ s, based on various experimental results [10]. But if there is enough information available to calculate K_{pt}, this approach allows for a more rigorous assessment of the applicability of the model.

3.3 Boundary conditions

Since our interest is to simulate enclosed indoor environments, it is evident that all flows will be wall bounded. This section discusses the mathematical representation of these physical boundaries. In fact, boundary conditions are a central element of the deposition model. We implement the calculation of the deposition flux -arguably the most important part of the model- as a boundary condition in all the walls. In this section we will also describe the relevant boundary conditions of the particle field in inlets and outlets. As we shall see, some of the most interesting numerical and conceptual problems arise from the implementation and interpretation of these conditions. Mathematically, boundary conditions are required in order to solve the transport equation (Equation 3.11), which we can express more concisely as:

$$\partial_t c = -\partial_{\boldsymbol{x}} \cdot c(\boldsymbol{u} + \boldsymbol{v}) + \partial_{\boldsymbol{x}} \cdot (\mathscr{D} + \varepsilon)\partial_{\boldsymbol{x}} c \tag{3.24}$$

Equation 3.24 is a second-order differential equation that requires a boundary condition in all the boundaries of the domain. Sections 3.3.4 and 3.3.5 describe the boundary conditions we use in inlets and outlets, respectively. At the walls of the domain, we provide this boundary condition as the total particle flux toward the wall, i.e. the deposition flux. But before being able to calculate this flux, we need some further insight into the physical phenomena that take place very near the wall, which differ from bulk behaviour, and drive us to the concept of boundary layers.

3.3.1 Boundary layer considerations

Very near a wall, we can observe two different very sharp gradients of air velocity and particle concentration. They are due to the concentration boundary layer and the turbulent boundary layer (Figure 3.3). Both boundary layers arise from the fact that, at the wall, air velocity and particle concentration must be zero, while they have some non-zero value in the bulk. These boundary layers are very thin in comparison with the velocity and concentration gradients of the surrounding flow. They are so thin, in fact, that we can safely assume that in most of the cases, it will not be practical to solve the momentum and mass transport equations within the boundary layer.

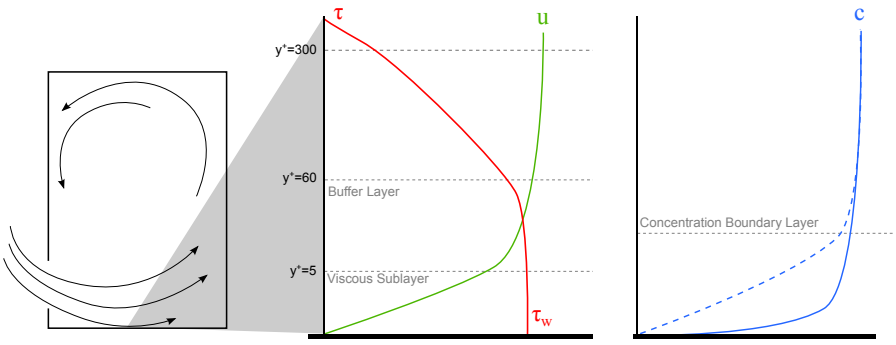

Figure 3.3: Schematic representation of the velocity and concentration boundary layers over a flat plate and their approximate thickness. The scheme in the left represents a room with air flow, and illustrates that in order to see these layers we have to look at a very short lengths near the walls of the simulated rooms. The wall thickness y^+ is defined in Equation 3.25

Until now, we have not dealt with any computational aspect of modelling. But in order to proceed we must decide whether to breach the boundary layers or to solve them using very fine computational meshes. Here, for the reasons given in Section 2.3.4, we will follow the first approach. We need to provide adequate boundary conditions for the equations solved in the bulk, and for this purpose we need the boundary conditions to reflect accurately the interior of the boundary layers.

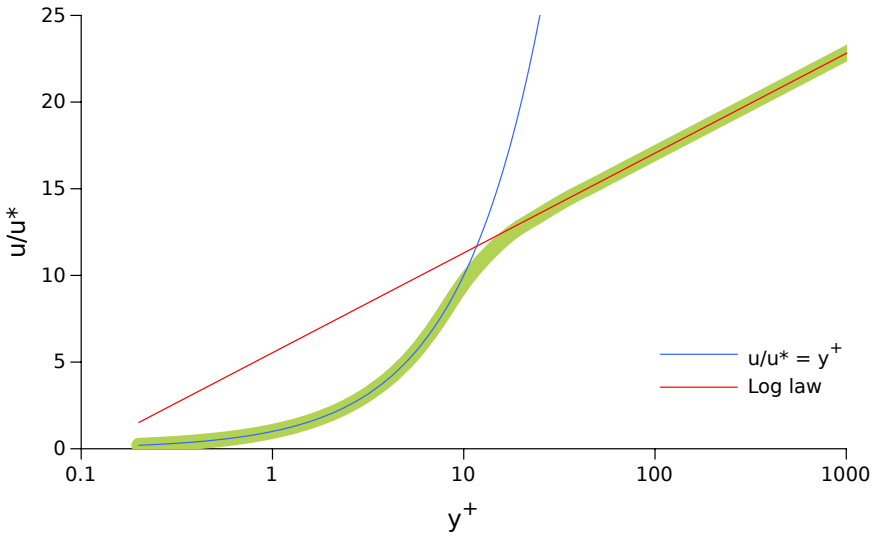

Figure 3.4: Non-dimensional velocity profile through the turbulent boundary layer. The actual velocity profile is well described by a combination of the Log-law (Equation 3.26 and the non -dimensional thickness (Equation 3.25).

Turbulent boundary layers have been studied in great detail. A turbulent flow over a flat surface can be divided in three layers: a viscous, a transition and a fully turbulent sublayer (Fig. 3.3). The thickness of these sublayers is typically expressed using the non-dimensional distance to the wall, y^+:

$$y^+ = \frac{yu^*}{\nu} \quad \text{with} \quad u^* = \sqrt{\tau_w/\rho} \tag{3.25}$$

where u^* is the friction velocity, τ_w is the wall shear stress and ν is the fluid viscosity. In the viscous sublayer, momentum transfer is dominated by viscous stresses, and turbulent (Reynolds) stresses are negligible. Numerous experiments show that Reynolds stresses are a small in comparison to viscous stresses up to $y^+ = 5$. Within the viscous sublayer, the velocity profile is linear ($u/u^* = y^+$), and the value of τ_w is constant. In the outer layer, turbulence is dominant, the shear stress is zero, and the velocity profile is well represented by the Log-law, which has the form [11]:

$$u/u* = 2.5\ln(u/u*) + 5.45 \tag{3.26}$$

In our case, we will use the following relationship:

$$\frac{U_p C_\mu^{1/4} k_p^{1/2}}{\tau_w/\rho} = \frac{1}{\kappa} ln \left(E \frac{\rho C_\mu^{1/4} k_p^{1/2} y_p}{\mu} \right) \tag{3.27}$$

where κ is the von Karman constant (0.4187), E and C_μ are empirical constants (E = 9.793, C_μ = 0.09), U_p is the mean fluid velocity at point P, k_p is the turbulence kinetic energy at point P, y_p is the distance from point p to the wall and μ is the dynamic viscosity of the fluid [12]. The Log-law is applicable roughly from $y^+ = 60$. Finally, between the viscous and turbulent sublayers, there is a transition or buffer region where the effects of viscous and turbulent stresses have the same magnitude. The velocity profile through these three sublayers is illustrated in Figure 3.4.

When solving the model, we will use equation 3.27 to obtain the value of the shear stress at the wall, τ_w, using variables from the bulk solution of the flow. As we will show, τ_w is fundamental for the estimation of deposition. The reader may have noticed that the purpose of the law of the wall is to obtain the velocity, U_p, at any point of the boundary layer, and that therefore, it can not be used to obtain τ_w as well - we would have a single equation with two unknowns. This, however, is only a problem in appearance. In a nutshell: due to the iterative nature of the solution, we will always have access to an estimation of U_p from the previous iteration (or time step) obtained from the solution of the momentum equation. This value of U_p can be used to calculate τ_w. Naturally, the values of U_p and τ_w will be matching when the solution reaches convergence.

The concentration boundary layer is generally contained within the viscous sublayer [10]. In fact, a concentration boundary layer develops because the transport of particles depends on several variables of the flux (such as u^* or ε) that take different values within the turbulent boundary layer. The resulting gradient of concentration generates the flux of particles towards the wall. In the next section, we will use information on the turbulence inside the concentration boundary layer to integrate an expression for the deposition flux.

3.3.2 Deposition boundary condition

Close to the wall, where the normal velocity is negligible, a one-dimensional particle concentration gradient is formed. This gradient generates a diffusive flux of particles that can be expressed with a version of Fick's law in which the diffusion coefficient is given by the addition of the molecular and turbulent diffusivities. The (total) deposition flux at the wall is given by the sum of this diffusive flux and of the convective flux due to the gravity-induced particle settling. Thus, we can write:

$$J = -(\varepsilon + \mathscr{D})\frac{\partial c}{\partial n} + (\boldsymbol{v} \cdot \boldsymbol{n})c \tag{3.28}$$

where J is the flux of particles entering the wall, $\partial c/\partial n$ is the partial derivative of the aerosol concentration in the direction normal to the wall, $\boldsymbol{n}$ is the unit vector normal to the wall and pointing to the exterior of the domain, and therefore $\boldsymbol{v} \cdot \boldsymbol{n}$ is the component of the settling velocity normal to the wall. One of the strengths of the drift-flux approach is that any additional velocities relevant to a particular system -such as electrical mobility drift velocity or thermophoretic velocity- can be easily added to the convective terms of Equations 3.24 and 3.28.

We use Equation 3.28 to calculate the deposition flux in all the wall boundaries. However, in

order to do so, we need to know the value of ε inside the concentration boundary layer. As we have said, we assume that $\varepsilon \sim \mu_t$. We have also mentioned that we do not solve the flow within the boundary layer. However, using the value of μ_t outside the boundary layer would result in an overestimation of deposition, as has been noted by [13]. Therefore, we need to use a model that can provide the turbulent variables within the unsolved area close to the wall region: a wall function.

3.3.3 Integration of deposition boundary condition through the boundary layer

In order to integrate Equation 3.28 through the boundary layer, we shall start by normalising it using bulk properties related to the near-wall phenomena. First, let us define the flux at the wall as:

$$J = u_d c_\infty \tag{3.29}$$

where c_∞ is the particle concentration just outside the concentration boundary layer, and u_d is the deposition velocity. We normalise the particle concentration, the distance from the wall and the deposition velocity as follows:

$$c^+ = \frac{c}{c_\infty} \tag{3.30}$$

$$u_d^+ = \frac{u_d}{u^*} \tag{3.31}$$

$$y^+ = \frac{y u^*}{\nu} \tag{3.32}$$

where c is the particle concentration. Let us begin by considering the simplest scenario: a vertical surface, in which case there is no gravitational settling and the deposition flux is due only to diffusion. Replacing these definitions in Equation 3.28 we obtain the following expression for the non-dimensional particle deposition velocity:

$$u_d^+ = \left(\frac{\varepsilon + \mathscr{D}}{\nu} \right) \frac{\partial c^+}{\partial y^+} \tag{3.33}$$

In order to know the value of u_d^+ we need to integrate equation 3.33 through the concentration boundary layer. However, to do that we need to know the value of ε all the way down to the wall. We can determine the ratio between turbulent viscosity ν_t and viscosity ν using a best fit exponential equation to DNS simulation results, as reported in [10]. This wall function divides the boundary layer in three sublayers, $0 \leq y^+ \leq 4.3$, $4.3 \leq y^+ \leq 12.5$ and $12.5 \leq y^+ \leq 30$. The value of ν_t through these three layers (Figure 3.5) is given by:

$$\frac{\nu_t}{\nu} = 7.669 \times 10^{-4} (y^+)^3, \quad 0 \leq y^+ \leq 4.3 \tag{3.34}$$

$$\frac{\nu_t}{\nu} = 1.00 \times 10^{-3}(y^+)^{2.8214}, \quad 4.3 \leq y^+ \leq 12.5 \tag{3.35}$$

$$\frac{\nu_t}{\nu} = 1.07 \times 10^{-4}(y^+)^{1.8895}, \quad 12.5 \leq y^+ \leq 30 \tag{3.36}$$

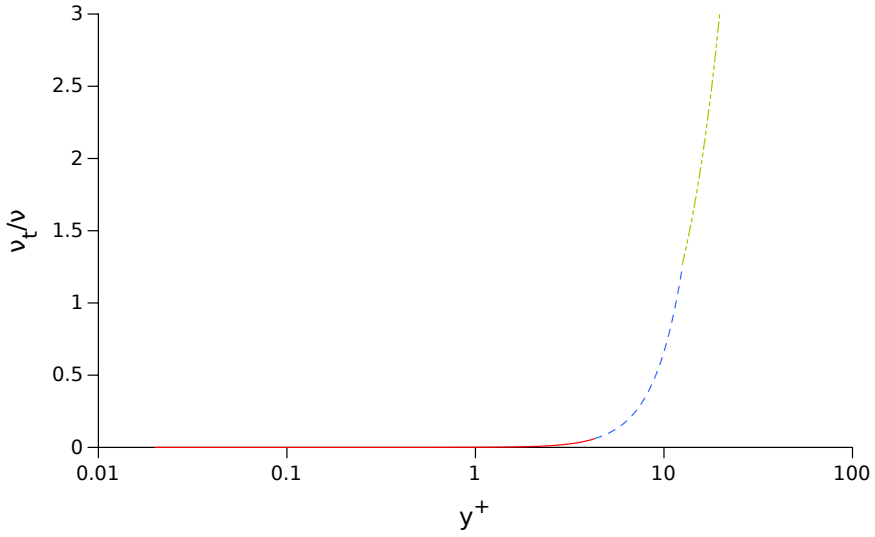

Figure 3.5: Profile of turbulent viscosity in the concentration boundary layer using a thee-equation fit to direct numerical simulation (DNS) data.

We can now rearrange Equation 3.33 in order to integrate. The limits for the integration are that $c^+ = 0$ when the particle is in contact with the wall (i.e. $y^+ = r^+ = (d_p/2)(u^*/\nu)$, and $c^+ = 1$ at $y^+ = 30$. Equations 3.34-3.36 have to be introduced in Equation and it must be integrated over the three sublayers of the concentration boundary layer.

$$\begin{aligned} I = \frac{1}{u_d^+} = &\int_{r^+}^{4.5} \left(\frac{\nu}{7.669 \times 10^{-4}(y^+)^3\nu + \mathscr{D}} \right) \mathrm{d}y^+ \\ &+ \int_{4.5}^{12.5} \left(\frac{\nu}{1.00 \times 10^{-3}(y^+)^{2.8214}\nu + \mathscr{D}} \right) \mathrm{d}y^+ \\ &+ \int_{12.5}^{30} \left(\frac{\nu}{1.07 \times 10^{-4}(y^+)^{1.8895}\nu + \mathscr{D}} \right) \mathrm{d}y^+ \end{aligned} \tag{3.37}$$

The integration of Equation 3.37 provides a function for I which depends on $\nu, d_p, \mathscr{D}$ and u^*. It can be rearranged as a function of the Schmidt number ($\mathrm{Sc} = \nu/\mathscr{D}$):

$$I = [3.64\mathrm{Sc}^{2/3}(a - b) + 39] \tag{3.38}$$

$$a = 0.5 \ln \left[\frac{(10.92\mathrm{Sc}^{-1/3} + 4.3)^3}{\mathrm{Sc}^{-1} + 0.0609} \right] + \sqrt{3}\, tan^{-1} \left[\frac{8.6 - 10.92\mathrm{Sc}^{-1/3}}{\sqrt{3}\, 10.92\mathrm{Sc}^{1/3}} \right] \tag{3.39}$$

$$b = 0.5 \ln \left[\frac{(10.92\mathrm{Sc}^{-1/3} + r^+)^3}{\mathrm{Sc}^{-1} + 7.669 \times 10^{-4}(r^+)} \right] + \sqrt{3}\, tan^{-1} \left[\frac{2r^+ - 10.92Sc^{-1/3}}{\sqrt{3}\, 10.92^{1/3}} \right] \tag{3.40}$$

The relation $I = \frac{1}{u_d^+}$ is only applicable to vertical surfaces. For surfaces in any other inclination we can follow the same procedure, and we would obtain the following expression:

$$\int_0^1 \frac{1}{u_d^+ + (\boldsymbol{n} \cdot \boldsymbol{v}^+)c^+} \mathrm{d}c^+ = I \tag{3.41}$$

which upon integration and substitution by the dimensional variables yields the following equation:

$$u_d = \left[1 - exp\left(-\frac{I\boldsymbol{v} \cdot \boldsymbol{n}}{u^*} \right) \right]^{-1} \boldsymbol{v} \cdot \boldsymbol{n} \tag{3.42}$$

Equation 3.42 is valid for all surface angles, even for vertical surfaces. Note that if a boundary wall is vertical, and consequently $(\boldsymbol{v} \cdot \boldsymbol{n})$ tends to 0, the expression for u_d (where we replace $(\boldsymbol{v} \cdot \boldsymbol{n})$ by x), reduces to:

$$\lim_{x \to 0} \frac{x}{1 - exp(-Ix/u^*)} = \lim_{x \to 0} \frac{x}{(1 + Ix/u^*) - 1} = u^*/I \tag{3.43}$$

In every wall where particles deposit, we will use Equation 3.42 in combination with Equation 3.29 as a boundary condition.

3.3.4 Outlet boundary condition

The need of a boundary condition in the outlets poses a conceptual problem in many cases. The purpose of the model is to predict unknown deposition rates, and in most of its potential practical applications, concentrations at the outlets will also be unknown. In some cases, it might be possible to set a zero concentration gradient at the outlet (i.e. a Neumann boundary condition [14]) thus considering that particle concentration does not vary at the end of the domain. This, however, is probably not applicable in many indoor environments. Another option is to set a fixed concentration (Dirichlet boundary condition [14]) or total flux (Robin boundary condition [14]) in the outlet, but unless they are zero, these values are unlikely to be known, and the total mass balance would not be closed. In order to inspect this issue, let us define the following dimensionless variables:

$$\boldsymbol{x}^+ \equiv \boldsymbol{x}/x_c \qquad t^+ \equiv t/t_c \qquad c^+ \equiv c/c_c \qquad \boldsymbol{u}^+ \equiv \boldsymbol{u}/u_c \qquad \boldsymbol{v}^+ \equiv \boldsymbol{v}/u_c \tag{3.44}$$

where x_c is the characteristic length over which the dependent variables vary significantly (in a building, it could be taken as the dimension of the room of interest), c_c is the inlet particle concentration, whilst u_c is the mean fluid velocity in the bulk. The time scale can be left undefined. We introduce these dimensionless variables in Equation 3.24, which becomes:

$$\partial_t c = -\{t_c u_c / x_c\} \partial_{\boldsymbol{x}} \cdot c(\boldsymbol{u} + \boldsymbol{v}) + \{t_c(\mathscr{D} + \varepsilon)/x_c^2\} \partial_{\boldsymbol{x}} \cdot \partial_{\boldsymbol{x}} c \tag{3.45}$$

where the $^+$ symbol over the variables has been removed to simplify the notation. Because t_c appears in both bracketed terms, the relative importance of these terms is unaffected by the value of the time scale and is given by the Péclet number, defined as follows [15]:

$$\mathrm{Pe} \equiv \frac{u_c x_c}{\mathscr{D} + \varepsilon} \tag{3.46}$$

where, to simplify the arguments reported below, we have assumed that $\mathscr{D} + \varepsilon$ is constant. In the cases when the Péclet number is far larger than unity, and the partial derivatives have order unity, we can conclude that in the bulk (where the scaling employed is correct) diffusion can be neglected, at least as a zeroth-order approximation. Doing so, however, reduces the order of Equation 3.45 [16].

This reasoning tells us that near some boundaries (those where we had to assign boundary conditions and can no longer do so in the simplified problem) the simplified equation would be incorrectly scaled. In these regions, the length scale characterising the gradients must be far shorter, so that diffusion is not negligible; this also means that within these regions the concentration varies sharply, as it occurs in boundary layers.

Setting an accurate value for this boundary condition is important in problems where the Péclet number is of order unity or less, for in such cases no boundary layer forms at the outlet boundary and the condition that one sets there affects a significant part of the solution. This may happen, for instance, when simulating indoor environments where air velocity and turbulence are low.

3.3.5 Inlet boundary condition

Inlet boundary conditions do not present a particular problem. The easiest way to set a particle inlet is by introducing the particle mass concentration at the inlet boundary (i.e. Dirichlet boundary condition). This will be the most common situation in which the model will be applied (open windows with known outdoors concentration, leakage through cracks...) However, in some applications -such as a burning cigarette, a vehicle exhaust or an accidental release of particles- this information might not be available. In such cases the only parameter related to the amount of particles that enter the system is the mass flow rate.

3.4 Energy and thermal effects

One of the strengths of the drift-flux approach is that any particle transport phenomena which are relevant to a particular system can be easily added to the transport equation and the deposition boundary conditions. In this section, we add thermophoresis to the model. Thermophoresis is the movement of particles following the gradients of temperature. It is due to the higher levels of collisions between molecules and particles in the warmer areas [17]. Since thermophoresis depends on the distribution of temperature, it is necessary to solve the energy transport equation, and to appropriately resolve the dependence of the fluid properties on temperature.

3.4.1 Energy transport

The energy transport equation solved by FLUENT is [12]:

$$\frac{\partial}{\partial t}(\rho E) + \boldsymbol{\nabla} \cdot (\boldsymbol{u}(\rho E + p)) = \boldsymbol{\nabla} \left(k_{eff} \boldsymbol{\nabla} T - h\boldsymbol{J} + (\tau_w \cdot \boldsymbol{u})\right) + S_h \tag{3.47}$$

where E is the energy, T is the temperature, k_{eff} is the fluid effective thermal conductivity, h is the enthalpy of air, J is the diffusive flux of air, and S_h is a source term that can include volumetric sources and radiation [18].

3.4.2 Convection

In the cases were natural convection occurs, we used the Boussinesq approximation [18]. This approximation is based in the assumption that density differences due to temperature gradients do not cause important differences in the inertia of the flow. Nonetheless, the differences are enough to generate significant differences of specific weight [19]. The change in density is calculated with the following expression:

$$\rho = \rho_0 - \rho_0 \beta (T - T_0) \tag{3.48}$$

where ρ is the density of the fluid at temperature T, and ρ_0 is a reference density at a reference temperature T_0. β is the thermal expansion coefficient. This approximation is accurate when changes in actual density are very small (typically for relative variations in T or ρ <10%) [19].

3.4.3 Implementation of thermophoresis in the deposition and transport equations

In 1980, L. Talbot [20] proposed an expression to calculate the thermophoretic velocity of a particle in a temperature gradient:

$$u_{th} = \frac{2C_s\nu\left(\frac{k_g}{k_p} + C_t\text{Kn}\right)\left[1 + \text{Kn}(A + Be^{-C/\text{Kn}}\right]\frac{\boldsymbol{\nabla}T}{T_0}}{(1 + 3C_m\text{Kn})\left(1 + 2\frac{k_g}{k_p} + 2C_t\text{Kn}\right)} \tag{3.49}$$

It is a function of the Knudssen number, Kn $= \frac{\lambda}{r}$, where r is the particle radius and λ is the mean free path, which in this case is calculated as;

$$\lambda = 2\frac{\mu}{\rho c} \tag{3.50}$$

with:

$$c = \left(\frac{8\mathscr{R}T}{\pi}\right)^{\frac{1}{2}} \tag{3.51}$$

where $\frac{k_g}{k_p}$ is the ratio of thermal conductivities of the gas and the particles, T is the temperature, ν is the viscosity, and $\mathscr{R}$ is the ideal gas constant. The various constants that appear in the equation have the following values;

$A = 1.2$ $\qquad$ $C_t = 2.18$

$B = 0.41$ $\qquad$ $C_m = 1.14$

$C = 0.88$ $\qquad$ $C_s = 1.17$

The thermophoretic velocity can be directly implemented into the drift-flux model as an additional velocity in the particle flux:

$$J = -(\varepsilon + \mathscr{D})\frac{\partial c}{\partial y} + (\boldsymbol{n}\cdot\boldsymbol{v})c + \boldsymbol{u_{th}}c \tag{3.52}$$

Which following the same procedure outlined in section 3.3.3, leads to the following expression for the deposition velocity:

$$\int_0^1 \frac{1}{u_d^+ + (\boldsymbol{n}\cdot\boldsymbol{u}^+ + \boldsymbol{u_{th}}^+)c^+}\mathrm{d}c^+ = I \tag{3.53}$$

After integration it results in the following deposition boundary condition:

$$u_d = \left[1 - exp\left(\frac{\boldsymbol{u_{th}} + \boldsymbol{n}\cdot\boldsymbol{u}^+}{u^*}\right)\right]^{-1}(\boldsymbol{u_{th}} + \boldsymbol{n}\cdot\boldsymbol{u}^+) \tag{3.54}$$

And finally, by introducing Equation 3.52 into the advection-diffusion equation, we obtain a new transport equation for the particle phase:

$$\partial_t c = -\partial_{\boldsymbol{x}} \cdot c(\boldsymbol{u} + \boldsymbol{v} + \boldsymbol{u_{th}}) + \partial_{\boldsymbol{x}} \cdot (\mathscr{D} + \varepsilon)\partial_{\boldsymbol{x}} c \tag{3.55}$$

3.5 Turbulence modelling

This section describes the models we use to simulate the turbulent motion of air in the next Chapters. We report three models: Spalart-Allmaras [21], $k-\epsilon$ [22] and $k-\omega$ [23]. They all are eddy viscosity models, the purpose of which is to express turbulence by determining the eddy viscosity of the fluid. They are three different solutions to the closure problem of the turbulent Navier-Stokes equations, which we will describe.

The RANS equation

We simulate the movement of air using the Navier-Stokes (N-S) equation and the continuity equation for an incompressible flow [11]:

$$\boldsymbol{\nabla} \cdot \boldsymbol{u} = 0 \tag{3.56}$$

$$\partial_t \boldsymbol{u} + \boldsymbol{u} \cdot \boldsymbol{\nabla} \boldsymbol{u} = -\boldsymbol{\nabla} p + \nu \boldsymbol{\nabla}^2 \boldsymbol{u} \tag{3.57}$$

which in the Einstein notation is:

$$\frac{\partial u_i}{\partial x_i} = 0 \tag{3.58}$$

$$\frac{\partial u_i}{\partial t} + u_j \frac{\partial u_i}{\partial x_j} = -\frac{\partial p}{\partial x_i} + \nu \frac{\partial^2 u_i}{\partial x_j \partial x_j} \tag{3.59}$$

Turbulent fluctuations are introuced in the N-S equation as a time-averaged velocity $\bar{u}$ plus a fluctuating term u':

$$\boldsymbol{u} = \bar{\boldsymbol{u}} + \boldsymbol{u}' \tag{3.60}$$

If we introduce 3.60 in Equation 3.57, after some manipulation we obtain

$$\boldsymbol{\nabla} \bar{\boldsymbol{u}}^2 + \boldsymbol{\nabla} \bar{\boldsymbol{u}'^2} = -\boldsymbol{\nabla} p + \nu \boldsymbol{\nabla}^2 \bar{\boldsymbol{u}} \tag{3.61}$$

which is the Reynolds Averaged Navier-Stokes Equation, which is steady state. The term $R = \bar{\boldsymbol{u}'^2}$ is generally referred to as the Reynold stress (even though to have units of stress it needs to be multiplied by ρ). It represents the stress caused by velocity fluctuations. The Reynolds stress

is an unknown in our equation system. The problem of finding a good estimate of R is known as the *closure problem*.

The closure problem of the RANS equations is as old as the study of turbulent flows. Several solutions and workarounds to the closure problem have been suggested for over a century, and new solutions are still being researched. Let us study this problem briefly. Considering, as a general case, that $\bar{u}$ is time averaged through a finite interval τ and using Einstein notation, Equation 3.59 becomes:

$$\frac{\partial \bar{u_i}}{\partial t} + \bar{u_j}\frac{\partial \bar{u_i}}{\partial x_j} = -\frac{\partial \bar{p}}{\partial x_i} + \nu\frac{\partial^2 \bar{u_i}}{\partial x_j \partial x_j} - \frac{\partial \bar{u_i'u_j'}}{\partial x_j} \tag{3.62}$$

In which case the Reynolds stress is $R_{ij} = \bar{u_i'u_j'}$. The first solution, suggested Boussinesq in 1887 [24], was to relate R_{ij} with the mean flow using the concept of eddy viscosity μ_t:

$$R_{ij} = 2\mu_t S_{ij} - \frac{2}{3}\rho k \delta_{ij} \tag{3.63}$$

where S_{ij} is the mean strain rate tensor:

$$S_{ij} = \frac{1}{2}\left[\frac{\partial u_i}{\partial x_j} + \frac{\partial u_j}{\partial x_i}\right] - \frac{1}{3}\frac{\partial u_k}{\partial x_k}\delta_{ij} \tag{3.64}$$

where $k = \frac{1}{2}\overline{v_i'v_i'}$ is the turbulence kinetic energy and δ_{ij} is the Kronecker delta, which is merely a way of expressing that the last term is only meaningful when i=j:

$$\delta_{ij} = \begin{cases} 0 & \text{if } i \neq j \\ 1 & \text{if } i = j, \end{cases} \tag{3.65}$$

The models that solve the closure problem by finding a value of μ_t in order to use the Boussinesq approximation are called linear eddy viscosity models. We will discuss three of these models: Spalart-Allmaras, $k-\epsilon$, and $k-\omega$.

$k-\epsilon$ turbulence model

The $k-\epsilon$ turbulence model was developed in 1974 by Launder and Spalding [22], and is described here as used in Fluent [12]. It is a two equation model that calculates the turbulent diffusivity as a function of the kinetic energy, k and its dissipation rate, ϵ:

$$\mu_t = \rho C_\mu \frac{k^2}{\epsilon} \tag{3.66}$$

It uses a transport equation for each of these variables. The transport equation for k is:

$$\frac{\partial}{\partial t}(\rho k) + \frac{\partial}{\partial x_i}(\rho k u_i) = \frac{\partial}{\partial x_j}\left[\left(\mu + \frac{\mu_t}{\sigma_k}\right)\frac{\partial k}{\partial x_j}\right] + P_k + P_b - \rho\epsilon - Y_M + S_k \tag{3.67}$$

And the transport equation for the rate of dissipation of the kinetic energy, ϵ, is:

$$\frac{\partial}{\partial t}(\rho \epsilon) + \frac{\partial}{\partial x_i}(\rho \epsilon u_i) = \frac{\partial}{\partial x_j}\left[\left(\mu + \frac{\mu_t}{\sigma_\epsilon}\right)\frac{\partial \epsilon}{\partial x_j}\right] + C_{1\epsilon}\frac{\epsilon}{k}\left(P_k + C_{3\epsilon}P_b\right) - C_{2\epsilon}\rho\frac{\epsilon^2}{k} + S_\epsilon \tag{3.68}$$

where P_k is the production of k due to mean velocity gradients, P_b is the production of k due to buoyancy and Y_M reflects the effects of compressibility in k (this parameter is only relevant for high fluid velocities and will not be used in our case). S_k and S_ϵ are source terms of k and ϵ. The production of k is defined as follows:

$$P_k = -\rho\overline{u_i' u_j'}\frac{\partial u_j}{\partial x_i} \tag{3.69}$$

Using the Boussinesq hypothesis we can calculate it as:

$$P_k = \mu_t S^2 \tag{3.70}$$

where S is the modulus of the mean rate-of-strain tensor, defined as:

$$S \equiv \sqrt{2 S_{ij} S_{ij}} \tag{3.71}$$

The generation of k due to buoyancy is calculated with:

$$P_b = \beta g \frac{\mu_t}{\mathrm{Pr_t}}\frac{\partial T}{\partial x_i} \tag{3.72}$$

where Pr_t is the turbulent Prandtl number. β is the coefficient of thermal expansion, defined as

$$\beta = -\frac{1}{\rho}\left(\frac{\partial \rho}{\partial T}\right)_p \tag{3.73}$$

And the remaining model constants are: $C_{1\epsilon} = 1.44, \quad C_{2\epsilon} = 1.92, \quad C_{3\epsilon} = -0.33, \quad C_\mu = 0.09, \quad \sigma_\epsilon = 1.3, \quad \sigma_k = 1.0$

RNG $k - \epsilon$ turbulence model

The RNG k-epsilon is a modification of the k-epsilon model by Yakhot et. al. [25] in which the turbulent viscosity is related to k and ϵ with

$$d\left(\frac{\rho^2 k}{\sqrt{\epsilon\mu}}\right) = 1.72\frac{\hat{\nu}}{\sqrt{\hat{\nu}^3 - 1 + C_\nu}}d\hat{\nu} \tag{3.74}$$

where $\hat{\nu} = \mu_t/\mu$ and $C_\nu = 100$. The transport equations for k and ϵ are also slightly modified:

$$\frac{\partial}{\partial t}(\rho k) + \frac{\partial}{\partial x_i}(\rho k u_i) = \frac{\partial}{\partial x_j}\left[\alpha_k \mu_t \frac{\partial k}{\partial x_j}\right] + P_k + P_b - \rho\epsilon - Y_M + S_k \tag{3.75}$$

$$\frac{\partial}{\partial t}(\rho \epsilon) + \frac{\partial}{\partial x_i}(\rho \epsilon u_i) = \frac{\partial}{\partial x_j}\left[\alpha_\epsilon \mu_t \frac{\partial \epsilon}{\partial x_j}\right] + C_{1\epsilon}\frac{\epsilon}{k}P_k - C_{2\epsilon}\rho\frac{\epsilon^2}{k} + S_\epsilon - R_\epsilon \tag{3.76}$$

The main difference is the addition of the R_ϵ term which improves the accuracy of the model in rapidly straining flows and which is defined as:

$$R_\epsilon = C_{2\epsilon} + \frac{C_\mu \eta^3(1 - \eta/\eta_0)}{1 + \beta\eta^3} \tag{3.77}$$

where

$$\eta = Sk/\epsilon \tag{3.78}$$

and $\eta_0 = 4.38$, $\beta = 0.012$ (found experimentally) and S is calculated with equation 3.71. α_k and α_ϵ are the inverse effective Prandtl numbers, calculated using the following equation:

$$\left[\frac{\alpha - 1.3929}{\alpha_0 - 1.3929}\right]^{0.6321}\left[\frac{\alpha - 2.3929}{\alpha_0 - 2.3929}\right]^{0.3679} = \frac{\mu}{\mu_t} \tag{3.79}$$

where μ is the fluid viscosity and $\alpha_0 = 1.0$. When the Reynolds number is very high, $\alpha_k = \alpha_\epsilon \approx 1.393$ [12]. The values of all of the constants, which in the RNG procedure are derived explicitly, are slightly different than the default values of the standard $k-\epsilon$ model: $C_\mu = 0.0845, \quad C_{1\epsilon} = 1.42, \quad C_{2\epsilon} = 1.68$.

$k-\omega$ turbulence model

Similarly to the previous models the $k-\omega$, developed by Wilcox in 1988 [23], uses two transport equations, for the turbulence kinetic energy (k) and the specific dissipation rate (ω), which are used to calculate the turbulent viscosity:

$$\mu_t = \alpha^* \frac{\rho k}{\omega} \tag{3.80}$$

$$\frac{\partial}{\partial t}(\rho k) + \frac{\partial}{\partial x_i}(\rho k u_i) = \frac{\partial}{\partial}\left[\Gamma_k \frac{\partial_k}{\partial x_j}\right] + P_k - Y_k + S_k \tag{3.81}$$

$$\frac{\partial}{\partial t}(\rho\omega) + \frac{\partial}{\partial x_i}(\rho\omega u_i) = \frac{\partial}{\partial}\left[\Gamma_\omega \frac{\partial_\omega}{\partial x_j}\right] + P_\omega - Y_\omega + S_\omega \tag{3.82}$$

where Γ are the effective viscosities given by:

$$\Gamma_k = \mu + \frac{\mu_t}{\sigma_k} \quad \text{and} \quad \Gamma_\omega = \mu + \frac{\mu_t}{\sigma_\omega} \tag{3.83}$$

The terms Y_k and Y_ω are the dissipations of k and ω. The term P_k represents the production of turbulence kinetic energy. In the same manner than the $k-\epsilon$ model, this term can be calculated with:

$$P_k = \mu_t S^2 \tag{3.84}$$

The production of ω is given by:

$$P_\omega = \alpha \frac{\omega}{k} P_k \tag{3.85}$$

where α is a correction for low Reynolds numbers. Expressions for α and α^* along with Y_k, Y_ω and the constants σ_k and σ_ϵ can be found in [12]

Spalart-Allmaras turbulence model

Spalart-Allmaras model consists of a single transport equation for a viscosity-like variable $\tilde{\nu}$ [21], known as the Spalart-Allmaras variable and related to ν_t. This model does not involve the kinetic energy k and thus ignores the second term of Equation 3.63 [26]. The turbulent eddy viscosity is given by:

$$\nu_t = \tilde{\nu} f_{v1} \tag{3.86}$$

$$\begin{aligned}\frac{\partial \tilde{\nu}}{\partial t} + u_j \frac{\partial \tilde{\nu}}{\partial x_j} = C_{b1}(1-f_t)\tilde{S}\tilde{\nu} - \left[C_{w1} f_w - \frac{C_{b1}}{\kappa^2} f_t\right]\left(\frac{\tilde{\nu}}{d}\right)^2 \\ + \frac{1}{\sigma}\left[\frac{\partial}{\partial x_j}\left((\nu+\tilde{\nu})\frac{\partial \tilde{\nu}}{\partial x_j}\right) + C_{b2}\frac{\partial \tilde{\nu}}{\partial x_i}\frac{\partial \tilde{\nu}}{\partial x_i}\right]\end{aligned} \tag{3.87}$$

with the following equations:

$$f_{v1} = \frac{\chi^3}{\chi^3 + C_{v1}^3}, \quad \chi = \frac{\tilde{\nu}}{\nu} \tag{3.88}$$

$$\tilde{S} \equiv S + \frac{\tilde{\nu}}{\kappa^2 d^2} f_{v2}, \quad S = \frac{1}{2}\boldsymbol{\nabla}^2 \boldsymbol{u} \tag{3.89}$$

$$g = r + C_{w2}(r^6 - r), \quad r \equiv \frac{\tilde{\nu}}{\tilde{S}\kappa^2 d^2} \tag{3.90}$$

$$f_w = g\left[\frac{1 + C_{w3}^6}{g^6 + C_{w3}^6}\right]^{1/6}, \quad f_t = C_{t3}\exp(-C_{t4}\chi^2), \quad f_{v2} = 1 - \frac{\chi}{1 + \chi f_{v1}} \tag{3.91}$$

where d is the distance to the closest surface and the various constants as used in [12]: $\sigma = 2/3$, $C_{b1} = 0.135$, $C_{b2} = 0.62$, $\kappa = 0.4$, $C_{w1} = C_{b1}/\kappa^2 + (1 + C_{b2})/\sigma$, $C_{w2} = 0.3$, $C_{w3} = 2$, $C_{v1} = 7.1$, $C_{t3} = 1.1$, $C_{t4} = 2$.

3.6 Implementation strategy

Until now we have been concerned with the mathematical description of the model, with few references to its numerical solution. In this section we will describe the implementation of the model in Ansys Fluent. Due to the popularity of Fluent and its status as an industry and academic standard, it is an ideal platform to support our mathematical model. This section uses terminology which is specific to this code and as used in its manual [12], to which we refer the reader in need of detailed information. Given the rising popularity of drift-flux models, we also hope that this section proves useful to potential users of the model.

Many of the equations that constitute our model are not included in Fluent by default, and need to be added using Fluent expansion capabilities. In a nutshell, this is the strategy we have followed: Firstly, the particle field is implemented into Fluent as a User Defined Scalar (UDS). The equations governing the motions of the particles are implemented using User Defined Functions (UDFs) that modify some of the default components of Fluent. The various sizes of particles are reflected introducing a UDS for every size-mode.

3.6.1 Implementing the advective flux

For an arbitrary scalar Φ Fluent solves the equation:

$$\frac{\partial \rho\Phi}{\partial t} + \frac{\partial}{\partial x}(\rho u\Phi - \Gamma\frac{\partial \Phi}{\partial x}) = S_\Phi \tag{3.92}$$

where Φ is the transported scalar, ρ the density of the carrier fluid and Γ is the diffusivity of the scalar. S_Φ is a source term which is zero in our case. Equation 3.24 can be expressed in a form consistent with equation 3.92.

$$\frac{\partial c}{\partial t} + \frac{\partial}{\partial x}[(\boldsymbol{u} + \boldsymbol{v}\cdot\boldsymbol{n})c - (\mathscr{D} + \varepsilon)\frac{\partial c}{\partial x}] = 0 \tag{3.93}$$

Any modifications to the advection term of Equation 3.92 must be introduced using the macro DEFINE_UDS_FLUX. The advection term in Equation 3.92 has the form:

$$\boldsymbol{\nabla} \rho \boldsymbol{u} \Phi \tag{3.94}$$

To define the advection term using this macro, the UDF needs to return the scalar value of $\rho \boldsymbol{u} \cdot \boldsymbol{A}$ which should be in SI units of mass flow rate (i.e. kg/s) and where $\boldsymbol{A}$ is the face vector normal to the face. By comparing Equations 3.92 and 3.24, it can be concluded that the macro should return to Fluent the following scalar value:

$$(\boldsymbol{u} + \boldsymbol{v}) \cdot \boldsymbol{A} \tag{3.95}$$

Note that, since the particle concentration c is a dimensional scalar, Equation 3.95 has already the appropriate units to be used in the Fluent UDS transport function. The UDS flux is set at every face of the computational domain. The macro does not loop automatically through all faces, therefore a loop must be created that makes the necessary assignments at every face. This loop needs to identify whether the face under examination is an interior face or lies at the domain boundary. For interior faces, the velocity is taken as the average value of velocities at the centres of the two adjacent cells.

The question may arise whether this flux must be also implemented in boundary faces, this is, in the walls of the domain where particles deposit. The particle flux towards surfaces (both diffusive and convective) is included in the equation for the deposition flux, Equation 3.28, which will be introduced as a boundary condition. Therefore, a convective flux towards wall boundaries should not be included using the macro DEFINE_UDS_FLUX. Since it will be defined by another function, the convective flux through boundary walls can be left undefined.

Implementing a size distribution The DEFINE_UDS_FLUX macro is implemented in Fluent ("hooked" in the software terminology) for each scalar, and it has access to the scalar identifier. The flux function contains the settling velocity ($\boldsymbol{v}$), which is a function of the particle diameter and therefore will be different for every scalar. However, to avoid writing a different UDF for every scalar, a condition can be introduced in the macro with the purpose of assigning the appropriate diameter to each scalar.

Hooking the UDF in Fluent The DEFINE_UDS_FLUX macro is implemented in the User Defined Scalar menu, selecting the option `user-defined` in the `Flux Function` drop down menu.

3.6.2 Implementing the diffusive flux

Modifications in the diffusion coefficient are introduced in Fluent using the DEFINE_DIFFUSIVITY macro. This is a straightforward implementation, since the macro automatically loops through

all cells, and the only calculation to be made is the addition of the two calculated diffusivities, Brownian and turbulent:

$$\Gamma = \mathscr{D} + \varepsilon \tag{3.96}$$

Implementing a size distribution Particle Brownian diffusion is also a function of particle diameter. It is not necessary to implement this UDF for every scalar, since it will automatically be applied to all the UDSs unless specified otherwise. As in the previous case, the UDS identifier is available to the macro, so an IF loop can be implemented that assigns the right value of diameter to each UDS.

Hooking the UDF in Fluent This UDF can be introduced in Fluent in the Materials menu, selecting `UDS Diffusivity - user-defined`.

3.6.3 Implementing the deposition boundary condition

We implement deposition at all the boundary faces of the domain except for inlet and outlet using the macro DEFINE_PROFILE. This is a very flexible macro that allows the definition of any variable in the selected boundary faces. It requires the use of a loop through all the faces in the face superthread. The deposition velocity is calculated on every face:

$$J = u_d c \tag{3.97}$$

where c is the particle concentration at the interface between the boundary layer and the fluid bulk, taken as the concentration of the cell adjacent to the face under examination. When a flux is set at a wall boundary, Fluent interprets this flux as a diffusive flux, i. e.:

$$J_{diffusive} = -\Gamma \frac{\partial c}{\partial x} \tag{3.98}$$

The deposition flux, however, is a total flux, representing the specific total flow rate of particles depositing at the wall:

$$J = J_{convective} + J_{diffusive} = c(\boldsymbol{u} + \boldsymbol{v} \cdot \boldsymbol{n}) - \Gamma \frac{\partial c}{\partial x} \tag{3.99}$$

Therefore, the flux to be used in Equation 3.98 is not the deposition flux, but only its diffusive component, given by:

$$J_{diffusive} = J - J_{convective} \tag{3.100}$$

where the value of $J_{convective}$ has already been calculated in the UDF for the convective flux.

Hooking the UDF in Fluent This UDF can be introduced at any wall present in the Boundary Conditions menu, selecting `Specified Flux` in the drop-down menu, and `user-defined` in the white space reserved for the input value.

Implementing a size distribution The deposition velocity is calculated from the integral I, which is a function of the Schmidt number, which depends on the diameter. Unfortunately, the DEFINE_PROFILE macro does not have access to the identifier of the UDS being solved. Consequently a macro has to be created for every UDS, every macro using the right value of the diameter, and every macro has to be hooked separately at every wall for each UDS.

3.6.4 Implementing thermophoresis

The calculation of the thermophoretic velocity can be added in the DEFINE_UDS_FLUX macro by adding $\boldsymbol{u_{th}}$ to Equation 3.95 and to the DEFINE_PROFILE macro by replacing the deposition boundary condition by Equation 3.54. The implementation of thermophoresis requires the calculation of temperature gradients, and therefore energy balances must be implemented. The energy transport equation is enabled in the menu `Define-Models-Energy`. By default Fluent does not store the temperature gradients required for computation of the thermophoretic velocity. This setting can be changed by running the following command in the text user interface (TUI):

```
solve/set/expert
```

and then selecting the following option:

```
Prevent temporary memory of being freed - Yes
```

3.6.5 UDS inlets and outlets

Inlet Particle inlets can be defined by introducing the particle mass or number concentration at the inlet boundary (i.e. Dirichlet boundary condition), along with the air velocity. As mentioned above, this will be the most common situation in which the model will be applied. For the cases in which the particle flux is known, a scalar flux can be defined in the UDS tab in the boundary conditions menu under the name `flux - user defined` . Since this flux refers to the diffusive flux, the same method used in the wall boundaries will have to be applied, subtracting the convective flux from the diffusive flux before returning it to Fluent. An UDF is required to do this calculation. Its function is to estimate the convective flux from the UDS concentration in the cells adjacent to the inlet boundary and the inlet velocity introduced by the user.

Outlet Fixed concentrations (Dirichlet boundary) or gradients (Neumann boundary) can be directly implemented in the boundary conditions menu.

References

[1] D. Marchisio and R. Fox. *Computational Models for Polydisperse Particulate and Multiphase Systems*. Cambridge Series in Chemical Engineering. Cambridge University Press, 2013.

[2] C. Brennen. *Fundamentals of Multiphase Flow*. Cambridge University Press, 2005.

[3] L. Gibilaro. *Fluidization Dynamics*. Elsevier Science, 2001.

[4] P. Reist. *Aerosol science and technology*. McGraw-Hill, 1993.

[5] R. Kohli and K. Mittal. *Developments in Surface Contamination and Cleaning - Methods for Removal of Particle Contaminants*. Developments in surface contamination and cleaning. Elsevier Science, 2011.

[6] M. Schnell, C. Cheung, and C. Leung. "Investigation on the coagulation and deposition of combustion particles in an enclosed chamber with and without stirring". *Journal of Aerosol Science* 37:11 (2006), pp. 1581–1595.

[7] A. Dewan. *Tackling Turbulent Flows in Engineering*. Springer, 2010.

[8] W. K. George and M. Tutkun. "Mind the gap: a guideline for large eddy simulation". *Philosophical Transactions of the Royal Society A: Mathematical, Physical and Engineering Sciences* 367:1899 (2009), pp. 2839–2847.

[9] T. Poinsot and D. Veynante. *Theoretical and Numerical Combustion*. Edwards, 2005.

[10] A. C. K. Lai and W. W. Nazaroff. "Modeling indoor particle deposition from turbulent flow onto smooth surfaces". *Journal of Aerosol Science* 31:4 (2000), pp. 463–476.

[11] H. Tennekes and J. Lumley. *A First Course in Turbulence*. MIT Press, 1972.

[12] FLUENT. *FLUENT 6.3 User's Guide*. Fluent Inc. 2006.

[13] P. W. Longest and M. J. Oldham. "Numerical and experimental deposition of fine respiratory aerosols: Development of a two-phase drift flux model with near-wall velocity corrections". *Journal of Aerosol Science* 39:1 (2008), pp. 48–70.

[14] T. Bick. *Elementary Boundary Value Problems*. Chapman & Hall/CRC Pure and Applied Mathematics. Taylor & Francis, 1993.

[15] W. Hinds. *Aerosol Technology: Properties, Behavior, and Measurement of Airborne Particles*. Wiley, 2012.

[16] A. Bush. *Perturbation Methods for Engineers and Scientists*. CRC Press Library of Engineering Mathematics. Taylor & Francis, 1992.

[17] D. Camuffo. "Wall temperature and the soiling of murals". *Museum Management and Curatorship* 10:4 (1991), pp. 373–383.

[18] R. Pletcher, J. Tannehill, and D. Anderson. *Computational Fluid Mechanics and Heat Transfer, Third Edition*. Series in Computational and Physical Processes in Mechanics and Thermal Sciences. Taylor & Francis, 2012.

[19] M. Favre-Marinet and S. Tardu. *Convective Heat Transfer*. ISTE. Wiley, 2013.

[20] L. Talbot et al. "Thermophoresis of particles in a heated boundary layer". *Journal of Fluid Mechanics* 101 (04 1980), pp. 737–758.

[21] S. A. P. Spalart. "A one-equation turbulence model for aerodynamic flows". *Recherche Aerospatialr* (1994), pp. 5–21.

[22] B. Launder and D. Spalding. "The numerical computation of turbulent flows". *Computer Methods in Applied Mechanics and Engineering* 3:2 (1974), pp. 269–289.

[23] D. C. Wilcox. "Reassessment of the scale-determining equation for advanced turbulence models". *American Institute of Aeronautics and Astronautics Journal* 26:11 (1988), pp. 1299–1310.

[24] J. Boussinesq. *Théorie de l'écoulement tourbillonnant et tumultueux des liquides*. Gauthier-Villars et fils, Paris, 1897.

[25] V. Yakhot et al. "Development of turbulence models for shear flows by a double expansion technique". *Physics of Fluids A: Fluid Dynamics (1989-1993)* 4:7 (1992), pp. 1510–1520.

[26] C. Rumsey. *NASA Turbulence Modeling Resource*. 2014. URL: `http://turbmodels.larc.nasa.gov/index.html` (visited on 08/06/2014).

4 Validation

4.1 Introduction

We have validated the model using two simple cases. The first case is an experiment obtained from the literature, which describes the spatial distribution of dust in a real room. The second case is an experimental tunnel that we designed in order to investigate some specific aspects of the model: its responsiveness in transient simulations, the suitability of different turbulence models, and the prediction of deposition under different flow regimes.

The choice of these two validation tests is guided by a common issue. As we have already discussed, our foremost interest is the spatial distribution of deposition. This purpose is what makes the simulation of heritage spaces distinct from other applications of aerosol models. We are not only interested in predicting deposition rates or suspended particle concentrations: we want to know where do particles deposit. The data collected in both experiments contains valuable information on the local variation of deposition.

In this Chapter we describe the application of the model in these validation experiments, providing an understanding of its flexibility, its limitations and its strengths. We also relate the applicability of the model to several non-dimensional parameters that describe particulate matter deposition and transport processes.

Our validation is based on the comparison of deposition and concentration measurements in simulations, laboratory small-scale experiments, and building large-scale experiments. In order to measure the accuracy or "correctness" of the simulations we are using data related to the final state of deposition. We are not comparing the processes which led particles to the walls in each of the three systems. We measure the outcome, not the process, e.g. we do not base our comparisons in measurements of air velocity or turbulence. This procedure might suggest that we assume that the movement of air and particles is comparable in the three systems -CFD,

laboratory, and buildings- or at least, that if the outcomes are comparable, we can consider the transport processes to be equally similar.

This is not necessarily true. Air movement in the tunnel experiments, for example, is relatively constant. Of course, air is turbulent and that implies fluctuations, but these fluctuations are within a very narrow range, and are given only by the geometry and the inlet properties, which are both constant and under control. Contrarily, air motion and turbulence regimes are very changeable in real buildings, and we can expect the final deposition to be due to a combination - or a succession - of different air flow patterns. Lastly, the simulated turbulence is the steadiest of all: once we set input parameters and define a geometry, we will obtain a certain distribution of air velocity with a very narrow uncertainity. If we obtain a value of deposition from these three types of experiments, and it happens to be the same, we should not assume in any case that the processes behind that measurement are identical.

This brings forward the issue of representation: a simulation of a building does not represent everything that can happen in the building, but one of its many possible states. We must ensure that the simulated state is significant enough. Our comparisons are only meaningful if we can show that the simulations are representative of processes that really occur, and that contribute significantlly to the measured outcomes. During the process of validation explained in the next two chapters, we must be able to show that each simulation is representative of real phenomena - and above all, of the most significant phenomena.

4.2 Validation against the literature

As mentioned in the introduction, the majority of the experimental validations of deposition models have two characteristics in common: the experiments are carried out in well-mixed volumes and the parameter of study is the decay rate of particles of different sizes. However, we revised the literature in search of experimental evidence that had other attributes: (i) an inhomogeneous environment with significant gradients of concentration, (ii) spatially-resolved deposition rates and (iii) velocities and a geometry comparable to the indoor environment. We excluded the extensive literature on deposition in the respiratory tract, not only because such simulations do not satisfy (iii), but also because generating the detailed mesh that would be required falls outside the scope of our project.

We found the experimental study of deposition described in paper by E. Sajo [1] to satisfy all these criteria. This work describes the controlled emission of particles of known properties in a room, followed by a study of their deposition patterns on the floor. It is a purely experimental piece of work that provides some very valuable information, such as the raw particle count data, and the exact location of every sampling point. Its only drawback for the purpose of the validation is that boundary conditions (particularly in the air inlets and outlets) are not clearly defined. However, as we shall see, there is enough information in the paper to find reasonable estimates of air velocity in these boundaries.

Description of the experimental data

In this work, the authors generated a cloud of monodispersed Co_3O_4 tracer dust, with an average diameter of 1.1 μm and with particles ranging from 0.01 to 15 μm. They used a burst of inert gas to resuspend 10 g of dust in 2 s. The nozzle that produced the emission was installed at the centre of an unfurnished room with dimensions 6.6x4x3 m, at a height of 2 m.

After the release, the authors let the particles deposit during 90 min. They collected the particles in 70 sticky samplers of dimensions 2.5x5 cm located in a grid on the floor of the room [1]. This procedure is similar to the one we use in a latter stage, which is described in detail in Appendix 1. They recorded the air flow pattern in the room during the experiment using a hand-held hot-wire anemometer and tracking the trajectory of a balloon against a gridded background. They detected air recirculation, with a speed of $\sim$0.25 m/s above 1.5 m and $\sim$0.20 m/s in the opposite direction below 1.5 m.

Geometry and boundary conditions

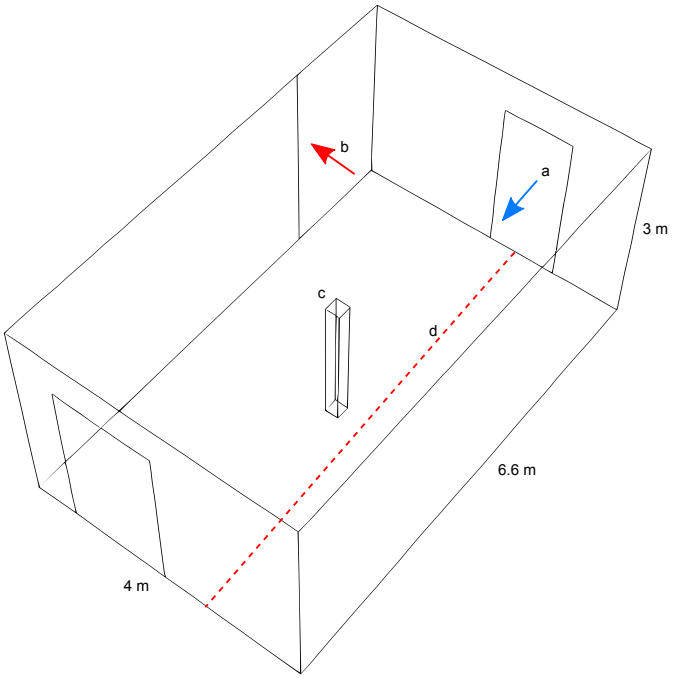

Figure 4.1: Geometry of the room with dimensions and the relevant boundary conditions. (a) air inlet (on the North Wall), (b) air outlet, (c) air nozzle with particulate matter inlet and (d) line along which we have carried out the comparison with the experimental data obtained from [1].

In the experiment, air was entering the room from the open door on the north wall (see Figure 4.1), and exiting through the corridor. Even though this pattern is not described directly in the article, we found it to be the only possible explanation to the observed velocities. We considered that the velocity in the inlet door was homogeneous, perpendicular to the door, and with a magnitude between 0.25 and 2 $\mathrm{m/s}$. This assumption provided a velocity profile which was very similar to the one described by the authors. Simulations would later reveal that only a velocity close to 1 $\mathrm{m/s}$ in the inlet door could explain the measured patterns of deposition. Particle concentrations in inlets and outlets were considered to be 0. In this case, this assumption did not imply the existence of a concentration boundary layer in the outlets, since as it is apparent from the results reported in the paper, most of the particles deposit on the floor, and virtually none leave the room. In other words, zero concentration in the outlets is a realistic description of the observed phenomena. We approximated the particle inlet as a 0.1x0.1 m surface with a particle flux of 5 $\mathrm{g/s}$, which was active for 2 s. This flux was implemented following the procedure detailed in Section 3.6.3. We used a tetrahedral mesh with a cell size of 0.2 m. A grid independence test using the accumulated deposition 10 s after release indicated that the result is constant when cells are smaller than 0.2 m (11000 nodes). and it is within $\sim$98% accuracy when cells are 0.3 m (3750 nodes).

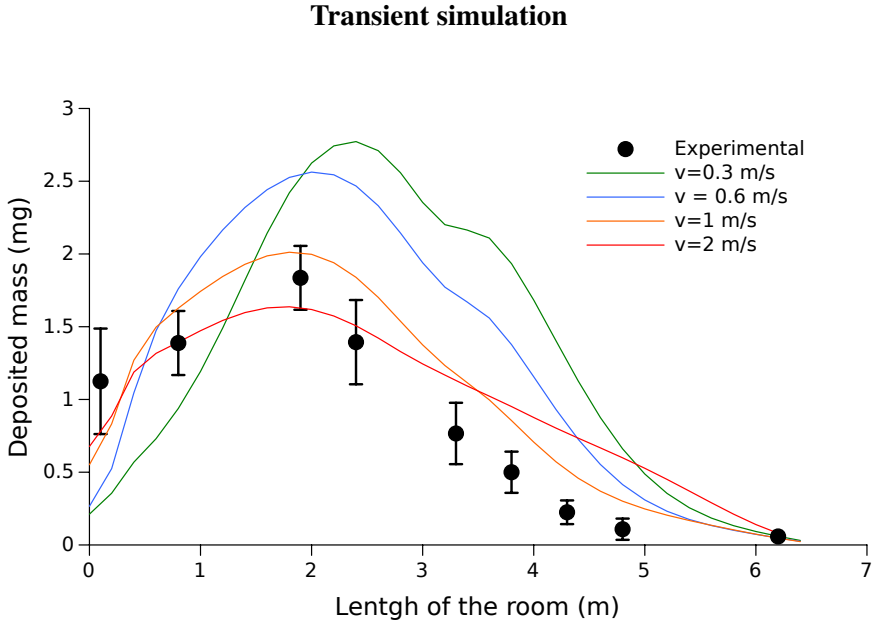

Figure 4.2: Experimental deposition on the floor of the chamber as reported in [1] and simulated deposition using different inlet velocities in the main door. In this plot, the inlet door would be located at 7 meters and the source of particles at 3. When the inlet velocity increases, more particles deposit on the opposite end of the room.

We produced a transient simulation of the deposition event. We assumed that particles had an average diameter of 1.1 $\mu\mathrm{m}$ and a density of 6100 $\mathrm{kg/m^3}$. We used a time-step of 1 s and

simulated 30 min (even though the original experiment lasted 90 min, simulations indicate that 30 min is the time required for 99% of the particles to deposit). Since the model only provides the instantaneous deposition flux, we had to add the functionality of calculating the accumulated deposition. This was very easily done with the following relation:

$$M_{(t=T)} = J_{(t=T)}\Delta t + M_{(t=T-1)} \tag{4.1}$$

where $M_{(t=T)}$ is the accumulated mass per unit area at the current time step, $J_{(t=T)}$ is the deposition flux at the current time step and Δt is the time increment between time steps. Computationally, this equation was implemented using the macro DEFINE_EXECUTE_AT_END, which is executed at the end of the solution for steady-state simulations and at the end of every time step for transient simulations. The simulations were carried out with the $k-\epsilon$ turbulence model as per the recommendations of other authors explained in Section 2.3.3. Different turbulent models will be tested in the next sections.

Figure 4.2 shows the comparison between the simulated and measured values of M through the straight line marked in Figure 4.1. One can easily see that the model successfully predicts the non-trivial pattern of the deposition on the floor, and it provides a good estimation of the magnitude of deposition. Figure 4.3 shows the contour of M on the floor and the concentration of suspended PM, c, at different stages of the simulation.

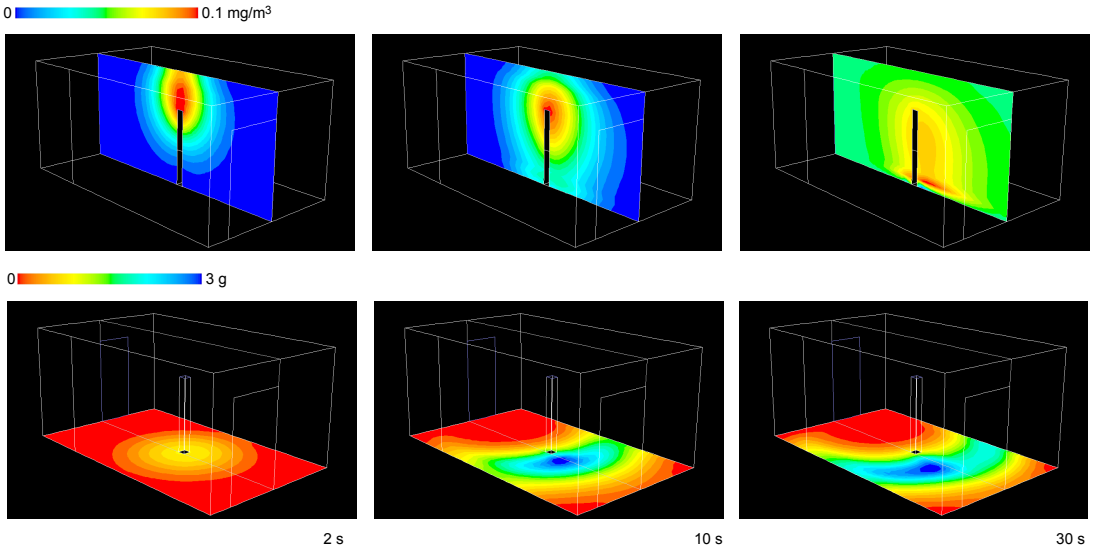

Figure 4.3: Evolution of the concentration profile of suspended particulate matter and of the accumulated mass on the floor, M.

4.3 Laboratory validation

We designed our own validation experiment in order to address several problems. Firstly, validation against the literature had allowed us to use a transient simulation, but we were only able to compare the final states. We needed an experimental dataset that we could use to validate the dynamic evolution of deposition. Secondly, we were interested in a design that reflected geometries and flow patterns encountered indoors: flat surfaces, straight turns, and walls interrupting the flow. Finally, we wanted to create an experiment of simple construction, quick, and well-suited to the available instrumentation. Many different tunnel geometries, wall configurations and sizes could fit these requirements, and the final configuration is to a certain extent arbitrary. The experiment we carried out is one of the many possible solutions to our design questions. However, as we shall see, it successfully enables the exploration of many aspects of the simulation of aerosol deposition.

4.3.1 Experimental set-up

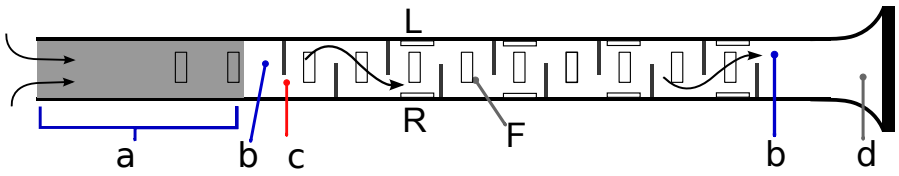

Figure 4.4: Diagram of the experimental tunnel showing the buffer area (a), the location of the condensation particle counters (b), the hot-wire anemometer (c) and the fan and diffuser system (d). F, R and L indicate the location of the floor, right wall and left wall glass slides used to collect particles in the natural background experiments.

The experimental tunnel has dimensions of 15 cm x 15 cm x 1.8 m, and is equipped with 10 internal barriers positioned every 13 cm. The dimensions of the barriers are 10 cm x 15 cm, and they leave a free Section of 5 cm x 15 cm. Air is displaced by a fan located at the outlet of the tunnel after a diffuser. We added a 1-m buffer Section with no barriers before the experimental tunnel with the aim of stabilizing the flow and ensuring that the introduced aerosol distributed evenly through the Section area.

The fan motor was equipped with a revolution regulator which allowed us to adjust the air velocity from 0 to 0.6 $\mathrm{m/s}$. Air velocity was measured at the inlet with a hot-wire anemometer. This anemometer was placed in the gap left by the first barrier, where the flow was more directional and could be measured with more accuracy. Particles were sampled at the inlet and outlet of the tunnel using two particle condensation counters (TSI P-Trak, TSI, Shoreview, US), which provided the number concentration of all particles in the size range of 0.02 $\mu\mathrm{m}$ to 1 $\mu\mathrm{m}$. See Appendix 1 for a detailed explanation of the choice and operation of these instruments.

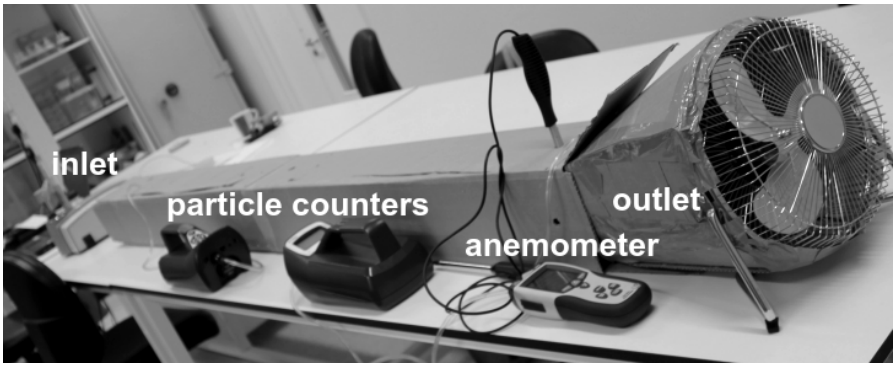

Figure 4.5: Figure of the tunnel during an experiment indoors, with two condensation particle counters and the anemometer.

Unless otherwise stated, the reported experiments took place indoors, in the ISH Heritage Science Laboratory at UCL (London). This laboratory is located in a basement and is mechanically ventilated. The background concentration of $PM_{0.02-1}$ was about $\sim$ 2000-4000 cm^{-3}. Since the purpose of this research is to test and prepare the model for its applicability in real-world scenarios we decided to use common sources of aerosols: resuspended dust, candle smoke, and untreated air from the environment as input. All the experiments were transient, i.e. the inlet concentration changed during the course of the experiment. However, as we shall see, some of these experiments can be modelled in steady-state simulations.

4.3.2 Preliminary outdoor experiments

With the purpose of understanding the behaviour of PM inside our experimental set-up we carried out some preliminary experiments in an outdoor location. This location was in the UCL Campus in Bloomsbury, London, a few meters from the Upper Woburn Place road. We left the tunnel outdoors for different lengths of time, during which we monitored the PM concentration in the inlet and the outlet using the P-Trak particle counters. The fan was permanently on, keeping a constant inlet velocity of 0.25 $\mathrm{m/s}$. We did not attempt to control the size of the PM absorbed by the system.

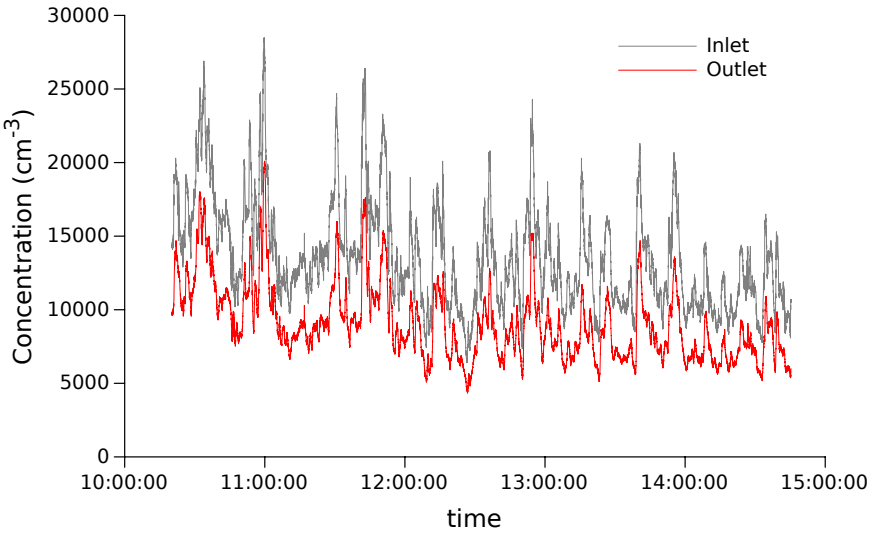

Figure 4.6: Simultaneous evolution of the inlet and outlet particulate matter concentrations during an outdoor experiment with the tunnel.

Naturally, the outdoor concentration changed continuously. This variations of c can be observed at different time-scales. Since the experiments topically lasted from 5 to 10 hours, we did not fully capture the daily variation related to the changing traffic density. The variation shown in Figure 4.6 occurs in smaller time scales and may be associated mainly with wind fluctuations, small scale turbulence, or the emissions from the individual cars passing by. Figure 4.6 also shows the concentration in the outlet of the tunnel during the same period, which is significantly lower than the inlet concentration. The inlet and outlet concentration display a nearly identical variation.

The first experimental observation is that, under constant velocity conditions, a fixed portion of the particles that are introduced into the tunnel will deposit on the internal walls. Figure 4.7 shows a scatter plot of the inlet number concentration versus the outlet number concentration in the tunnel. In this plot, colour indicates time (blue dots being at the beginning of the experiment and red dots at the end). This colouring illustrates that - as the outdoor concentration varies- the inlet/outlet ratio, which is the slope of the regression line with zero intercept, maintains a constant value (in this case, $c_{out} = 0.86 c_{in}$).

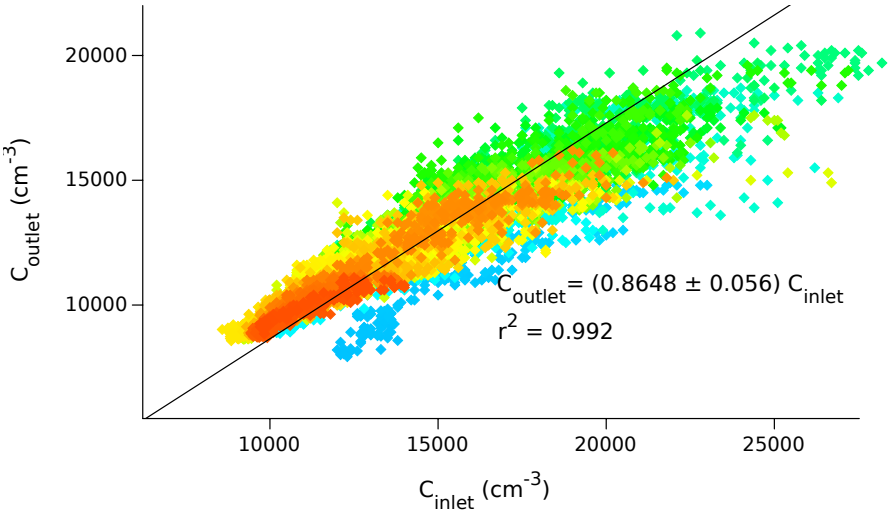

Figure 4.7: Inlet vs. outlet concentrations in the experimental tunnel during a 12-h outdoor experiment. The colouring of the dots reflects time (blue = start, red = end of the experiment). Sampling frequency = 1 s^{-1}.

We can conclude that deposition fluxes are directly proportional to particle concentration. This is a property of the system that can also be inferred by inspection of the mathematical model. The deposition velocity, u_d, is a function of several parameters of the flow (plus the geometry of the system), but not of the amount of particles. Since the deposition flux, J, is defined as being directly proportional to u_d and c in Equation 3.29, it follows that J increases linearly with concentration, as observed. Of course, this property has an upper limit, which is when coagulation occurs. But before particle number is high enough to favour coagulation, the proportionality between J and c is maintained for a wide range of concentrations and flow regimes. When this assumption holds, concentration can be non-dimensionalised with the inlet concentration. This property is going to prove very useful in the forthcoming simulations.

4.3.3 Single-burst experiments

The outdoors experiments revealed that the outlet concentration is directly proportional to the inlet concentration. The constant of proportionality is a function of the flow regime and the geometry of the system. In this section, we describe an experiment based on the same principle but carried out in a laboratory set up, under much more controlled conditions. Instead of allowing the inlet concentration to change freely, we generated single bursts of particulate matter. This experiment allowed us to record, in real time and with a good temporal resolution, how a group of particles travels through the tunnel.

We carried out experiments with two different types of particles: household dust and candle smoke. Both are representative of common coarse and fine combustion particles found indoors. We also used two different strategies to introduce particles into the system. The first strat-

egy was to direct a burst of a commercially available air spray (Ambersil Air Duster, flow rate 0.5 $\mathrm{g/s}$, ρ =1210 $\mathrm{kg\ m^{-3}}$) towards the neighbouring surfaces of the experimental area, causing uncontrolled dust resuspension. Even though this strategy was patently uncontrollable, it proved to be an effective method of creating clear concentration peaks at the inlet of the tunnel that were higher than the background concentration and that could be clearly visualised. Despite the manufacturer claim that the output was in gas phase, and that any small droplet would quickly disappear due to its high volatility, we feared that the introduction of droplets from the duster itself could be a potential source of error. However, analysis of the spray with an optical microscope did not show any droplet in the detectable size range ($\geq$ 0.5 $\mu\mathrm{m}$) and, in any case, the analysis of the data did not reveal any particle removal process apart from deposition. The conclusion was that, even if a proportion of droplets was introduced in the system, they were indistinguishable from the resuspended particles for the purpose of the experiment.

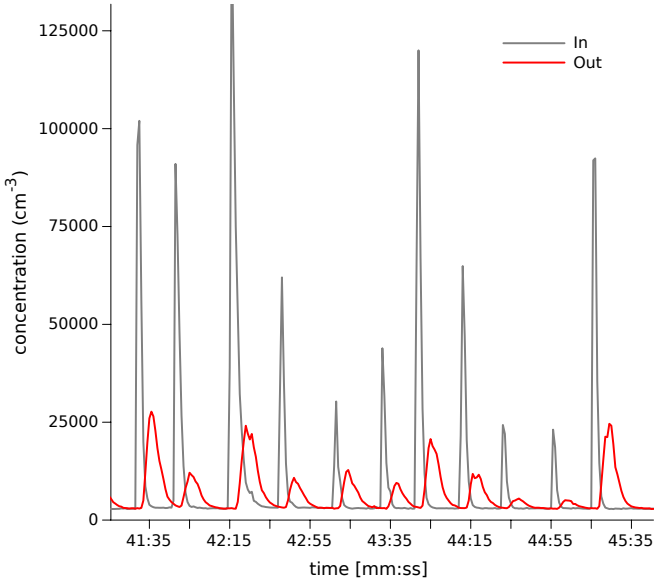

Figure 4.8: Example of inlet concentration peaks and their reflection in the outlet. Plot shows part of a 1 h experiment.

The second strategy consisted in using the aerosol emitted from a burning candle. The candle was placed at the inlet Section of the experimental tunnel for short periods of time ($\leq$ 2 s). This experiment required the use of a buffer Section of the tunnel in order to let the flow stabilise and the particles spread evenly before the experimental section. It is likely that some of the emitted particles are smaller than 0.02 $\mu\mathrm{m}$ [2], however, we will focus our analysis on the particles that can be counted with our instrumentation (0.02-1 $\mu\mathrm{m}$).

Several concentration peaks were produced using each strategy while the inlet and outlet concentrations were continuously monitored with a frequency of 1 s during $\sim$ 1 h. As can be seen in Figure 4.8, every concentration peak measured at the inlet undergoes a change within the tunnel, and emerges at the outlet displaying a smoother signal. We excluded the peaks that did not meet

the following inclusion criteria from the experiment: inlet peaks should reach a maximum and decrease in no more than 2 s (so that the peak can be idealised mathematically with a 1-s step), and they should not be higher than 10^6 cm^{-3} (as a precaution to avoid coagulation).

Experimental observations

The smoothing of the peaks is due to the combined effects of dispersion and deposition, which are both independent from the total concentration. Deposition is directly proportional to the number of particles, as demonstrated by equation 3.97, and so happens with their transport (Equation 2.23). Therefore, when the concentration profiles in the outlet are normalised with the inlet concentration (taken as the highest value of the inlet peak), they conform to a common shape (Experimental points in Figure 4.12). This property allows for a high repeatability of the experiments and enables the combined assessment of two aspects of the model: its accuracy in predicting particle deposition rates and its ability to reflect the diffusive dispersion of particles through the tunnel. The spread of the particles is due to the existence of a certain sectional velocity profile, as well as a variable turbulent diffusivity/viscosity, which result in the distribution of residence times. This dispersion is illustrated in Figures 4.9a, 4.9b and 4.9c, which show selected frames from a dynamic simulation.

The experimental points in Figure 4.12 (which will be discussed later) reveal some differences in the behaviours of candle smoke and resuspended dust. While both display very similar slopes in the increases and decreases of concentration, they reach different maximum concentrations. Even though this difference is within the standard deviation of the experiment. There are several possible explanations: the model might be underestimating slightly the deposition of small particles, or coagulation is taking place in the case of candle smoke, which is not reflected in our model. Despite our caution on limiting the number concentration, coagulation can occur due to various other factors, such as the initial high turbulence of the smoke emission [3].

Simulation set-up

The temporal variation of the concentration in the outlet of the tunnel expressed in Figure 4.8 was reproduced using a dynamic simulation. In this simulation, u_{inlet} = 0.25 m/s, particle diameter is assumed to be the average diameter in the measured size range (d_p = 0.5 $\mu\mathrm{m}$), and the density is assumed to be ρ_p=1500 $\mathrm{kg\ m}^{-3}$. A peak of particles is created by setting a non-dimensional particle concentration of 1 at the inlet during the first second of the simulation, which was zero during rest of the simulation. The outlet boundary condition is implemented as $c = 0$, which is not true to reality, but provides accurate results in the bulk. The implications of this boundary condition are further discussed in Section 4.3.5.

As in the above section, one size mode is implemented. This condition is imposed by our experimental instrumentation, which counts particles in a single size mode. Fortunately, the assumption that particles can be characterized with an average diameter and density is reasonable in this case because, in the flow regime of operation and within the size range of interest, these two variables have a very limited impact on the overall deposition flux.

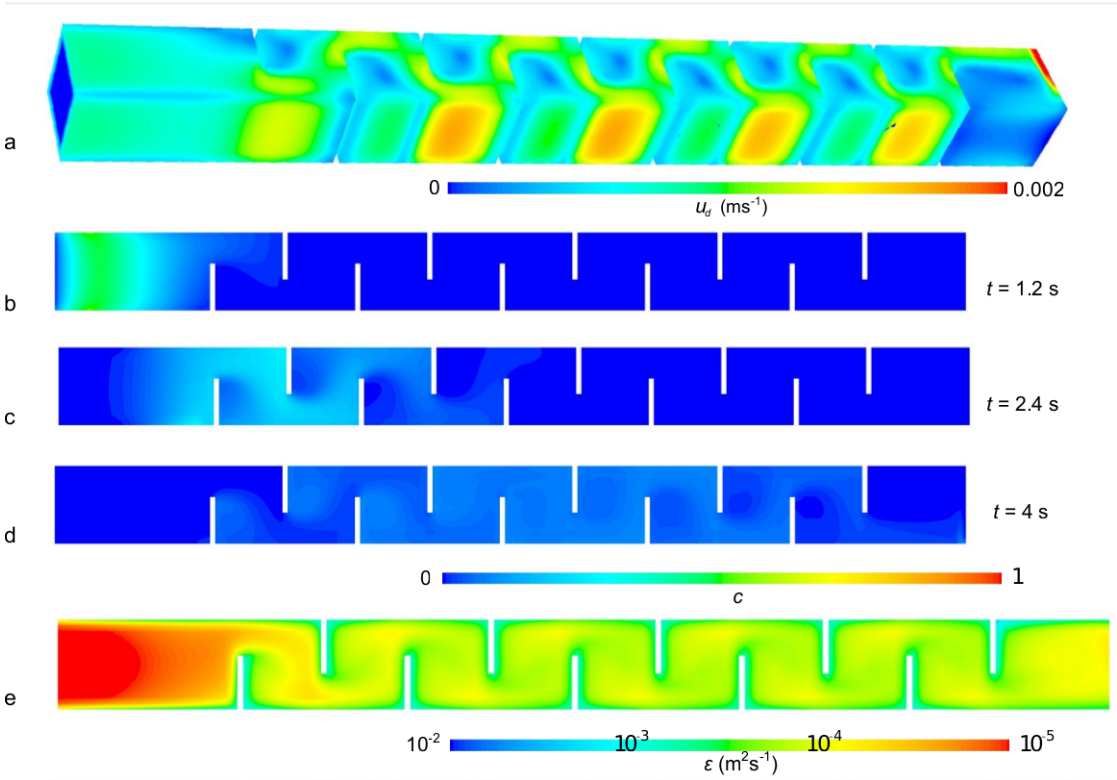

Figure 4.9: Contour images of several parameters from the simulations. From top to bottom: deposition flux (a), three stills of the dynamic solution of the single peak experiment (b,c,d) and turbulent diffusivity (e). In (a) contours are shown in the walls in perspective view, while the next images show the central sectional cut of the tube viewed from above.

This can be verified by a simple solution of the deposition model. A simulation of the air flow provides an estimation of the turbulent diffusivity, μ_t, which we assume is equivalent to the turbulent diffusivity of the particles. These values are between 10×10^{-4} and 10×10^{-3}, as illustrated in Figure 4.9. Figure 4.10 shows a solution of Equation 3.42 for a single cell. This plot illustrates that deposition rates become independent of the properties of the particles when ε is orders of magnitude higher than Brownian diffusivity. The values of ε in Figure 4.9 indicate that our experiment is designed in such a way that this will always be the case. Under our experimental conditions the differences between the deposition rates of different size modes are not significant, and using several UDS for different size modes would be superfluous.

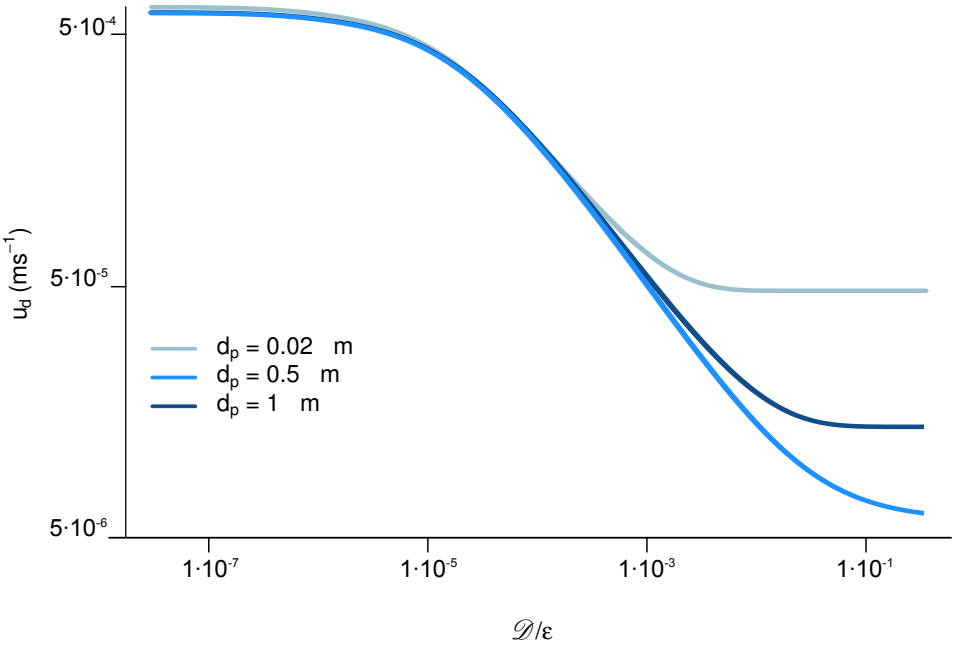

Figure 4.10: Deposition velocity in a single cell with different values of turbulent diffusivity (ρ_p = 1500, u^* = 1 cm/s.

The air flow simulation also provides the necessary information to estimate the values of K_{pt} in our system. As explained in Section 3.2.1, for small values of K_{pt} we can assume that $\varepsilon \sim \mu_t$. Its calculation (Equation 3.21) requires the Reynolds mean square velocity u_{rms} and the length scale l. We obtained the range of values of u_{rms} characteristic of our system from a dynamic simulation using the $k - \epsilon$ turbulent model, which has an order of magnitude of $u_{rms} \sim 1\ \mathrm{m/s}$. The order of magnitude of l is $\sim 0.1\ \mathrm{m}$, both if we use Equation 3.23 or if we take the hydraulic diameter of the tunnel.

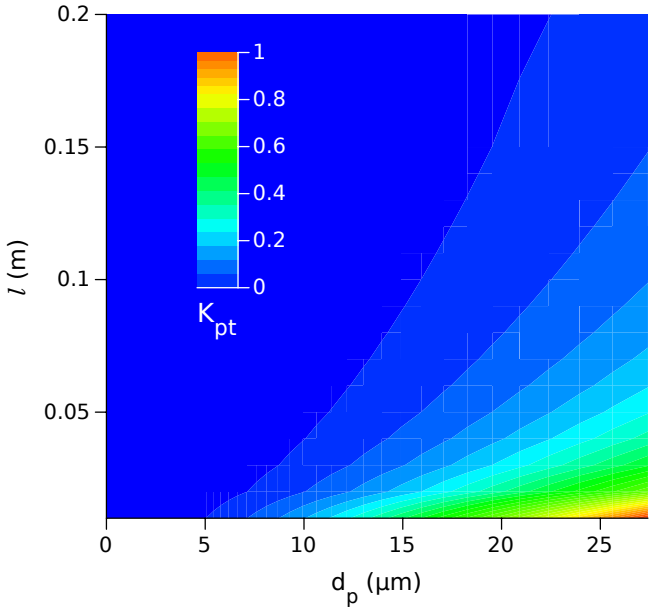

Figure 4.11: Characteristic values of K_{pt} for our system. u_{rms} obtained from unsteady simulations.

Figure 4.11 shows the values that K_{pt} can take in our range of turbulence and diameter of interest. It can be seen that we are safely within the area of applicability of the model, with values of K_{pt} considerably smaller than unity.

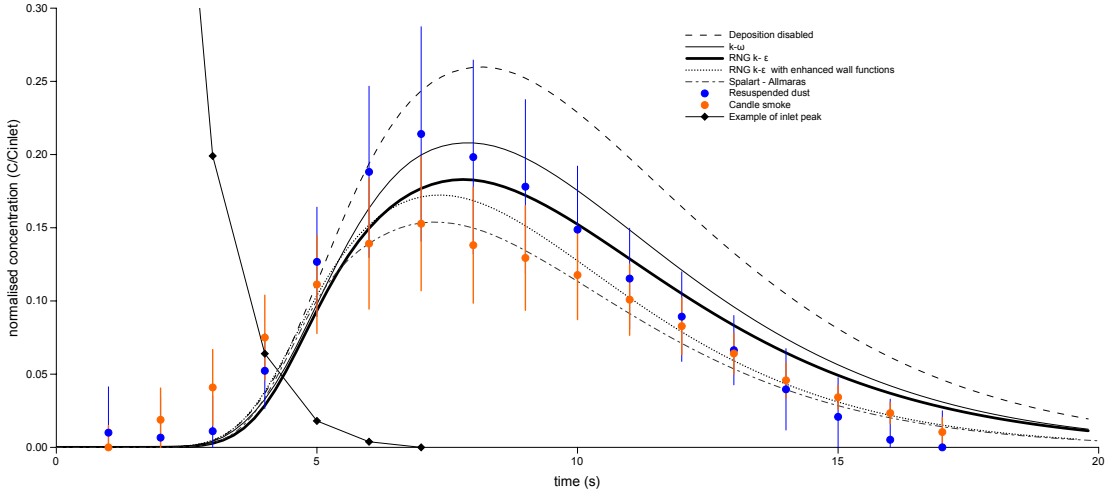

Figure 4.12: Normalised concentration profiles in the outlet of the tunnel and comparison with the CFD simulation results.

Figure 4.12 compares the experimental values of outlet concentration with the results obtained with different turbulence models available in Fluent (Spalart-Allmaras, $k-\omega$, $k-\epsilon$, RNG $k-\epsilon$ [4] and RNG $k-\epsilon$ with enhanced wall functions enabled). All the models capture the non-trivial shape of the concentration peak. The $k-\omega$ underestimates deposition but, nonetheless, the results are within the standard deviation of our experiments for most of the average peak. The RNG $k-\epsilon$ model with enhanced wall functions seems to offer a better match with the decreasing slope, but it also seems to overestimate deposition slightly when it is compared with the resuspended dust curve. Spalart-Allmaras is the model that overestimates deposition more clearly.

4.3.4 Natural background experiments

In the natural background experiments we let the tunnel collect air from its surroundings, as we did in the preliminary experiments. In this occasion, however, the tunnel was placed indoors and we measured deposition in the interior walls using glass slides. The air displayed a variable aerosol concentration related to fluctuations in the outdoor concentration. The experiment lasted 72 h, during which we monitored the inlet number concentration continuously. We sampled the deposited particles using glass slides placed inside the tunnel at the locations specified in Figure 4.5. We installed 11 slides on the floor (F_{1-11}) and 4 on the right (R_{1-4}) and left (L_{1-4}) walls of different compartments (the space between barriers). We placed two of the floor slides in the buffer Section to ensure it was effectively separating the experimental Section from the surrounding environment. Slides R_{1-4} were placed on walls adjacent to the gap left by the barriers, while slides L_{1-4} were placed just after a barrier. As a consequence, the air flowing

next to the slides L_{1-4} and R_{1-4} had different levels of turbulence. We counted the number of deposited particles in each slide once the experiment was finished. The glass slides were photographed with an optical microscope and the particles were counted with the method specified in Appendix 1. Particle deposition fluxes were calculated for every particle size as:

$$J_{experimental} = \frac{N_i}{At} \tag{4.2}$$

where N_i is the total number of particles of size i counted on the sampled surface, t is the exposure time (the duration of the experiment) and A is the area of the sampled surface. This method allows us to count any particle larger than 0.5 μm.

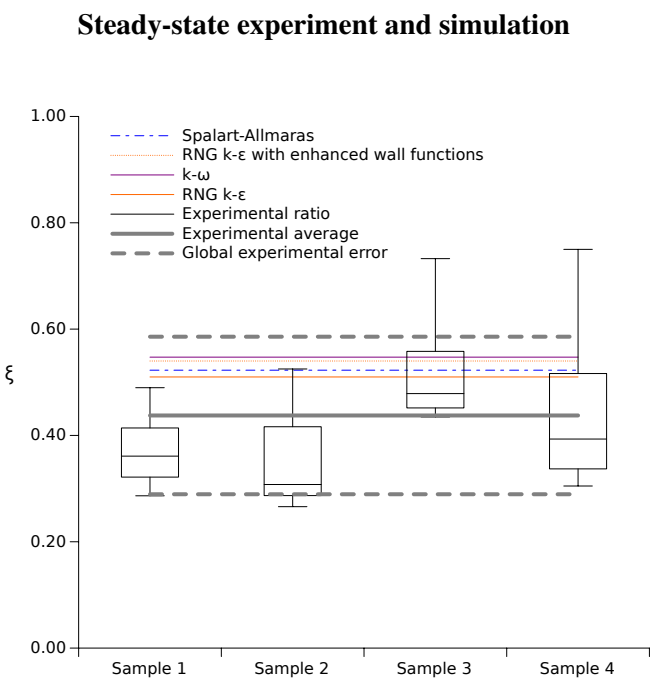

Figure 4.13: Experimentally determined values of the left-to-right ratio of deposition velocities ($J_{L_{1-4}}/J_{R_{1-4}}$) compared with the ratios predicted by different turbulence models.

The simulations clearly indicate that deposition fluxes are not homogeneous in the tunnel. Deposition on the floor decays slowly throughout the tunnel due to the overall reduction of particle concentration, and we have seen this reduction experimentally in samples F_{1-11}. Most importantly, in the contours of simulated deposition velocity, u_d, displayed in Figure 4.9a, we can observe that deposition is always higher just before a barrier. We can also see this difference experimentally. Samples R_{1-4} are located immediately after the gaps left by internal barriers, in a position parallel to the direction of the flux, while samples L_{1-4} are always located after a barrier, in an area of low air velocity (see Figure 4.5). Since we want to assess the ability of the

model to reflect spatial variations, the simulation of the difference of deposition fluxes between the right and left samples is of special interest.

This difference is a consequence of important features of the air flow. We have observed that air in contact with the R_{1-4} samples displays a high velocity tangential to the wall that leads to increased wall shear stress, τ_w, while ε has a similar value near both sampling points (as seen in the diffusion contours of Figure 4.9e). τ_w is related to the deposition velocity through Equation 3.43 (where it is expressed as the friction velocity). Therefore, it is natural to expect that deposition will be higher in the regions with high values of τ_w.

We expressed the difference in deposition between left and right walls as the ratio of deposition fluxes, $\xi = J_{L_{1-4}}/J_{R_{1-4}}$. The experimental deposition fluxes measured using glass slides and calculated with Equation 4.2 correspond to average deposition fluxes during the experimental period. This implies that ξ is constant during the experiment, and it does not depend on particle concentration. Therefore, it can be predicted with a steady-state simulation. We simulated the natural background experiments using the same model set-up explained in the previous section: we introduced a normalised concentration ($c_{inlet} = 1$), and used a single particle size (d_p = 1 μm).

The ratio has an average value of ξ_{exp} = 0.42$\pm$ 0.16 across the tunnel if we calculate it for all particle sizes. This implies that deposition in areas close to tangential air flow is twice as much as the deposition in areas protected from air flow. We also obtained ξ experimentally for different particle sizes (0.5 to 1, 1 to 2, 2 to 3, and 3 to 10 μm) and for the different pairs of right and left samples. An analysis of variance (ANOVA) did not reveal any significant differences at the probability level $p \leq 0.05$ in the left-to-right ratio of deposition between different particle sizes (F[3,3] = 0.203) or between different positions across the length of the tunnel (F[3,3] = 0.329). This evidence further confirms that there are no significant differences of behaviour between particles of different sizes in our system.

Figure 4.13 compares the experimental results with the ratios obtained in the CFD simulations with different turbulence models. Simulations indicate an average of ξ_{sim} = 0.51 $\pm$0.12, and this value is independent of particle size in the 0.5 - 10 μm range used in the comparison with the experiments. The computed ratios systematically overestimate the deposition ratio by $\sim 20\%$, but this error is within the standard deviation of the experiments. Furthermore, no significant differences are observed between different turbulent models. This contrasts with the observations made in the previous section, where the simulations suggested that some turbulence models significantly underestimate deposition. This suggests that while some turbulence models predict more or less deposition than others, all the tested models are consistent in the spatial distribution of deposition for this system.

4.3.5 Numerical considerations

Péclet and the outlet boundary

We have shown in Section 3.2.1 that the solution of Equation 3.24 in our tunnel should be independent of the outlet boundary condition when the Pe is very large. We know that the dimension of the tunnel is x_c=0.15 m, and that the fluid velocity will be of the order of $u_c \sim 1\ \mathrm{m/s}$. A representative value of turbulent diffusivity in the tunnel is $\varepsilon = 10^{-4}\ \mathrm{m^2 s^{-1}}$, as shown in Figure 4.9. Given these estimates, we can expect Pe $\sim 10^3$. Since the Péclet number is far larger than unity, we conclude that in the bulk (where the scaling employed in Section 3.2.1 correct) diffusion can be neglected.

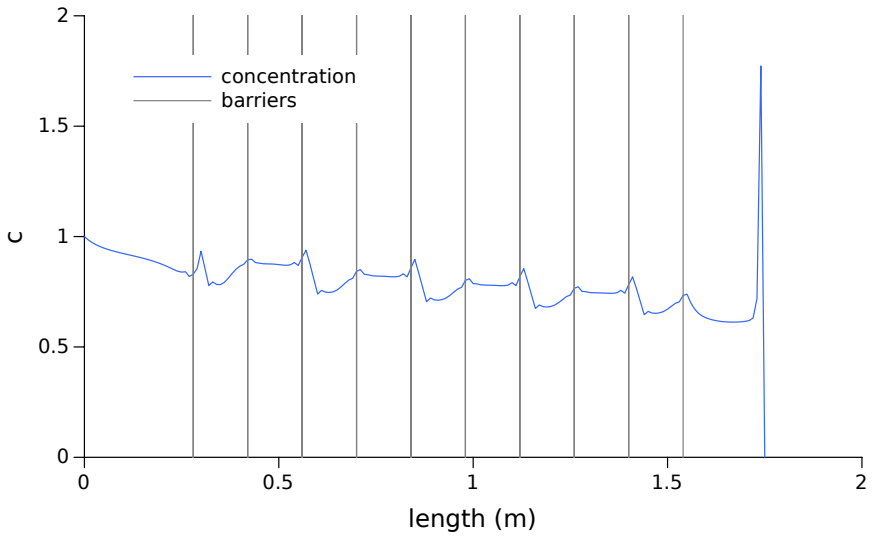

Figure 4.14: Example of the decay of concentration throughout the tunnel displaying a concentration boundary layer in the last cells of the domain. All the profile is realistic except for the concentration in the last few computational points, which display a numerical error in order to meet the outlet boundary condition, in this case, $c_{outlet} = 0$.

When we introduced a Dirichlet boundary condition, as expected, we observed that the outlet concentration boundary has a limited effect in the results far from the outlet boundary area. Figure 4.14 shows an example where we set a concentration of 0 in the outlet. Deposition only removes $\sim$25% of the particle concentration, which decreases steadily throughout the tunnel. The small peaks of particle concentration inside the tunnel are caused by the barriers. Note that, as expected, the concentration changes in the last few cells in order to meet the boundary condition. This change creates a boundary layer, which is very thin in comparison with the length of the tunnel.

Grid independence

We tested grids with different cell densities using the particle deposited fraction ($\eta = c_{out}/c_{in}$) as reference value (Figure 4.15). Constant values of η are achieved when cells are smaller than 0.5 cm ($\sim 4{\times}10^5$ cells), and the difference with the stable solution is within 5% when cells are smaller than 1 cm ($\sim 2{\times}10^5$ cells). Therefore, the simulations have been carried out with 1 cm cells.

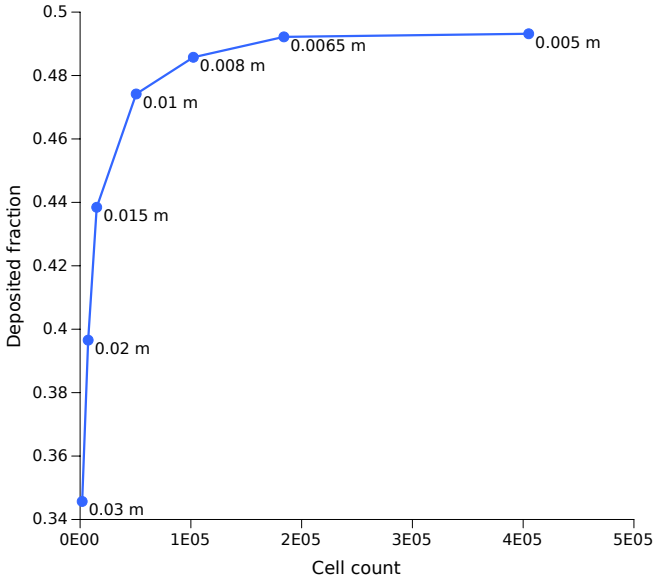

Figure 4.15: Grid independence test. Labels on the dots show cell size in every simulation.

4.4 Discussion and conclusions

The two validation cases presented in this chapter clearly illustrate the validity as well as the flexibility of the model. In the first case, which describes a deposition event in a room, the experimental data were based on mass measurements, while in our experiment we obtained data based on particle counts. Due to the direct proportionality between mass and number, the model can simulate both cases without any change in the equations, provided that the boundary conditions are defined consistently.

The two cases have also quite different dimensions and time scales. In the first case, we simulated an unsteady system that evolved for 90 min, for which we had information only about the initial and final stages. In our own experiment, we simulated a transient system which evolved during a few seconds. Since the proportionality between deposition flux and concentration allows us to work with a time-averaged experimental data and boundary conditions, we are also able to simulate the same system in stationary state for several days.

Every type of simulation -either stationary or transient, either recording the evolution or the

accumulation of PM- provides different types of information. In the built environment, this will mean that the model can be used to approach problems from various angles, depending on the questions that need to be answered. If, for example, the interest is in knowing the behaviour of particulate matter affected by an intermittent source of air movement, such as a ventilation system, perhaps a transient simulation recording the accumulation of dust would provide the most insight into the problem. The interest may also be in knowing which rooms in a building are more prone to accumulation of dust. In such cases transient simulations would likely not be useful, and we should resort to a steady-state, time-averaged simulation in order to predict the spatial distribution of PM.

Spatial distribution of deposition

The modelling approach seems to be well capable of describing the spatial distribution of deposition. In the tunnel simulations, it successfully reflected the difference in deposition rates on the walls caused by local differences in the flow regime. The experiments show very clearly the effect of turbulence on the overall deposition flux. Walls in contact with air that has a strong tangential velocity component experienced two times more deposition than walls surrounded by air with lower turbulent intensities. In the case of the room, the model predicted a non-trivial profile of deposition that was due to the combined effects of diffusion (which would led to a Gaussian spread of particles) and convection (which gave the distribution of deposition its particular pattern.)

The comparisons between different turbulent models did not reveal important differences in the prediction of the distribution of deposition. RNG $k-\epsilon$ offered the best fit to the dynamic concentration data and also reflected correctly the ratio between deposition on the right and left walls. This seems to coincide with the observations of previous studies, which as noted in Section 2.3.2, tend to recommend the use of RNG $k-\epsilon$ for deposition in indoor environments [5]. However, other turbulence models also provided a similar fit to the experimental data of left-to-right ratio in the tunnel, overestimating this ratio by approximately $\sim$20%. This slight overestimation seemed to be very consistent, and independent of d_p, ρ_p, or the turbulence model used.

Applicability of the model

During the development of the model described in the previous chapter, some non-dimensional parameters arise that characterise our system. Some of these parameters have appeared again in the description of the validation experiments, and have been useful to describe the applicability of the model. After the validation exercise, we can recommend some safe values for the relevant non-dimensional parameters. These parameters are summarized in Table 4.1.

Table 4.1: Ranges of the relevant non-dimensional parameters in which the model is applicable.

Parameter	Formula	Value range
Stokes	$\mathrm{St} = \frac{\tau u}{L}$	$<< 1$ to assume one-way coupling
K_{pt}	$K_{pt} = \frac{\tau u_{rms}}{l}$	$<< 1$ to assume that $\varepsilon \sim \mu_t$
Péclet	$\mathrm{Pe} = \frac{u_c x_c}{\mathscr{D}+\varepsilon}$	$>> 1$ to ensure that the solution in the bulk is independent of outlet boundaries
Schmidt of the particles	$\mathrm{Sc} = \frac{\varepsilon}{\mathscr{D}}$	$>> 1$ to ensure that $u_d \neq f(d_p, \rho_p)$
Volume fraction	$\Phi = \frac{3}{4}\frac{1}{cd_p^3\pi}$	$< 10^{-4}$ to ensure that coagulation is negligible

We observed that if the flow regime and total particle concentrations are such that coagulation can be neglected, it follows that deposition fluxes are directly proportional to the particle concentration (and are only a function of the geometry and the air flow regime). This allows particle concentration profiles to be normalised with the inlet concentration and studied as a non-dimensional scalar. We gathered enough evidence to ensure that this assumption is applicable in our range of turbulence intensity, particle sizes and concentrations. Our literature review (Section 1.6.6) indicates that number concentration is not a sufficient indication of the absence of coagulation [3]. Further research is needed to establish a clear threshold, but, as an approximation we can use the void fraction Φ, which indicates the dilution of particles.

In several instances we insisted that in the experimental tunnel, the deposition velocity was not a function of particle properties, specifically of the particle diameter. We have shown that when the turbulent diffusivity of the particles is orders of magnitude higher than the Brownian diffusivity, we can effectively consider that deposition is independent from diameter. In buildings, turbulent diffusivity will be larger than Brownian diffusiviity as long as there is air movement. Only in rooms where air is totally steady we may see turbulent diffusivities lower than Brownian diffusivity. Of course, this is not an unlikely scenario, but it is clearly an scenario where CFD is not necessary. There might be intermediate cases, in which there are flows that can be simulated with CFD but that, for example, do not induce turbulence in the whole of the room. Flows generated by natural convection might also induce very low turbulence. In order to assess such unclear situations, the relationship between the two diffusivities leads us to the definition of a Schmidt number for the particle phase, $\mathrm{Sc} = \varepsilon/\mathscr{D}$. When Sc is very large, the deposition velocity does not depend on the particle diameter.

The advantage of this situation is that particles can be simulated using only one size mode. This

saves us some computational cost and makes the model simpler, avoiding some of the duplication of functions described in Section 3.6. Of course, this is only useful as long as we are merely interested in the total count of particles in suspension or on surfaces. In the following sections we will see situations in which, even though this assumption holds from a physical perspective, we are interested in knowing the area coverage of particles of different sizes, and this requires us to simulate different size modes.

Other relevant non-dimensional parameters have already been discussed at length in the previous sections, but we can add a few remarks. In a system with large values of Pe we can safely use Dirichlet conditions in the outlets. If this is not the case, we must consider other boundary conditions or redefine our system. If there is no alternative and we do solve a system with a Pe ≤ 1, we know that we have to interpret the gradients close to the outlet boundaries with special care, for they will represent a computational error rather than a physical phenomenon. Naturally, some of these parameters are closely linked. For example, it will be rare to find a situation in which air is turbulent (Re > 2300) and where simultaneously Sc is too small. In other words, if the air flow is turbulent, chances are that deposition will be dominated by turbulence. In that sense, Re and Sc are conceptually linked. It suffices to say that, if air is not turbulent, the application of the model altogether should be questioned, because it is based on the simulation of turbulent flows.

It can be the case, however, that the air is turbulent but particles do not follow all the scales of turbulent flow (K_{pt} is large), perhaps because of spatial restrictions, or perhaps because they are too big or heavy. That case is one of the limits of applicability which is easier to reach. Many common particulate pollutants, and many common indoor flow regimes, can lead to values of K_{pt} close to the limits of applicability of the drift flux approach. In the following sections, we shall see some real cases in which we use the model in such limit conditions. As one can imagine, this group of parameters is of great importance to judge the suitability of the model before undertaking the complex task of simulating a real-life building. In the next two chapters they will be employed to the best advantage.

References

[1] E. Sajo, H. Zhu, and J. Courtney. "Spatial distribution of indoor aerosol deposition under accidental release conditions". *Health physics* 83:6 (2002), pp. 871–883.

[2] S. Zai, H. Zhen, and W. Jia-song. "Studies on the size distribution, number and mass emission factors of candle particles characterized by modes of burning". *Journal of Aerosol Science* 37:11 (2006), pp. 1484–1496.

[3] P. Duru, D. Koch, and C. Cohen. "Experimental study of turbulence-induced coalescence in aerosols". *International Journal of Multiphase Flow* 33:9 (2007), pp. 987–1005.

[4] V. Yakhot et al. "Development of turbulence models for shear flows by a double expansion technique". *Physics of Fluids A: Fluid Dynamics* 4:7 (1992), pp. 1510–1520.

[5] S. Parker, T. Foat, and S. Preston. "Towards quantitative prediction of aerosol deposition from turbulent flows". *Journal of Aerosol Science* 39:2 (2008), pp. 99–112.

5
Case Studies (I)

5.1 Introduction

In this Chapter we will describe in detail the simulation of deposition in real buildings. We embarked on most of these simulations as the project evolved. The selection of case studies treated in this Thesis surpasses by far our initial intentions, which were to focus our efforts only on a single building: Apsley House. Finally, the case studies reported here are based on four buildings: the Wellcome Collection, the Wellington Arch (English Heritage), Apsley House (Enlish Heritage), and Hampton Court Palace (Historic Royal Palaces). These simulations are reported in approximate chronological order, but our work on them mostly overlapped. The order in which they are discussed also reflects the gradual validation and extension of the model, since we have usually applied the lessons learned in the previous case study to the simulation of the following one.

These four cases are as varied as heritage buildings can be, and they offer very different challenges that cover most of the range of applicability of the model:

Fine and coarse PM. In some cases (Apsley House, Wellington Arch and the Wellcome Collection) we have simulated the deposition of fine, traffic generated particulate matter, while in Hampton Court we have simulated coarse dust introduced into the building by visitors.

Outdoor and indoor origin. In some cases particles infiltrated from outdoors, through cracks, leaks or openings in the building envelope, while in some others the sources were within the building.

Different time and size scales. Our simulations cover a wide range of time scales, from minutes or hours to several months and up to a year. The volume of the simulated geometries also covers some orders of magnitude, ranging from 300 to 12000 m^3.

Steady and dynamic. We have simulated some buildings in steady-state, reflecting average behaviours over long periods of time or hypothetical scenarios, in others we have found that dynamic simulations of particular phenomena over a few minutes or hours provide more insight into the problem.

Flux and concentration. We have compared our simulations with experimental measures of deposition or with values of suspended particulate matter.

Our criteria to include the case studies changed during the course of the project. Initially, we were interested in spaces that (1) were highly polluted with fine PM of outdoor origin and (2) had a strong influence of the ventilation system, which would allow an easy introduction of boundary conditions. We selected the Apsley House and Wellcome Collection case studies because they satisfied these criteria. However, as we developed and optimised the methods for deposition monitoring, we realised that in order to obtain useful data buildings should have other properties. The criteria to obtain good quality deposition data is that (3) there are significant differences of deposition between rooms, or significant gradients within a single room and that (4) monitoring can be carried out during periods of days or weeks during which the environment is relatively unchaged. Monitoring in the Wellington Arch was our first attempt to satisfy criteria (3) and (4), but these criteria were most successfully met by our experiments in the Hampton Court Palace. Finally, after monitoring many sites polluted by fine particles, we dropped (1) and became interested in testing the model in situations where coarse dust is predominant.

All the case studies described here display multiple sources and sinks of PM, and different sources of air motion. In the simple case of the tunnel we used for validation, there was no separation between the source of particles and the source of air motion: particles and air were introduced in the system through the same inlet. But real buildings are more complex than that. To interpret the case studies we will introduce two new concepts: *sources of PM* and *drivers of deposition*.

Sources of particles and drivers of deposition

A source of PM is anything that introduces particles into the system. A driver of deposition is anything that brings these particles to the walls. This distinction becomes clearer from the definition of the deposition flux, Equation 3.29, which we repeat here for clarity:

$$J = u_d\, c \tag{5.1}$$

A source of PM is anything that increases the value of c, and a driver of deposition is anything that increases the value of u_d. A cigarette, a candle, a leak in the wall with negligible velocity, can be sources of PM. A ventilation inlet, a fan, or a heating point that generates a convective flux can be drivers of deposition. Some factors, such an open window, can be both simultaneously. In the following sections we will use this distinction to understand our results and boundary conditions.

5.2 Wellcome Collection building

This building, and particularly the way in which we simulated it, stands in a middle point between the tunnel described in the previous chapter and the other buildings described below. The main hall and staircase of the Wellcome Collection can be approximately represented as a tunnel with a single inlet (See Figure 5.1 and the computational grid displayed in Figure 5.3). We used this relatively simple system to perform a first test of the performance of the model in large spaces.

Figure 5.1: The Wellcome Collection building. (a) façade of the building, (b) main hall, (c) staircase. The lines overlapped in images (b) and (c) indicate the shape of the computational geometry that we will use for the simulations.

The Wellcome Collection building is located in Euston road, comparatively one of the most polluted streets in London [1] with levels of $PM_{2.5}$ regularly exceeding 30 $\mu g\ m^{-3}$ [2], which is the limit value recommended by the World Health Organization [3]. Outdoor fine particulate matter infiltrates into the building directly through the main entrance. Due to the large vehicle flow in Euston road and the absence of indoor sources, we can assume that particles in the size range $PM_{0.02-1}$ are traffic-generated. At the time of the experiments, the reception hall, staircase, and some exhibition areas were directly connected to the Euston road environment via an automatic sliding door. Visitors enter and exit the building continuously and daily through this door to access the exhibitions and other facilities such as a library, a shop and a café.

The study of this building was motivated by the interest of the Conservation and Collection Care team of the Wellcome Collection in understanding how urban pollution penetrated indoors. Redevelopment works in the building were to start in Autumn 2013, and they decided to monitor indoor air quality before and during the works. This could provide a snapshot of pollutant penetration before the redevelopment that could be used for comparison with future measurements, and would also provide a record of the impact of the construction works in the ingress of pollutants, particularly in coarse dust deposition.

We were particularly interested in understanding the ingress of fine particulate matter, and to use the opportunity to further validate the model. There was a concern that a fraction of the particles introduced through the main door could be transported around the building and reach

Table 5.1: Vaules of fine PM concentration and NO_2 in several locations of the Wellcome Collection building.

Location	$PM_{0.02-1}$ (cm^{-3})	NO_2 (ppb)
Main Hall	2×10^4-4×10^4	16.85
Library (2nd floor)		13.2
Rare materials room	1×10^4	13.2
Conservation department		13.9
Average other areas	3.5×10^4	6.4 $\pm$0.4
Average filtered store rooms	below limit	1.8 $\pm$0.5
Roof	1.5×10^4	16.0
Street	4×10^4	53.0

areas were sensible materials are stored, particularly the library and exhibition areas in the 1st and 2nd floors. If the number of particles was high enough, this could also be a health concern for the users of these areas.

In order run the model we needed to identify all the relevant particle inlets. We imagined that the main source was the main gate, but we also wanted to know if there were other sources of fine PM, such as leakage or the ventilation system. We hoped to detect these sources in various ways. Occasionally leakage can be directly detected with a particle counter. Most commonly, it can be deduced from bulk measurements in a room. For example, if a certain room has a particle concentration which is higher than in the neighbouring areas, and which cannot be explained by infiltration from the main door.

5.2.1 Data collection

In order to determine which PM sources should be included in the model, we monitored the number concentration of fine PM using a P-Trak condensation counter in several locations inside the building, and on different days (10/06/2013 and 23/09/2013). During the period 29/01/2013 to 04/03/2013 we also measured the concentration of some gaseous pollutants (NO_2 and O_3) using Gradko diffusion tubes. We monitored gases to provide a better assessment of the indoor air quality. Additionally, NO_2 is also a good marker of traffic pollution [4], and its measurement can help the interpretation of the PM measurements. A summary of the locations and measured values is displayed in Table 5.1.

Two observations can be derived from the results summarized in Table 5.1. Firstly, the survey of suspended PM and NO_2 concentration suggested that there are three types of environments in the Wellcome Collection which can be defined by the Indoor/Outdoor (I/O) ratio of fine PM:

- High concentration areas, directly in contact with the outdoor environment, with I/O > 0.5.
- Intermediate concentration areas, far from the outdoor environment, with 0.1 < I/O < 0.5.

- Filtered areas with no contact with the outdoor environment and minimum pollutant concentration with I/O < 0.1.

We also observed that the values of concentration varies greatly between different days. This is probably due to the fact that the concentration of $PM_{0.02-1}$ inside the building is linked to the outdoor concentration. The average outdoor concentration (which we obtained from the LondonAir monitoring network, maintained by King's College, [2]) was 15.1±6.4 $\mu g\ m^{-3}$ on the first day of monitoring and 17.5±6.6 $\mu g\ m^{-3}$ on the second day. These daily averages are very similar, and we should expect to see also a similar indoor concentration every day. However, on these two days we measured two very different concentrations in the Main Hall, $\sim 2\times10^4$ and $\sim 4\times10^4\ cm^{-3}$. But we should not compare our measurements with the daily average outdoor concentration. If instead we look at the concentration during the experiments (more or less at noon) we see that on the first day it is 8.8±1.7 $\mu g\ m^{-3}$ and 20.1±3.4 $\mu g\ m^{-3}$ on the second, giving a similar I/O ratio for both days. A sensible conclusion is that the indoor and outdoor fine PM concentrations are closely connected, and that the indoor concentration responds quickly (in a few hours) to changes outdoors.

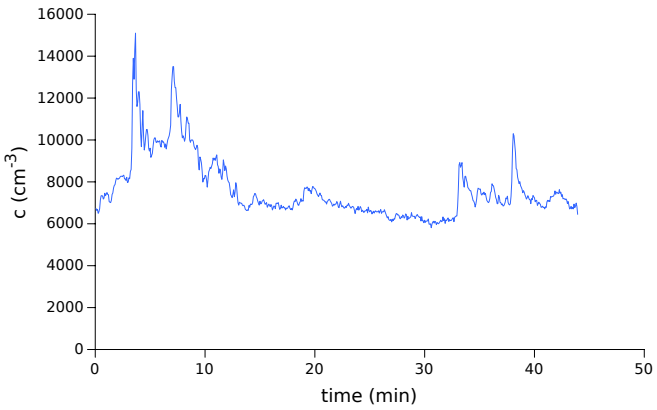

Figure 5.2: Evolution of the concentration in the main door of the Wellcome Collection building during the length of the experiment.

We carried out detailed measurements in the high concentration areas, specifically in the Section between the entry gate, the Main Hall, and the staircase. We had special interest in these areas of the building because they displayed the most pronounced concentration gradients, which allow a comparison with simulations. In order to measure these gradients we used two condensation particle counters, one monitoring continuously in the main entrance and a second one which we placed in several sampling points for periods of 5 min, to compensate for the travelling time of the particles. Both particle counters measured simultaneously. The ratio between the concentration values measured by each counter is the fraction of particles that penetrate from the street level to the sampling point. We used a hot wire anemometer in the inlet to record the air velocity near the door (which oscillated between 0.5 and 1 m/s). The outdoor concentration fluctuated during the experiment, with an average of 7.6±1.4×10^3 cm^-3. Figure 5.2 displays

the outdoor concentration during the experiment. The decay of the relative particle concentration from the main door to the top floor is illustrated in Figure 5.4, where it is compared with the simulations.

5.2.2 Simulation

Since the outdoor concentration changes significantly several times in a minute, the indoor concentration can only be simulated in two ways: either using a dynamic simulation that reflects the fluctuations or with a steady-state simulation that uses the concept of I/O ratio. The first option would be computationally intensive, and the results would be specific to the few seconds for which we have input data, and therefore not easily generalisable. Therefore we used the second approach, a steady state simulation, and we attempted to reproduce the decay of concentration displayed in Figure 5.4. The simulation set-up is: $u_{inlet} = 1\ \mathrm{m/s}$, $c_{inlet} = 1$.

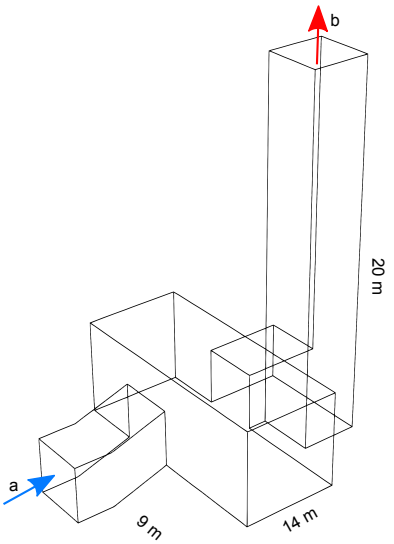

Figure 5.3: Diagram of the geometry used for the simulation of the hall and staircase of the Wellcome Collection building.

We generated a very simple mesh that merely reflects the main features of the geometry: a short entrance, which leads to a hall with a larger volume, connected to a staircase, represented as a long, square chimney. We used a structured mesh with cubic cells of $1\ \mathrm{m}$, after a grid test using the deposited fraction as the indicative parameter, which revealed that the solution is independent of the grid for cells smaller than $1\ \mathrm{m}$. In spite of the simplicity of the grid, the simulations successfully reflected the features of the curve of decay in concentration.

The comparison with the experimental data can be seen in Figure 5.4. In this figure the x axis does not reflect a linear distance, but several positions inside the building, roughly equidistant. The experimental data display two local maximums. A possible explanation for the first one are the fluctuations of the outdoor concentration, which affected this measurement (Figure 5.2

displays higher fluctiations at the initial minutes of the experiment). The second local maximum is produced when particles penetrate into the Main Hall, after a reduction of c due to dilution, and this one is reflected in the simulations. After that, c seems to decay at a constant rate through the staircase, from 0.85 to 0.49. The model predicts fairly well the slope of this decay, from 0.84 ± 0.1 at the beginning of the staircase to 0.57 ± 0.11 at the end.

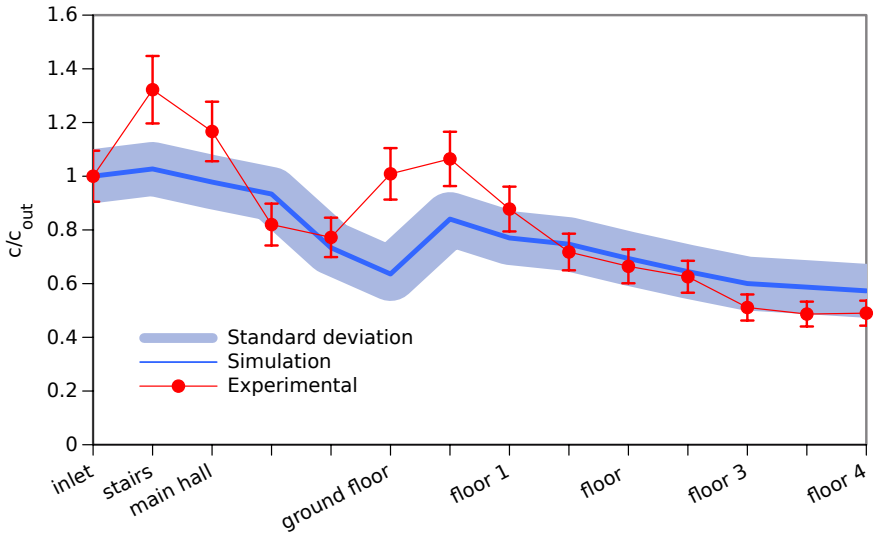

Figure 5.4: Comparison of simulations and measurements of the decay of concentration from the street level to the fourth floor. The y axis shows the ratio between the outdoor concentration and the concentration at every point.

Figure 5.5 shows the contours of c in some cross-sections of the volume. It is obvious that the actual concentration profile might not display such smooth gradients. The mesh does not include features like steps in the staircase or the reception desk, which clearly would change the local details of the concentration contours. But it contains the essential elements (the position of the walls, the relative size of connected volumes, the dimensions) that alter the air flow in our scale of interest. Finding the relevant level of detail is the first step of any simulation of deposition indoors. This first exercise with minimal detail, without any architectural feature larger than 1 m, has been successful. However not all buildings are as simple, and to simulate the case studies to follow we will have to include much more physical features in our geometry.

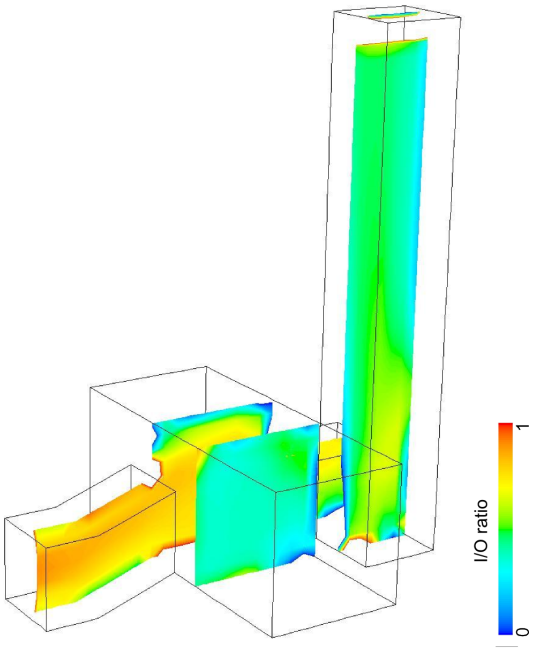

Figure 5.5: Contours of non-dimensional c in the hall and staircase of the Wellcome Collection building.

This case study demonstrates that when PM concentration is dominated by a single source (in this case, the main door) the relative concentration (which in our case is equivalent to the I/O ratio) can be easily simulated. The simulation of the Wellcome building reveals that approximately half of the outdoor particles will reach the top floors, independently of how much is the concentration outdoors. The changeable nature of the outdoor environment is not a limitation to the applicability of the model. However, we have excluded from the simulation areas of the building where the source of particles cannot be so easily related to the main door. To include such spaces we would need a more detailed geometry with several inlets, and the concept of the I/O ratio would become less useful.

5.3 Wellington Arch

We decided to explore deposition in the Wellington Arch after staff working on-site reported unusually high levels of black PM deposition. The building is located in the centre of the Hyde Park Corner roundabout in London, UK, just opposite Apsley House, the simulation of which is discussed in the next section. The source of fine particulate matter in both buildings could be expected to be outdoor traffic, however, staff reports indicated that deposition in the exhibition areas of the Arch were much higher than in Apsley House. In fact, dust deposition required only a day to become visible to the naked eye in vertical surfaces, which had to be wiped daily. It was apparent that either more particles infiltrated this building, or some effect was increasing

deposition. At one point, it was suspected that deposition could be due to the build-up of static electricity on the newly acquired plastic labels for a temporary exhibition. The answer, however, was to be found in the structure of the building.

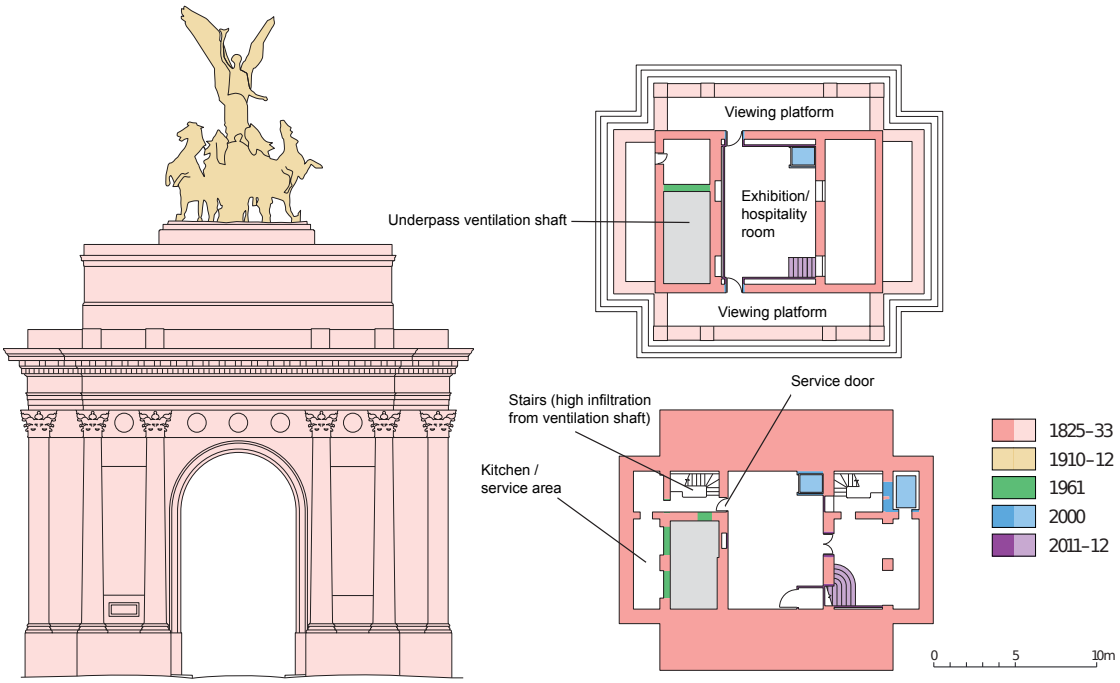

Figure 5.6: Plan of the Wellington Arch showing the evolution of the structure and the location of the pollution source. Image adapted from [5]. Colour codes indicate time of construction of each architectural feature.

The Welligton Arch has not always been open to visitors. It was built in 1825 as a commemorative building, and stood empty for many years. In the sixties it operated as a police station, and was conveniently adapted with the construction of offices. At that time, the building underwent another important modification. Its north column, which is shallow, was converted into a ventilation shaft for the Piccadilly road traffic underpass. It was not until 1999 that the Arch opened to the public, hosting temporary exhibitions, sporadic events, and acting as a viewing platform for St. James Park. At that point the interior of the building was totally refurbished, with the addition of disabled access, lifts, and improvement of the internal spaces. However, the ventilation shaft was left unchanged. In principle, it should have been totally isolated from the exhibition spaces, and the air flow confined into a chimney that runs through the north column. However, during the course of this project it quickly became apparent that the airtightness of the arch ventilation system was far from perfect.

5.3.1 Data collection

The data collection was carried out in three different stages with different objectives: to clarify the origin of the observed black deposits, to collect the necessary information to set-up a simulation, and to validate experimentally the predictions of the simulation. We carried out the following measurements:

1. Analysis of suspended fine particles $PM_{0.02-1}$ and detection of leaks and sources.
2. Monitoring of deposition with glass slides and suspended PM for comparison with simulations, and determination of temperature, velocity and concentration boundary conditions.
3. Follow-up monitoring of deposition with glass slides and concentration of $PM_{0.02-1}$ in the whole building.

Leak detection and conservation intervention

During the first stage of monitoring we detected a clear gradient of concentration in the first floor exhibition space, with $PM_{0.02-1}$ concentration (measured with a TSI P-Trak) increasing sharply towards the service door (See Figure 5.6). Such a pronounced gradient is rare in small indoor spaces, unless there are significant sources and sinks of particles. Behind this door, the levels of fine PM reached $74\times10^4\pm7.8\times10^4$ cm^{-3}, a level which increased continuously as we descended downstairs through the north column. It was clear from these observations that the ventilation shaft was very poorly isolated from the service stairs. These concentrations are not only a threat to heritage surfaces, but first and foremost they are above the safety levels for human occupancy. As mentioned in Chapter 1, such levels are established by the World Health Organisation to be 30 $\mu g/m^3$. In order to enable a comparison our values had to be transferred from number to mass concentration, but even using the most conservative estimates of diameter and particle mass, the recorded concentrations are higher than the recommended limits. This result led to immediate action by English Heritage, and 48 h after we reported the concentrations, the sealing of the service door was improved.

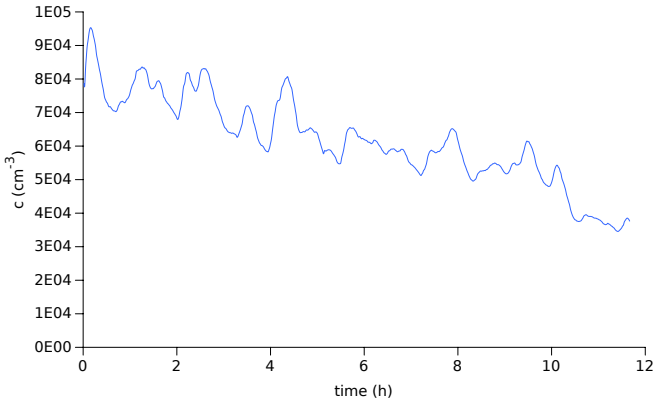

Figure 5.7: Concentration of $PM_{0.02-1}$ during 12 h in the kitchen and service area of the arch (3/5/2013).

This prompt action also discarded any possibility of monitoring PM deposition in the exhibition spaces, since the concentration of fine PM was reduced significantly, and the concentration gradients were lost, preventing a comparison similar to the Wellcome Collection case study. Furthermore, the frequent use of the building did not allow enough flexibility to place the necessary instrumentation there for several days or weeks. Therefore we decided to study deposition in the kitchen and service area (Figure 5.6) which at the time of the experiment had not yet been isolated from the extremely polluted service stairs. This led us to the second experimental stage.

Deposition monitoring

The second stage was our first attempt to collect all the necessary data to define the boundary conditions required to run the model in a real building, as well as collect the experimental deposition data required for validation. The high levels of deposition in the kitchen area offered a good opportunity to obtain deposition data in a short time, without the need of exposing samples for several weeks. We organised a four day (3/5/2013 to 6/5/2013) monitoring campaign during which there were no scheduled events, and the environment remained undisturbed. The ventilation system was switched off for the duration of the experiment. We placed glass slides in the locations indicated in Figure 5.9. We analysed the deposition with an optical microscope, which allowed us to count deposited particles with a diameter >0.5 μm. We also measured air speed continuously in the gap under the kitchen door using a 3D Ultrasonic anemometer, as well as fine PM concentration in this inlet (these methods are described in Appendix I). The velocity in the inlet varied during the day. It is probably related to the movement of vehicles and wind in the traffic underpass, as well as the pressure difference between the interior of the arch and the underpass. We used a thermal camera to look for relevant temperature gradients that could affect deposition. We only found some exposed warm pipes, but we assessed that their effect would be very localised and we did not include them in the simulation. The dimensions of the Room were scanned using an ultrasonic distance meter.

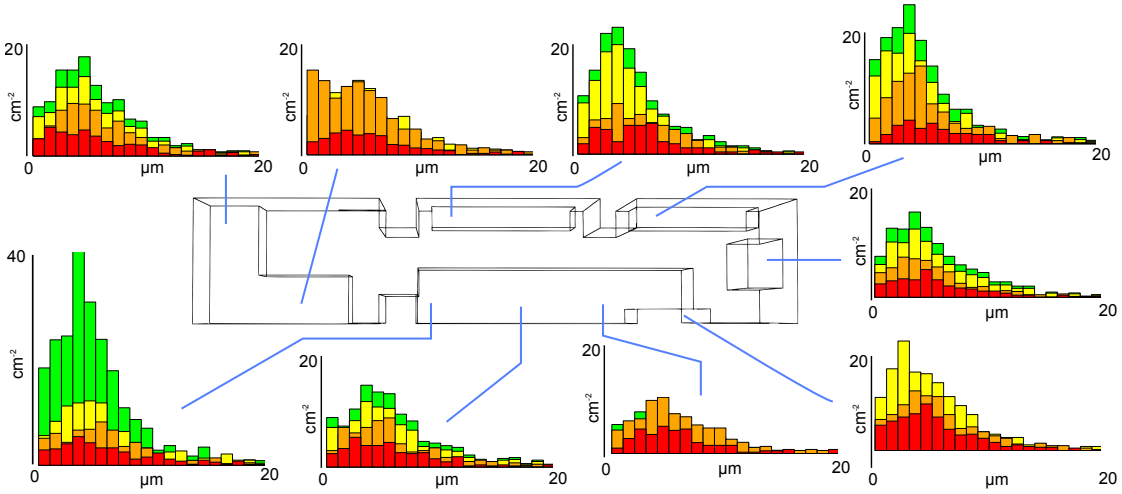

Figure 5.8: Size-resolved particle counts during the monitoring period in the kitchen. The shading of the colour bars corresponds to each of the four days of monitoring.

As can be seen in Figure 5.8 deposition for all particle size modes increased by a very similar amount every day. We did not find any significant differences between the different sampling locations, which indicated that the Room was well mixed, and that the absence of strong sources of air motion resulted in a homogeneous distribution of deposition. The measurements of CO, RH and T also indicated that the Room was well mixed. This would be further confirmed with simulations.

Follow-up monitoring

We monitored deposition in the exhibition areas during the weeks following the intervention that reduced the particulate matter concentration. The main purpose of this experiment was to ensure that deposition was effectively reduced after removing the main source. For a period of 2 weeks we exposed glass slides and SEM stubs on top of the display cases and on the door frames. Analysis of this data did not reveal significant differences of deposition. In two occasions during this period (3/5/2013 and 6/5/2013) we monitored suspended fine PM concentrations. These experiments revealed that the Rooms were now well-mixed, indicating that the presence of particles originated in a number of smaller sources. The concentration of $PM_{0.02-1}$ was still high $\sim$ 10-20 $\times 10^4$ cm^{-3}, but now comparable to the outdoor concentrations and the concentration in Apsley House. The main sources of fine PM after the intervention are the various air inlets of the building: the visitor staircase and leakage through the doors that lead to the balcony.

5.3.2 Simulation

We carried out different simulations that correspond to the different experimental evidence that we collected. The first simulation attempts to reproduce the evolution of c in the kitchen area

once the particles begin to be introduced in the Room. The second simulation involves the whole of the building geometry with the purpose of determining the percentage of particulate matter that can be attributed to the ventilation shaft. This simulation provides complementary evidence that supports the decision of air-tightening the service door.

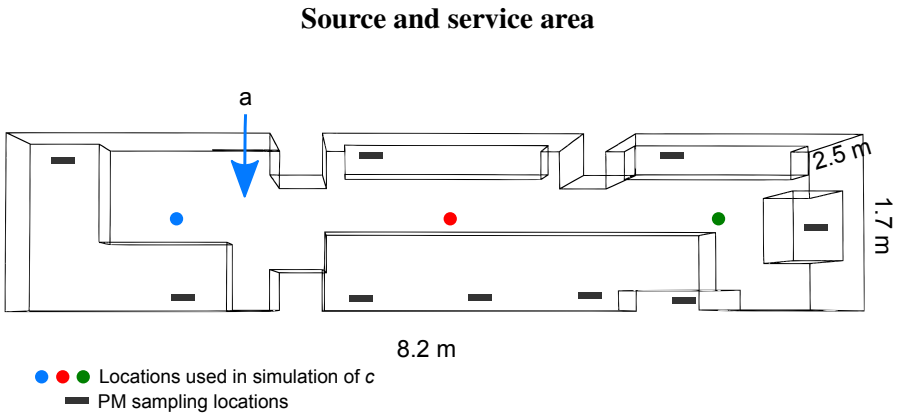

Figure 5.9: Geometry of the kitchen area used in the simulations. (a) indicates the particle and air inlet, which is the gap under the door. The dots indicate the location of the points that have been used to report c in the simulation. The colour code corresponds with Figure 5.10. All locations are at a height of 1.5 m.

The kitchen has a very simple geometry with no outlets and a single particulate matter inlet, which is the infiltration of fine PM from the ventilation shaft through the gaps left by the door, mainly the gap under the door. This is also the only source of air motion (and is, therefore, a source of particles as well as a driver of deposition). In this study we produced a transient simulation. The simulation set-up is: u_{inlet} = 0.5 $\mathrm{m/s}$, c_{inlet} = 1, and Figure 5.9 shows the geometry of the grid. This approach provides information on the time required for the Room to become well-mixed and for the fine PM to disperse and deposit. It assumes no particles in the environment prior to the experiment. The simulation could be understood as the behaviour of the Room in the early morning, when road traffic starts and the ventilation shaft begins to transport particles into the arch.

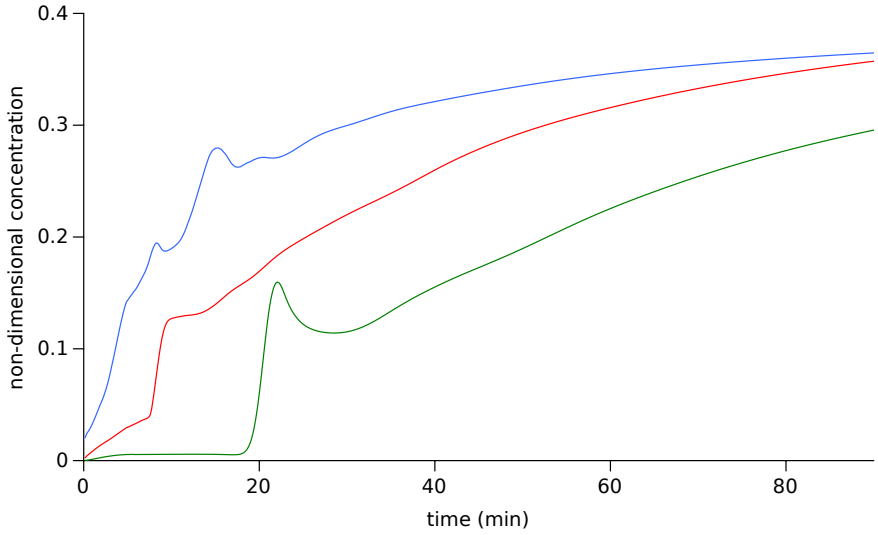

Figure 5.10: Simulated evolution of c in different locations in the kitchen after particles start penetrating into the environment.

The simulations indicate that the environment becomes well mixed in about 120 min. Figure 5.10 illustrates the increase in concentration close to the inlet and on the opposite side of the Room (The colour of each line indicates the location of the computational points as marked in Figure 5.9). The concentration at different locations in the Room gradually approaches a constant value, which is a fraction of the concentration at the inlet.

The necessary time for the particles to distribute evenly through the Room is much smaller than the time resolution of our deposition data measurements, which was daily. One can imagine that the process we simulated occurs at various times during the day, every time a burst of combustion gases and fine particles penetrates into the building, the particles disperse and deposit homogeneously around the volume.

Given the homogeneous nature of the suspended PM concentration and deposition fluxes, the comparison between simulations and experiments is straightforward and provides little insight: both show a well-mixed room. This represents one of the limitations of the model, i.e. the calculation of deposition rates in a well mixed environment does not require CFD; deposition rates could have been obtained using a much simpler approach for well-mixed volumes. The use of the model provided, nonetheless, knowledge on the dynamics of particle dispersion, and an indication of the time scale of the mixing process which would have been impossible to find with simpler methods.

Exhibition areas

This simulation attempts to explore to which extent would the concentration of $PM_{0.02-1}$ be reduced if the ventilation shaft leak was completely eliminated. We simulated the I/O ratio in

two scenarios. In the first scenario, we make a distinction between "polluted" air originated in the traffic underpass and outdoor air. The ventilation shaft introduces polluted air with five times the outdoor PM concentration. This concentration is comparable to our measurements. The leaks under the windows of the top floor (see Figure 5.11) introduce outdoor air, and have an inlet concentration equal to the concentration in the air surrounding the building.

In the second scenario all the inlets have been reduced to the outdoor concentration. The simulation set-up is: u_{shaft_leak} = 1 $\mathrm{m/s}$, $u_{balcony\_leak}$ = 0.01 $\mathrm{m/s}$, c_{shaft} = 3, $c_{outdoor}$ = 1. The concentration is dimensionless, and can be interpreted as a I/O ratio. The geometry of the computational grid and location of the boundaries is shown in Figure 5.11.

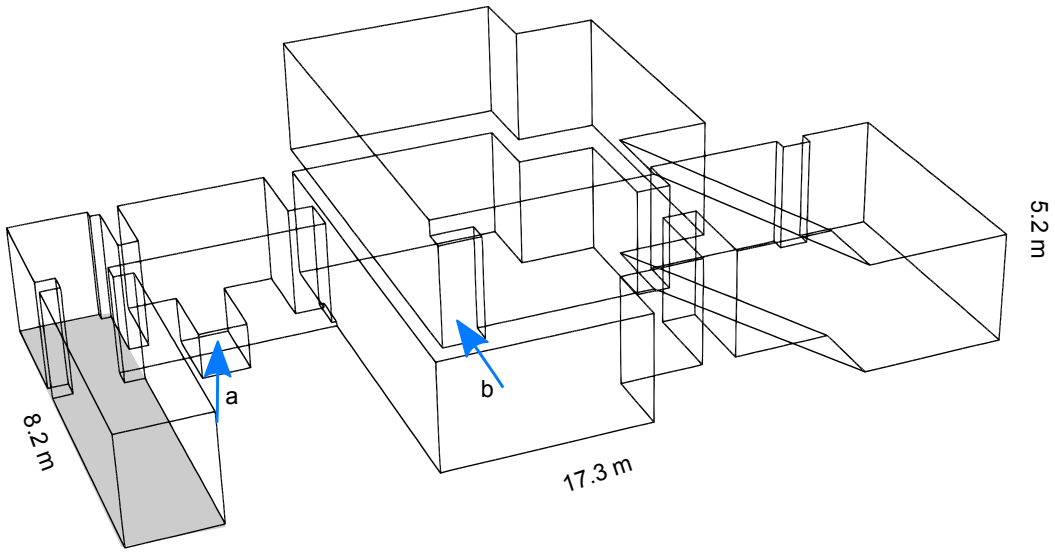

Figure 5.11: Schematic view of the indoor spaces of the arch used in the simulation of the exhibition areas. The shaded area corresponds to the kitchen (now without furniture). (a) indicates the inlet of PM coming from the ventilation shaft, (b) indicates the inlet of PM related to infiltration through the balcony door.

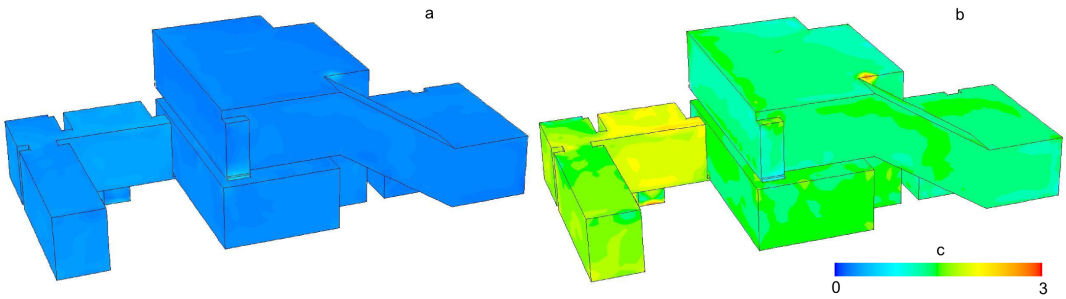

Figure 5.12: Contour plots of c (dimensionless) in the indoor spaces of the arch.

Figure 5.12 shows the I/O ratio in both simulations. The inlet concentration in the ventilation shaft is to a certain extent arbitrary (it could be anything between 3 and 10 times the outdoor concentration). But independently of this value the simulation provides two interesting pieces of evidence. Firstly, the simulations show that when the ventilation shaft is open we observe pronounced gradients of concentration between floors and within rooms, as were measured. Concentration indoors ranged from several times the outdoor concentration to just above it in the top floor. Secondly, if this inlet is removed, the exhibition spaces become well mixed, and c is always a fraction of the outdoor concentration that would be between 0.3 and 0.6. This, of course, may depend on other factors such as ventilation, frequency of use of the balcony door or wind direction. Further in this Chapter we will investigate how to include these parameters in our simulations.

5.4 Apsley House

The simulation of Apsley House is, quantitatively and qualitatively, a step beyond the previous simulations. Not only are the dimensions larger (in terms of the time scales of the relevant phenomena, the size of the geometry, the number of rooms and the number of sources), but its operation is much more complex than the previous cases. Apsley House is essentially unsteady, and it is difficult, if not totally misguided, to search for a weekly, monthly or yearly regularity in its operation.

Figure 5.13: Apsley House and image of the Waterloo Gallery, its largest room.

In order to simulate the House and the different events that define deposition, we have to break them down into problems of a workable scale. It is a largely intuitive process that is, perhaps, as important to the success of the model as its mathematical foundations. But before tackling the issue of the sub-division of the problem, let us summarize the general traits of the main phenomena involved;

Fine and coarse particles Apsley House is a clear example of a building where the suspended PM concentration is dominated by outdoor air. However, visitor numbers are also consid-

erable, and that results in notable levels of coarse PM deposition. The particles found in the House can be broadly classified into these two groups, which behave independently, each own with its sources and its characteristic life-cycle. Our simulations will focus primarily on fine particles, but our experimental data include both, and coarse particles will also be part of the discussion.

Sources of particles Fine particles penetrate from the outdoor environment through cracks and leaks in the windows, through the main door and some sections of the ventilation system. The rates of penetration depend strongly on the outdoor concentration, which changes daily -but does not display important monthly trends- and the wind direction -which does display clear trends throughout the year. Coarse particles are brought in by visitors and resuspended by cleaning activities.

Drivers of deposition The most important sources of air motion in Apsley House are the different components of the ventilation system. The main ventilation system operates in the Waterloo Gallery. It was not in operation during the time we collected data (however, its outlets were still open). One of the Rooms, the Plate and China Room, is equipped with electrical heaters with fans. Some air motion is also caused by infiltration of outdoor air, for example through the main door or the gap under the main door, but this contribution is relatively small if the ventilation system is on. Finally, the heating systems (in-wall and visible radiant heaters) are in continuous operation exclusively during the winter months.

Cleaning activities and resuspension The House is regularly cleaned following a strict schedule. There are daily, weekly, monthly, bi-monthly and yearly tasks. Some of these tasks rotate from room to room. Some cleaning operations have a duration of a few hours and some of days or weeks. These cleaning activities resuspend coarse dust, and have little effect on fine particles from outdoor origin.

Surface properties The rich collection of art, household objects and furniture of Apsley House contains a wide range of materials that display many different surface properties. From the smoother to the rougher surfaces, the collection contains items such as polished metal, ceramics, paper, marble, oil paints, wood or textiles. These different levels of roughness affect deposition and resuspension. These effects are not included in the model for two reasons. Firstly, we do not have the means to validate predictions involving roughness, since we measured deposition on smooth surfaces. Secondly, given the diversity of surfaces, it would be impractical to survey the roughness of every surface and generate a model that includes this information as a boundary condition. Nonetheless, in Section 7.3.4 we will shortly discuss the potential impact of roughness on the accuracy of our predictions.

5.4.1 Experimental data

We have collected data on the behaviour of Apsley House from many different sources. Different types of data have been used for different purposes. In brief:

- We used deposition data collected by English Heritage during 2009 and 2010, which offered information on the Room-to-room variation of deposition
- We collected deposition data which complemented the former with spatial variation of J within rooms, and we also measured c outdoors and indoors for different size modes.
- We captured thermal images to detect cracks and leaks and to find temperature boundary conditions.
- We retrieved wind data from the UK Meteorological (MET) Office.
- We used Ultrasonic and hot-wire anemometers to understand air flow in the building.

This data were not only used to provide boundary conditions and to validate the model, but also, quite often, it provided interesting insights into the behaviour of the House. Each data type is explained in detail in the next Sections.

English Heritage deposition data

We obtained deposition data from a monitoring campaign carried out by English Heritage in the course of a year, from May 2009 to May 2010 following the method described in [6]. Environmental particles were collected in horizontally placed glass slides located at the top of painting frames, at an approximate height of 1.5 m. Particles were counted down to the size of 1 $\mu\mathrm{m}$. An optical microscope was used to obtain 50 images (in 5 rows of 10) from every sample, and the size of every image was 2×2 mm. The location of the samples reflects the variation of concentration between several rooms and is illustrated in Figure 5.14. We will refer to every sample by the name of the Room.

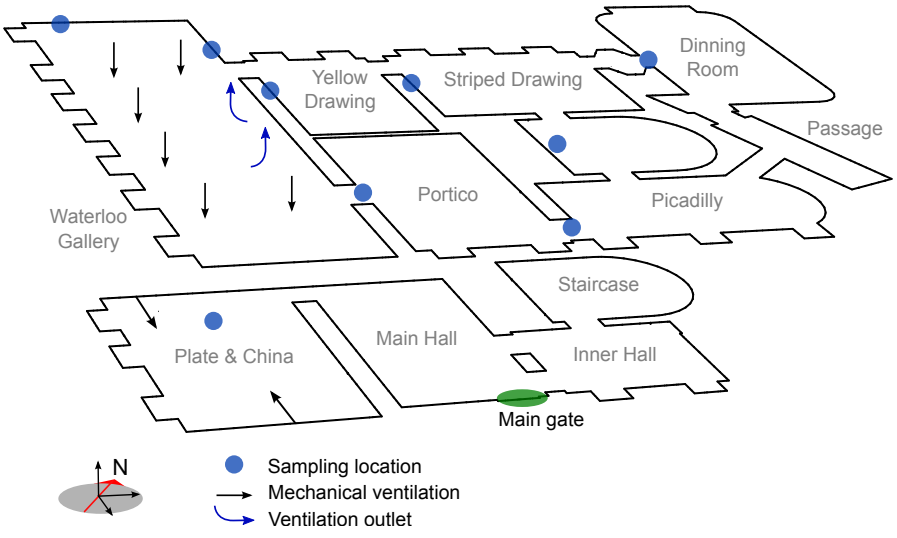

Figure 5.14: Floor plan of Apsley House with monitoring locations.

The raw data are in particle counts per 30 days; however, in this part of the work we will use the yearly averages. The experimental values are summarized in Figure 5.33 where they are used for the comparison with simulations. In order to enable a comparison with the simulated results, we converted particle counts into deposition velocities using the following relation:

$$u_{d,exp} = \frac{N}{At}\frac{1}{c} \tag{5.2}$$

where N is the total particle number, A the area of the surface where the particles were counted, t the elapsed time (a month in seconds), and c is the number concentration of particles surrounding the deposition sampler.

Naturally, the value of c changes throughout the year. In order to obtain a range of realistic values of $u_{d,exp}$ we shall consider not only the yearly average of c but also its variation. Unfortunately, we do not have direct measurements of the variation of c in Apsley House during the whole period of the experiment, but we do have daily measurements of particle concentration in several rooms and on selected days, which may convey an idea of the typical variability of indoor concentrations. Figure 5.15 shows a density estimation of the variation of c of particles with $d_p = 1 - 7.5$ µm. A density estimation is a reconstruction of a probability distribution, and can be interpreted as a histogram.

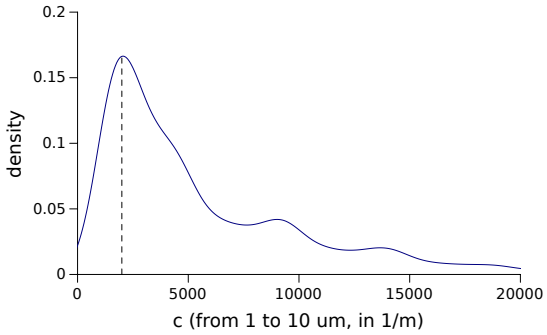

Figure 5.15: Distribution of concentration of suspended $PM_{1-7.5}$ (c). The *density* displayed in the y axis indicates the relative occurrence of each concentration.

The main phenomena accountable for the variation of c are the presence of cars, the presence of visitors and the operation of the ventilation system, all events that change on an hourly basis. Therefore, we can expect minute -or second- averages of c to vary more significantly during a day than daily averages during a year. As an example, the yearly average of PM_{10} concentration measured in Oxford Circus and Marylebone Road during the period of the experiment (which lasted six months) had a relative standard deviation of 34% and 31%, respectively. In other words, while the average daily concentration is fairly stable during the year, the instantaneous concentration displays a great variation within single days. This will be explored further with our own measurements of c.

Own monitored deposition data

The deposition data collected by English Heritage reflects very well the variability of deposition between rooms. We decided to complement this dataset by measuring the variability within rooms. We installed samplers in 16 locations, mostly in two spaces: the Plate and China Room on the ground floor and the Waterloo Gallery on the first floor. We also chose some other locations in different areas of the House. Figure 5.16 shows the sampling locations. We used carbon SEM stubs to collect the particles, and we monitored the monthly deposition for a period of 6 months, from 21/Jan/2012 to the 21/Jul/2012. We counted the deposited particles using a SEM microscope, which allowed us to count particles down to 0.05 μm.

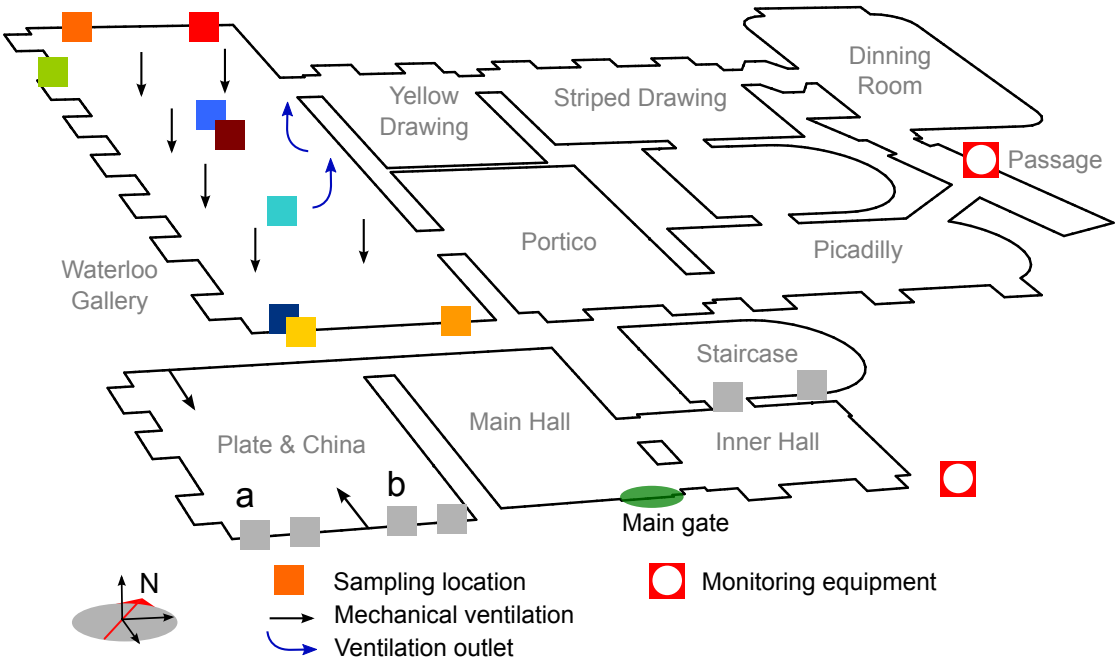

Figure 5.16: Floor plan of Apsley House indicating the locations of the particle samplers and the monitoring equipment, which consists of a set of particle monitoring instruments and is described in detail in Appendix I.

Figure 5.17 shows shows how the particle size distribution of the deposited particles changes with time. Each line in Figure 5.17 corresponds to a size distribution in a given month, and the comparison between different months illustrates how particles accumulate. The x axis is divided in the size-bins used for particle counting. Note that, in order to obtain the number of particles per cm^2 for each of the size-bins, the value on the y axis should be multiplied by the width of each size-bin. Figure 5.18 illustrates the accumulation of fine and coarse particles in all the sampling locations of the Waterloo Gallery.

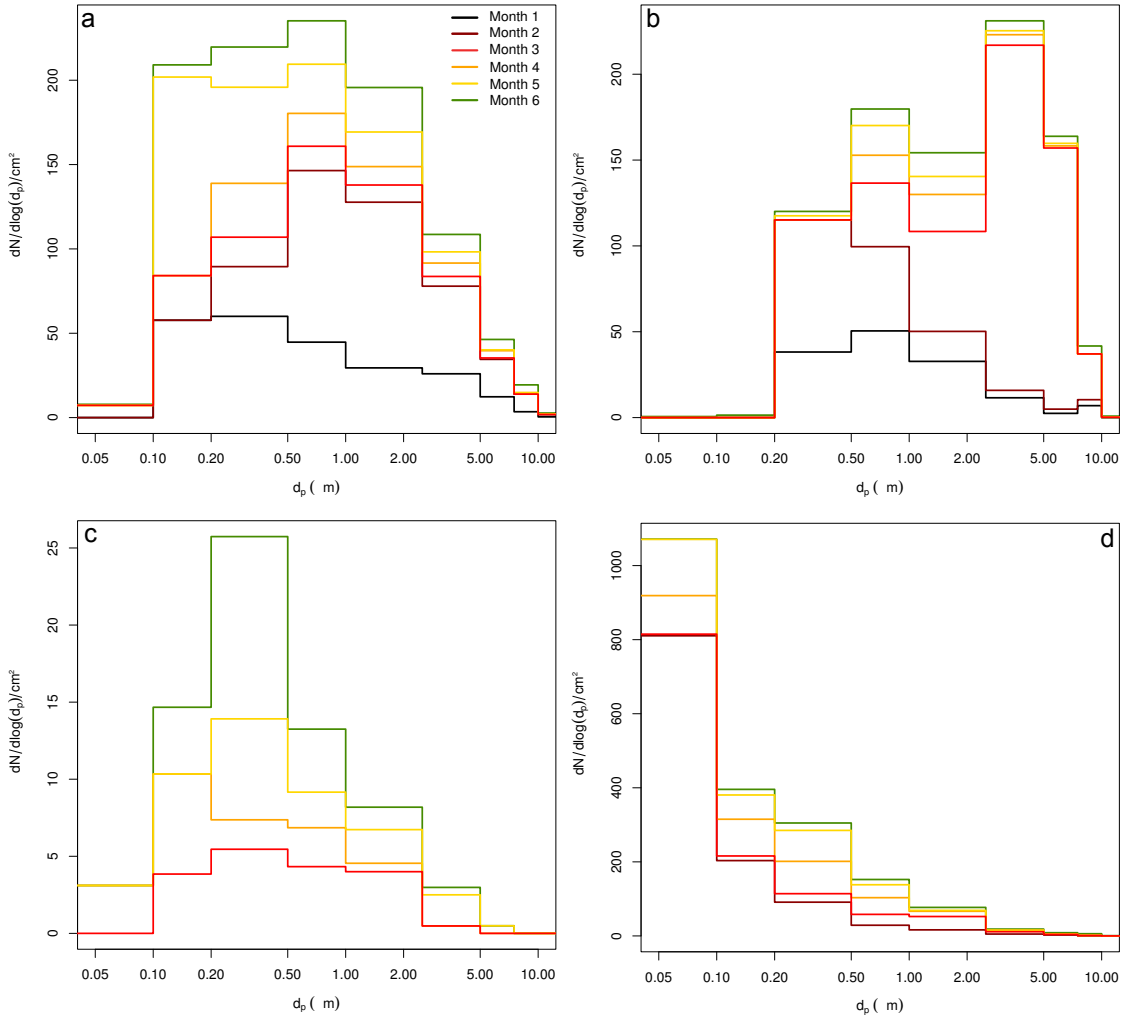

Figure 5.17: Number of particles in four locations in each month of the monitoring campaign. Locations are: (a) painting frame on the south wall, (b) painting frame on the north wall, both in the Waterloo Gallery, (c) a door frame in the first floor and (d) outdoors, in the service stairs.

Figure 5.17 clearly illustrates the differences in behaviour of the various size modes. We can see in Figures 5.17c and 5.17d that fine particulate matter deposition increases in more or less regular steps. We can see a similar progression in the smaller particles of Figure 5.17a, while the deposition of particles >0.5 μm occurs mostly in month 2. The reason for this is that intensive cleaning of the painting frames, involving the use of scaffolding, took place close to the sampling location during the last weeks of month 2 (see operation of the House in Figure 5.25). If we look at the same data collected in another location (Figure 5.17b), we realise that the increase in the deposition of coarse dust does not occur until month 3. As it happens, the cleaning of the frames lasted several weeks, and it was not until the beginning of month 3 that it reached the sampling location depicted in Figure 5.17b. Figures 5.17c and 5.17d, on the other hand, show

the accumulation of PM in two outdoor locations where there are no significant differences of sources or drivers of deposition between different sizes. The location represented in Figure 5.17d was close to the road, and we can observe that fine particle deposition is dominant.

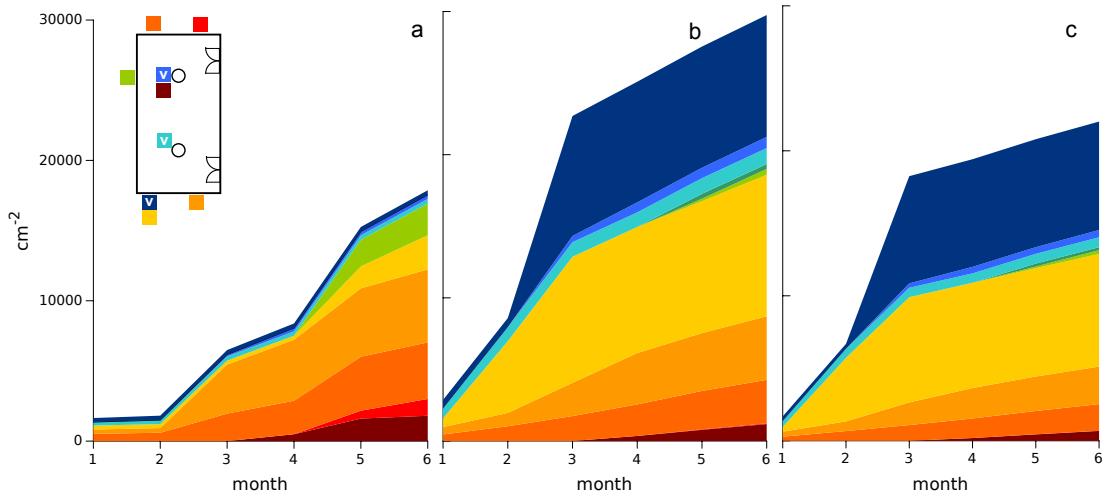

Figure 5.18: Evolution of PM deposition at different monitoring locations in the Waterloo Gallery. Figure (a) shows surface accumulation of $PM_{0.05-0.5}$, (b) of $PM_{0.5-2.5}$ and (c) of $PM_{2.5-10}$. The letter V indicates that a sampler was positioned vertically.

Figure 5.18 summarizes all the data collected in the Waterloo Gallery. There is a good agreement with the size resolved deposition shown in Figures 5.17a and 5.17b. Deposition of fine particles in all locations increases roughly linearly or at least with a regular monthly increase. However, the accumulation of larger particles occurs in bursts related to particular deposition events. In the case of $PM_{2.5-10}$, for example, most of the particulate matter accumulated after the 6-month monitoring period can be attributed to deposition that occurred in two sampling points in months 2 and 3.

This evidence may serve as a initial indication that there are at least two different types of PM (or ways in which PM behaves) in Apsley House. We could broadly define these as fine and coarse. The two size modes coexist, but have different sources, sinks and life-cycles and behave independently. Of course, the distinction between these two types (of particles or of life-cycles of particulate matter) is all but clear, and we must expect some overlap in their behaviour: some fine particles might be of indoor origin, and some coarse might infiltrate from outdoors. A study of the suspended PM concentration will provide further insight into this distinction.

Suspended PM concentration data

The model can simulate PM that penetrates from the outdoor environment or which is emitted within the House. However, it cannot include particulate matter which is introduced by visitors, because at the present stage we do not simulate visitor movement. Fine particles are more likely

to penetrate from outdoors, and we should expect their concentration to be related to the outdoor concentration. On the other hand, coarse particles are transported into the house on the clothing and footwear of visitors [7], and their number should correlate with visitor numbers.

In order to investigate how does PM interact with the outdoor environment we monitored the concentration of suspended PM in two locations, indoors and outdoors, for a period of six months, from 21/Jan/2013 to 21/Jul/2013. The two sampling locations are illustrated in Figure 5.16. We used two sets of three laser particle counters (Gradko DC1010) calibrated at the following size modes: from 0.5 to 2.5 μm, from 2.5 to 10 μm and > 10 μm (The operation of these instruments is described in detail in Appendix 1). We measured the number concentration of each size mode every minute, which resulted in more than $24 \times 60 \times 30 \times 6 = 259200$ experimental points for every size. The monitored data are shown in Figure 5.19 as a scatter plot of the concentration in the two monitoring locations -indoor vs. outdoor- for each of the three size modes.

Figure 5.19 further confirms the different behaviours of different size modes. Note that the concentration of fine particles indoors correlates very well with the outdoor concentration. The slope of the regression line is an indication of the I/O ratio. This slope is 0.34 ± 0.2. Note, however, that this is neither the mean nor the mode of the I/O ratio during the experimental period. Linear regression gives higher relative importance to the points with higher values, and contrary to what we saw in the tunnel (Section 4.3), the I/O ratio in Apsley House is not necessarily independent of the magnitude. A better assessment of the I/O ratio may be obtained using a histogram. Figure 5.21 shows a histogram of the I/O ratio for the 0.5-2.5 μm particles during the whole monitoring period. We can clearly see that the most common values are between 0.5 and 0.65.

Figure 5.19 shows that the concentration of fine PM indoors depends on the outdoor concentration. Contrarily, the concentration of coarse particles indoors is totally unrelated to the outdoor concentration, as demonstrated by the scatter plot of coarse PM_{10-100} in Figure 5.19. The middle size mode, $PM_{2.5-10}$, displays an intermediate behaviour. The instruments detected high values of coarse PM indoors (probably due to the presence of visitors or to cleaning activities), at times where the concentration outdoors was very low. Conversely, when the concentration outdoors is high, the concentration indoors remained unaltered. The monthly average concentration of PM_{10-100} does in fact correlate well with visitor numbers, as Figure 5.20 shows.

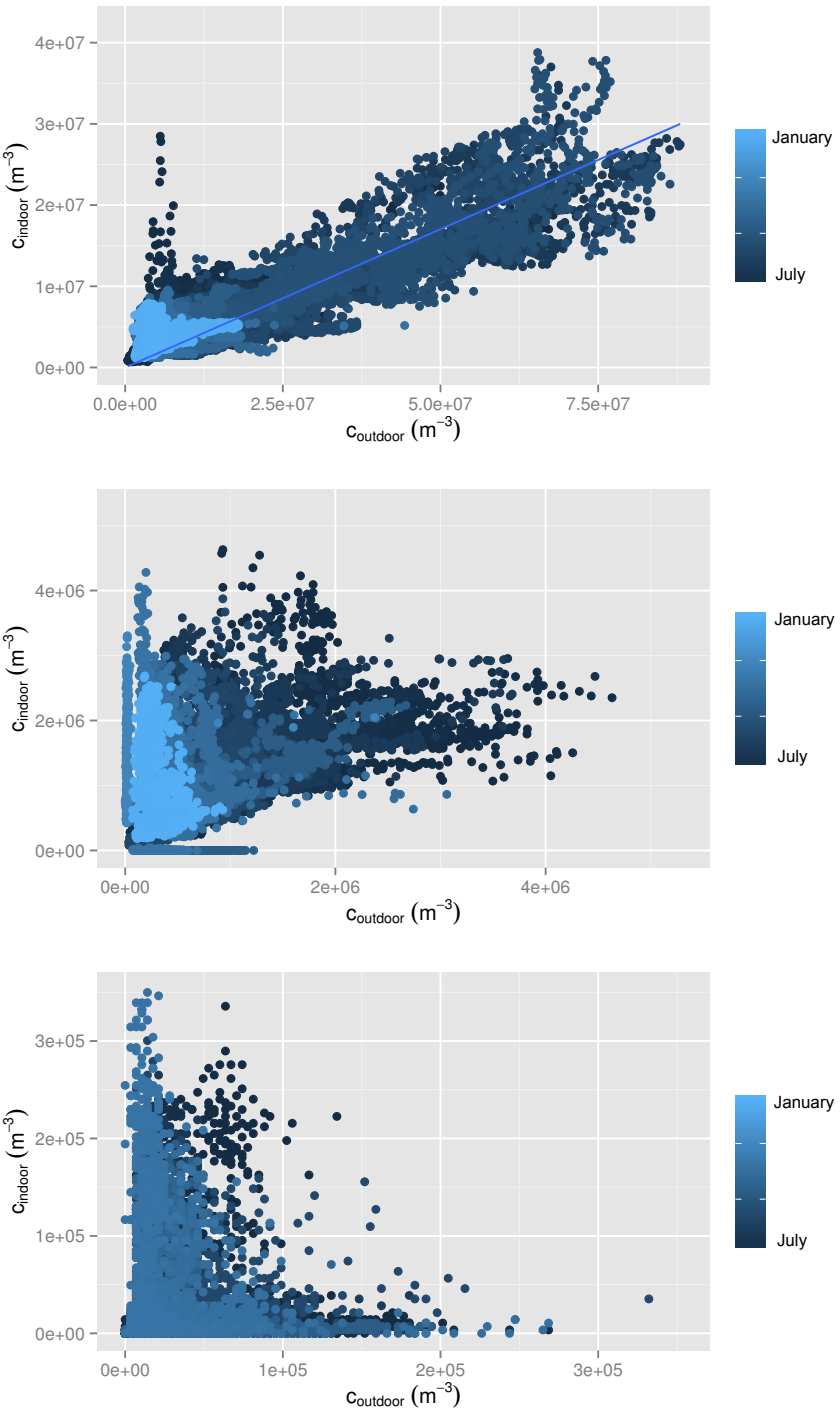

Figure 5.19: Scatter plots of inlet vs. outlet concentration measured in the indoor and outdoor monitoring locations in Apsley House for three different size modes, from top to bottom: $PM_{0.5-2.5}$, $PM_{2.5-10}$ and PM_{10-100}. The plot shows that the indoor concentration of fine particles is very well correlated with the outdoor concentration, which may indicate infiltration. In opposition, coarse particles indoors seem totally independent from coarse particles outdoors. The colour of points indicates the specific time of monitoring, illustrating that the relationship between indoor and outdoor concentration is similar during the monitoring period.

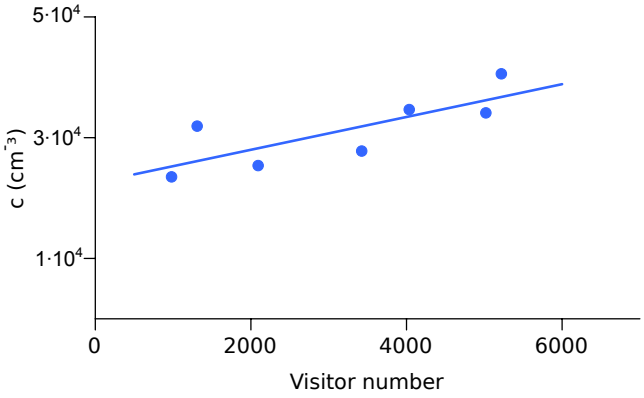

Figure 5.20: Average monthly concentration of PM_{10-100} related to the number of visitors to the House.

As Figure 5.21 shows, the I/O ratio is very changeable: during the experimental period it took many values between 0.3 and 0.8. However, we must note that for the most part this variability is neither seasonal, nor weekly or monthly. The time scale in which most of the variability of I/O ratios occurs is a single day. Figure 5.22 shows the autocorrelation of the data series of I/O ratio for the smallest particles. The autocorrelation factor is obtained by correlating a signal with itself and calculating the quality of the correlation. The measure of the goodness of the correlation is given by a correlation coefficient or autocorrelation factor. This process is repeated with different time lags. If the signal displays any periodicity, the quality correlation should improve periodically, and thus the correlation factor will oscillate.

We can observe that the autocorrelation factor increases in periods of 1440 min. (i.e. 24 h.). This is due to the fact that most indoor fine particles are related to road traffic. Early in the morning the House is clean, and as the vehicle flow increases, the I/O ratio increases. During the night, as particles deposit, the I/O ratio goes back to its minimum value.

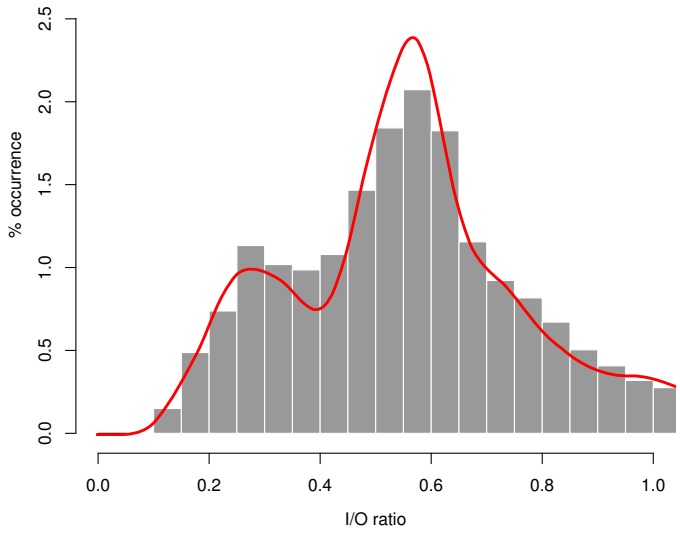

Figure 5.21: Histogram of I/O ratio of $PM_{0.5-2.5}$ during the entire monitoring period with overlapped probability density function.

However, not all the variation is related to car flow only. As we will see, wind has an important effect on particle penetration, and therefore on the I/O ratio. Consequently, the seasonality of wind also affects the trends of indoor fine PM. This is also reflected in our data, as we will show below.

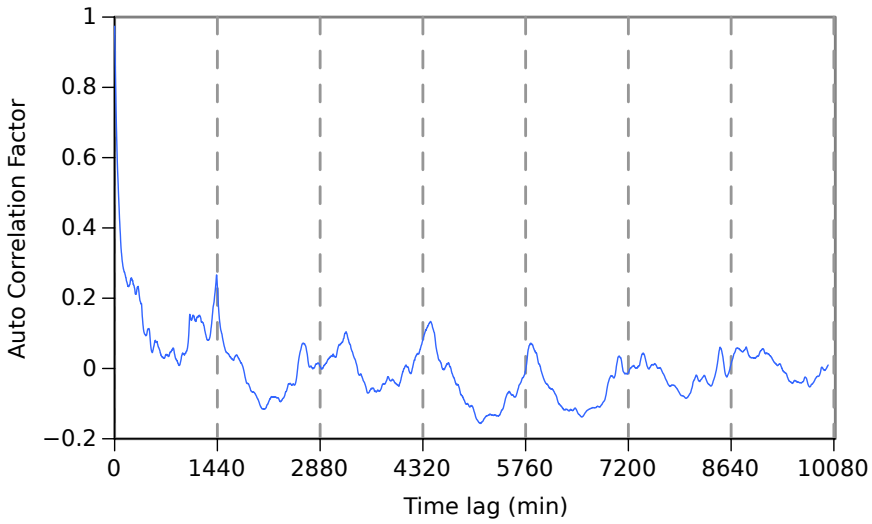

Figure 5.22: Autocorrelation plot for the I/O ratio of $PM_{0.5-2.5}$. The period of monitoring is 1 min. The vertical grid lines are placed every 1440 min (i.e. a day).

Leakage

We used a thermal camera to locate cracks and leaks in the building envelope. This technique requires a difference of temperature between the indoor and outdoor environments. Consequently, we carried out this survey on a December day (outdoor temperature $\sim$ 8°C), during which the heating system of the House was activated, keeping indoor air at $\sim$15-20 °C. Under such conditions, air infiltration appeared in the thermal images as a thin line indicating the outdoor temperature. An example is provided in Figure 5.23.

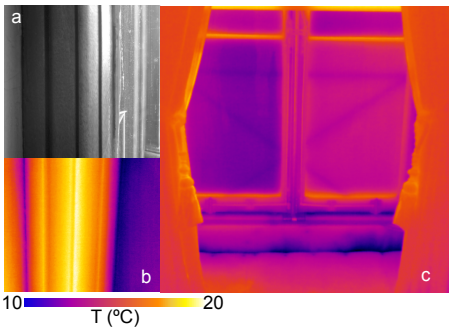

Figure 5.23: Example of a thermograph of a window. (a) is a picture of window frame and (b) a thermal image of the same frame. (c) shows a thermal image of the whole of a window.

Our survey revealed that all the detectable leaks were located in the frames and fittings of the windows. The most visible ingress of outdoor air took place from the bottom and top of the windows, in the small gap left between the shutters and the window frame (Figure 5.23c). This was observed consistently in all the windows. Another typical leakage point is the vertical joint between the two window shutters. This leakage is present in all windows to some degree, generally stretching over 1 m around the handlebar and the bottom of the windows, but in some cases air leaks between the two shutters from top to bottom. These two points of leakage are visible in images of the whole window; however, other leaks require a closer inspection. Close-up images of the window frame revealed the presence of leaks in the fittings between the window frames and the walls. These leaks were also present in all windows over different sections of the window perimeter, typically covering $\sim$ 20-50 % of the total perimeter. We did not detect any cracks in the glass or in the fittings of glass and window frames.

The size of these cracks is not easy to quantify, but they certainly have characteristic dimensions. The depth of a crack can be no larger that the thickness of the window frame, and therefore a representative dimension might be 10 cm. The height of the crack, even on the most visible case of poor fitting of the window shutter in the frame, was significantly smaller than 0.5 cm, and 0.1 cm might be a good estimate of the average cracks found in the House. A particular point of air entry, a gap under the main gate, deserves separate mention. Its dimensions are greater than those of the average leakage paths, with the height of close to 1 cm.

Air velocities and wind data

We obtained hourly wind data from the MET Office. The closest locations to the site are the Kew and Heathrow weather stations, which display very similar wind roses. Figure 5.24 shows data from Kew. We assume that wind velocities and directions in Apsley House will not be significantly different (see Appendix 1 for a detailed explanation).

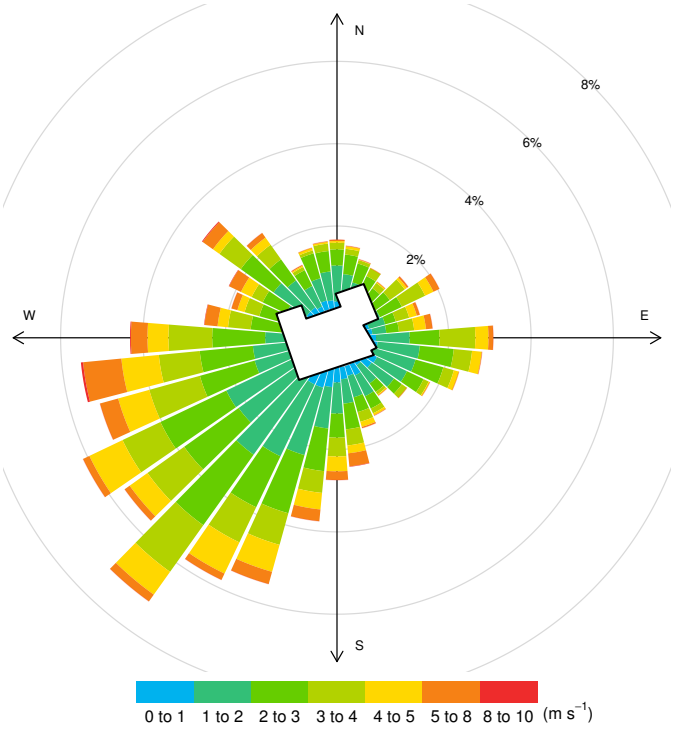

Figure 5.24: Windrose for the monitoring period with the contour of Apsley House superimposed with the appropriate orientation.

We used two 3D Ultrasonic anemometers to determine indoor velocities and flow patterns. We placed the anemometers in the doors between rooms for periods of 1 h. We also used the anemometers to find representative air velocities for the ventilation system.

Dynamics of the House

All the experimental variables reported above display a significant seasonal variation. Figure 5.25 summarizes the main trends of wind, concentrations and operation of the House during the experimental period. We can observe various simultaneous trends, which may be interrelated: Visitor numbers are higher in the summer months, and the concentration of coarse PM also increases as summer approaches. Wind changes monthly. It displays a prominent South-West direction every month, with the exception of March, in which it is North East, and perhaps

February, which displays the greatest wind variation. The operating regime of the house is also changeable, with many cleaning operations during the Winter months -when visitor numbers are low- and less cleaning combined with extended opening hours starting in April.

By looking at Figure 5.25 one realises the challenge of simulating Apsley House using steady-state simulations. We can not find a period of time larger than a month during which all the variables (wind, I/O ratio, cleaning and visitors) are constant. But at the same time, simulating all this variation dynamically would be impractical and very computationally demanding. Contradictory as it may seem, steady state simulations can describe this changeable environment more easlily than dynamic simulations. Of course, a steady state simulation does not directly represent a period of time, it simply represents a situation that does not change in time. But the inputs to the simulation (for example, the outdoor concentration) are necessarily related to a certain time period. In order to choose an appropriate length of time to simulate, we can pick an instantaneous measurement, a daily average or a monthly maximum, and use that to simulate deposition for a second, a day or a month.

In the following sections we will try to find a compromise, a time scale for the model which is solvable and that reflects, at least, the phenomena that define deposition. In other words, we are looking for the longest time-span that can be represented with a steady state simulation, and that provides useful and realistic results.

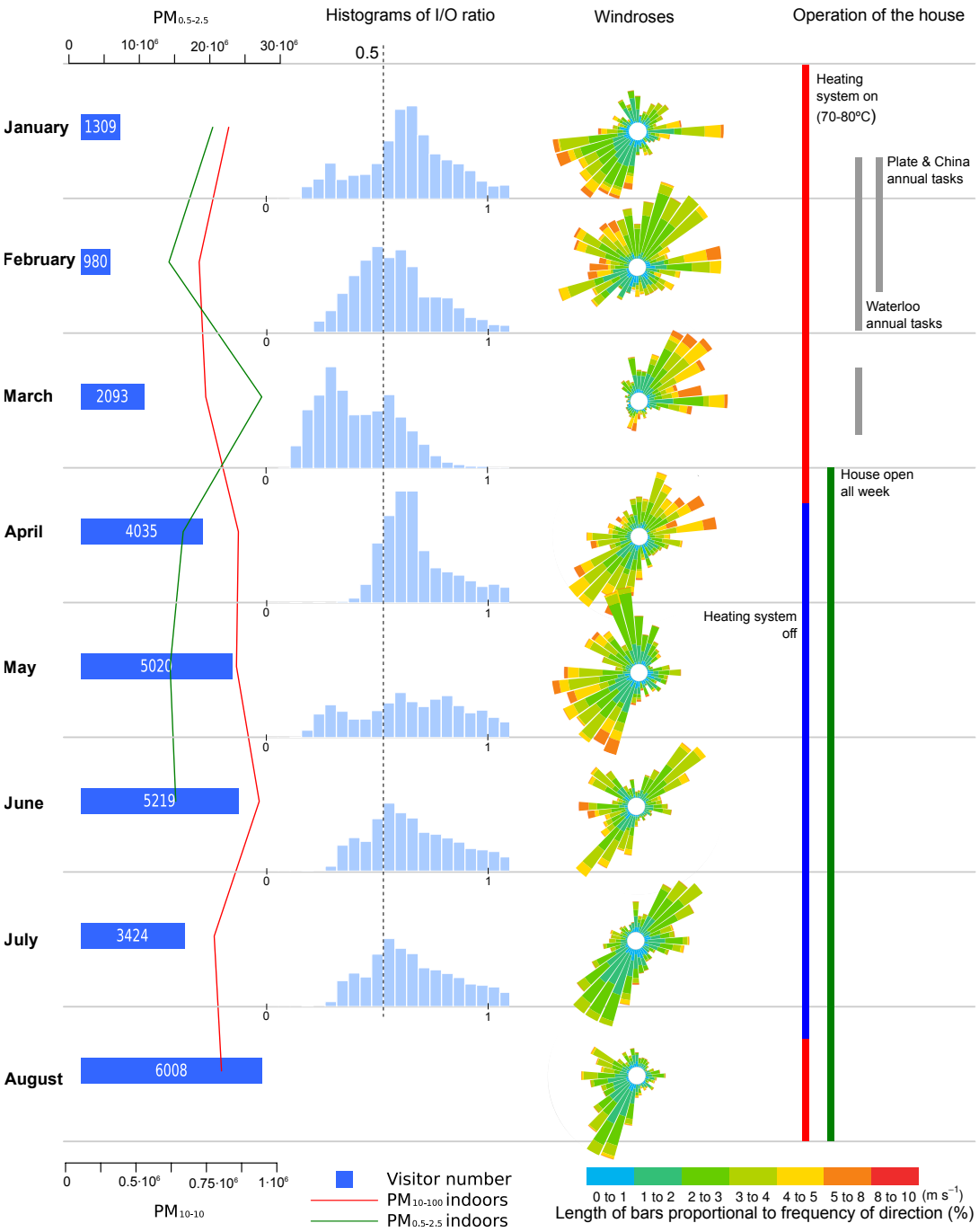

Figure 5.25: Graphical summary of the variations seen in the House during the monitoring period. This plot is useful to visualise the number of parameters that change in the house, and to identify the main differences between months. It shows how the visitor number increases as summer approaches, and how the number of coarse particles follows the same trend. The monthly histograms of I/O ratio demonstrate that it is highly changeable, whith an average that might be below or above 0.5 depending on the operation of the house. The wind rose for every month is also very variable, but we can also perceive that a few months are characterised by very directional winds. The last column indicates the schedule of cleaning and operation of the heating system.

5.4.2 Applicability of the model

The applicability of the model can be related to a set of dimensionless numbers, as explained in Section 4.4. Here we investigate the value of some of these parameters in the current system. Perhaps the most relevant parameter defining the applicability of the drift-flux model is K_{pt}, which describes the ability of the particles to be transported by all the scales of turbulent motion. We obtained the range of values of u_{rms} from a transient simulation (using the computational set-up that will be described below). Figure 5.26 shows the histogram of the values of K_{pt} in Apsley House for the case of 2.5 μm particles. This histogram reflects the values at every computational node of the 3D grid used for the simulations described in Section 5.5. K_{pt} is well below 1 in all the domain, and therefore PM movement can be simulated with our modelling approach.

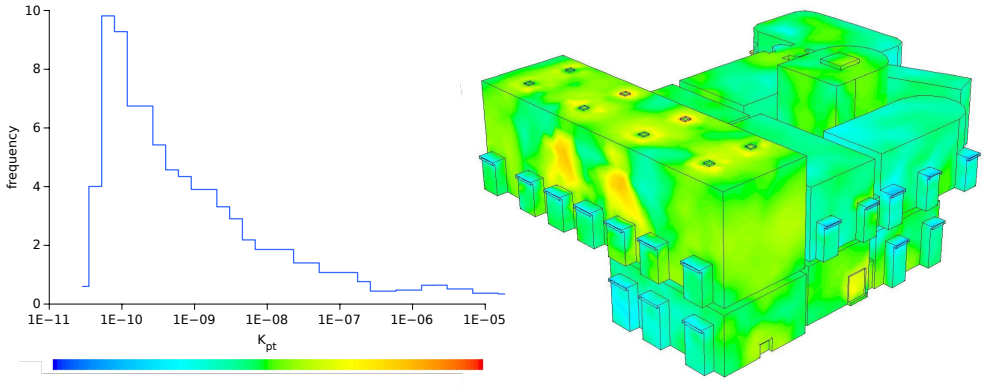

Figure 5.26: Histogram and contour plots of K_{pt}.

The second dimensionless number in the order of importance is the Péclet number, Pe, which indicates the transport mechanism that dominates the particle flux, i.e. diffusive $Pe < 1$ or convective $Pe > 1$. In our system, as we shall see, we need to deal with some outlet boundaries where the concentration of aerosols is unknown. We can avoid the problem of estimating these concentrations if $1/Pe$ is very small. Fortunately this is the case in our system, as Figure 5.27 shows, the Péclet is generally far larger than unity. However, note that in some occasions it approaches 10. This is an issue in rooms such as the Plate and China Room where the air flow is mild (particularly when the ventilation is off). Very small Péclet values can cause wrong estimations of the concentration profile near outlet and inlet boundaries. We shall see the consequences of this in Section 5.5.2.

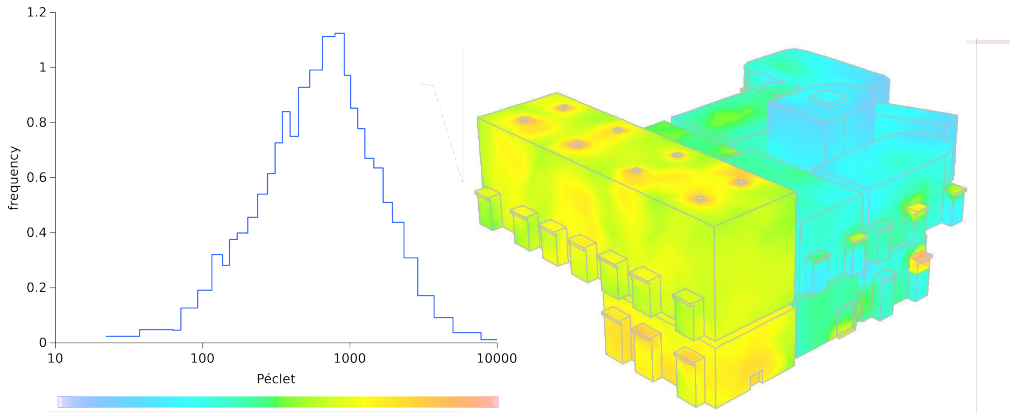

Figure 5.27: Histogram and contour plots for the Péclet number.

5.4.3 Preliminary simulations of the outdoor environment

We divided the simulation into four stages. In the first stage, we investigated the fraction of outdoor aerosol that penetrates indoors through cracks and gaps in the building envelope. In this stage we used CFD simulations of the outdoor environment surrounding the House to obtain the pressure on the walls, coupled with a model of the penetration efficiency of particles through cracks and leaks. In the second stage, we produced a CFD simulation of the indoor environment, where the penetration factors obtained in the first phase were introduced as boundary conditions. We simulated every stage separately and with different computational meshes. In the third stage we attempted to take advantage of the richness of our data in order to simulate different periods of operation of the House. Finally, in the fourth stage we used the model to produce exploratory simulations of selected rooms, investigating how their operation affects deposition.

Penetration factor model

In order to obtain the values of u_i and P for the boundary conditions we solved the model proposed by [8] to predict the penetration factors of spherical particles through rough building leaks. This model understands the penetration factor, P, as the proportion of particles of a given size that manage to penetrate through a gap without depositing on its internal walls. The model assumes that particles deposit on walls due to gravitational settling and Brownian diffusivity. P is defined as the product of the penetration factors due to these separate phenomena:

$$P \equiv P_d \times P_g \tag{5.3}$$

where P_d is the penetration factor due to Brownian diffusivity and P_g due to gravitational settling. P_d is calculated with the following equation:

$$P_d = exp\left(-\frac{1.967\mathscr{D}L}{[H-2(0.45k+d_p/2)]^2 u_i}\right) \tag{5.4}$$

where k is the wall roughness (a representative height of the surface irregularities), d_p is the diameter of the particles, L is the length of the crack (its depth towards the interior of the wall) and H is its height. We calculate the penetration factor due to gravitational settling with the following equation:

$$P_g = 1 - Lv/(H-d_p)u_i \tag{5.5}$$

where v is the settling velocity. The calculation of P_g and P_d requires the mean air velocity in the crack, u_i which is calculated as:

$$u_i = \sqrt{\Delta p + \left(\frac{1.208\times10^{-4}}{H^2 L}\right)^2} - \frac{1.208\times10^{-4}}{H^2 L} \tag{5.6}$$

where Δp is the pressure difference between the two sides of the crack. Atmospheric pressure has the same value indoors and outdoors. We also assume that the pressure on the indoor walls caused by internal ventilation is negligible in comparison with the pressure caused by wind on the outdoor walls. Under these assumptions, we can consider that the pressure difference through cracks in the walls is equivalent to the total pressure exerted by the wind:

$$\Delta p = \frac{1}{2}\rho_f u^2 \tag{5.7}$$

where u is the wind velocity. Due to the shape of the building, the changing wind direction, and the presence of columns and other architectural features that may alter the air flow, we can not assume that Δp has the same value in all the leaks. For this reason, we have obtained Δp with a CFD simulation of wind pressure on the building façade. This simulation is briefly described in the next section.

Particle penetration factors

The purpose of the outdoor simulations is to obtain Δp in all the leaks (in fact, in all the façade, even though we are interest only in the value in the leaks) for any wind speed and direction. We used two separate computational grids for the outdoor and indoor environment. The outdoor grid includes only the main features of the façade, while the indoor grid contains more detail and represents the indoor layout, with walls, doors and ventilations inlets and outlets (see Section 5.5). We used a cell size of 1 m in the building surface for the outdoor grid. As seen in Figure 5.28, the geometry consists of an octagonal space surrounding Apsley House. This allows us to set a velocity boundary condition in any face of interest. As an example, we report simulations corresponding to a S-W wind direction (the predominant direction during the experimental period) and wind speeds of 3 $\mathrm{m/s}$.

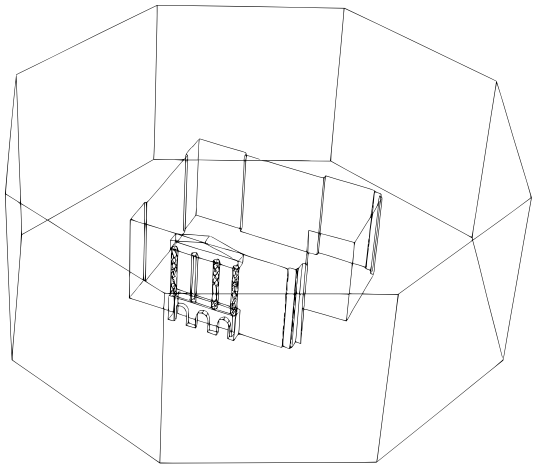

Figure 5.28: Geometry of the outdoor environment used in the simulations of the outdoor environment. Each of the faces of the octagon can be set up as an inlet or an outlet of air in order to define wind boundary conditions.

We use the values of Δp to calculate u_i and P at every leak using Equations 5.6 and 5.3. The simulation of the particle penetration factors provided high values of P in the sides of the House that face the predominant wind directions. There is a clear distinction between the South and West façades, where values of P are close to 1 for the most common wind velocities 3 $\mathrm{m/s}$, and the North and East façades, in which the pressure is generally negative and therefore leads to no particle penetration. Figure 5.29 clearly reflects this difference.

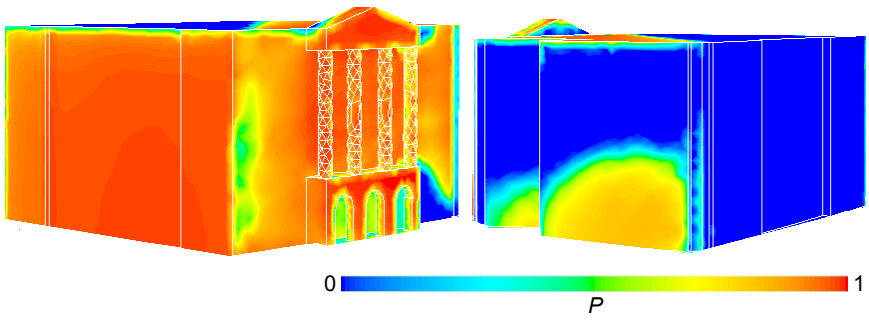

Figure 5.29: Contours of the penetration factor P on the four faces of Apsley House.

As Figure 5.30 shows, there are no significant differences in the value of P between different rooms. When wind speeds are about 0.5 m/s (mild wind, occurrence of $\sim$10%) penetration factors drop significantly. Our simulation indicates that under typical wind conditions, PM of any size up to 10 μm will penetrate efficiently through the building envelope. In mild wind, this penetration is significantly reduced, and differences in size are less significant.

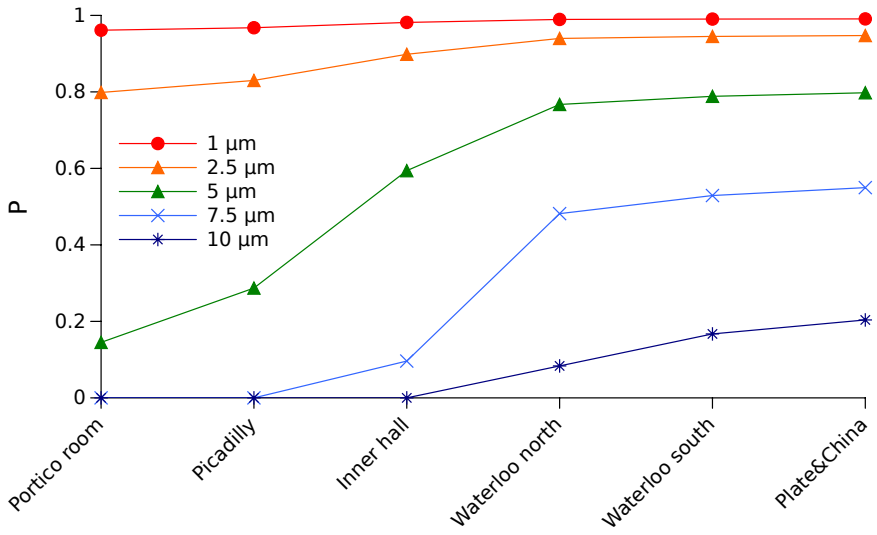

Figure 5.30: Simulated values of P. Wind speed = 3 m/s; crack wall roughness, k = 1 µm.

Given these estimations, we produced a simplified summary of penetration factors and inlet velocities to be used in simulations of the different cases. We will report these boundary conditions for each of the simulations explained below. Table 5.3 includes this information for the initial simulations, which correspond to the distribution of P illustrated in Figure 5.29.

5.5 Initial simulations: yearly average

Despite the complexity of the indoor environment in Apsley House, we firstly approached the problem using annual averages as inputs to the model. In this Section we use representative values of pollutant fluxes through cracks, outdoor wind speeds and velocities in the ventilation inlets. We use steady-state simulations. Certainly, this approach requires a number of assumptions and simplifications which we explain and justify in detail throughout the text. Our results will also determine whether and which additional pieces of information could improve the accuracy of the predictions. This simulation is based on several scenarios, and the scenarios are based on our hypotheses on the sources of PM and the drivers of deposition.

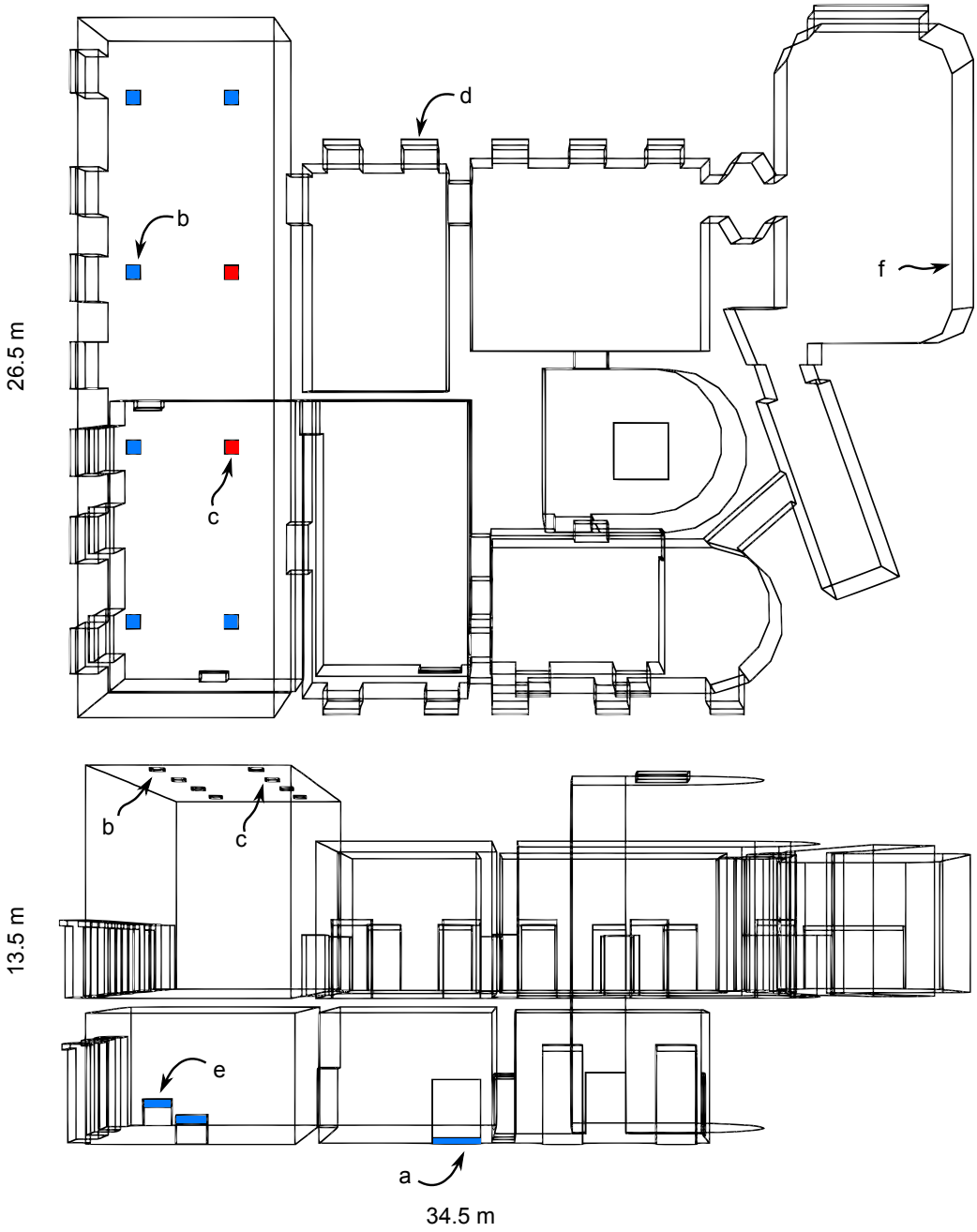

Figure 5.31: Schematic view of the interior of Apsley House as used in the meshes for the simulations of the indoor environment. Top: plan view, bottom: side view. (a) Gap under the main door, which is an air and PM inlet, (b) ventilation air inlet, (c) ventilation air outlet, (d) a window, each of which acts as an inlet or outlet of air, (e) heated ventilation inlet, (f) location of one of the in-wall radiant heaters. Blue indicates inlet, red indicates an outlet, white a wall.

Scenario definition

Figure 5.25 illustrates vividly that the indoor environment of Apsley House is dominated by a complex combination of different phenomena. Outdoor pollution penetrates mainly through leakage, which is present in all the window frames. Leakage is triggered by the outdoor wind, which can cause a positive or negative pressure on the building walls, thus turning cracks into inlets or outlets of air. Only one of the Rooms, the Waterloo Gallery, is equipped with an HVAC system that pumps filtered air of outdoor origin into the volume. This system is in continuous operation. The only other room equipped with mechanical ventilation is the Plate and China Room, where two electrical heaters can blow air (of indoor origin) into the Room. This system operates intermittently, generally as staff requires, and no record of its operation is maintained. In order to investigate which of these systems has a greater effect on particle deposition, let us artificially divide them in three different modes that can be on and off:

- Mechanical stirring. When this is in place, recirculation of the HVAC system in both the Plate and China Room and the HVAC system in the Waterloo Gallery introduce clean air into the volume.
- Main door. When activated, the gap under the main door allows air to penetrate into the building.
- Leakage. If enabled, the cracks placed on the windows with positive pressure will allow outdoor air to filter with certain penetration factors and air velocities. This option could also be understood as wind on/off.

Based on these binary options, we defined five different scenarios (or Cases) which we summarize in Table 5.2. The different boundaries are defined as follows, "W" are wall boundaries with the boundary condition defined in Section 3.3.2, "O" and "I" are Dirichlet outlet and inlet boundaries as defined in Section 3.3.4. These cases do not reflect actual operational set-ups of the House. Rather, they are designed to investigate the relative influence of the different mechanisms that cause deposition, and their synergistic effects.

Table 5.2: Case definitions for the simulation of Apsley House. "1" means enabled. The table also indicates if a boundary is considered an outlet (O), an inlet (I) or a wall (W) in each case.

Case	**A**	**B**	**C**	**D**	**E**
Main door	1			1	
Mechanical Stirring		1		1	1
Leakage			1		1
Ventilation outlet	O	O	O	O	O
Waterloo inlets	W	I	W	I	I
Main door	W	W	W	I	I
Positive p walls	W	W	I	W	I
Negative p walls	W	W	O	W	O

We used a grid based in the geometry displayed in Figure 5.31, after a grid test described in Section 5.5.3. Figure 5.31 indicates the location of the different boundaries. Leaks in this geometry are represented as gaps on top of the windows. This gap has an inlet velocity u_i' which is calculated from the actual velocity in the crack , u_i, obtained with Equation 5.6, corrected to account for the difference in area between the actual cracks and their computational representation:

$$u_i' = u_i \frac{A_1}{A_2} \tag{5.8}$$

where A_1 is the Section area of the crack, and A_2 the Section area of the inlet that represents the crack in the computational mesh. We were concerned that an excessive velocity in the crack inlets would increase u_d, adding a driver of deposition that does not exist in the actual House. Cracks should be simply sources of particles, with very little power to drive deposition. We ensured that cracks and leaks always had velocities that did not alter the patterns of deposition unrealistically, i.e. that cracks are not able to drive deposition. Figure 5.32 demonstrates how the sum of the deposition velocity in a room increases when the velocity in the crack inlets is high. However, when this velocity is <0.01 $\mathrm{m/s}$, the contribution of cracks to u_d becomes insignificant.

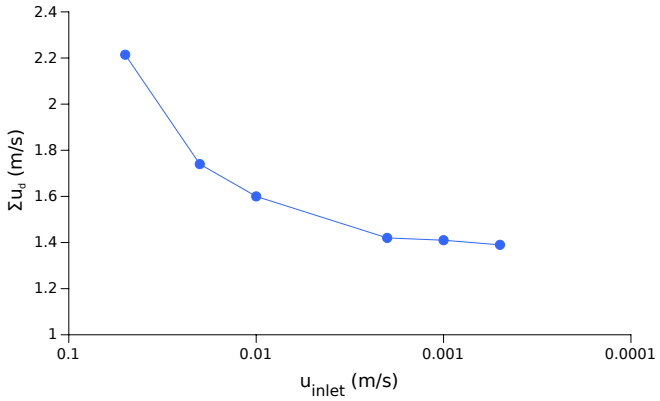

Figure 5.32: Test of the influence of the inlet velocity in the crack inlets.

Scenario simulation

We solved the four cases in Fluent for particles of the size $PM_{0.5-7.5}$. The reason why we choose these particles is that we have shown experimentally that their behaviour is (for the most part) related to outdoor c, and also because this is the smallest size fraction that we can compare with the data obtained by English Heritage. Particles were characterised with an average diameter of d_p = 2.5 µm with a particle density of ρ_p = 1500 kg/m^3. We normalised the concentration with respect to the outdoor concentration (thus assuming that Apsley House is immersed in air with a homogeneous aerosol concentration). Consequently, inlets which are directly connected to the outdoor environment have a concentration of 1, and the leakage inlets have a concentration

Table 5.3: Simulation set up and boundary conditions. u is in m/s.

Boundary	c	u **(max/min)**
China inlets	0.0	(1.5 / 0.5)
Waterloo inlets	0.0	(0.5 / 0.2)
Main door	1	(1 / 0.2)
China leaks	0.90	0.01
Waterloo leaks	0.95	0.01
Piccadilly leaks	0.80	0.01
Portico leaks	0.80	0.01
Simulation set-up:		
d_p = 2.5 μm		
Simulation: steady state.		

which is equal to their estimated value of P.

Figure 5.33 shows a comparison between the experimentally determined values of u_d and the computational predictions. The most evident result is that the deposition predicted in all cases is within the range of the experimental values. It is also apparent that the effects of the main door alone do not suffice to explain the observed deposition, while leakage and ventilation seem to be accountable for most of the deposition. However, the simulations of these phenomena differ in the prediction of the spatial distribution of deposition. The simulations including forced ventilation can account for the differences in deposition between rooms, but in some cases overestimate the deposition rates. On the other hand, the simulations of leakage underestimate deposition, and do not reproduce the observed marked differences between rooms.

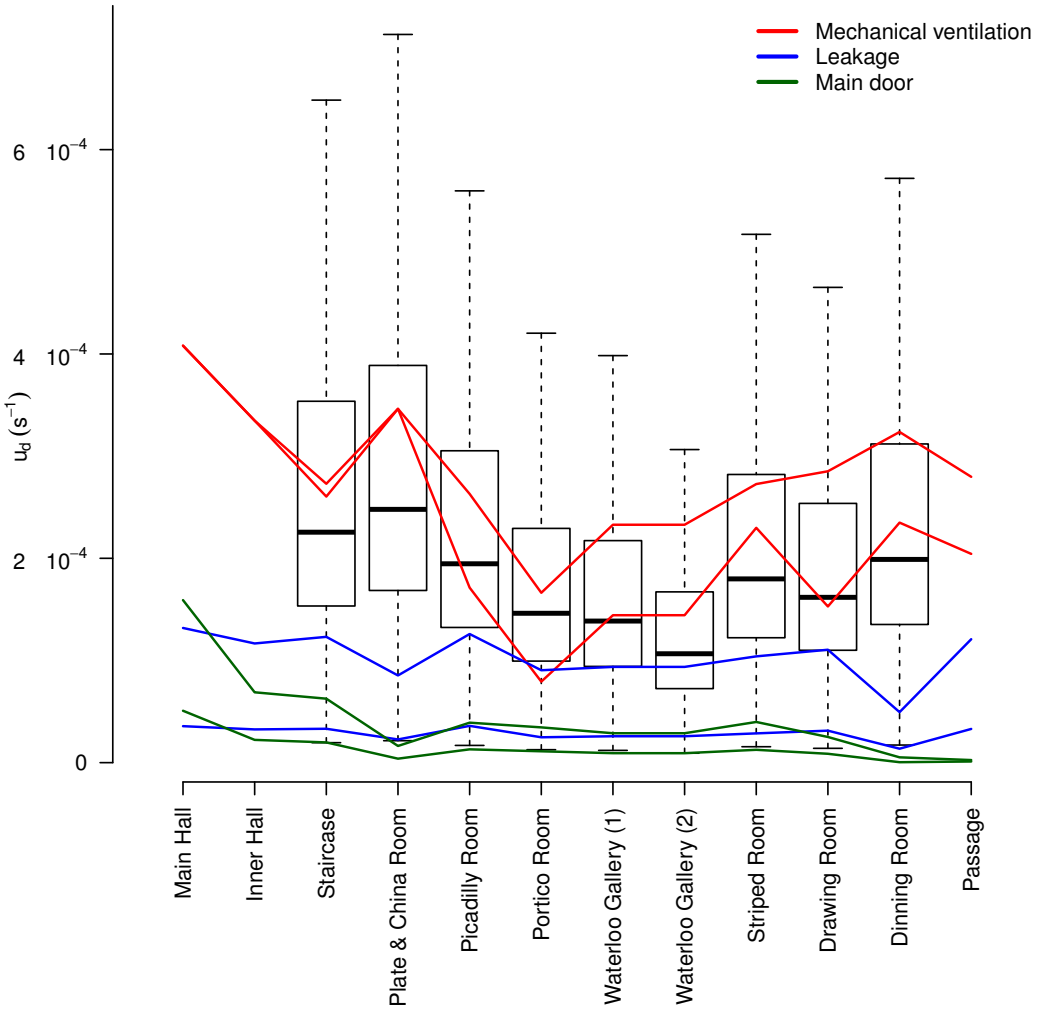

Figure 5.33: Predicted deposition velocities compared with experimental yearly averages. The continuous lines indicate upper and lower estimations based on the maximum and minimum boundary conditions reported in Table 2 for three different scenarios. The error bars in the experimental values reflect the monthly variation of deposition. We include predictions for some rooms which lack experimental values.

Interestingly, the deposition that is caused by the ventilation system acting during the whole year corresponds with the maximum measured levels of deposition. This suggests that the introduction in the model of discontinuous or seasonal operation which reflects different operating regimes might reduce this prediction of deposition and bring it closer to the observed yearly averages. A closer inspection of the results reveals that the Dining Room is the only room where deposition is more markedly under-predicted by leakage. This could be related to the fact that

this room is equipped with radiators along all of its perimeter. Thermal effects can have an impact on deposition that has been ignored in this Section.

We have shown that a CFD simulation of indoor deposition based on roughly estimated parameters (crack size and number, wind speed and concentration yearly averages), that ignores the yearly variation of some effects (ventilation or heating) and some physical phenomena (heat and coagulation) can deliver fair predictions of overall deposition and its spatial variation. However, this simulation also demonstrates that more precision can not be achieved unless the variation of every boundary condition is introduced as an input parameter, and that this variation must be, of course, time-dependent. In other words, seasonal fluctuations must be taken into account if more detail is to be achieved.

5.5.1 Second simulation: periodization

We have seen in Section 5.4.1 that the operation regime of Apsley House changes almost continuously during the year. Implementing all these changes in the model as changing boundary conditions would be very laborious, and we will not attempt it in this work. There is, however, an opportunity for simulating some of the variation if we can prove that the influence of a certain factor is dominant over the others. We have, for example, enough evidence to suspect that wind direction is sufficient to explain the different I/O ratios of $PM_{0.02-1}$, even perhaps of $PM_{0.5-2.5}$. The connection between wind and I/O ratio is evident if we look at the wind and concentration data displayed in Figure 5.25. Similarly, we may wonder whether the operation of the heating system is similarly related to the differences in I/O observed between summer and winter. In this Section we will try to explore these relationships computationally.

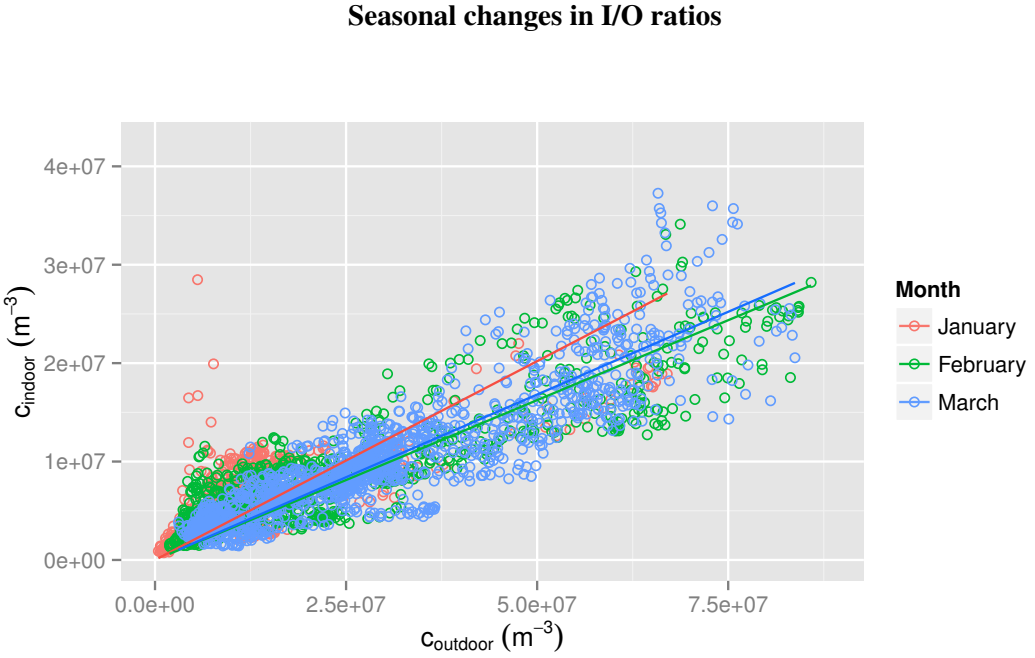

Figure 5.34: Scatter plot of indoor vs. outdoor c of $PM_{0.5-2.5}$ with regression lines. The slope of the lines is an indication of the I/O ratio and it is 0.43 for January, 0.31 for February and 0.32 for March.

One of the clearest patterns visible in Figure 5.25 is the change in I/O ratio between January, February and March. This variation is also reflected in the scatter plot of fine particles (Figure 5.34) and the variation of I/O ratio in Figure 5.35. All these three plots show that the average I/O ratio of $PM_{0.5-2.5}$ was higher in January than in March. That is, outdoor particles infiltrated more efficiently indoors in January. The average for January and March appears in Table 5.5.

Interestingly, the wind rose for these months is also significantly different. In the previous Section we have shown that infiltration, which depends strongly on wind direction and intensity, explains the observed distribution of PM deposition. As a first approach to the periodization of the simulation we decided to simulate the difference between January and March. Both being winter months, all their boundary conditions are identical except for the wind direction, which changes the direction of leakage (Table 5.4).

Table 5.4: Simulation set up and boundary conditions. u is in m/s. W is a wall, O is an outlet, otherwise, boundaries are inlets.

	SW wind - January		**NE wind - March**	
Boundary	c	u	c	u
China inlets	0.0	0.5	0.0	0.5
Waterloo inlets	0.0	0.8	0.0	0.8
Main door gap	1.0	0.2	1.0	0.2
China leaks	1.0	0.01	0.0	O
Waterloo leaks	1.0	0.01	0.0	O
Piccadilly leaks	1.0	0.01	0.0	O
Portico leaks	1.0	0.01	0.0	O
Dinning leaks	0.0	O	1.0	0.01
Drawing leaks	0.0	O	1.0	0.01
Striped	0.0	O	1.0	0.01
Simulation set-up:				
d_p = 2.5 μm				
Simulation: steady state				

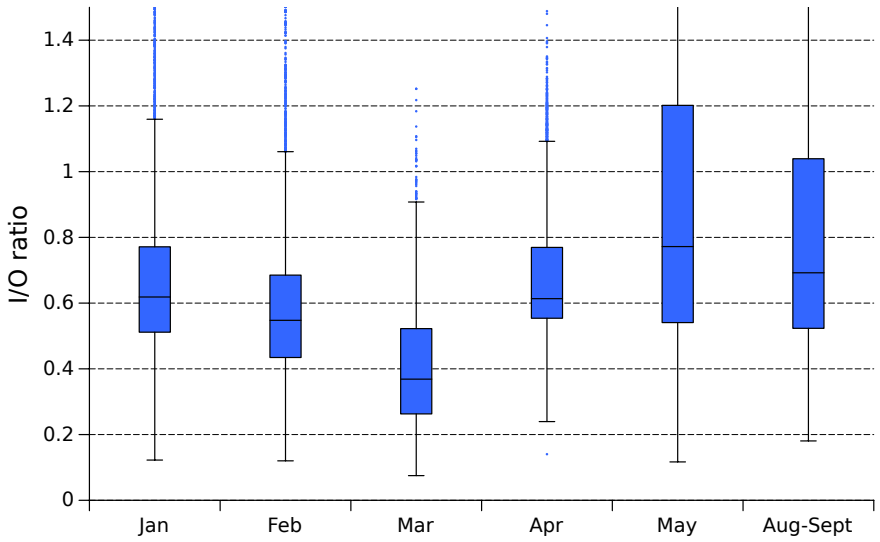

Figure 5.35: Variation of the monthly average of the I/O ratio during the monitoring period.

Figure 5.36 shows the contour of suspended fine PM corresponding to each month. They are notoriously different. We must bear in mind that the change of wind direction does not only determine the walls where infiltration will occur: since every wall has a different number of windows, wind direction also determines the number of sources and the total flux of particles, and the relative location of these sources. As expected, this change in wind direction leads to two different average I/O ratios.

The model estimates of these values, displayed in Table 5.5, correspond quite well with the experimental values. These values were obtained by averaging the I/O ratio calculated in all the points of the room where the monitoring equipment was installed (its location can be seen in the floor plan of Figure 5.14).

Table 5.5: Comparison of experimental ans simulated I/O ratios.

Scenario	Experimental	Simulation
SW wind (January 2013)	0.67±0.37	0.64
NE wind (March 2013)	0.39±0.24	0.34

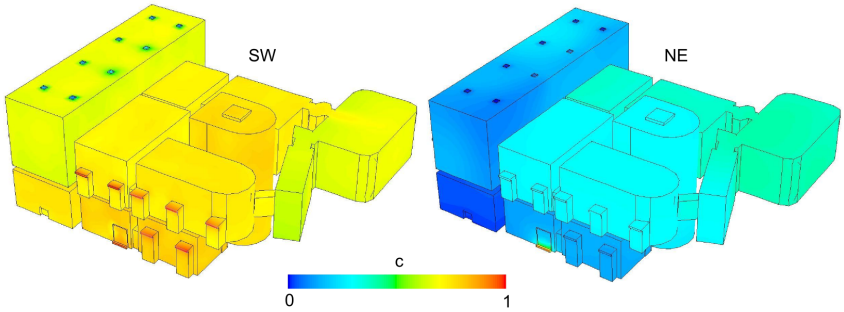

Figure 5.36: Contours of c on the walls of Apsley House for January (a) and March (b) 2013.

This example tells us, firstly, that if a deposition system is controlled by wind and infiltration of outdoor particles, we can simulate it with periods that correspond to changes in wind behaviour. More generally it tells us that if we are able to identify a single factor that has a major influence on PM behaviour (which is what we could call a "defining" factor) in a given system, we can use the variation of this factor to break down long-term simulations in shorter periods.

The effect of heating

The other side of this observation is that, if we want to simulate a building during a certain time period, we must be able to find a defining factor whose variation characterises the time period. The simulation of the effects of heating can be a good counter-example. If we compare the summer with the winter months, we do not observe big changes in the boundary conditions. The obvious difference in ambient temperature does not have an important effect on indoor deposition. The average wind direction does not display fundamental differences with the winter months. If we leave aside the visitor numbers -which for the time being we will consider as if they do not have a big effect on the deposition of fine PM- the only significant parameter left to explain the differences is the operation of the heating system.

At least in theory, heating can promote deposition in two ways: by generating upward convective

flows near the walls, and by promoting thermophoresis [9]. In order to investigate the effects of the temperature boundary conditions we produced simulations of January and June. We used the same simulation set-up summarized in table 5.4, but adding temperature boundary conditions in the locations illustrated in Figure 5.37, with a value of $T = 350$ K. We also used the Energy equation and the buoyancy equations described in Section 3.4.

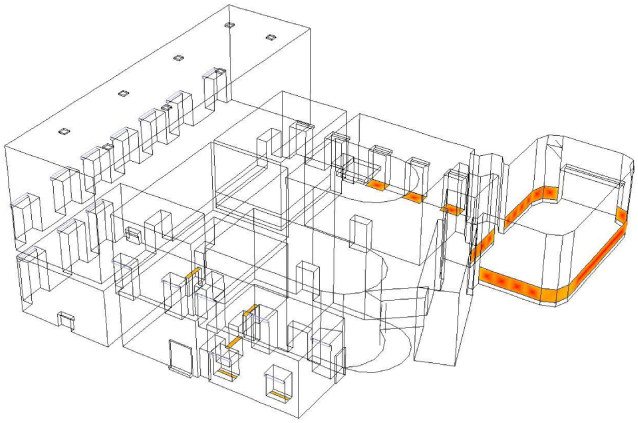

Figure 5.37: Temperature boundary conditions in Apsley House. All the marked boundaries are at $T = 350$ K.

However, these simulations do not show any noticeable difference. The overall deposition velocity, averaged through all the walls of the House, increases by a statistically insignificant amount when heating is on. Even if we compare the effect of deposition exclusively on the Rooms that are heated, we do not see a significant increase. We can conclude that deposition caused by the heating system is a highly localised phenomenon that does not have an important effect on deposition in the building as a whole. Secondly, we must conclude that heating does not suffice to explain the observed differences in J or I/O ratio between January and June 2013.

We perhaps should look for an explanation for these observed differences in the factors that we have not introduced into the model: did the presence of visitors during summer alter the environment in a way that increased the deposition of fine particulate matter? Our data do not allow us to go further than that. It is doubtful that we could validate any shorter scale simulation with the available data. There is another lesson to be learned from these simulations: even though on the month-by-month basis we observe differences that we cannot introduce in the model, the yearly average simulations still offer meaningful results.

5.5.2 Third simulations: scenario exploration

In the previous sections we have compared the simulations with the deposition data collected by English Heritage. This data are useful to explore the differences of deposition between rooms, but does not have enough resolution to appreciate gradients of deposition within single rooms. In this Section we will use own monitored data to validate simulations of independent rooms:

the Plate and China Room and the Waterloo Gallery.

Operation of the Plate and China Room

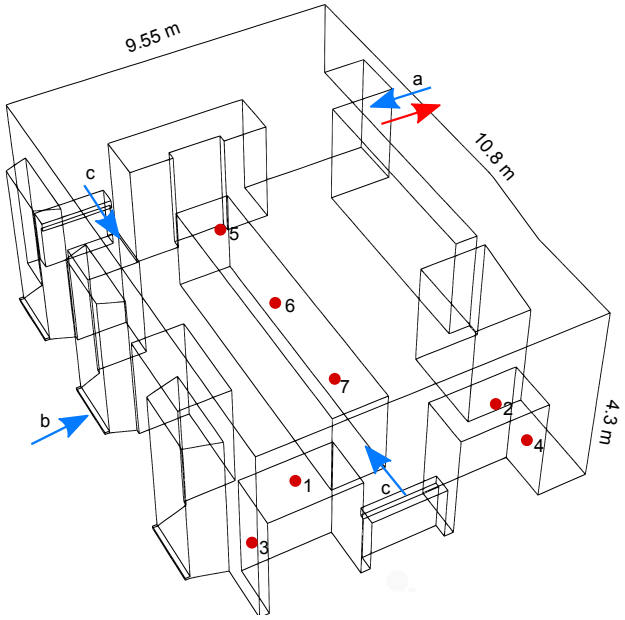

Figure 5.38: Geometry of the Plate and China Room used in the simulations. (a) Is the main door, which can be an inlet or an outlet of air and PM, (b) indicates one of the gaps in the windows, (c) corresponds to the inlet of the heated ventilation. The red dots indicate the location of particle samplers.

The Plate and China Room has two sources of fine particles: the cracks and leaks in the windows and the door that leads to the Main Hall (Figure 5.38). The drivers of air motion and deposition are the air flow from this door and from two electrical heaters equipped with a fan, which are operated manually by the staff in winter months. The windows face the South-west, and therefore the average pressure on them is positive and there is leakage during most of the year. Typically, particles will infiltrate through the window frames, and the door will act as an outlet with a very small air velocity. When the wind direction is inverted, the air flow might be reversed: the door can become an inlet of air, and indoor air could exfiltrate through the cracks. In either case the ventilation system can be on or off. This set of sources leads us to three possible scenarios, summarized in Table 5.6. We simulated each scenario with two particle sizes: 10 and 0.5 μm, which is the smallest size we could compare with our measurements of suspended PM. The results of the simulations are displayed in Figure 5.39

The simulation of the Plate and China room revealed a variety of PM behaviours. We can observe some evident differences in the contours of deposition of Figure 5.39 i.e. the contrast between figures 5.39d and 5.39e. Note that when the ventilation system is off, the deposition

Table 5.6: Simulation set up and boundary conditions. u is in m/s. W is a wall, O is an outlet, otherwise, boundaries are inlets.

	A		**B**		**C**	
Boundary	c	u	c	u	c	u
Main door	0.5	O	0.5	0.1	0.5	O
Ventilation	0.0	W	0.0	0.5	0.0	0.5
Leakage	1.0	0.01	0.0	W	1.0	0.01
Simulation set-up:						
d_p = 10 and 0.5 μm						
Simulation: steady state						

velocity, u_d, is higher on the horizontal areas, and when it is on, u_d is higher on the vertical areas. In fact, when air is at rest, particles seem to deposit on top of the display cases more than when air is in movement. This may appear counter intuitive, given our insistence on the fact that air velocity increases deposition. The cause of this difference can be found in Figures 5.39a and 5.39b. These illustrate that in scenario B, air velocity has a certain vertical component that actually prevents coarse particles from depositing on upward facing horizontal surfaces. This "protective" effect is much higher when particles are small. We also can see that when particles are small, even if the ventilation system is off, there is no difference between horizontal and vertical surfaces (5.39g).

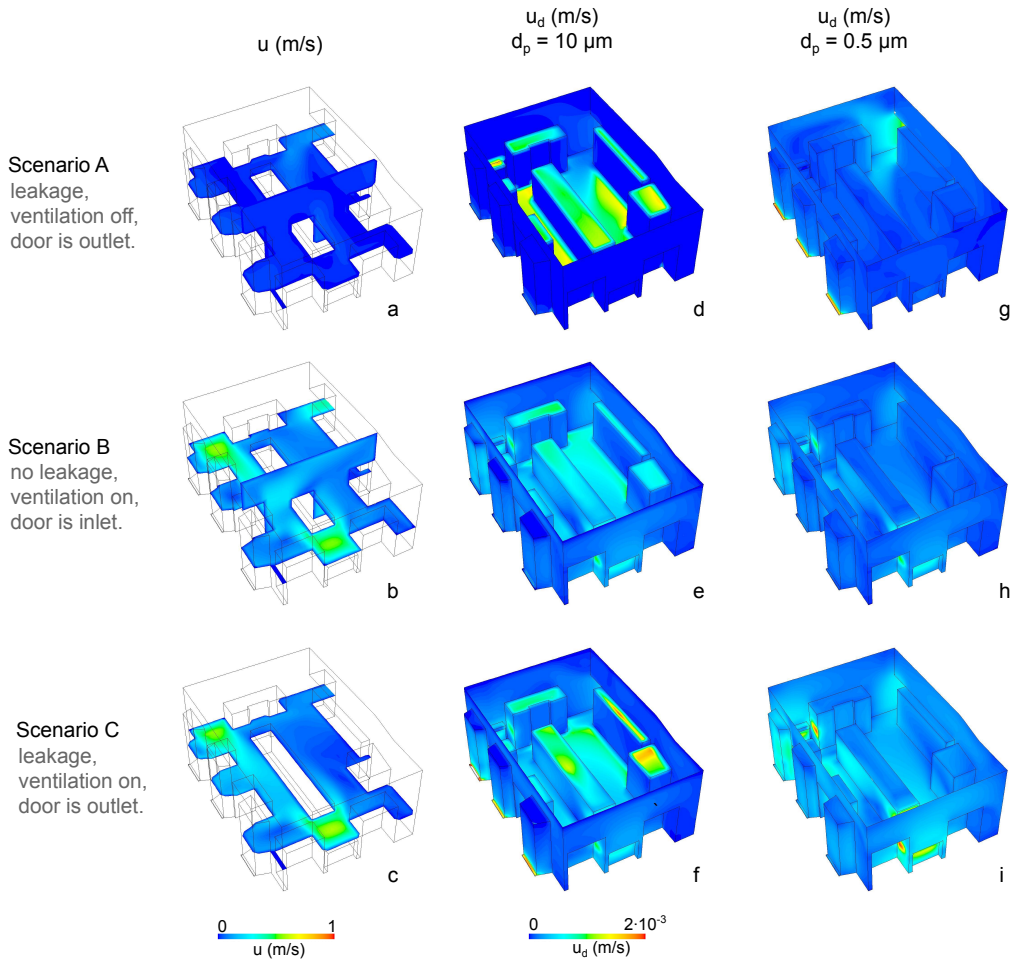

Figure 5.39: Simulated contours of u_d and c in the Plate and China Room under different operation scenarios.

Figure 5.40 helps to underline two important points. The contours of J and c displayed in this Figure correspond with scenario B. Note, firstly, that the contours of c are almost homogeneous. They only display two mild gradients: one near the door (where c is slightly higher) and one near the ventilation inlets (where c is slightly lower). These gradients are computational errors, due to the fact that Pe is small in this room (as we pointed out in Section 5.4.2), and therefore a gradient arises near the boundaries where we have set a fixed value of c. In this case, this error has a small influence in the overall prediction of J, and we display it as an example.

Secondly, observe that the profile of the deposition flux J displays important gradients (and therefore, for the purpose of deposition, the Room is anything but "well mixed"). Naturally, since c is homogeneous, J has the same contour than the profiles of u_d.

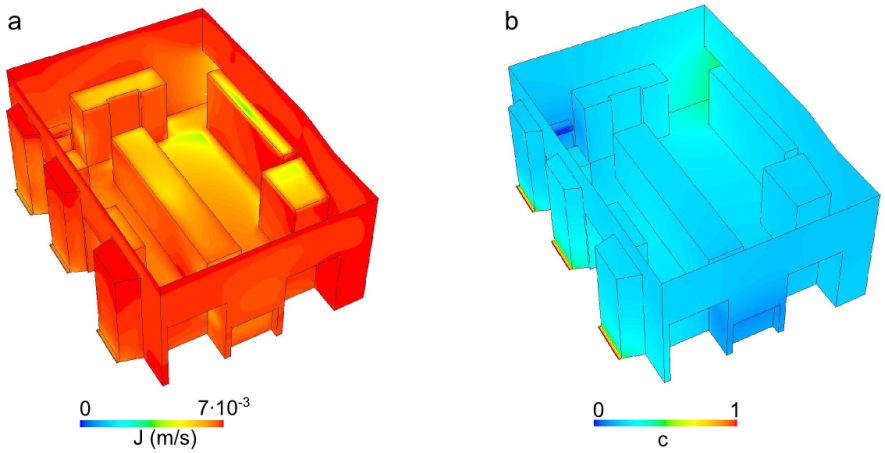

Figure 5.40: Deposition flux J and concentration c in the Plate and China Room.

We compared the simulated patterns of deposition and suspended particle matter with our measurements. Figure 5.41 shows this comparison for scenarios B and C. The deposition velocities have been calculated using Equation 5.2, taking as J the monthly average of our own measurements of deposition in the Plate and China Room and taking as c the indoor values of $PM_{0.5-2.5}$ plotted in Figure 5.19. Rather than an experimental error, the box-plots in Figure 5.41 reflect the variation of c during the monitoring period, which results in a distribution of u_d. The reader will realise that this distribution spans over two orders of magnitude, which is why we have plotted the results in a logarithmic plot.

Unfortunately, most of our sampling points were in locations that do not display important changes of PM deposition between the different scenarios, and we can only produce a meaningful comparison for the locations that show the most extreme variations. Figure 5.41 shows measurements of u_d on locations 1-4, which are represented Figure 5.38. Locations 1 and 2 where on top of display cases, and locations 3 and 4 on the vertical walls of the cases, which translates in marked differences in deposition. Locations 5-7, on the other hand, were on top of the central case, where measurements of deposition didn't show significant differences.

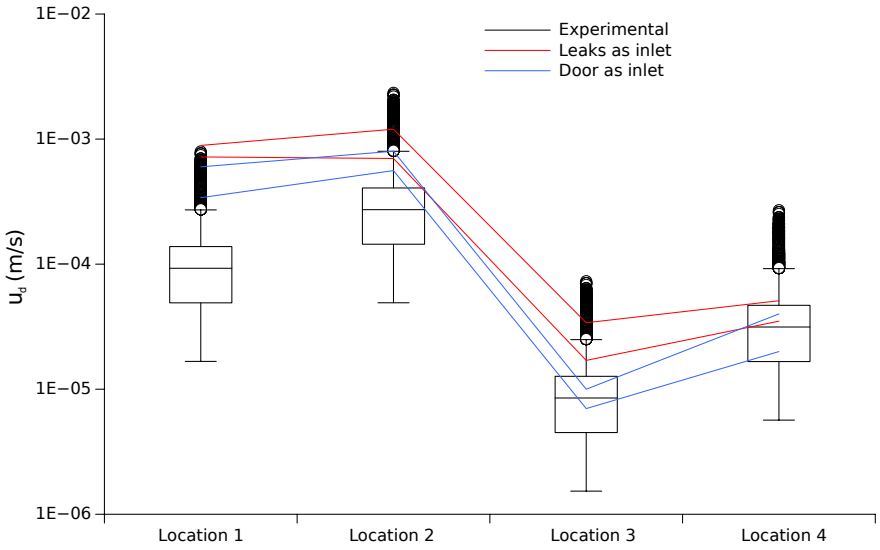

Figure 5.41: Comparison of simulated and experimental deposition velocities, u_d, in four locations in the Plate and China Room, for $PM_{0.5-2.5}$.

The results show, firstly, that we can observe variations in the deposition velocity of several orders of magnitude in a space which is otherwise well mixed, if we only look at gradients of c. This case also demonstrates the importance of the representativeness of the sampling locations. We choose the top of the display cases for obvious reasons: the samples are out of reach and not visible to visitors. However, our locations have proven useless in making a distinction between different operation modes of the Room. In fact, as we have shown, deposition on top of the display cases is largely gravity-led, except when the ventilation is on and for the smaller particles.

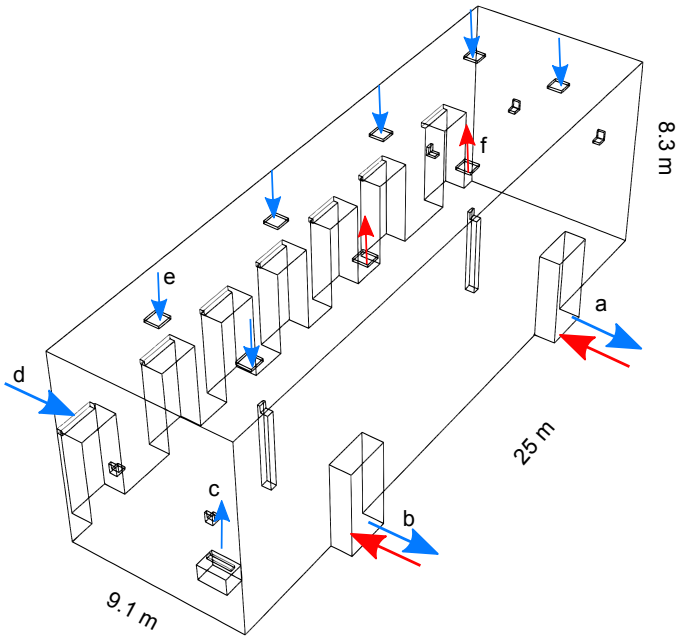

Figure 5.42: Geometry of the Waterloo Gallery used in the simulations. (a) and (b) are the doors that led to the rest of the House, which can be an inlet or an outlet of air and PM, (c) is the inlet of a humidifier, (d) is the gap in one of the windows, (e) is an inlet of the ventilation system and (f) is an outlet of the ventilation system. All inlets painted in blue and all outlets in red.

The Waterloo Gallery is equipped with a ventilation system which has six inlets and two outlets in the ceiling (see Figure 5.42). This ventilation system was switched off for maintenance during our monitoring campaign, and therefore the only drivers of air motion and deposition were the two doors that communicate with the rest of the House. Air flow through these doors is remarkably changeable. During our measurements of wind direction they acted as inlets (as determined with anemometer measurements) but this depends strongly on the combination of open and closed doors in the House, the direction of the wind and the operation of the ventilation system. When the ventilation system is on, the doors are clearly outlets of air. During the experimental period the gallery also contained a humidifier which blew air vertically. The four simulated scenarios shown in Figure 5.43 attempt to reflect some of the possible combinations of sources of particles and drivers of deposition. These scenarios are described in Table 5.7. The results of some of these scenarios coincide with our experimental deposition data.

Table 5.7: Simulation set up and boundary conditions. u is in m/s. W is a wall, O is an outlet, otherwise, boundaries are inlets.

	A		B		C		D	
Boundary	c	u	c	u	c	u	c	u
Doors	0.5	0.05	0.5	0.05	0.5	O	0.5	O
Ventilation	0	W	0	W	0	0.8	0	0.8
Ventilation outlets	0	O	0	O	0	O	0	O
Leakage	1	0.01	1	0.01	1	0.01	1	0.01
Humidifier	0	W	0	0.1	0	W	0	0.1
Simulation set-up:								
$d_p = 1$ μm								
Simulation: steady state								

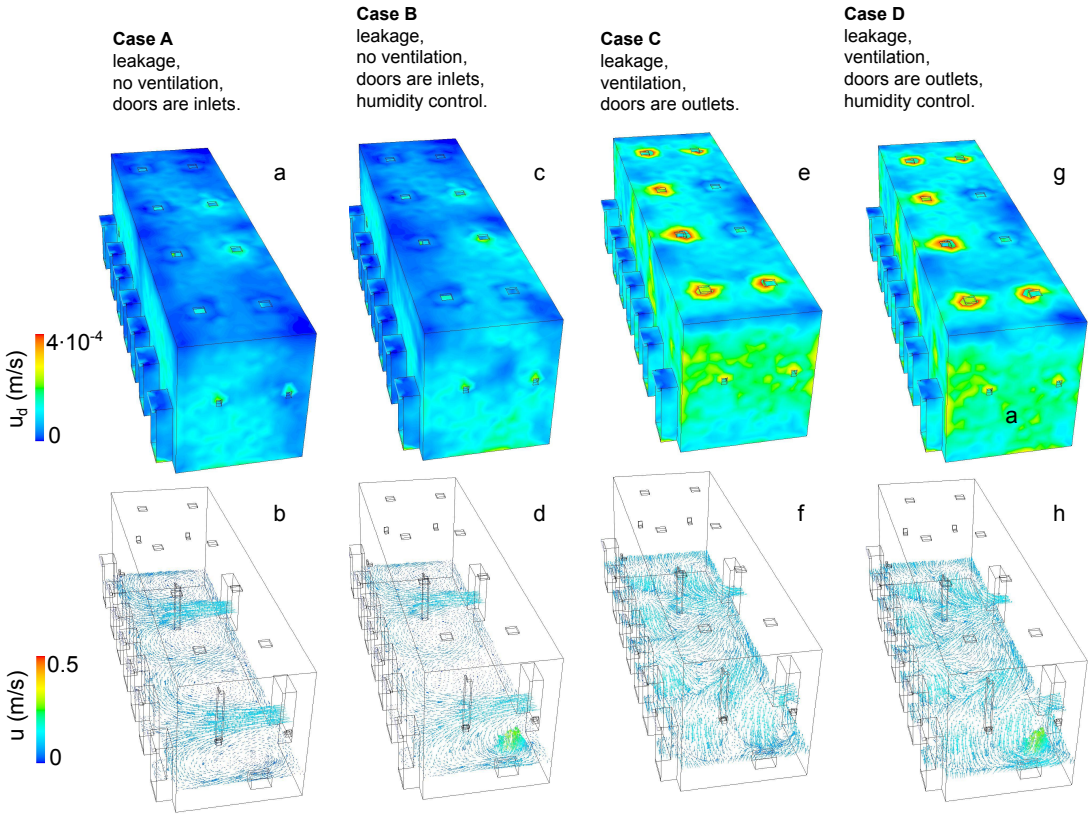

Figure 5.43: Contours of u_d and u in the Waterloo Gallery.

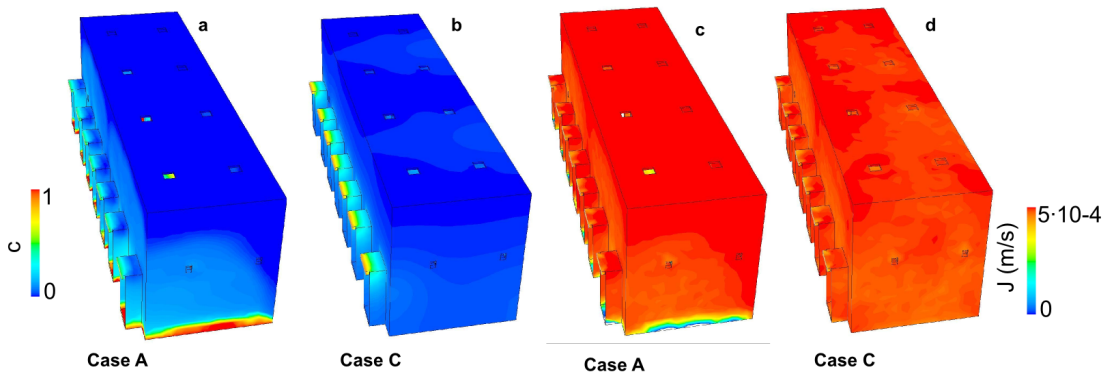

Figure 5.44: Contours of J and c in the Waterloo Gallery.

The simulations predict that the behaviour of PM in the Room changes completely when the ventilation system is in operation. The contours of c (Figure 5.44) show that when the ventilation system is off there is a vertical gradient of concentration due to gravitational settling. Note that the contour of c in Figure 5.44a shows an accumulation of PM near the floor which results in high deposition fluxes (Figure 5.44c). When the ventilation is on, the Room becomes better mixed, and the gradients of c are reduced. The vectors of air velocity (Figure 5.43) demonstrate the radical change in air movement patterns that occurs when the ventilation system is on. Some noteworthy features are the increased velocity near the walls and a higher degree of turbulence. The air flow induces higher deposition velocities, u_d, in the areas close to the inlets and outlets (Figure 5.43e). The presence of the humidifier increases slightly the deposition velocity in the neighbouring wall (the wall labelled as (a) in Figure 5.43g).

The simulations of the Waterloo Gallery provided a relatively good fit with the experimental data, as shown in Figure 5.45. The colour codes of this figure refer to the sampling locations illustrated in the floor plan of the house, Figure 5.14. Some of these sampling locations (6, 7, 8 and 9) were vertical. The model predicted well the large differences between vertical and horizontal surfaces, but failed to predict more subtle differences due to the position of the samplers. For example, it predicts the same deposition in locations 1, 2, and 3, while in reality the measurements show a significant difference. This may be due, once more, to the choice of locations. Many of these samplers were located on top of painting frames, which have different shapes. In view of the results, it is likely that the shape of the painting frame, and the proximity of other frames, altered the air flow and affected the levels of deposition. In other words, the measurements are probably affected by factors other than the spatial distribution of the samplers. However, we can safely conclude that, in general, the model reflects the main trends of the data, and predicts well the order of magnitude of deposition.

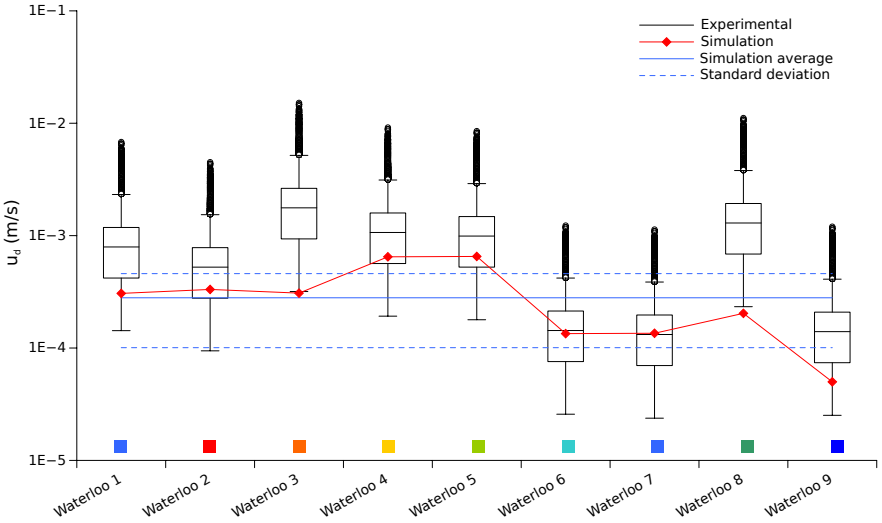

Figure 5.45: Comparison between simulated and experimental deposition velocities of $PM_{0.5-2.5}$, u_d, in several locations in the Waterloo Gallery. Colour codes refer to the labels of the locations in Figure 5.18.

5.5.3 Numerical considerations

We produced two computational meshes for Apsley House, representing the outdoor and indoor environments. We used a cell size of 1 m in the building surface for the outdoor mesh, and a cell size of 0.3 m for the indoor mesh. Both meshes were tetrahedral and unstructured. We also produced meshes for the Waterloo Gallery and the Plate and China Room. The Plate and China Room is the only room sufficiently symmetrical and geometrically simple to allow the use of a structured mesh. Both mesh densities were determined after a grid independence test using the average deposition velocity as a test parameter.Figure 5.46 shows the mesh tests for the different geometries used in this section.

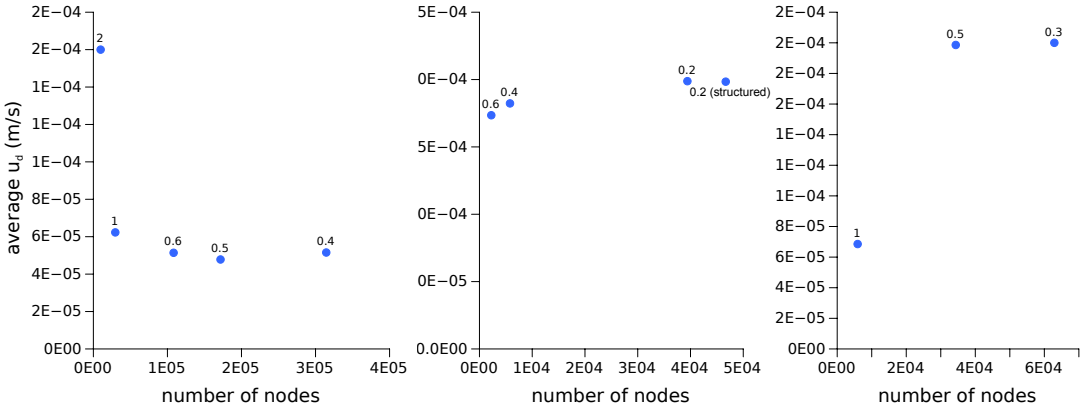

Figure 5.46: Mesh tests for the different meshes used in this section. Left: Apsley House. Centre: Plate and China Room. Right: Waterloo Gallery.

In Section 3.2 we explained that we use a law of the wall to simulate the near-wall turbulence and estimate τ_w. In Fluent this law is applied when $y^+ \geq 12$ [10], which should be the minimum size of our grid (Fluent establishes this limit in terms of their own version of y^+, the wall unit or y^*, but these two quantities are approximately equal in equilibrium turbulent boundary layers). As we also say in Section 3.2 we correct the turbulent viscosity ν_t near the wall using a wall function that spans up to $y^+ = 30$. Another limitation in the mesh size is that the centre of the first cell should be sufficiently far from the concentration boundary layer so that the value of c is representative of the bulk and can be considered uniform [11]. Of course the size of the grid in terms of y^+ depends on the flow regime. Table 5.8 shows that the average y^+ of our computational grids is acceptable in the different simulations reported above.

Table 5.8: Values of y^+ of the first cell near the wall of each grid in various simulations.

Simulation	**average** y^+
Apsley House, SW wind	27.9
Apsley House, NE wind	26.2
Apsley House, SW wind with ventilation	104.2
Apsley House, NE wind with ventilation	69.8
Plate and China Room	49.1
Waterloo Gallery	16.4

5.6 Conclusions

We have seen that predictions of the model coincide with measurements in many different situations. We have used boundary conditions of u, c and T averaged during different periods of time as an input, and we have compared the output of the model with values of c or u_d averaged during the same periods. These periods can be anything from an hour to a year. A steady state simulation can represent any steady situation, no matter how long. Our choice of the time frame should depend not only on the questions we want to ask, but also on the variation of the input or comparison data. We have seen that in order to simulate a large and changeable space such as Apsley House, we need to rely on "defining factors", which are constant over a certain period and determine the behaviour of the house. In our case, wind direction and intensity sufficed to describe changes in the distribution of fine PM concentration and deposition.

We have also seen that each of the three key parameters of deposition (c, u_d and J) has advantages and limitations with respect to the validation of simulations:

c In the absence of indoor sources, c is always a fraction of the outdoor concentration. Therefore, in almost every situation we can use a non-dimensional c which can be interpreted as an I/O ratio. This liberates the simulations from the dependence on the continuously changing outdoor concentration, and makes results more generalisable.

u_d The deposition velocity depends exclusively on the aerodynamic behaviour of the building. Therefore, the use of u_d for contour-plots stresses the forces that bring particles to the walls and also the relative distribution of deposition. However, u_d is difficult to interpret and to relate with a deposition flux.

J The total deposition flux is the ideal output of the model, because it is defined as the number of particles reaching a surface in a certain time. However, to calculate J in these terms it is necessary to have a dimensional value of c. In time-averaged simulations, c is always associated with a standard deviation, which may be very large and adds uncertainty to the prediction.

In this Section we have limited the output of our simulations to these three variables because they can be easily compared with experiments. However, the model allows us to simulate any scenario, and its outputs can take many forms. The need to validate the model with experimental data imposes a constraint on the type of output that we can produce. But if we assess that the model has been sufficiently validated, and that therefore we can rely on it to explore purely speculative scenarios, the number of possible outputs multiplies.

We have centred many of our efforts on using this flexibility to produce results that are useful to practitioners and can support decision making. The next Chapter will discuss some of these results.

References

[1] AQEG. *Fine particulate matter (PM2.5) in the United Kingdom*. London: Defra, 2012.

[2] S. Hope-Evans et al. *London Air Quality Network*. 2014. URL: http://www.londonair.org.uk/LondonAir/Default.aspx (visited on 08/06/2014).

[3] *Air quality guidelines for Europe*. Tech. rep. Copenhagen: World Health Organization Regional Office for Europe, WHO Regional Publications, 2000.

[4] I. Kreis et al. *Essentials of Environmental Epidemiology for Health Protection: A Handbook for Field Professionals*. OUP Oxford, 2013.

[5] E. Heritage. *Wellington Arch: History and Research*. 2014. URL: http://www.english-heritage.org.uk/daysout/properties/wellington-arch/ (visited on 08/06/2014).

[6] H. D et al. "Monitoring dust in historic houses". *Proceeding of Conservation Science*. London: Archetype Publications, 2002.

[7] Y. H. Yoon and P. Brimblecombe. "Cloth-ing as a source of fibres within museums". *Journal of Cultural Heritage* 1:4 (2000), pp. 445–454.

[8] L. Tian et al. "Mathematical model of particle penetration through smooth/rough building envelop leakages". *Building and Environment* 44:6 (2009), pp. 1144–1149.

[9] D. Camuffo. "Wall temperature and the soiling of murals". *Museum Management and Curatorship* 10:4 (1991), pp. 373–383.

[10] FLUENT. *FLUENT 6.3 User's Guide*. Fluent Inc. 2006.

[11] A. C. K. Lai and W. W. Nazaroff. "Modeling indoor particle deposition from turbulent flow onto smooth surfaces". *Journal of Aerosol Science* 31:4 (2000), pp. 463–476.

6
Case Studies (II)

6.1 Introduction

If in the previous Chapter we focused on obtaining data from simulations that we could compare to measurements, in this Chapter we will look at data that provide information of interest to the managers of cultural heritage. In some cases, this data cannot be obtained through any other method than simulation. As a consequence, such simulations often cannot be validated with our current methods. This is the case of the simulations of Apsley House presented in Section 6.2. These simulations are exploratory, and rely on the confidence we built in the model in the previous Sections. In Section 6.3 we will use the model not to predict deposition but to interpret deposition data collected in Hampton Court Palace. This Section will also assess the ability of the model to deal with very coarse dust ($d_p \sim 65\ \mu\mathrm{m}$).

But before introducing these simulations, let us begin by exploring new ways of visualisation of our results. In the previous Sections we have shown many contour plots of the deposition velocity, u_d. This parameter has been very useful to visually express the variation of deposition in space. For example, in Figure 6.1 we readily see that deposition of fine PM is quite homogeneous, while deposition of coarse PM is clearly more important on horizontal surfaces. The main advantage of u_d is that it illustrates neatly the relative importance of the drivers of deposition.

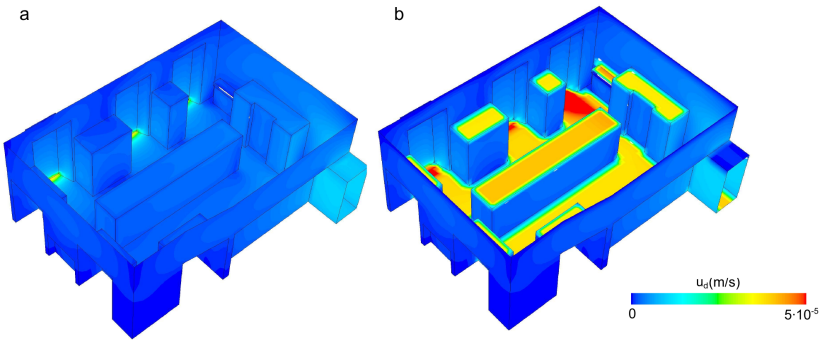

Figure 6.1: Contours of deposition velocity in the Plate and China Room. (a) $d_p = 0.1\mu\mathrm{m}$ and (b) $d_p = 10\mu\mathrm{m}$

However, its magnitude is not so easily understood. u_d has units of velocity, typically $\mathrm{m/s}$ or $\mathrm{cm/h}$. It's not straightforward to relate u_d to a physical process of which we have direct experience in our daily life. One should multiply it by a concentration, c, to obtain a flux, J, which expresses an amount of particles per time and area. But even J is hard to interpret intuitively. A manager of cultural heritage faced with an estimation of J in units of $\mathrm{m^{-2}s^{-1}}$, might rightly wonder *how much* it actually is.

A possible solution is to convert the flux, J, into monthly area coverage. This of course requires not only the output of the model (u_d), but also a reasonable estimate of c for the period of interest and a representative diameter of the particles. To produce Figure 6.2 we have used the two sizes reported in Figure 6.1. Evidently, the profile of area coverage looks rather similar to the deposition velocity of coarse particles, which in this case dominate the area coverage. But note that this depends on the relative concentration of the different size modes. The more size bins are used, the better the prediction of area coverage will be.

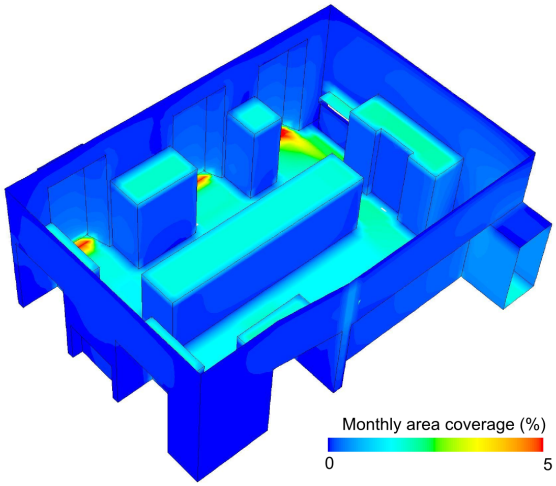

Figure 6.2: Contours of monthly area coverage in the Plate and China Room.

We can relate the percentages of area coverage expressed in Figure 6.2 with the daily practice of heritage institutions. Area coverage is a commonly measured parameter, and universally understood. But we can still go one step further and convert these values to a scale that can be measured even more easily: the time required to reach visible coverage. In Figure 6.2 we show the time to reach 5% area coverage, which we could consider to be the typical threshold of unacceptable deposition (see Section 7.2.1.) The values represented in Figure 6.3 can be directly related to the cleaning schedule of institutions.

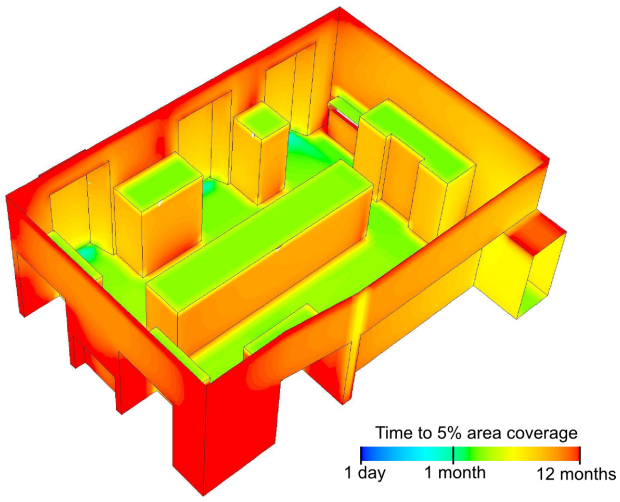

Figure 6.3: Time required to reach 5% area coverage.

The reader will realise that the contours in Figure 6.3 are coloured following a logarithmic

gradient. This is because some areas (close to the leaks in the windows, for example) will reach unacceptable levels of deposition in some days, while others (such as the wall close to the ceiling) will reach the same level after many years. This plot shows, once more, that even if the concentration of suspended particles is homogeneous, deposition flluxes can vary within orders of magnitude in a very small space. In other words, a "well-mixed" approach is only justifiable if our interest is in concentration. The spatial distribution of deposition is characteristically inhomogeneous.

6.2 Investigative simulations of Apsley House

The results discussed in the last Sections give us enough confidence in the accuracy of the predictions to simulate purely speculative scenarios. We will simulate some scenarios for which we may have no direct experimental data. These simulations serve a double purpose. On the one hand they illustrate the potential of the model as an exploration tool. On the other hand, they provide some insight on the behaviour of PM that can be of use to the managers of Apsley House.

Operation of the House

Unfortunately, the ventilation system was off during the monitoring period and therefore our data cannot reflect the consequences of its operation. In this Section we explore how the scenarios simulated in Section 5.5.1 (i.e. wind in the S-W or N-E directions) would change if the ventilation system was on. In other words, we simulate again January and March 2013, but in the hypothetical scenario that the ventilation system was in operation. We use the same boundary conditions and model set-up detailed in Table 5.4, but we add air velocity inlets in the ventilation inlets indicated in Figure 5.31. We set a velocity of $0.8\ \mathrm{m/s}$ in all the ventilation inlets.

The operation of the ventilation system affects both the concentration of particles and the deposition velocities. Accordingly this simulation offers an interesting comparison between the consequences of a simultaneous change in c and u_d. Intuitively, we can predict two contradictory effects: we know that increased velocity will imply increased u_d and thus more deposition, but we can also imagine that the ventilation system will create a positive pressure inside the Waterloo Gallery, thus preventing the ingress of PM migrating from other areas of the House, resulting in a reduction of c in this gallery. The simulated deposition profiles can be seen in Figure 6.4

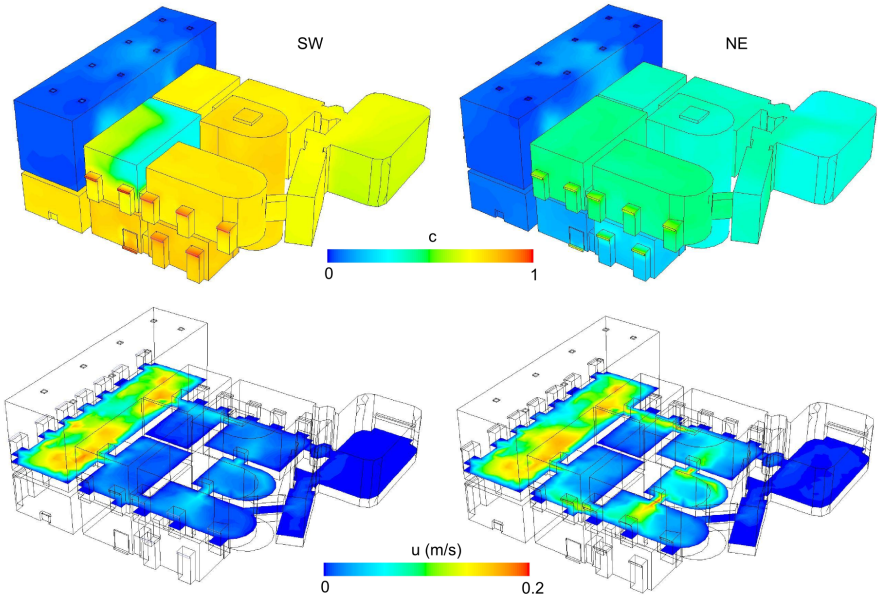

Figure 6.4: Simulated contours of concentration and air velocity in Apsley House when the ventilation system is on and the wind direction is S-W or N-E.

In the contours of Figure 6.4 we can readily see that the ventilation system cleans the Waterloo Gallery of particles in both wind scenarios. However, if we look at the total deposition flux, J, in the S-W scenario as reported in Figure 6.5 we realise that the reduction in deposition caused by ventilation is not as dramatic. Indeed, ventilation has cleaned the room of particles, but has also increased the ability of the remaining particles to deposit. These two mechanisms lead only to a mild reduction of deposition. There is a balance to be found, and the parameter to tune is the air flow of the ventilation system (which, in fact, is not changeable in the current system). We have assumed a velocity of 0.8 $\mathrm{m/s}$ in the ventilation inlets, but we were unable to measure the actual velocity. It might well be lower; in which case the ventilation system would further reduce deposition.

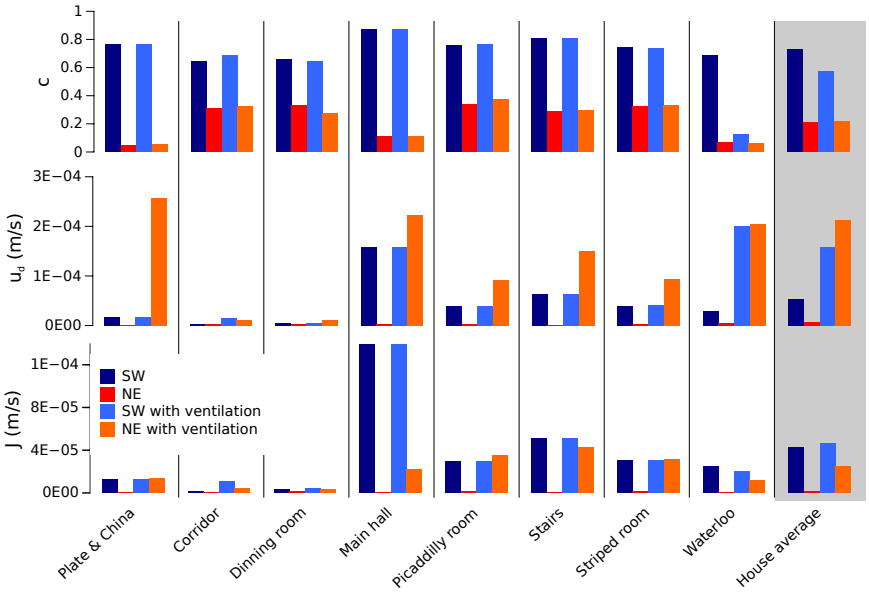

Figure 6.5: Summary of the average values in every room of J, c and u_d in different operating modes of Apsley House.

The changes in c, u_d and J are summarized in Figure 6.5, which reflects many interesting phenomena. We can see that generally, even if the concentration is very high, we will detect low values of deposition flux if u_d is low. This is the case, for example, of the Plate and China Room with SW wind, or the corridor, in any configuration. Figure 6.5 also includes the average behaviour of the House. We can see that the amount of particles inside the House depends on wind direction and changes very little with ventilation, however, ventilation alters u_d and consequently it also affects J. Based on these results, it seems that the configuration with minimum deposition is NE wind with no forced ventilation.

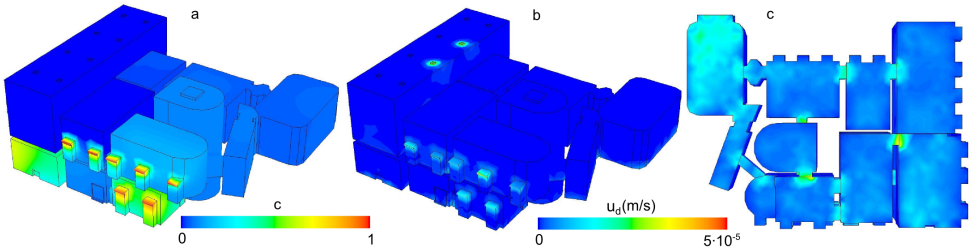

Figure 6.6: Simulated contours of concentration and deposition velocity in Apsley House when the ventilation system is on, wind is SW, and all the internal doors are closed.

We also simulated the S-W wind scenario, with ventilation, in the case that the internal doors of the House are closed. In this case, the air flow is reduced, but the exchange of PM between rooms is maintained by leakage through the doors. The internal doors are specially leaky, with

gaps in all the perimeter, which we represented in the model as a single gap under each door. In such case the deposition velocity is reduced to a minimum. As we can see in Figure 6.6c, deposition is only visible in the floor, where it is led by gravitational settling. The isolation of the Waterloo Gallery in combination with the cleaning effect of the ventilation system result in very low values of c in this space.

The representativeness of sampling points

Our own choice of sampling locations is an example of the problem of blind choice: the deposition measurements in the Plate and China Room do not reflect the variability we are interested in. In Section 5.5.2 it would have been interesting to appreciate experimentally the spatial variation of deposition caused by the ventilation system of the Plate and China room, but our sampling locations, most of them on top of display cases, were not sensitive to these changes. They did not reflect well the variation that existed in the room.

Conversely, if we want an indication of the "average" deposition in a room, we must be careful to select representative locations, that are not affected by local drivers of deposition (which would lead to an overestimation) or that are excessively protected. Monitoring in an excessively protected area such the back of a display case or on a very exposed area, near an air source, can provide a wrong assessment of deposition. The model can aid the choice of representative locations. Figure 6.7 compares the simulated deposition rates in the sampling locations used by us and by English Heritage with the simulated yearly averages of deposition in the rooms and in the whole house. We can see clearly that some locations (for example, Waterloo 1-3) are closer to the average, and therefore more appropriate if we are interested in finding a representative value of the average deposition.

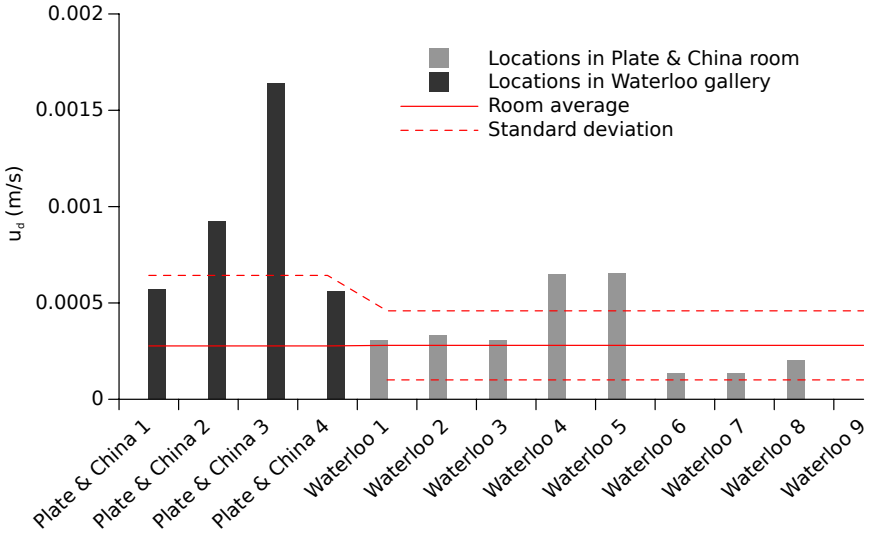

Figure 6.7: Comparison of simulated deposition velocities in different common sampling locations with the average value in the room where particles are sampled.

The sampling points that appear in Figure 6.7 are in the following locations: Plate and China 1, 2, 3, and 4 are on top of display cases. Waterloo 1 and 2 are on top of the candelabra in the centre of the room, while Waterloo 3-9 are on top of painting frames.

Relative importance of the main door

During the time of the experiment the gap under the main door was the largest single source of particles into the House. Measurements revealed a high concentration near the gap ($\sim$ 10.000 $\mathrm{cm}^{-}3$) which decreased with distance from the door. Beyond the main hall, the I/O ratio approaches the average and it is impossible to distinguish experimentally whether particles are originated by this source or by a combination of sources elsewhere in the House. CFD can help to identify how influential a given source is. To demonstrate this concept, we investigated the influence of the main door gap in isolation by simulating the dynamic evolution of c once the gap is open. In this simulation, d_p = 1 µm, $c_{inlet} = 1$, $u_{inlet} = 0.5$ m/s.

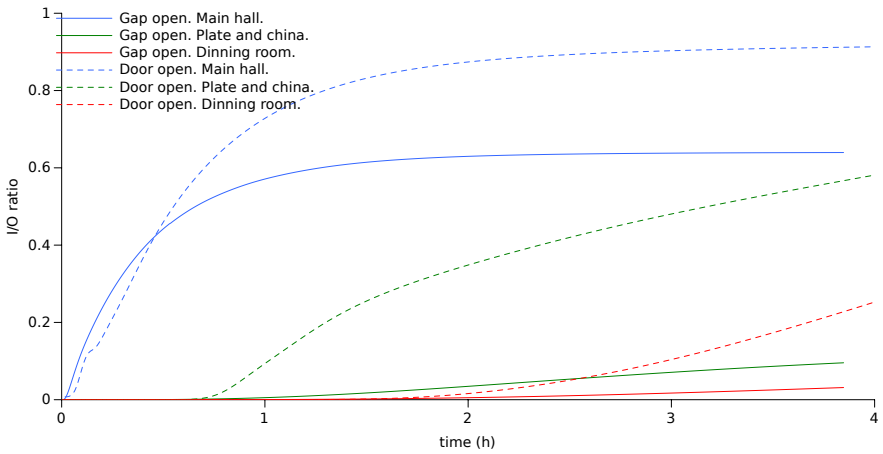

Figure 6.8: Simulated evolution of c in different locations of Apsley House when the main door is left open and in the case that air flows continuously from the gap under the main door.

Figure 6.8 shows how the concentration in different rooms increases when particles start to penetrate through the gap under the main door. After approximately 1 h a steady state is reached in the main hall. When the concentration ceases to evolve, the concentration in the rooms further away from the source is still very low (I/O $\sim$ 0.1). This implies that all the particles introduced into the House through the door gap deposit in the main hall, and do not reach the upper floor. By closing this gap, we would reduce deposition significantly in the rooms close to the main hall.

If we leave the main door completely open, the situation is different. Now we do not only have a source of particles, but also an important driver of deposition (i.e. the draft through the open door). In this case a steady state in the main hall is reached in a similar time and with a higher

value of c. However, particles can travel further into the House without depositing, and after $\sim$3 h we even detect an increase in c in the Dining Room, on the second floor. This simulation may serve as an example of the potential of the model to study different phenomena in isolation.

6.3 Coarse dust in the Hampton Court Palace

Figure 6.9: View of the Great Watching Chamber of the Hampton Court Palace.

This Section explains the results obtained from the simulations of PM deposition in the Great Watching Chamber (Figure 6.9) in the Hampton Court Palace, managed by Historic Royal Palaces (HRP). The Great Watching Chamber is the second largest space in the Hampton Court Palace, and stores a valuable collection of historical tapestries. Figure 6.10 shows an schematic floor plan of the Great Watching Chamber and surrounding rooms.

This case study was motivated by a very specific research question. In the framework of a research project aimed at establishing a scientifically based conservation strategy, HRP had carried out a year-long dust monitoring campaign at the location of the tapestries in the Great Watching Chamber. The monitoring campaign provided a very rich dataset of fortnightly area coverage with a high spatial resolution, with many sampling points at each tapestry. However, this detailed data presented many challenges to interpretation. It was suspected that most of the dust was carried in the building by visitors, but beyond this, it seemed difficult to extract more insights from the data.

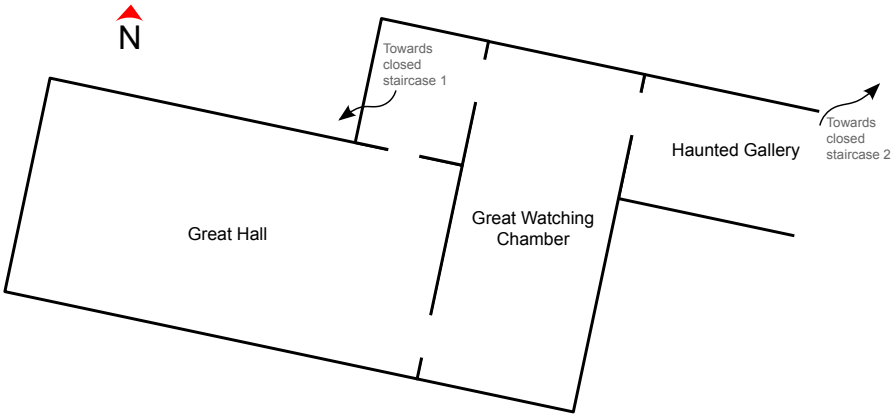

Figure 6.10: Schematic view of the Great Watching Chamber and the surrounding spaces.

We decided to use the model to investigate the causes of the observed deposition, and, if possible, to investigate mitigation strategies. In addition, this case study would also be useful for testing the performance of the model with coarse dust.

We developed this case study in three different stages. The first Section includes an experimental assessment of the environment, which will determine the applicability of the model and provide the necessary input data. The next Section discusses the simulation of the causes of deposition. The purpose of this Section is to identify whether CFD can reproduce the experimentally observed deposition and link it to potential causes (visitors, ventilation, heating, air movement). The third and last Section describes the simulations of various scenarios, involving different visitor numbers and locations, different air movement patterns, and different physical arrangements of the doors of the Chamber. The purpose of the third Section is to identify how deposition depends on different factors.

6.3.1 Data collection

As in the previous cases, we collected experimental data to define the boundary conditions. We compared the simulations with deposition data collected by Historic Royal Palaces.

Deposition data

The deposition data were collected from January 2012 to January 2013 using a system developed by HRP. The set-up consisted of horizontal glass slides, exposed horizontally at three different heights (0.65, 1.8 and 3 m) at short distance from the tapestries. There were 126 sampling points distributed around the four walls of the room. In 15 day intervals a sample was retrieved and particles were counted with an optical microscope following the procedure described in [1] and Appendix 1. The total count and the area covered by particles were recorded. Figure 6.11 shows the contour of deposition on the tapestries in some selected weeks that illustrate the main features of the data.

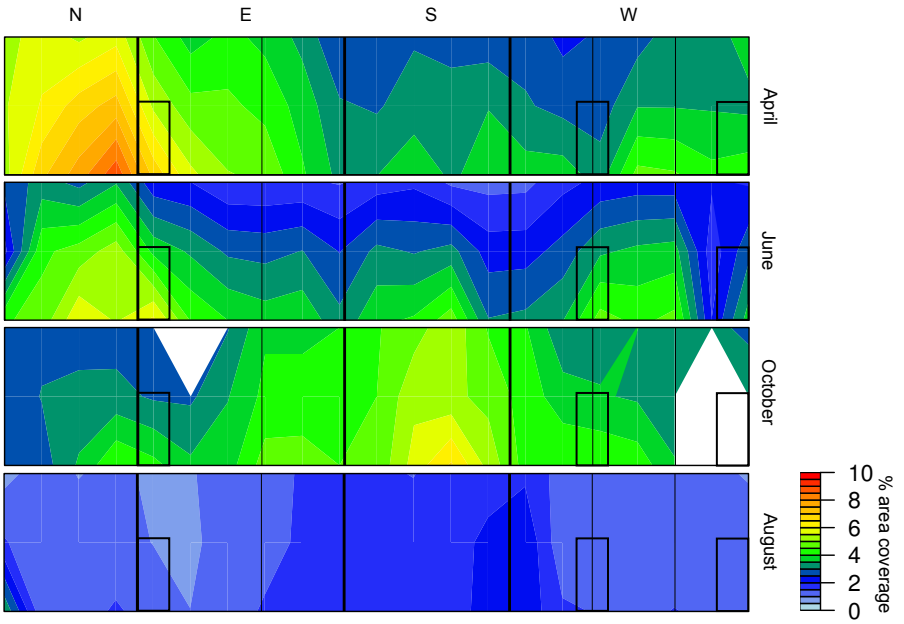

Figure 6.11: Experimental deposition data (area coverage) from different weeks (always first two weeks of each month) in the tapestries of the Great Watching Chamber. These profiles correspond to the four walls of the Chamber, which have been unfolded. Each wall is identified as North, East, South or West. The smaller rectangles represent the position of the three doors that are open.

Some noteworthy features are the hotspot of deposition which appears in several months between the North and East walls. This hotspot coincides with a door. We can also see that there is some stratification, with more deposition in the lower part of the tapestries. The overall deposition is reduced in the winter months due to the low visitor numbers.

We used this data to obtain an average size of the particles. The collected data are available in two units: area coverage, x, (in %) and number by area, N (in cm^{-2}). Note that x is defined as $x = (A_{particles}/A_{sample}) \times 100$, i.e. the area of the particles divided by the sampling area. And similarly, N is defined as $N = n_{particles}/A_{sample}$, i.e., it is the number of particles found in the sampling area. Therefore, if we divide x by N, we obtain the area of a single particle, a_p, and therefore its diameter:

$$a_p = \frac{x}{N} \;\; ; \;\; d_p = 2\sqrt{\frac{a_p}{\pi}} \tag{6.1}$$

This calculation gives a mean diameter of 64.7$\pm$7.0 $\mu\mathrm{m}$, with a surprisingly low standard deviation. If we perform the same calculation for each bi-weekly set of data, we observe that the average diameter of the deposited particles changes slightly but significantly during the year (Figure 6.12). The average diameter is apparently larger during the winter months. A possible explanation is that there may be more large fibres emitted from clothing in winter. Heating in winter reduces the relative humidity indoors, and this encourages the release of fibres and dust

from clothing [2]. However, it is difficult to be more precise with the available information. What is certain is that the problem of deposition in the Hampton Court tapestries is clearly related to very coarse PM, i.e. PM_{50-100}. Here we will use the term "dust" to refer to these particles, and we will characterise them with an average diameter $d_p = 65\mu\mathrm{m}$

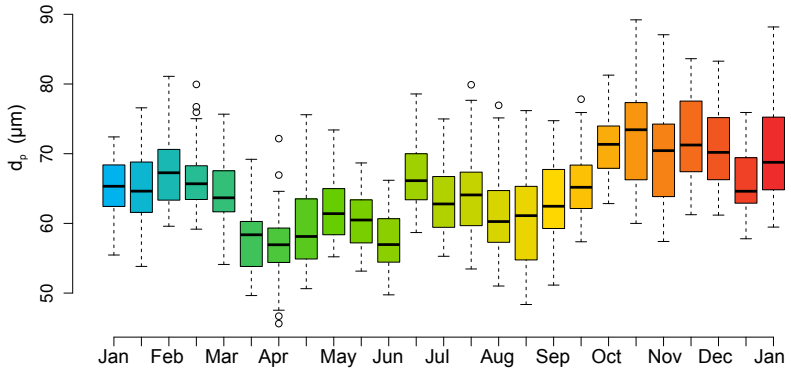

Figure 6.12: Evolution of the average particle diameter of the deposited particles during the monitoring campaign. This data are obtained by operating with all the area and number measurements. The experimental uncertainty and the spatial variation are reflected in the box-plots, which show the first quartile (box) and the maximum and minimum values (whiskers.)

Inlets and outlets

We carried out short measurements of air velocity in all the doors of the Great Watching Chamber. Due the limited time available to measure without affecting the visitors, we were able to measure only for 5 min. in each doorway. However, these measurements provide some interesting insights.

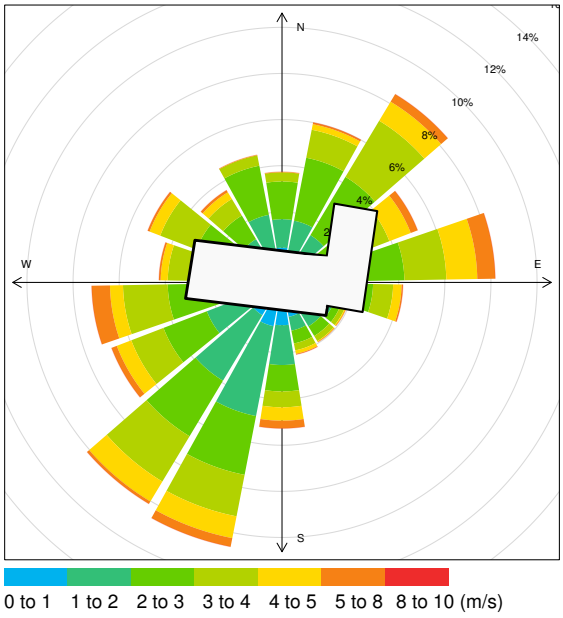

Figure 6.13: Average outdoor wind direction and velocity during 2012 and 2013. The outline of the Great Hall and the Great Watching Chamber (the small room on the right) is superimposed to the wind rose. Values obtained from the Kew weather station, as described in Appendix 1.

All the doors can act as inlets and outlets of air, most predominantly in these two combinations: air enters the room either through the West doors, and leaves through the East door (W-E), or it enters through the East door and leaves through both West doors (E-W). The predominant South-West and North-East wind directions (Figure 6.13), favour these two recirculation scenarios. But because of the arrangement of the building, and the proximity to doors that communicate with the outdoor environment, air will most commonly travel from the Haunted Gallery towards the Great Hall.

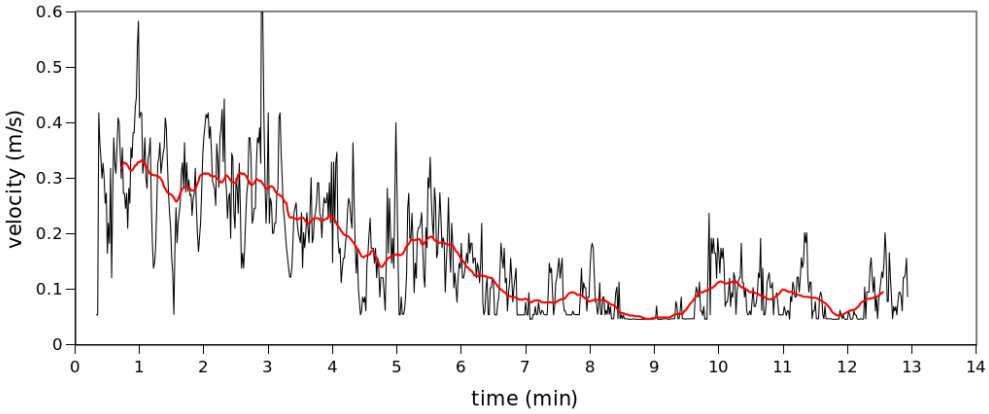

Figure 6.14: Variation of air velocity in the door between the Great Hall and the Great Watching Chamber. The outer doors of the Great Hall were shut in the 5-6 minute, and this causes the air flow to decrease quickly.

The intensity of the draft depends strongly on the outdoor conditions. Figure 6.14 shows how air velocity in the door of the Great Hall changes when the Hall main doors are open or closed. Up to minute 5, the door of the Great Hall was open to the environment, and we can see how air penetrates into the room with a velocity of 0.5 $\mathrm{m/s}$. After 5 min., we closed the door and curtains of the Great Hall, and in less than a minute the velocity was reduced to <0.2 $\mathrm{m/s}$.

Heating and lighting

Heating in the room has a mild effect on the overall temperature and velocity profiles (Figure 6.15). The temperature of the floor heating panels is about 50 $^{\circ}\mathrm{C}$, but natural convection generates very small air velocities (only around 5 $\mathrm{cm/s}$ at 10 cm distance from the heating panel) and the distance from the wall prevents the formation of strong turbulence (this is further explored in Section 6.3.3). The candelabra located in the vicinity of the tapestries produce a gradient of temperature of around 5 $^{\circ}\mathrm{C}$ (Figure 6.16), which may alter the deposition of fine particles locally, but probably does not have an important effect on the deposition of coarse dust (if it does, it is not appreciable in the data.)

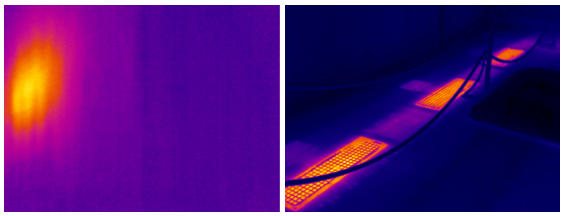

Figure 6.15: Left: thermal image of the impact of a light bulb of the candelabra on a tapestry. The temperature difference between the coldest and the warmest points is 5 ^{o}C. Right: Thermal image of the floor heating.

Leakage

We investigated the presence of leaks in the windows using a thermal camera, following the same procedure as outlined in Section 5.4.1. However, since the windows are located near the ceiling these images were taken from a considerable distance and it was impossible to test if the colder areas correspond to actual gaps or are simply indicating the presence of thermal bridges. There seems to be potential for air infiltration in all the windows, but given the absence of outdoor pollutants, this may not be a significant issue. Cracks and leaks are therefore most likely not a source of particulate matter.

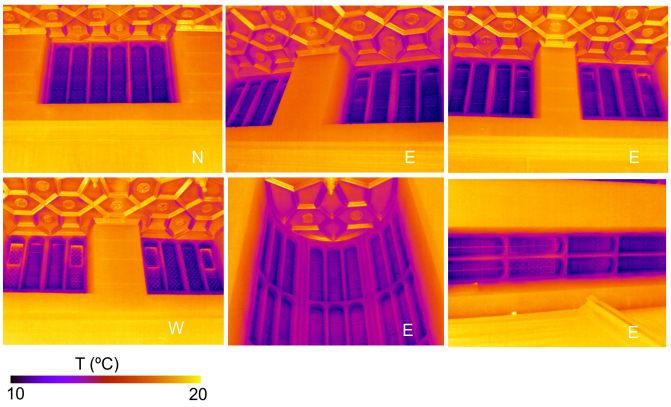

Figure 6.16: Thermal images of the windows in the Great Watching Chamber. The letters on the images indicates the wall in which they are located.

Fine particulate matter

Measurements of fine particulate matter (0.02-1 μm) showed concentrations smaller than those we have measured in some of the cleanest spaces in Central London, of around 500-1500 cm^{-3}. These values are two orders of magnitude smaller than those measured, for example, in the Wellington Arch (Section 5.3). Most interestingly, the measurements revealed that the concentration in the room is generally homogeneous. There is only a small gradient from the Great Hall towards the north end of the room. The concentration of particles increases steadily once we leave the room and walk downstairs, either from the Haunted Gallery or through the west staircase (See schematic floor plan in Figure 6.10). This seems to indicate important infiltration of air through the staircases. The concentrations of fine particles are almost double at the bottom of both staircases, probably due to the proximity to the kitchen and the fireplace.

6.3.2 Applicability of the model

The simulation of the Great Watching Chamber presents two challenges to the model. Firstly, the lack of forced ventilation means that the only driver of air movement is the natural ventilation of the building. We should expect low air velocities and moderate turbulence (i.e. low values

of u and u_{rms}). Given the large diameter of the particles, we can also expect high values of the relaxation time τ.

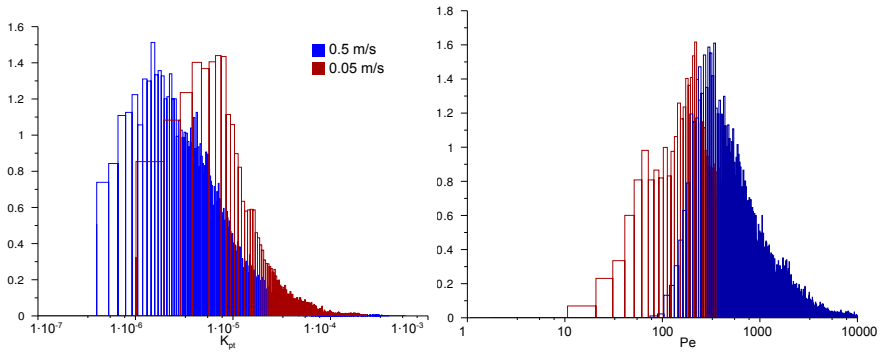

Figure 6.17: Histogram of K_{pt} and Pe in the Great Watching Chamber under two possible velocity regimes in the doors.

Figure 6.17 shows histograms of K_{pt} and Pe in the system in two scenarios: an air draft in the West doors of 0.05 and 0.5 $\mathrm{m/s}$, which can be taken as maximum and minimum estimates, based on our measurements. We can see that, while neither of these values reaches the threshold (Pe is always larger than 1 and K_{pt} always smaller), this simulation is closer to the limits of applicability of the model than any of the previous cases.

In principle, we are operating within safe values of the applicability criteria. But if in some of the scenarios any of this values exceeds its limits, we should expect two effects:

1. Due to the low Pe, we may see gradients of c arise close to the boundaries where we set Dirichlet boundary conditions (as we discussed in Section 3.3.4 and experienced in Section 5.5.2).

2. Due to the high values of K_{pt}, we should expect an overestimation of the diffusivity of dust in areas of low turbulence.

We should be aware of these effects when interpreting the results. Simply, the concentration very close to the doors will not be a reliable estimate. Regarding the overestimation of diffusivity, it will mean that coarse particles may behave as smaller particles. This is something we should be able to see in the comparison with the experimental results.

6.3.3 Simulation of the causes of deposition

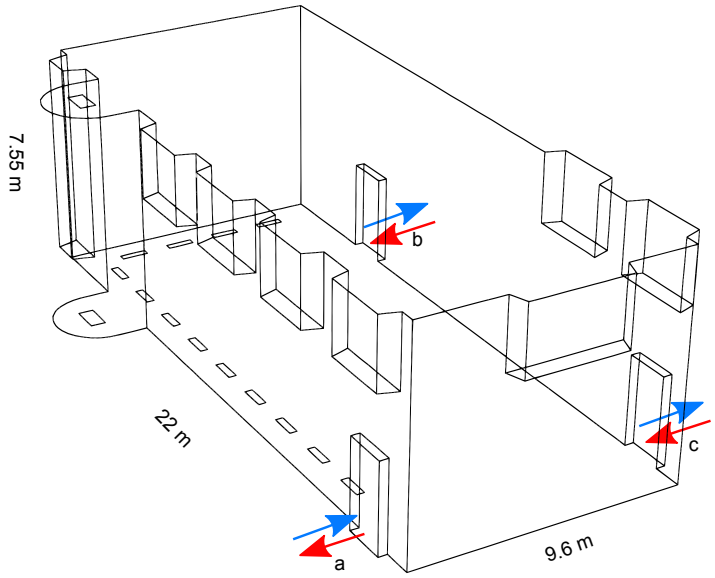

Figure 6.18: Mesh of the Great Watching Chamber used in the simulations. (a), (b) and (c) are the doors, which can be inlets or outlets of air.

This Section describes several simulations that attempt to describe the observed levels of deposition. Each simulation is based a different hypothesis about the source of particulate matter. Figure 6.18 shows the geometry of the grid we have used in the simulations, with the relevant boundaries. We have produced an unstructured grid with cells of 0.3 m, as determined with a grid independence test. Some of the spatial features, such as the semi-circular window, prevent the use of an structured grid. Generally, we will use the two most likely wind directions (E-W and W-E), as described by 6.19.

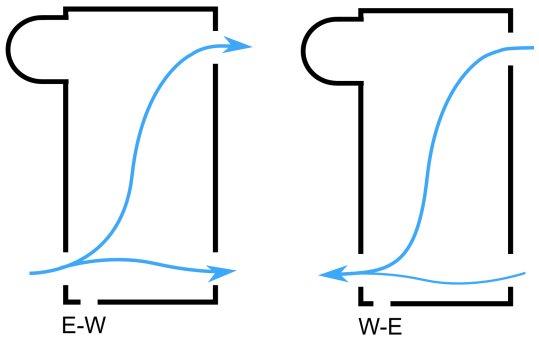

Figure 6.19: Draft direction scenarios used in the simulations.

Air flow simulation

Simulations of the air flow provide a general understanding of the patterns of air movement in the Great Watching Chamber. The air flow simulations presented in this Section focus exclusively on air movement, and particles will be included in a later stage. As mentioned in the previous section, our understanding of the system is that the most common flow direction will be from East to West (E-W) rather than West to East (W-E). However, in order to verify this hypothesis we would need either longer term air movement data or larger scale simulations of the building, which would fall outside the scope of this case study. For the following simulations we assumed that air can flow in both directions, and that eventual direction shifts exist.

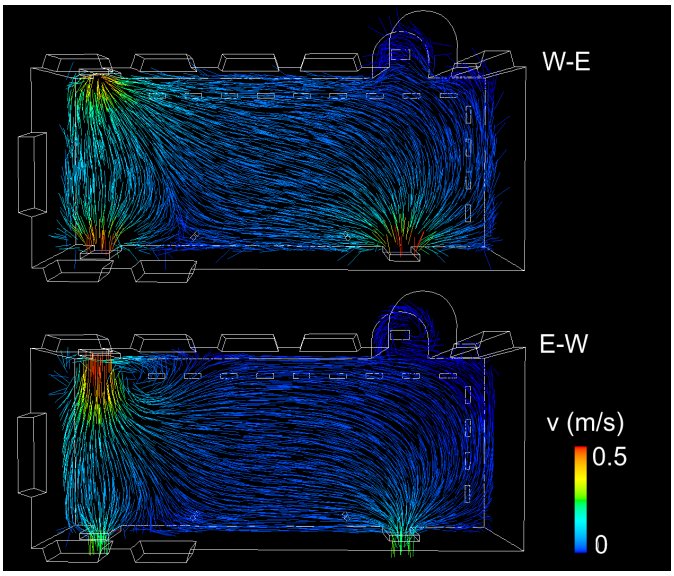

Figure 6.20: Air streamlines coloured by air velocity. The figure illustrates the two most common ventilation scenarios: draft direction from East to West and from West to East

Figure 6.20 shows air streamlines for two simulations taking into account the two most frequent flow directions. Note that there are only a few differences between the E-W and W-E scenarios. Even though the direction of the draft is opposite, the general features of the flow are similar. The stronger draft is always parallel to the North wall (and as we shall see later, this has an effect on deposition on this wall). The steadiest air is always in the South-East corner and the semi-circular window area. The overall flow in the room always follows a more or less diagonal route between the Great Hall and the Haunted Gallery.

Note as well that when a door acts as an outlet air flow tends to be parallel to the surrounding walls. This feature of the flow has interesting consequences to PM behaviour. We will relate this effect to deposition in the next Sections.

Heating as a driver of deposition

The simulations did not indicate heating as an important driver of particulate deposition. Due to its placement near the tapestries, the underfloor heating has the potential to create a vertical hot air flow. This would be a classical example of deposition caused by convection and thermophoresis from hot air to a cold wall [3]. However, the low heat flux combined with a short -but significant- distance from the walls, translates into a very mild deposition effect. This is further reduced by the large average size of the particles, which implies that they tend not to follow upward vertical flows. Based on the simulations, the heating system can be safely discarded as a possible instigator of deposition.

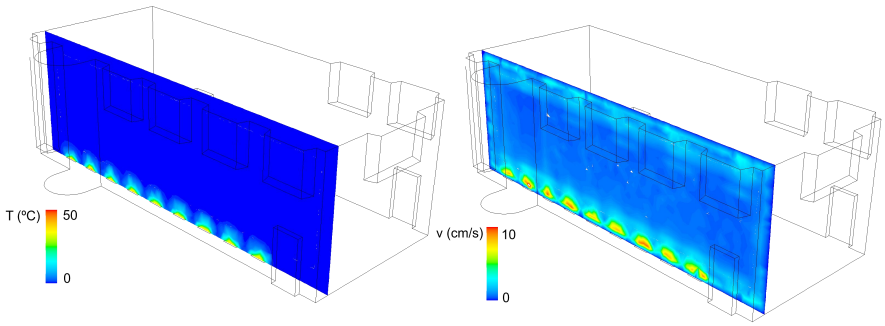

Figure 6.21: Contours of air temperature and air velocity above the heating system of the East wall

Tapestries as sources of particles

Before proceeding any further with the simulations, we deemed necessary to discard the possibility that the tapestries themselves could be emitting particles during the monitoring campaign carried out by HRP. The hypothesis was that dust embedded in the tapestries or fibres could have been resuspended (by the effects of drafts, vibration or visitor movement) and that this dust could have significantly affected the deposition on the glass slides. In order to test this hypothesis we carried out a simulation of the Chamber assuming that one of the tapestries were the source of particles. We compared the deposition predicted in this simulation with the deposition measured in different glass slides. This comparison can be seen in Figure 6.22.

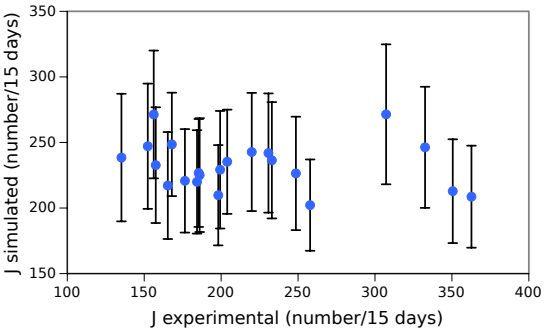

Figure 6.22: Comparison between measured deposition and deposition under the hypothesis that the tapestries are a source of particles.

The comparison shows no correlation, and the two variables seem independent. This indicates that, even if the tapestries are a source of particles, their contribution on the total deposition flux is small in comparison with the particles originated elsewhere.

Deposition caused by visitors

The experimental evidence discarded outdoor sources and leakage, and the simulations discarded the heating system or the tapestries themselves as sources of particles. At this stage, the last plausible hypothesis is that visitors are the main factor behind the observed deposition. In this Section we will describe the introduction of visitors into the model and we will show that the simulations of visitor emissions show a good agreement with some features of the experimental data. Due to the investigative nature of these simulations, many of the visitor-related scenarios are speculative, and will therefore be included in the next section, where scenario simulations are discussed.

We designed a new way of simulating visitor impact to particulate matter deposition. Visitors were introduced in the model as cylinders of height and surface area similar to a human body (between 1.4 and 1.8 m^2 [4]). The emission factors from visitors were obtained from the work of Yoon and Brimblecombe [2] who estimated that a moving adult person could emit between 20 and 200 $\mu\mathrm{g}$ of dust/hour depending on clothing and level of activity. We chose to use an emission of 100 $\mu\mathrm{g}/\mathrm{h}$ per visitor. This is of course a coarse approximation that should be used to approximate the order of magnitude. But as we shall see, these emission factors are in agreement with the average total deposition measured in the Chamber. To produce this comparison we have assumed that all the particles emitted by visitors deposit in the same room. Figure 6.23 shows the comparison between the measured deposition and the predicted emission using the number of visitors at Hampton Court Palace during the monitoring period and the emission factors by Yoon and Brimblecombe.

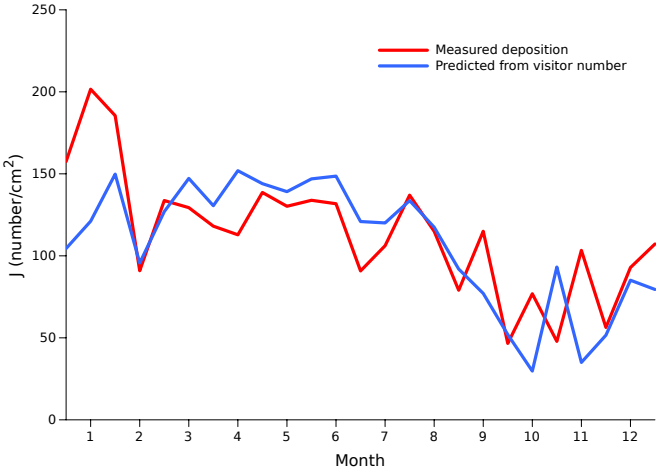

Figure 6.23: Comparison between total measured deposition and deposition predicted using the Yoon and Brimblecombe emission factors, and the number of visitors.

This fit is obtained assuming a particle diameter of 65 $\mu\mathrm{m}$, and a density of 2500 $\mathrm{kg/m^3}$, which seems plausible. It also contains the implicit assumption that all visitors to Hampton Court walk through the Great Watching Chamber during their visit, which is also a reasonable assumption. We calculated the total measured deposition multiplying the rate measured in the glass slides by the total area of the room. Figure 6.23 tells us that we can use Yoon and Brimblecombe's emission factors to describe the amount of particles that the visitors bring into the room.

To illustrate the general features of the particle flows generated by visitors, let us simulate a case which we can argue to be usual:

- The Chamber is occupied by 50 visitors, which remain there for 20 min.
- The visitors are homogeneously distributed in the space.
- All the visitors stand at an appropriate distance from the tapestries.
- The air flow is predominantly E-W, with an average inlet velocity of 0.2 $\mathrm{m/s}$.

Figure 6.24 shows the distribution of suspended particulate matter. It is concentrated around the visitors, because due to its large mass and diameter it tends to deposit close to the emission source. Figure 6.25 shows the deposition fluxes towards surfaces. Several features of this profile of deposition are noteworthy. Firstly, deposition is higher in all the horizontal surfaces, such as the window sills. This is due to the large size of the particles, which contributes to more prominent gravitational settling and therefore a predominance of deposition in horizontal surfaces.

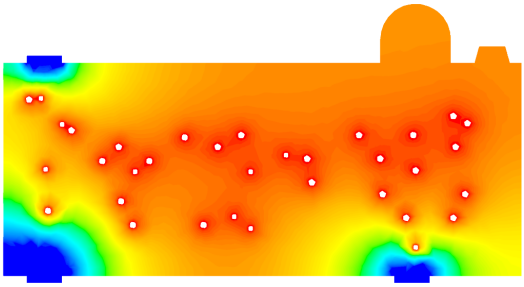

Figure 6.24: Concentration of PM around visitors. This concentration is non-dimensional (it only indicates which areas have relatively higher or lower concentrations)

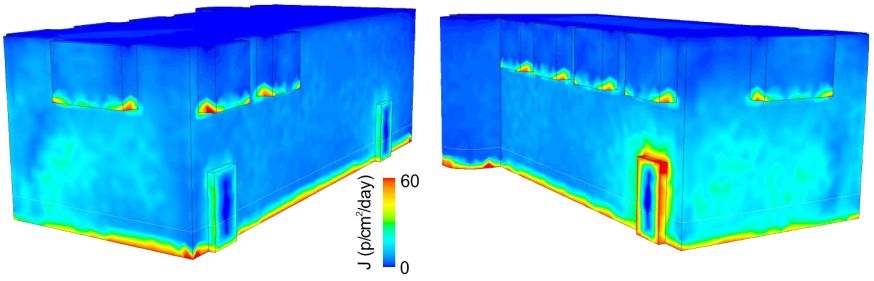

Figure 6.25: Deposition fluxes towards all the walls of the Great Watching Chamber.

Another important feature is the increased deposition in the area surrounding the door frames, particularly in the East wall. Deposition around this doorway can also be observed in the dust deposition data from the HRP monitoring (the contour of deposition around the East door measured experimentally is displayed in Figure 6.11).

Increased deposition around the inlets and outlets

Close to the outlet doors, air frequently moves at a higher velocity than in the bulk. Typically, an air current exists very close to the area of the wall where the door is located. This air current is parallel to the wall. In the Great Watching Chamber, this feature of the air flow can be observed near the East door (Figure 6.26).

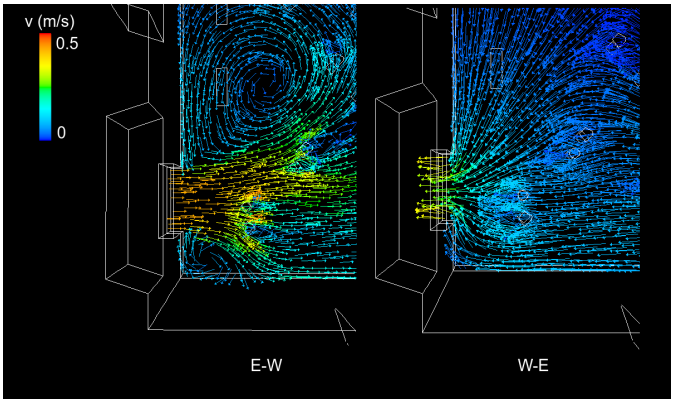

Figure 6.26: Velocity streamlines close to the East door

This tangential air flow generates a high friction velocity, which is related to deposition rates. Equation 3.42 expresses this relationship between u_d and u^*. We have also seen this effect experimentally in the tunnel experiments described in Section 4.3, where we found that the walls close to the free stream of air experienced twice the deposition than the walls protected by barriers that interrupted the flow. In the Great Watching Chamber, the areas with high friction velocity correspond well with the hotspots of deposition observed in the monitoring campaign. This is illustrated in Figure 6.27. Even though this figure illustrates a qualitative comparison, it is also a partial validation of the accuracy of the model.

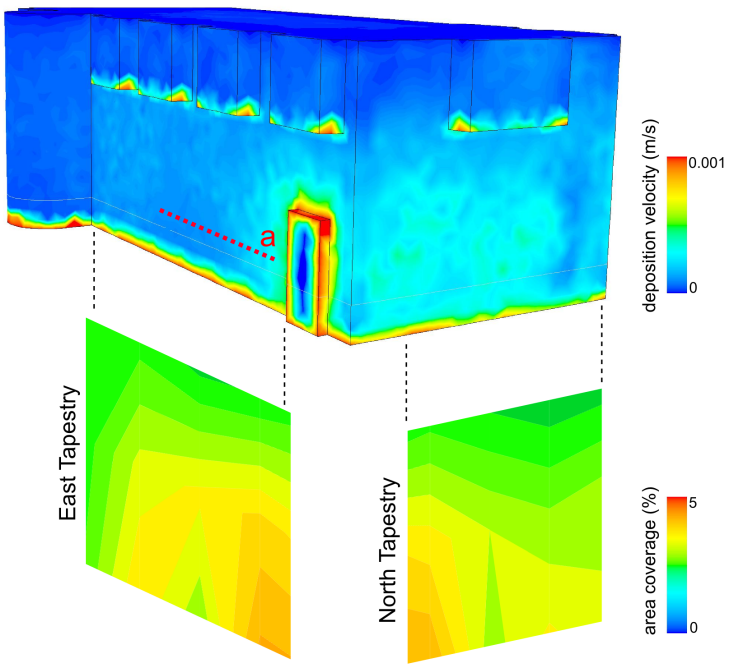

Figure 6.27: Visual comparison of the experimental contours of area coverage, and the simulated contours of deposition velocity. The dotted line (a) indicates the section, which is assessed quantitatively in 6.28

Deposition decreases along the East wall. On the five meters next to the East wall door there are only three experimental points, but they are enough to capture the slope of the decay of deposition. Figure 6.28 demonstrates that the decrease in deposition along the East wall, from the door towards the South wall, fits reasonably well with the simulated gradient. This phenomenon is not visible near the other doors of the Chamber in the West wall, for the simple reason that their wings are opened inwards. In view of the experimental data, we hypothesize that these door wings prevent the formation of a tangential air current, and thus reduce deposition in the vicinity of the door. In Section 6.4 we will further explore the effect of such wings on air motion and PM deposition, and we will consider a hypothetical installation of similar protective elements in the East wall inspired by the positive effect of the West wall door wings.

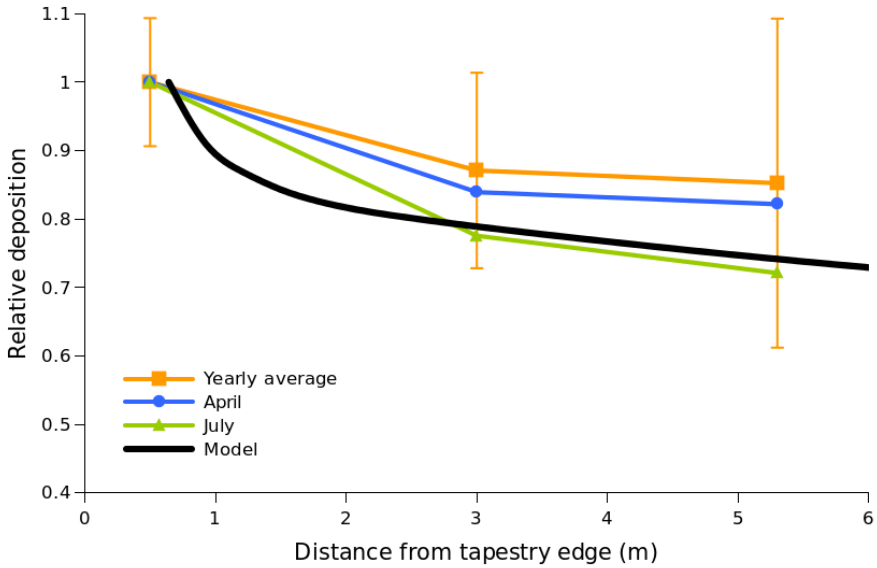

Figure 6.28: Comparison of experimental and theoretical deposition profiles near the East door (along the dotted line (a) in Figure 16.27). The deposition flux is normalised by the highest value, which is found immediately beside the door. The error bars reflect the variation of this profile between the different months.

6.4 Scenario simulation

We have simulated different hypothetical scenarios. These simulations have two purposes. Firstly, they contribute to our understanding of the dynamics of deposition in the Great Watching Chamber. Secondly, they allow us to identify possible mitigation strategies.

Many of the scenarios include different arrangements of visitors. Deposition caused by visitors is a particular phenomenon because visitors are simultaneously a source of particles and a driver of deposition. They are a source of particles because they bring particles indoors, which are resuspended from their clothes or carried on their footwear. In the Great Watching Chamber these particles are emitted at a rate that, as we have shown in the previous section, can be approximated with the rates found by Yoon and Brimblecombe. Visitors are also a driver of deposition through two mechanisms:

1. A passive effect on the air flow. They obstruct and alter air drafts, creating new flow patterns that affect the way particles deposit in the room.
2. An active effect on the air flow, causing moderate levels of air movement that can cause deposition -particularly if visitors move close to walls.

Our simulations will contemplate visitors as a source of particles and as a passive modifier of air flow (1), but we will not include their active aerodynamic effects. Namely, such a problem is

complex and computationally too demanding to be tackled in the framework of this case study. Some studies have attempted to study the airflow around a walking human and even its effects on aerosol motion ([5, 6], but the state of this research is not mature enough and it has not been experimentally validated, so it cannot be easily incorporated in a simulation in this study.

Visitor distance to the tapestries.

We have simulated the deposition caused by a single visitor standing at different distances from the tapestries. Figure 6.29 shows the distribution of PM concentration around the visitor at 0.5, 1,1.5, 2, and 2.5 m from the tapestry. These concentration contours should not be understood as the location of the actual particles, but rather as an indication of the areas where particles falling from clothing are more likely to be.

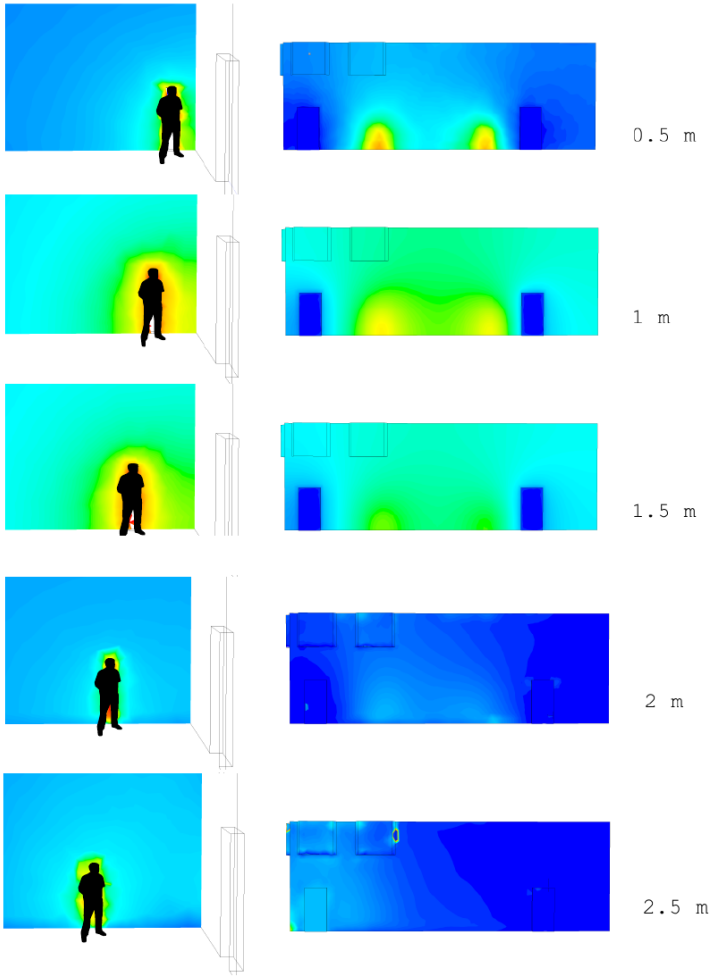

Figure 6.29: Simulations of dispersion of clothing-related PM from visitors at different distances from a wall in the Great Watching Chamber. Contours show dimensionless distribution of PM concentration.

The most important conclusion to be derived from this simulation is that direct deposition of dust carried by visitors is reduced significantly with the distance to the wall. When a visitor is very close to a wall, deposition seems to be largely independent of what happens in the rest of the room. In that situation, particles that fall from the clothing deposit gravitationally on the nearest surfaces. This situation can only be worse if a visitor moves quickly and generates airflow by doing so, because air movement generally increases deposition in vertical walls. However, if visitors stand away from a wall, particles emitted from their clothing will no longer deposit directly, but will be captured by the dominant air flows in the room. This does not imply that particles will not deposit, but that they will deposit elsewhere in the space. In other words, at a sufficient distance from the walls, particles emitted by visitors become part of "bulk" air motion, and their fate is determined by the overall air motion in the room. This is also illustrated in the

right column of contour plots in Figure 6.29, where we notice an apparent reduction of particle concentration near the wall if visitors stand 2 m from the tapestries.

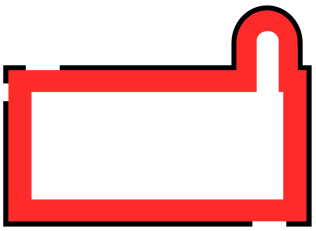

Figure 6.30: In red, the area where PM from clothing directly deposits on the walls. At the current stage of research, CFD simulations are more reliable if they involve visitors located in the white area, because we are unable to simulate the direct effects of visitor movement on the air close to the walls.

Finally, there are some remarks to be made on the interpretation of these results. The simulations tell us that there is a threshold value in visitor-to-wall distance, below which particles start to deposit directly on the walls. However, it is difficult to say with certainty if this threshold is 1.5 or 3 m, since it depends on many parameters, such as visitor movement, which is not captured by our model. Nevertheless, we can safely say that the barriers currently installed in the Chamber protect tapestries from most of the direct deposition, and that the current furniture (cushions, chairs and small tables) plays a role in preventing visitor movement very close to the wall. Note also that visitor movement is particularly important in this near-wall area (as highlighted in Figure 6.30), while in the bulk, the passive effects of visitors on flow will be more important. These passive effects are what the current model can capture.

Visitor number

We produced several simulations of deposition caused by different numbers of visitors standing in the Great Watching Chamber for 20 min. In all the simulations described in the section, visitors were randomly distributed in the space, as can be seen in Figure 6.31.

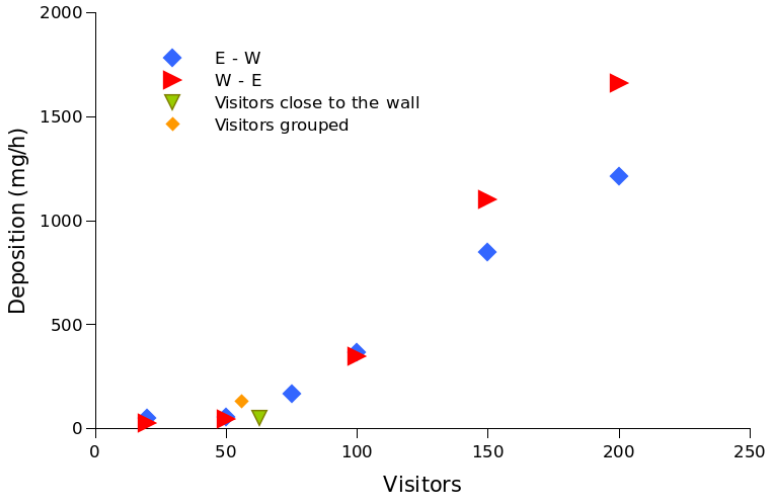

Figure 6.31: Simulated correspondence between deposition and visitor numbers

The relationship between visitor number and overall deposition is not linear (Figure 6.31). Up to roughly 50-75 visitors, as their number increases, the total deposition increases proportionally. However, above this number the slope changes and deposition starts to increase faster. A reason for this increase may be that, above 50-75 visitors, the effect of visitors on the air flow starts to be significant. As before, this threshold could vary with many parameters, such as the intensity of the activity of visitors. But despite this limitation we can safely conclude that the number of visitors has an important effect on the total deposition.

We can also conclude that deposition increases sharply when the visitor density is such that the visitors limit the natural cross-ventilation of the room. We repeated all simulations with the two likely ventilation scenarios, E-W and W-E. Both cases exhibit identical trends, but deposition is systematically higher when air flows in the W-E direction.

Visitor location and grouping

Visitors are not randomly distributed in the room, on the contrary, they tend to move in groups and to cluster around activities or guides. We simulated several scenarios that exemplify some common groupings of visitors. These can be seen in Figure 6.32.

The simulation of groupings did not show significant differences in the deposition levels in most of the cases. As long as visitors are in the centre of the room, and independently of their exact position, most of the particles they emit will be captured and transported by air. Air movement is what dictates the spatial distribution of deposition. Therefore, the position of a specific visitor is not very important once particles from their clothing have been captured by air in motion.

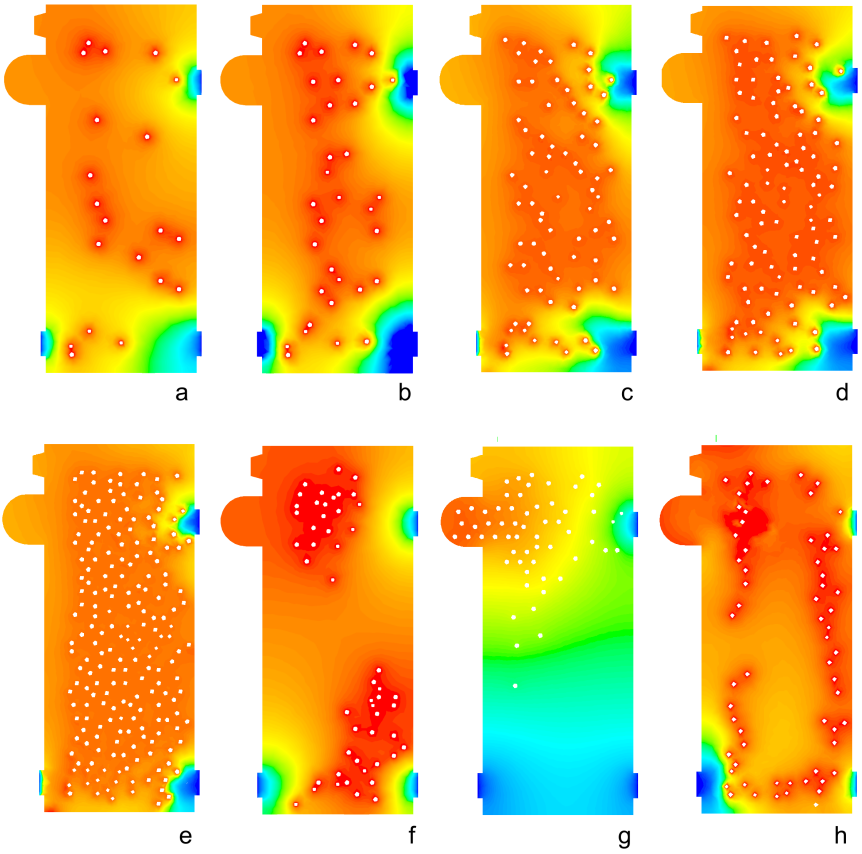

Figure 6.32: All the scenarios with varying visitor numbers and locations, showing the dimensionless distribution of suspended PM.

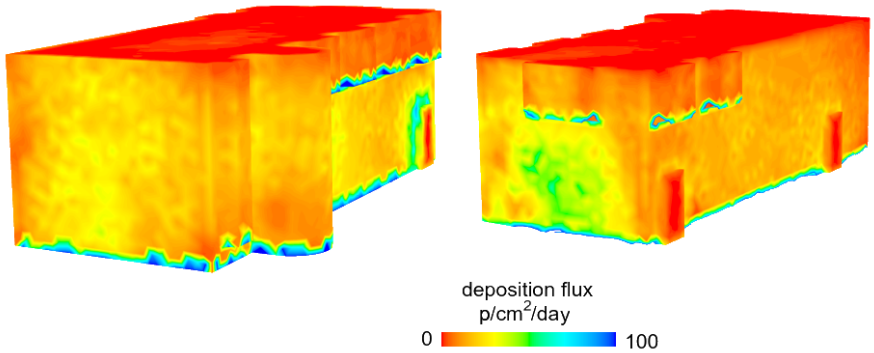

Figure 6.33: The most generally encountered deposition flux distributions.

Consequently, even though the total deposition changes with the visitor number, the spatial

distribution of deposition remains unaltered. That is to say that it is unaltered as long as visitors stay close to the centre of the room (of course, it can be argued that when the room is crowded, the possibility that a visitor walks close to a wall increases). This results in a very similar spatial distribution of deposition in the simulations (a) to (f) of Figure 6.32. This "typical" spatial distribution of deposition is illustrated in Figure 6.33.

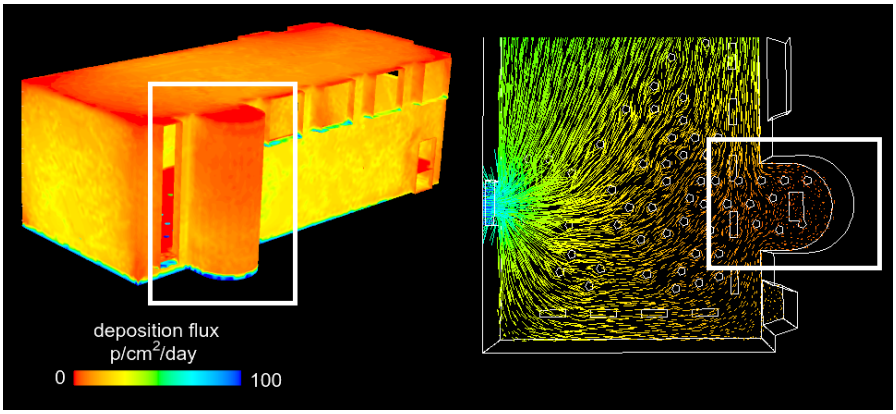

Figure 6.34: Distribution of deposition if visitors are clustered at the South end of the room (Scenario g of Figure 17)

This general observation has some noteworthy exceptions. As we said above, individual visitors can cause deposition locally if they are close enough to the tapestries. This effect can be seen in some of the simulations. Figure 6.35 shows a deposition pattern that corresponds to the distribution of visitors in Figure 6.32h. In that case, visitors have a very visible passive effect on air movement, and create turbulent eddies, and even some vertical movement of air. This results in a distribution of deposition which is very different from the general case of Figure 6.33. Another example of the diverse situations that can arise from the position of visitors corresponds to the scenario shown in Figure 6.32g. In this case, visitors are located mostly inside the semi-circular window area. Even though they are very close to the walls, they partially block air movement in the South-East corner. The air velocity streamlines of Figure 6.34 show clearly that velocity in the semi-circular area is very low. As a consequence, even though visitors may release a lot of particles in this corner, deposition is very low. This example illustrates once more the importance of air movement as a driver of deposition.

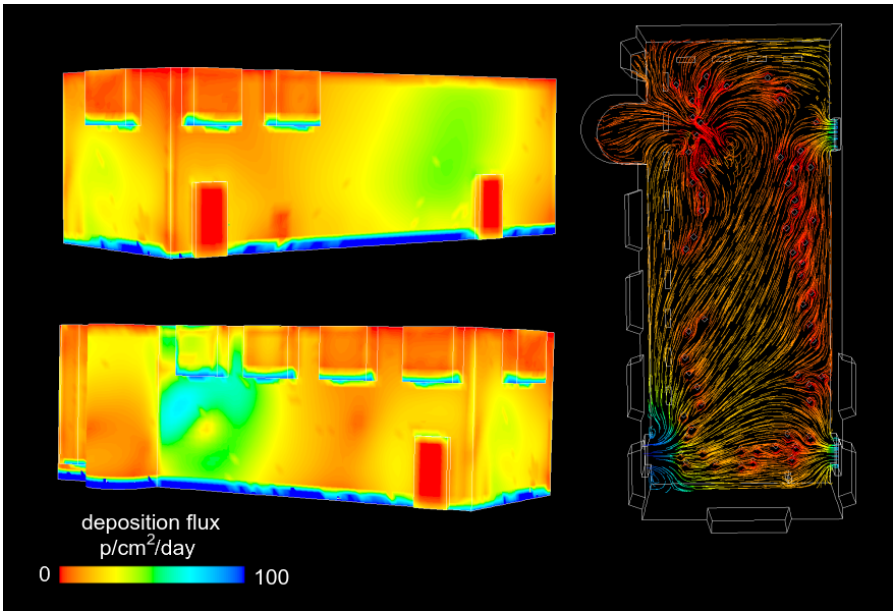

Figure 6.35: Deposition flux when visitors are close to the walls (Scenario (h) of 6.32 17)

Inlet and outlet velocities

Air velocity in the inlets changes very frequently, as we have seen in short monitoring periods (Section 6.3.1) and according to staff reports it changes direction several times per day. It depends on the external wind direction, as well as the combination of open and closed doors and curtains in the surrounding spaces. It is almost impossible to simulate a complete day with all the fluctuations in the inlet velocities. It might also be unnecessary. In this Section we will take a much simpler approach and we will examine the dependence of deposition fluxes on the air velocity.

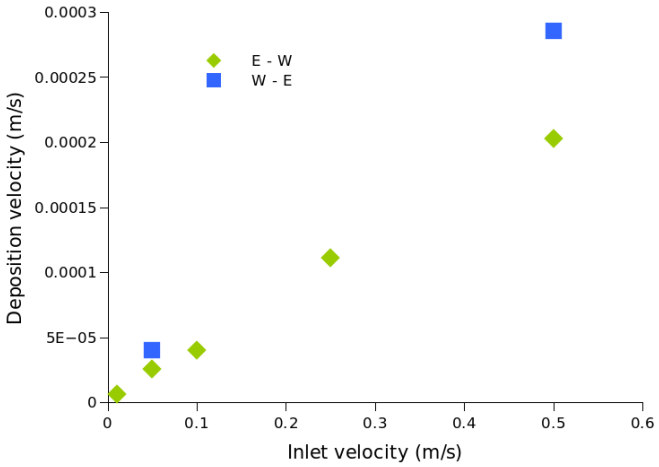

Figure 6.36: Dependence of deposition on the inlet velocities of the doors in the Great Watching Chamber

The simulations have shown that deposition increases linearly with the inlet velocity, as can be seen in 6.31. With a fixed number of visitors in the room, deposition fluxes increase if the inlet velocities increase. The limiting case would be a room with a completely steady air, where particles cannot travel far from the source. In such a case, virtually all of the emitted particles deposit on the floor. Since half the air velocity implies half the deposition, there is a great benefit to be gained from limiting air movement in the room.

Turbulence deflectors

We have shown that the high levels of deposition close to the doors are possibly related to air turbulence. A layer of air moving tangentially to the walls is formed near inlets and outlets of the Chamber, and tangential velocity increases deposition rates, as seen in Section 6.3.3. This Section explores the possibility of interrupting this tangential layer using a physical obstacle. Given that this flow occurs near the doors, a non-intrusive solution would be using the door wings, or a panel of a similar size, to interrupt strong air flows close to the tapestries. By comparison, two of the four doors to the Chamber have door wings opened inwards that already prevent PM deposition - albeit unintentionally.

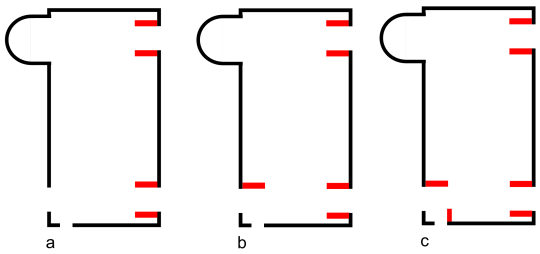

Figure 6.37: The three simulated scenarios with different arrangements of door wings and deflectors.

We simulated the addition of a similar wing -which can be pictured simply as a wall- to the East door, and the impact it would have on deposition on the East tapestry. Figure 6.37 illustrates the three different cases we simulated. In case 6.37b, only one wing is added, close to the East tapestry (where a deposition hotspot is most commonly observed). In case 6.37c, we added a wing on the smaller door that links the Great Chamber with the small adjacent room, hoping that it would also protect the South tapestry.

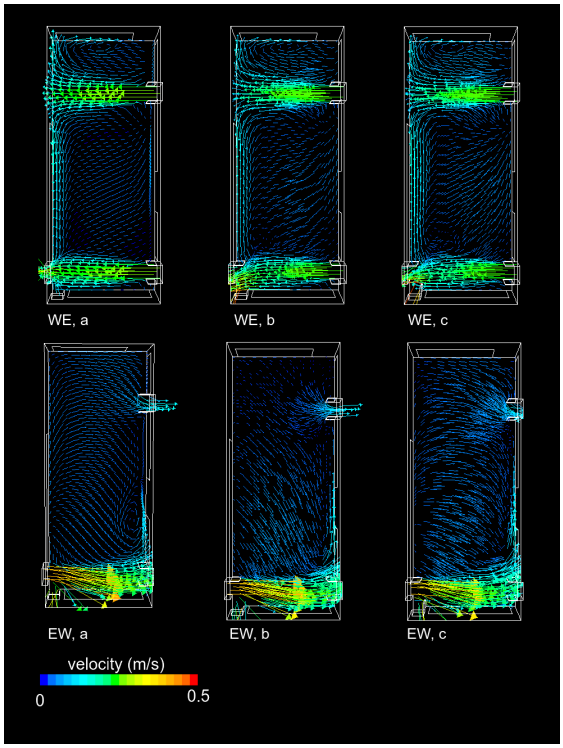

Figure 6.38: Air velocity streamlines with door wings are added to the East doorway, taking two likely air directions: E-W and W-E.

This example shows the sensitivity of air movement to small changes in the geometry. Figure

6.38 shows the simulated air streamlines for the three different cases illustrated in Figure 6.37, all simulated in the two possible air directions. Two phenomena stand out. Firstly, when air flows from West to East, that is, entering through two doors and exiting through one, the addition of walls in the East door does not cause important changes in the bulk movement. As figure 6.38 shows, the velocity streamlines of subfigures a, b and c are very similar. This can also be appreciated in the contours of deposition displayed in Figure 6.39. Secondly, when air flows westwards (i.e. enters through a single door and leaves through the two doors in the West wall) the addition of door wings does have a visible effect on air motion in the centre. This can be appreciated in Figures 6.39EWa, EWb and EWc.

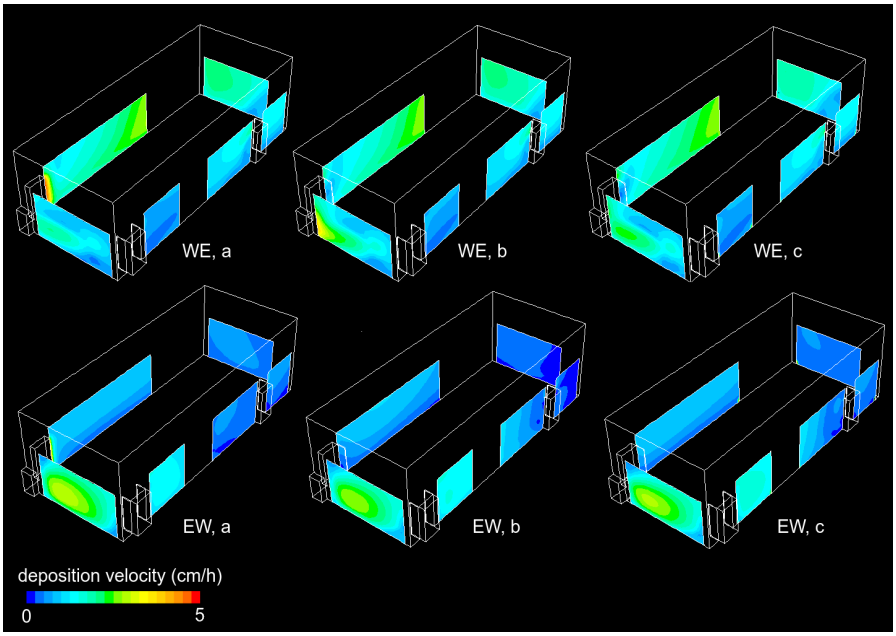

Figure 6.39: Contours of deposition on the tapestries under different scenarios of Figure 6.37.

6.5 Conclusions

In this Chapter we have demonstrated three ways in which our simulations can feed in into the practice of preventive conservation and heritage management. Firstly, we have shown that the output of our simulations can be transformed into intuitive and clear information in terms of area coverage and time to unacceptable deposition. This conversion requires assumptions on concentration and particle properties, which might be unknown or too variable, and therefore reduces the value of the scientific data. At the same time, however, it enhances its readability and usability.

Secondly, we have also shown that the model can answer many questions that would be too complex to explore experimentally, or that would suppose an unnecessary threat to the collection.

The simulation of the increase in indoor concentration of $PM_{0.02-1}$ when the main gate is open is a good example of a phenomena which may not be worth the effort (or the risk, for it would imply leaving the main gate fully open for several hours) of an actual experiment. However, to a property that is located in such a polluted environment as Apsley House, it provides interesting information on the nature of the ingress of particles every time a group of visitors opens the door.

And finally, we have also seen that while the model cannot replace measurements, it can inform and improve them. It can aid, for example, to the planning of a monitoring campaign. If the interest is in knowing the room average deposition, the model can be used to find a representative location. If our interest is in knowing the spatial distribution of deposition, it can be used to find locations which display meaningful differences in deposition. Another use of the model is to interpret and understand existing deposition data. In the case of the Great Watching Chamber we discarded the effects of fibre emission from tapestries or the heating system, demonstrating that they have a very reduced effect on the observed deposition. We also demonstrated that the observed deposition patterns are the result of visitor-related emissions and air movement. The Great Watching Chamber is not a flexible environment, and the options for additions or changes in the room layout are minimal. In this context our simulations can provide a very detailed understanding of the physical phenomena leading to deposition, and help to understand changes in the room layout that can effectively reduce the amount of particles that reaches the surfaces.

References

[1] H. D et al. “Monitoring dust in historic houses”. *Proceeding of Conservation Science*. London: Archetype Publications, 2002.

[2] Y. H. Yoon and P. Brimblecombe. “Clothing as a source of fibres within museums”. *Journal of Cultural Heritage* 1:4 (2000), pp. 445–454.

[3] D. Camuffo. “Wall temperature and the soiling of murals”. *Museum Management and Curatorship* 10:4 (1991), pp. 373–383.

[4] I. Herman. *Physics of the Human Body*. Biological and Medical Physics, Biomedical Engineering. Springer, 2007.

[5] J. Wang and T.-T. Chow. “Numerical investigation of influence of human walking on dispersion and deposition of expiratory droplets in airborne infection isolation room”. *Building and Environment* 46:10 (2011), pp. 1993–2002.

[6] J.-I. Choi and J. R. Edwards. “Large-eddy simulation of human-induced contaminant transport in room compartments”. *Indoor air* 22:1 (2012), pp. 77–87.

7 Particles on surfaces

7.1 Introduction

The work so far presented in this Thesis has principally dealt with the mechanisms that bring particles to the walls. We have taken for granted that particles attach to surfaces, and that their presence in surfaces is a sufficient indicator of any potential loss of value. This Chapter focuses on challenging this view by describing the phenomena that affect or are caused by the deposited particles. We do that in two ways: firstly we explore the consequences of deposition, and we present experimental evidence of the chemical effect of particles deposited on paper. Secondly, we study the physics of a deposited particle, reviewing attachment, indentation and resuspension, and revealing how these processes relate to our modelling approach and to heritage surfaces.

7.2 Loss of value

7.2.1 Towards a threshold of acceptable deposition

In the literature review we mentioned four possible mechanisms that could lead to the loss of value of surfaces (Section 1.7): Visual impact, chemical degradation, biological growth and cleaning/handling. These four mechanisms depend on different properties of the particles and the deposition process. In order to find a threshold value of acceptable deposition, we should take into consideration the characteristics of each degradation process.

Visual impact. It depends only on the amount of light-absorbing or light-scattering particles on a surface. It could be measured in number or mass, but a better indicator is percentage of area covered $\%A$, which also takes into account particle size. Limits for visual impact

have the form:

$$L_{visual} = f(\%A) \tag{7.1}$$

Even particles smaller than the visible wavelength of light (0.39 μm) can in theory alter the appearance of surfaces. Deposited fine aerosols can cause light scattering and reduce visibility [1]. This effects may not be simply explained by area coverage. However, this has not been investigated from the perspective of its aesthetic consequences.

Biological growth. It depends on the amount of particles on a surface. Existent research does not specify the size of the particles, but the references to "dust" suggest that coarse particles may be more important [2, 3]. Biological growth also depends on humidity [4] and age of the dust [5]. This limit could have the form:

$$L_{biological} = f(\%A, RH, t) \tag{7.2}$$

where RH is the relative humidity and t is the time since the particles have deposited on the surface. However, more research is needed to quantify this threshold.

Physical cleaning and handling. Loss of value through cleaning can occur through different mechanisms. It can be due to the removal of strongly adhered particles, which depends on particle properties, most importantly diameter. Damage can also occur because of excessive cleaning and handling, although this has not been quantified yet, as discussed in Section 1.7.5.

Chemical degradation. Given the indications found in the literature (See discussion in Section 1.7.3), it might be related to the amount of particles (N) and their composition (C).

$$L_{chemical} = f(N, C) \tag{7.3}$$

Further research is needed about each of this mechanisms in order to stablish realistic limits and if they exist at all, and in order to assess their relative importance. In the framework of this Thesis we explored the probably least known chemical effect of deposited particles on paper, as a typical representative of a natural organic material openly exposed in historic houses (such as are wall-papers, carpets, curtains).

7.2.2 Which are the most area-covering particles?

We have focused our simulations on particles with a diameter between 0.1 and 10 μm. The reader may rightly wonder whether this is the most relevant size range. It could well be that most of the perceived area coverage is due to the larger particles, and therefore, at least regarding the alteration of the aesthetic value, the fine range is relatively unimportant.

We can use our measured data of deposition to explore this issue. Figure 7.1 shows the area-covering capacity of the particles collected in three different locations. What this plot shows is the relative contribution of each particle size to the total area coverage. The capacity of a certain particle type to cover an area depends on its diameter, but also on its number concentration in a given location. We can see, for example, that the 10 μm particles in the Waterloo Gallery contribute to 10% of the observed area coverage. This should be interpreted with care, because 10 μm, in this figure, is the mean diameter of a size bin. Using lines to plot this information might not be the more adequate solution, but it is convenient in order to compare different locations.

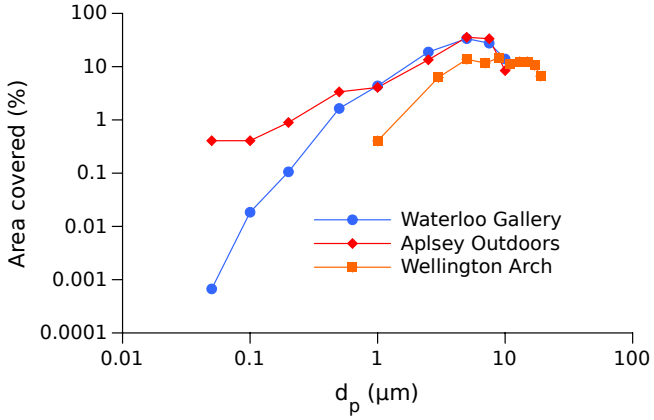

Figure 7.1: Relative contribution of each particle size to the total area covering measured in different locations.

The first noteworthy result is that in all three locations the most area covering particles are between 1 and 10 μm. Note that these locations are quite diverse: Inside Apsley House, particles between 0.5 and 2.5 μm are almost exclusively of outdoor origin, while particles larger than 10 are almost exclusively carried by visitors. In the Arch, most of the particles are black soot generated in the Piccadilly underpass. Outside Apsley House, we detect a mixture of road debris and combustion particles. Despite this differences, the most area-covering particles are similar in all three locations.

Another interesting consideration is that the high number of fine particles outdoors (almost ten times more than coarse particles as seen in Figure 5.17d) does not suffice to give them an important role in area-covering. The location where more area is covered by fine particles is clearly the outdoors Apsley location, but even there the area covered by 0.05 μm particles does not reach 1%.

Finally, we should note the fact that the diameters around $\sim$1 μm are precisely the ones which typically display lower deposition velocities (As seen, for example, in Figure 2.1). We could be tempted to conclude that this will help counteract their area-covering ability. However, this is unlikely the case: Figure 7.1 is based on counts of deposited, and not suspended, particles. Therefore, the fact that the middle-sized particles deposit more slowly is already contained in

these results. In other words: even though $\sim$1 μm particles tend to deposit more slowly, they still appear to be the ones with a larger capacity to cover surfaces.

Probably, if we had measured particle mass and not diameter, we would have observed a similar distribution. With this data we can only speculate, but if we assume that particles of all sizes have a similar denisity we can convert Figure 7.1 in order to express the relative contribution to mass delivery. By multiplying each curve by a particle diameter and density, we would obtain an approximmation to the mass by area for each particle size. This operation would not change the shape of the curve, which would still peak between 1 and 10 μm. If anything, we would see more marked differences between sizes. Even though large particles carry more mass tu the surfaces, and small particles are more numerous, the size distribution in the locations we have studied is such, that the particles which deliver more mass have a diameter around 1 μm.

7.2.3 Chemical degradation

We suspected that particles embedded in paper could accelerate the degradation of the surrounding cellulose fibres. To investigate this issue, we studied the chemical degradation of paper samples exposed to environmental particulate matter. Clearly, such degradation must be a very localised effect, because particles can only interact with the adjacent fibres. The thickness of cellulose fibre threads we have measured is generally between 5 and 20 μm , which is comparable to the diameter of particulate matter. Figure 7.2 shows some particles embedded in a Whatman filter paper, consisting of pure cellulosic fibres, heavily soiled with environmental PM collected outdoors close to a road. This SEM image may convey a sense of the relative size of the particles and the cellulose fibres.

This experiment faces two main challenges. Firstly, we should expect degradation to be limited to the surroundings of the particles. However, the low spatial resolution of our method to measure the degradation of cellulose means that we can only provide information on the average properties of a paper sample. We measure degradation which is surely local and disperse, using bulk analysis of the paper and yet, as we shall see, we are able to show a statistically significant effect of particles on the overall degradation. The second major challenge of this experiment is to isolate the effect of PM on paper samples that have been exposed to the urban environment, and have therefore been in contact with gases and under fluctuating T and RH conditions.

Paper exposure to environmental PM

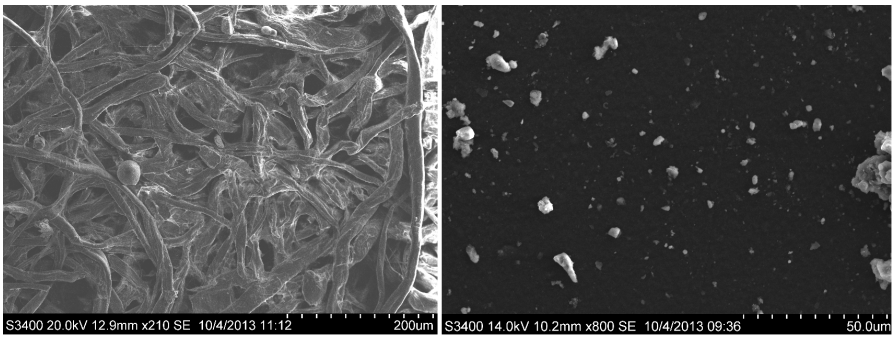

Figure 7.2: Example of PM embedded in a sample of Whatman paper and the carbon stub used to collect particles in the same location.

In the previous chapters we have referred extensively to our measurements of PM deposition. We took advantage of this monitoring campaign and we exposed samples of Whatman paper alongside the PM samples we used to measure deposition fluxes. We exposed paper samples in five different locations, two indoors and three outdoors. The outdoor sample racks were in sheltered locations. Our motivation to expose samples outdoors and indoors was to cover a wide range of deposition rates, and to ensure we had a high proportion of fine particulates. We exposed the samples for one to six months, removing a sample from each location every month. The exposure locations were:

1. Plate and China Room, Apsley House, ground floor. Top of the central display case (See Figure 5.38 or the contour plots of deposition in Figure 6.2).
2. Corridor, Apsley House, first floor. Same location than the suspended PM monitoring system (See Figure 5.16)
3. Wellcome Collection building, roof. Completely sheltered from rain and wind in well-ventilated shed.
4. Service Stairs, Apsley House, basement, open to outdoor environment. Sheltered on top.
5. Window, Apsley House, below street level. Sheltered on top. Same location that the outdoor suspended PM monitoring system (See figure 5.16).

The samples were laid out in a sample rack that contained a sample for every month of exposure. In order to isolate the effects of particulate matter and gaseous pollutants, we covered part of the samples using a permeable polymer membrane (Clopay MicroPro). This membrane protected the sample from particulate matter and light, but allowed gases to penetrate. We used a UV Logger (Hanwell ULM-Universal Light Meter) to ensure that it blocked 99.1 % $\pm$ 0.2 % of the incident UV light, and we used diffusion tubes (Gradko) to ascertain that the membrane allowed

77% of the O_3 and 94% of the NO_2 present in the environment to reach paper samples, which is enough to ensure that the paper interacted with this gasses. On the other hand, SEM analysis of the protected paper samples did not reveal the presence of a measurable amount of particulate matter larger than 0.1 μm.

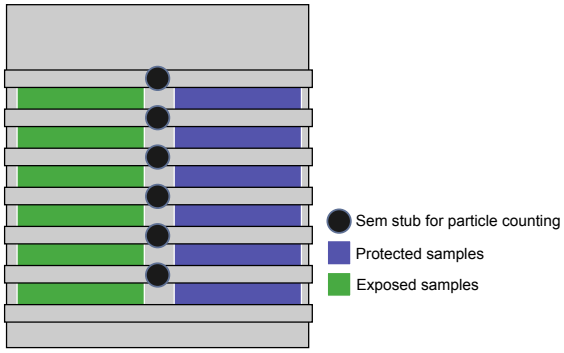

Figure 7.3: The sample rack used in this experiment.

Not all the exposed paper samples could be used in the final experiments. Either a problem with the exposed paper or with the SEM stubs for particle counting can result in a loss of an experimental point. Firstly, we had to discard 6 out of 30 samples due to problems related to particle counting. Some of these were discarded merely because in the initial months, the deposition on some indoor samples was below the detectable threshold. Some samples were also accidentally damaged during collection or transport, causing a loss of an important amount of deposited particles. We also experimented some issues related with the exposed paper. Exposing such a sensitive material as paper for six months to the environment implied some loss of samples, in spite of our precautions. For example, some outdoor samples were too damaged by water to provide meaningful results, showing visible staining. In total we lost 9 paper samples in addition to the 6 that were discarded. At the end, we could include in our analysis half of the intended experimental points. These problems are summarized in Table 7.1.

Chemical analysis

We analysed the elemental composition of the deposited particles using inductively coupled plasma mass spectrometry (ICP-MS). This technique is described in Appendix 1. Figure 7.4 shows the results of this analysis.

Table 7.1: Summary of the samples used in the paper degradation experiment.

Location	Month	Particle monitoring	Paper sample
Plate and China	1	particles below threshold	
	2	particles below threshold	
	3		
	4		
	5		
	6		
Corridor	1	particles below threshold	
	2	particles below threshold	
	3		no degradation detected
	4		no degradation detected
	5		
	6		
Wellcome	1	particles below threshold	
	2	damaged	
	3	damaged	
	4		
	5		
	6		
Service stairs	1		no degradation detected
	2		sample missing
	3		
	4		damaged
	5		damaged
	6		
Window	1		
	2		
	3		damaged
	4		damaged
	5		damaged
	6		

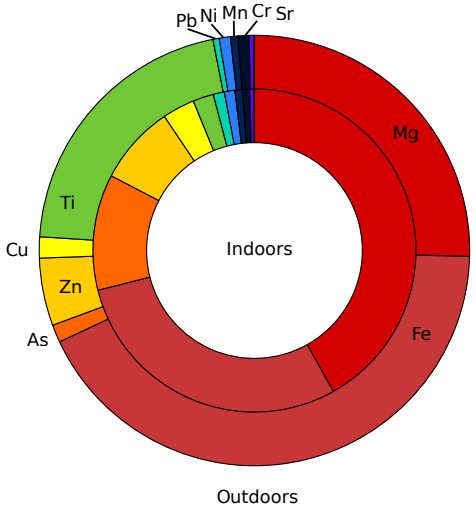

Figure 7.4: Elemental composition of the indoor and outdoor samples of particulate matter. The percentages are based in measurements done in $\mu g\ cm^{-2}$.

The results of the chemical analysis are comparable to other elemental analyses of urban PM_{10} in the UK. For example in Birmingham it was also found that the most abundant metal (in mass) was Fe (38%) followed by Mg (29%), Ca (14%), Zn (5.6%) and others [6]. Iron concentrations are higher in street sites than in rural sites, and can indicate a contribution of suspended road dust [7]. We have detected iron in all our sampling locations, indoors and outdoors. Road dust may explain the origin of Iron in site 5 (in a window in Apsley House), which is below the street level in a busy road, but not in site 3, which is on a roof. Iron has also been found to be the second most abundant metallic element in diesel particulate matter after Ca, also followed by Mg, and Cr, Zn [8]. We are probably observing a combination of both sources of Fe. Figure 7.4 shows that iron is also more abundant outdoors than indoors, but relatively less than titanium. Ti is also a product of the combustion of fossil fuels [9], which explains its relatively higher presence outdoors.

Viscometric determination of DP

With the purpose of accelerating the effects of the deposited particles on the paper substrate, we additionally degraded all the samples for 2 and 3 weeks at 80 °C and 65% RH (ISO 5630-3). We then used viscometry to measure the change in the degree of polymerisation, DP, which is proportional to the decrease in the average molecular weight of cellulose. We determined the DP following ISO 351:2010. The experimental procedure is further explained in Appendix 1.

We calculated the loss of DP due to PM deposition as the difference between the DP of the unprotected samples (which were affected by PM and gases) and the protected samples (which were only affected by gases):

$$DP_{loss} = DP_{unprotected,\,aged} - DP_{protected,\,aged} \tag{7.4}$$

However, DP_{loss} does not tell us how much did the paper degrade during exposure and how much during accelerated degradation. This information is contained in the relative degradation, x:

$$x = \frac{DP_{unprotected,\,not\,aged} - DP_{unprotected,\,aged}}{DP_{protected,\,not\,aged} - DP_{protected,\,aged}} \tag{7.5}$$

x could be interpreted as the relative increase in degradation due to PM deposition over the baseline of degradation that could be expected from the rest of the environment.

A possible degradation pathway

Several metals found in the deposit on the paper samples -Fe, Cu, Cr and Ni- can catalyse the degradation of cellulose through the Fenton reaction [10]. This is the name given to the generation of a hydroxyl radical from hydrogen peroxide in presence of an iron catalyst, a reaction discovered by Henry Fenton in 1894 [11]:

$$Fe^{2+} + H_2O_2 \rightarrow Fe^{3+} + .OH + OH^-$$

Since iron is the most abundant of the Fenton metals detected in the chemical analysis, we will use it to study their relationship with paper degradation.

The effect of PM on DP loss

Figure 7.5 shows the correlation of DP_{loss} with the total particle count ($PM_{0.5-10}$). We can see that the overall correlation is poor, however, some locations, namely the Plate and China Room (indoors) and the window (outdoors) display clear correlations. This may indicate that particulate matter from different locations has a different effect on DP loss. This might be due to a varying chemical composition.

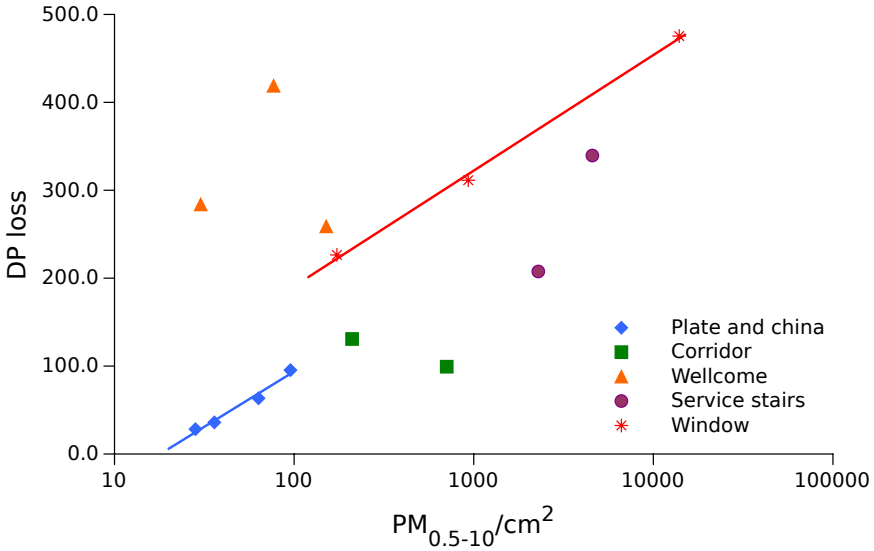

Figure 7.5: Relationship between DP_{loss} and deposited number of $PM_{0.5-10}$ in different locations.

In fact, when we plot the DP_{loss} against the iron concentration on the paper surface, Figure 7.6, we obtain a much clearer correlation. Note that there are more than 15 experimental points in this plot because the measurements of Fe concentration are unaffected by the loss of SEM stubs. Note also that some experimental points in this correlation correspond to interpolated concentrations of iron. This is because elemental analysis was only available for months 1, 3, and 5. Since in all the locations this composition increases approximately linearly, we found it justified to interpolate the concentrations of months 2, 4 and 6 (Interpolation could lead to apparent linearity, and because of that these points are clearly marked in Figure 7.6).

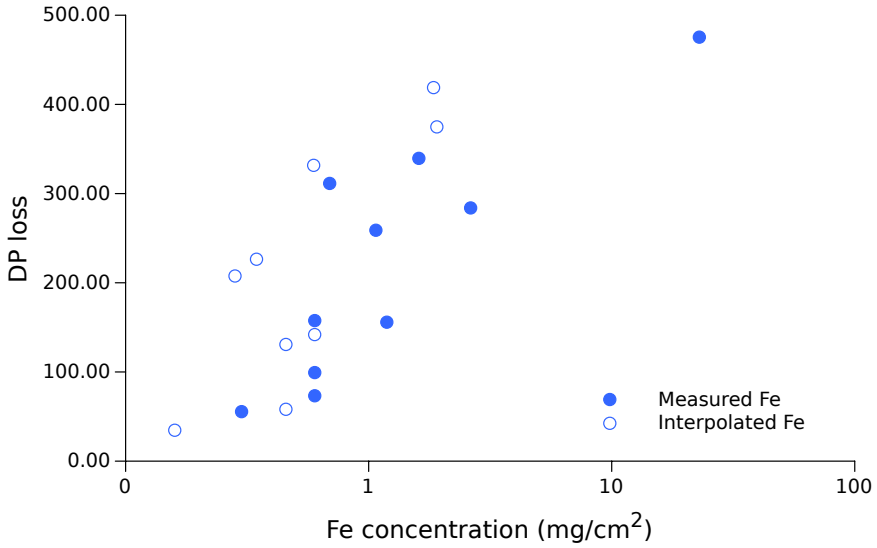

Figure 7.6: Relationship between DP_{loss} and C_{Fe}.

We produced a multivariate regression relating DP_{loss} with both the number of particles on the surface (N) and the iron concentration C_{Fe}, the resulting regression reads: $DP_{loss} = ln(N) \times 36.24 \pm 3.86 + ln(Fe) \times 81.63 \pm 31.71$ with $R^2 = 0.96$ and F-Value = 24.6. The factor multiplying the iron concentration is larger than the factor multiplying N, indicating that the composition of particles explains the observed degradation better than the amount of particles. Of course this is only valid if C_{Fe} and N cover the same range of DP_{loss}. The logarithmic relationships observed in Figures 7.5 and 7.6 are characteristic of the degradation of cellulose.

It is clear that the effects of particles are not equal in the different locations. Figure 7.7 shows the mean value of x according to the location. We can readily see that in the indoor samples the contribution of particles to the overall degradation is not statistically significant (x is close to 1). However, in the outdoor sheltered samples, the contribution of PM to degradation becomes increasingly significant as the exposure to traffic related particulates increases.

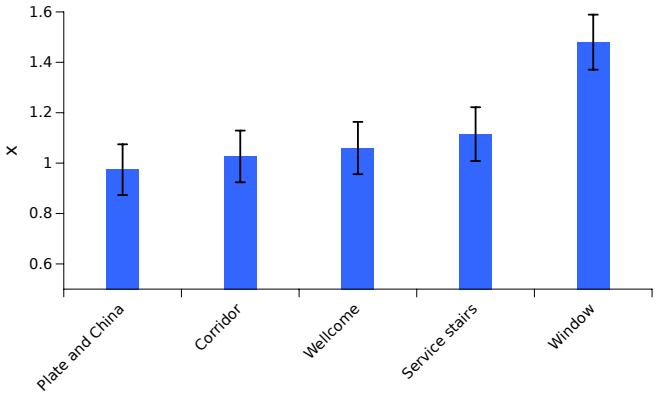

Figure 7.7: Contribution of PM to paper degradation in different locations.

The amount of deposited iron in each of these locations is slightly different. As expected, we observe a positive correlation between x and the iron concentration (Figure 7.8).

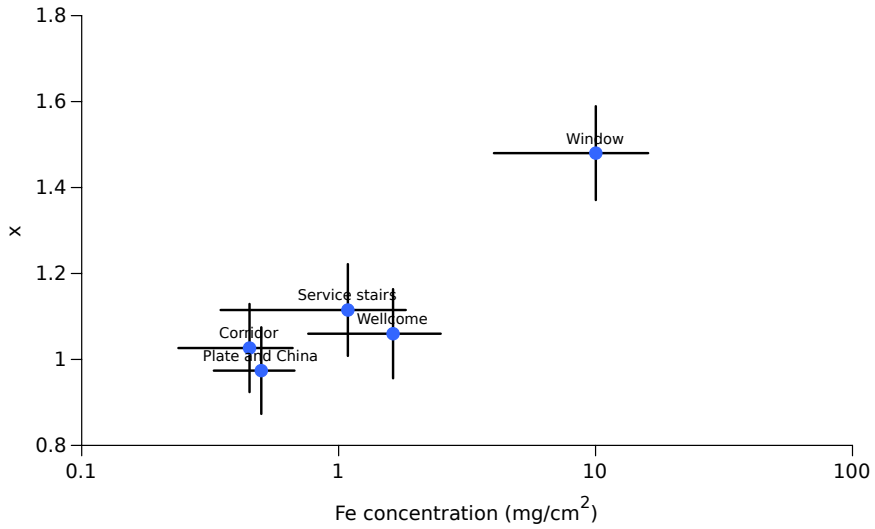

Figure 7.8: Relationship between C_{Fe} and the relative contribution of PM to the degradation of paper, x. The vertical error bars reflect the uncertainty in the determination of x and the horizontal bars de variation of iron concentration between samples exposed in the same location.

This is a significant result for two reasons. Firstly, it shows very clearly that the effect of deposited PM on paper is not dependant on the amount of particles but on their composition - and we may be able to extend this conclusion to any comparable organic material, such as textiles, because Fenton reaction-mediated oxidation leads to production of highly reactive organic species such as hydroxyl radicals, reacting with any organic matter at a diffusion-controlled rate. However, there could be other factors affecting degradation of organic matter, e.g. organic car-

bon in PM which could oxidize itself, as well as any acidity associated with PM. We haven't quantified these possible degradation paths, and remain a matter of future study. Secondly, we have shown that, depending on the composition, the presence of PM can increase the degradation rate of paper by a factor between 1.1 and 1.5.

7.3 Basic physics of a deposited particle

Throughout this Thesis we have regarded walls as passive sinks. In the scale of time and space we have approached the problem, this may be a reasonable assumption. However, along the development of this project many questions have arisen that require a more detailed understanding of surface phenomena. For example, we have asserted that more needs to be known about the loss of value related to physical cleaning activities. Any quantification of this damage must start with an understanding of particle attachment and the ability of the particles to penetrate on the substrate. We have also ignored important parameters such as relative humidity or surface roughness, or phenomena such as resuspension.

This Section focuses on a force balance of the micro-scale phenomena that affect particles deposited on surfaces. Research shows that attachment may not only be due to physical interactions but also to chemical changes. The cementation of dust particles is a case in point. In high humidity, the formation of microcrystalls can adhere particles to surfaces in a matter of hours [12]. This process depends on the composition of the deposited particles and the nature of the substrate. In this chapter, however, we will focus in physical processes that are easily quantifiable using few variables (air velocity, particle diameter and mass), and which can be introduced in our broader conceptual framework - or, if possible, in the mathematical model. This section is largely based on the literature, with the exception of some small contributions.

Let us begin where the model ends: particle deposition. Once a particle has reached a surface, it is affected by various attachment forces [13]. Some of these forces act not only on the surface but in a certain perimeter around it (therefore, at least in theory, they could increase deposition). However, this perimeter of influence is often so small compared with the diameter of particulate matter, and these forces are so small compared to air flow, that they do not become relevant until a particle is in physical contact with the surface [14]. They are important as contact forces, but not as attractive forces. This Section presents a reasoned balance of these forces.

7.3.1 Attachment

The main force responsible for the adhesion of small particles to surfaces is the Van der Waals force. These are long-range attractive forces between molecules, that are due to the dipoles present in any material as a result of random electron movement [15]. Obviously they are "long range" in relation to the size of the molecules. In fact, the Van der Waals forces decay rapidly when the separation between surfaces increases:

$$F_{adh} = \frac{Ad_p}{12x^2} \tag{7.6}$$

where A is the Hamaker constant (which depends on the material and is between 6×10^{-20} and 150×10^{-20} J), and x is the separation distance between the surface of the particle and the surface [15]. When a particle is deposited on a surface the separation distance x will be as small as the asperities on the surface of the particle and the substrate [15]. Once in contact with the surface, the adhesion forces for hard, perfectly smooth surfaces are described by:

$$F_{adh} = Wd_p\pi/2 \tag{7.7}$$

where W is the work of adhesion (i.e. the energy required to separate one square meter of interface reversibly [16]). Equation 7.7 is known as Bradley's rule, and it is a seminal result in the history of adhesion theory. By adding the Van der Waals forces for all molecules in two particles in contact, Bradley demonstrated [17] that the adhesion force should be proportional to particle diameter [13]. This result is particularly interesting when the adhesion forces are compared with other forces acting on the deposited particle, for example the gravitational force, which is proportional to the mass of the particles m and therefore to the cube of the diameter [13]:

$$F_g = mg = \frac{4}{3}\pi(d_p/2)^3\rho_p g \tag{7.8}$$

Another relevant force acting on small particles is the electrostatic adhesion. It has been known since the experiments of Coulomb in 1785 that the force between two point charges is proportional to the square of the distance between them. Some particles carry a small charge q, which generates an attractive force [14]:

$$F_e = \frac{1}{4\pi\epsilon_0}\frac{q^2}{d_p^2} \tag{7.9}$$

where ϵ_0 is the permittivity of the medium [14]. Finally, when there is a layer of liquid between the particle and the surface, surface tension can also increase the adhesion. For a liquid with surface tension γ [15] reports the equation:

$$F_s = 2\pi\gamma d_p \tag{7.10}$$

In the case of water the above equation is valid for relative humidities higher than 90% [15]. Due to the effect of capillarity, the total adhesion force is also a function of humidity. This has led to the development of experimental correlations such as Equation 7.11, valid for d_p > 20 μm [15]:

$$F_{adh} = 0.063d[1 + 0.009(\%RH)] \tag{7.11}$$

By comparing these forces it is evident that Van der Waals and capillary forces are directly proportional to d_p, electrical forces are proportional to d_p^2 and gravity is proportional to d_p^3. As a result, the relative importance of these forces will vary with the diameter.

Figure 7.9 shows a comparison of the different attachment forces acting on a particle (ρ_p = 2.5 gcm^{-3}, charge obtained from experiments with diesel particulates by [18], q = 1.3×10^{-16} C, RH = 55%, surface tension of water, γ = 0.073 $\mathrm{N/m}$). Figure 7.9 shows two curves for the Van der Waals forces, one for perfectly smooth surfaces (Bradley's rule) and a correction for rough surfaces. The reason why Van der Waals forces are reduced if surfaces are rough is simply that the contact area is reduced and the average distance between the bodies in contact increases due to the presence of asperities in the contact area [16]. The roughness correction of the Bradley rule displayed in Figure 7.9 is adapted from the curve reported in [16].

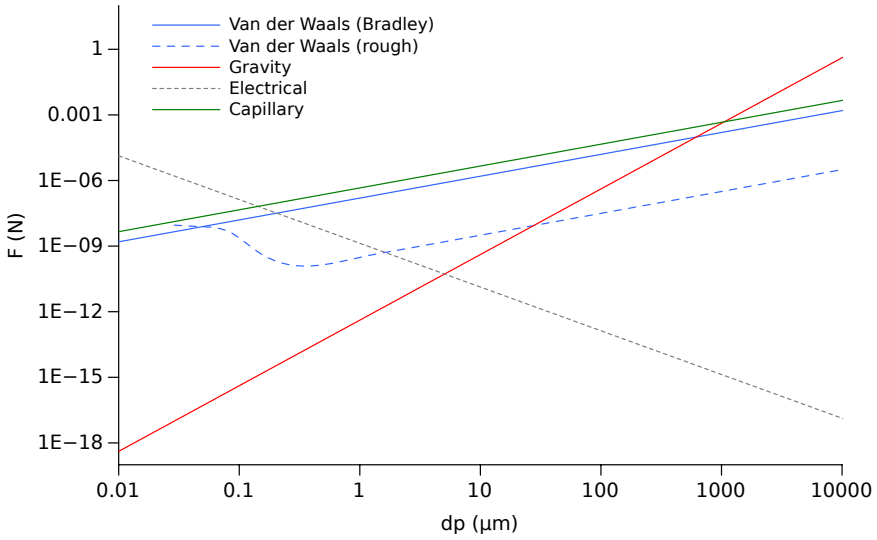

Figure 7.9: Forces that contribute to adhesion of particles in surfaces. The curve for the Van der Waals forces reduced by roughness is adapted from [16].

We observe in Figure 7.9 that gravity is only more important than adhesion forces when particles are larger than 1 mm. This implies, for example, that if we place an ideally spherical particle of 1 mm on an ideally flat vertical wall, it won't fall. However, the irregularity of the particles and the roughness of the wall can lower this threshold down to 10 $\mu\mathrm{m}$. This result, albeit based on very simple correlations, coincides with our experiments and our daily experience. All particulate matter can attach to vertical surfaces, and remain attached in the absence of other forces. Figure 7.9 also indicates that capillary forces (which can result from high humidity) are comparable in magnitude to the Van der Waals forces. Consequently the attachment force can double in environments with high RH. We also observe that electrical forces are only relevant for very fine particles.

Figure 7.9 shows that matter can be naturally classified in two categories according to its size: the microscopic and "sticky" realm of adhesion forces, and the macroscopic realm of gravita-

tional forces. The point in Figure 7.9 where the line of the Bradley rule meets the line of the gravitational force (around 50 μm) is perhaps the clearest upper limit to what we can call "particulate matter". Of course this criteria is totally oblivious to air movement, because under the adequate level of turbulence anything can behave like a mote of dust. But the realm of the Van der Waals forces clearly identifies which are the particles that can stick to walls and ceilings, and remain attached.

7.3.2 Indentation

If adhesion forces are higher than the resistance offered by the surface, particles will begin to penetrate into the substrate. This is what we call indentation. Here we present a force balance based on the newly developed model by Style et. al. [19]. This model explains the indentation of spherical particles in soft elastic solids, as could be a polymer-based work of art, or the surface of an oil painting. Firstly, the Hertz theory of elastic contact states that the force required to make a spherical indentation of depth d and radius r is:

$$F_e \sim \frac{E r^{1/2} d_p^{3/2}}{(1-\nu^2)} \tag{7.12}$$

where E is the Young modulus, and ν is the Poisson ratio. The main innovation by [19] is the inclusion of the force required to increase the surface area, considering indentation as a spherical cap in a flat plane this force is:

$$F_s \sim \pi \sigma_{sv} d \tag{7.13}$$

where σ_{sv} is the surface tension of the solid (in units of work, $\mathrm{N/m}$). For solids, the concept of surface tension can be understood as the work needed to create additional surface area by stretching. Finally the attachment force is calculated with equation 7.7. In Figure 7.10 we plot these three forces as a function of indentation for a particle of $d_p = 0.01$ μm. For this example, the young modulus has been extracted from nano-indentation experiments carried out in paintings by Van Gogh [20], where the young modulus was found to vary between 1 GPa and 0.01 GPa. Here we use 0.1 GPa. We could argue that the tip of a nanoindentation apparatus is comparable with a deposited particle. Regarding the surface tension, in the examples given in the article σ_{sv} has order $\sim$0.1 $\mathrm{N/m}$ and this is the value we take in our solution.

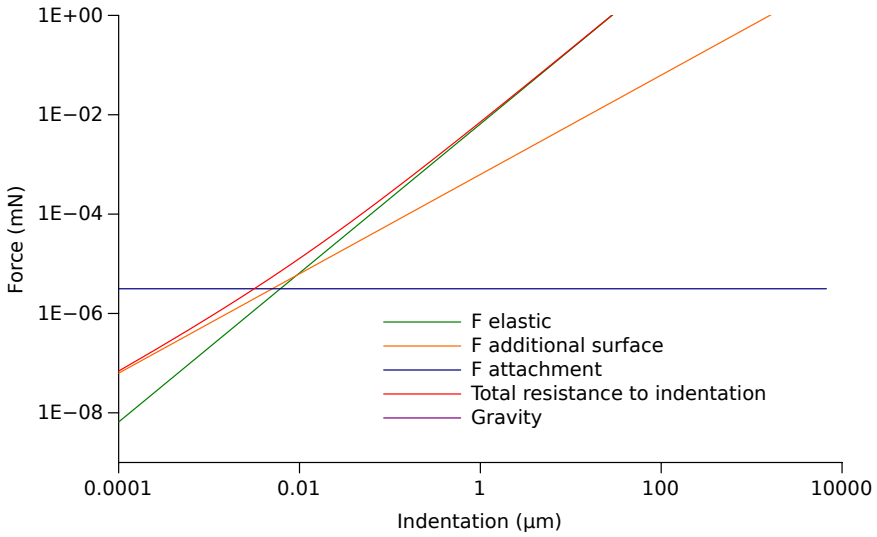

Figure 7.10: Forces that contribute to adhesion of particles in surfaces.

Figure 7.10 can be interpreted as the force needed to indent a particle at different depths. We can see that, up to a depth approximately equal to the diameter, the attachment forces are superior to the resistance of the surface. As indentation increases, the resistance forces increase, and the particle would stop indenting when they become higher than the attachment forces. This equilibrium situation is given by the balance:

$$\frac{Er^{1/2}d_p^{3/2}}{(1-\nu^2)} + \pi\sigma_{sv}d - 2\pi Wr = 0 \tag{7.14}$$

If we solve this balance for a range of d_p we find that the particles which are more prone to penetrate into the substrate are the small particles. Figure 7.11 displays the equilibrium indentation for particles of different sizes in the range of E found in the Van Gogh paintings. We can appreciate that particles with $d_p \sim 0.01 - 0.1\mu\text{m}$ are the only ones that can penetrate to a significant depth in comparison with their diameter (i.e. they capable of "sinking" into the material). Coarse particles with $d_p \sim 10 - 100\mu\text{m}$ only penetrate some fractions of a micron into the substrate.

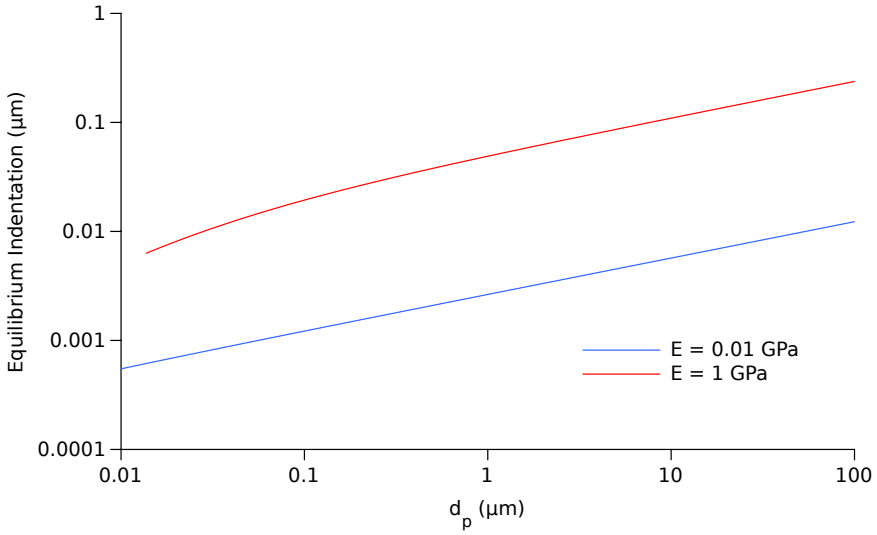

Figure 7.11: Forces that contribute to adhesion of particles in surfaces.

Indentantion may represent a conservation issue. These calculations show that fine particles can become totally embedded in a painting surface, which may require complicated and potentially damaging cleaning operations. But Figure 7.11 also shows that coarse particles will penetrate only to a negligible depth inside the painting layer before reaching an equilibrium. This suggests that the accumulation of coarse dust in paintings is in many cases only superficial, and in principle easily removable.

7.3.3 Resuspension

If the air flow near a surface produces lift forces that are higher than the adhesion forces, the particles will resuspend. However, resuspension is a dynamic process which is more complex than a simple force balance. Under a steady burst of air, the affected particles will begin rolling on the surface [21]. Since surfaces and particles are irregular, the outcome of the rolling process might be that the particle will find another equilibrium state, either by depositing elsewhere in the surface or by changing its position, in a way that increases the adhesive forces. Some of the particles will not find a new equilibrium and will be resuspended. This is the reason why resuspension processes are dynamic, and they typically evolve exponentially with time, with most of the particles being resuspended at the beginning of a burst of air. This is shown in Figure 7.12:

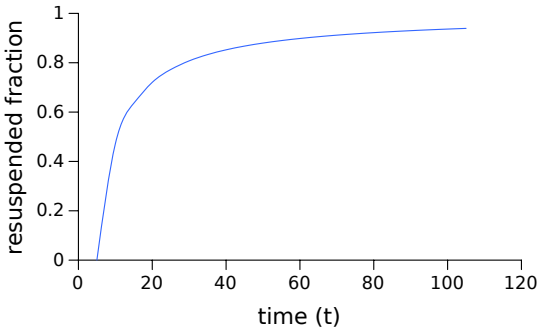

Figure 7.12: Example of the loss of particles on a surface during a resuspension event.

The curve of resuspended fraction versus time shown in Figure 7.12 has been obtained by solving the semi experimental correlation by [22]:

$$\eta = \frac{0.42 u^{*2.13} d_p^{0.17}}{t^{0.92} z_0^{0.32} \rho_p^{0.76}} \tag{7.15}$$

where η is the resuspended flux in particles per unit time, u^* is the friction velocity and z_0 is the mean roughness. We have solved it for a case in which $u^* = 0.05$ m/s, $d_p = z_0 = 1$ μm and $\rho_p = 2500 \mathrm{kg/m^3}$. Resupension can also be approached using a simple mass balance, which would only involve the lift force. This force was estimated by [23] for the case of particles being resuspended from a surface and is calculated as:

$$F_L = 60.87 \mu \left(\frac{d_p}{2} \right)^2 R \tag{7.16}$$

where R is a resuspension factor that depends on the friction velocity and can be estimated with:

$$R \approx 0.01 \frac{u^{*3}}{\nu^2} \tag{7.17}$$

Therefore, the total lift force is [24]:

$$F_L = 0.076 \rho \nu^2 \left(\frac{d_p \, u^*}{\nu} \right)^3 \tag{7.18}$$

We can compare this lift force with the adhesion forces, calculated with Bradley's rule (Equation 7.7), to obtain:

$$X_r = \frac{\text{lift force}}{\text{adhesive forces}} \sim \frac{\rho \nu^2}{d_p} \left(\frac{d_p \, u^*}{\nu} \right)^3 \tag{7.19}$$

Our suggestion is that X_r could be implemented in our model, and estimated in every surface. It would not solve solve the need for an estimation of resuspension but it could function as an additional criteria for the applicability of the model. If on a certain surface $X_r > 1$, we would know that resuspension is stronger than adhesion and that, therefore, the model is overestimating the amount of particles that reach surfaces.

Undoubtedly, it would be interesting to fully implement resuspension in our deposition model. Ideally this should be done with a resuspension flux or (resuspension velocity) that we could subtract from the deposition flux. However, all the resuspension models available in the literature involve individual particles in transient simulations [21, 25–28], and none of them is well suited for implementation in an Eulerian framework.

We could, however, take advantage of the fact that we are often producing simulations which are averaged over a long period of time. Here we suggest a method of implementing the resuspension flux in steady-state simulations of deposition, as a flux that balances deposition. Even if the simulation is steady state, the turbulence model tells us how air velocity fluctuates, and some of these fluctuations may cause resuspension. The time scale of the turbulent fluctuations can be approximated with [29]:

$$t_n = \left(\frac{\nu}{\epsilon}\right)^{1/2} \tag{7.20}$$

In Apsley House, for example, the time scale of the velocity fluctuations varies notably, from 0.1 s near air inlets and up to 100 s in rooms with little air motion. But if we are interested in the resuspension that occurs over a very long time, τ (which is far lager than t_n), we may be able to consider that the loss of particles due to resuspension occurs approximately linearly. That is, we observe a step-wise loss of particles with the shape shown in Figure 7.12 every time period t_n, during a simulated time τ. This is shown schematically in Figure 7.13.

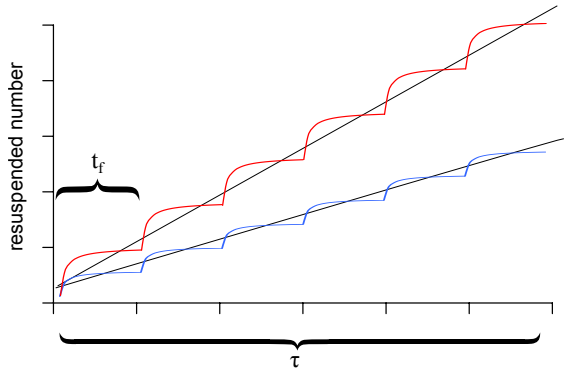

Figure 7.13: Step-wise loss of particles due to resuspension at each turbulent fluctuation, occurring every t_n seconds during a simulation of length τ. The two lines illustrate that different resuspension curves would lead to different slopes, and thus different resuspension fluxes.

We could consider that in a given surface, the time period in which a resuspension event devel-

ops, reaches an equilibrium, and begins again is $\sim t_n$. If this is true, we can calculate the total number of particles resuspended during a turbulent fluctuation, N, by integrating any simple model of resuspension, such as Equation 7.15, over t_n:

$$N = \int_0^{t_n} \frac{0.42 u^{*2.13} d_p^{0.17}}{z_0^{0.32} \rho_p^{0.76}} \frac{1}{t^{0.92}} \mathrm{d}t \tag{7.21}$$

This loss of particles would occur t_n/τ times during the simulation. Knowing this total loss, a resuspension flux can be calculated, and subtracted from the deposition flux.

7.3.4 The effect of roughness on deposition

Surface roughness increases particle deposition. At a first glance, this may suggest that deposition increases due to an increase of the surface-to-volume ratio. It is common experience to see more dust in paintings with high impastos than in flat photographs, or to see dust accumulated in the interstices of baroque altarpieces. And in fact, the particles suspended in a room with uneven surfaces and richly decorated furniture will deposit faster than those in a room with perfectly flat walls. But this does not necessarily imply *faster* deposition, it just implies *more* deposition towards the extra surfaces. Using the concepts introduced earlier, it implies a higher sum of the total deposition flux, J, but no matter how baroque, furniture does not increase the deposition velocity, u_d.

On the other hand, roughness does increase u_d. We must consider first that there is a separation of scales. Large irregularities such as decoration or furniture alter air movement in a scale from various meters to various centimetres, i.e. a scale orders of magnitude larger than a particle. We can simulate these effects without breaching the assumption that particles behave as a continuous field. However, roughness interacts with particles in a scale from a few microns to a few millimetres. This scale is comparable to the size of the particles, and our underlying assumption fails to reflect this interaction. The interaction between a particle and a rough surface cannot be described by a mass balance approach or an Eulerian simulation. However, this can be introduced into the model if we consider the aerodynamic effects of surface roughness [30, 31].

The effects of roughness on turbulence are well known and have been studied since the early days of turbulence modelling [32]. It was the German physicist Nikuradse who first quantified experimentally, in 1933, how turbulence increases over rough surfaces [33]. One of the effects of surface roughness is to increase the thickness of the turbulent boundary layer [32, 34]. Many models describe this effect. One of the oldest and more known is by Elliot [35], from 1958, which describes the response of the boundary layer thickness to a step change in roughness, from z_1 to z_2. We introduce it here only to convey an idea of the general form of this relationship:

$$\frac{\delta}{z_2} = (0.75 - 0.03 ln(z_2/z_1)) \left(\frac{x}{z_2}\right)^0 .8 \tag{7.22}$$

where δ is the boundary layer thickness and x is the distance in the direction of the flow. Such relationship is very useful, since we have already discussed how the thickness of the turbulent boundary layer is related with deposition. In Section 3.3.3 we have integrated the deposition flux through the concentration boundary layer, taking in consideration how diffusivity changes within the turbulent layer (Equation 3.37). We only have to introduce the boundary layer thickness calculated with Elliot's relationship, or with a more advanced model, into the integration of the deposition boundary condition.

Some authors have developed modified deposition models that account for roughness in this manner. The most recent, by [30] uses two parameters to describe roughness: a peak to peak distance, L and a peak height, K. They use a modified boundary layer thickness ($\delta + F^+$), and calculate F^+ with a pseudo-empirical correlation:

$$F^+ = \begin{cases} \frac{54.86*u^*}{\nu} ln\left(\frac{K}{L}\right) + \frac{222.02u^*}{\nu}, & 0.0175 < \frac{K}{L} < 0.082 \\ 0, & \frac{K}{L} < 0.0175 \end{cases} \tag{7.23}$$

This model implies that, if the irregularities that make the surface rough are very separated, or if they are large but very close, roughness does not have an effect on deposition. We measured K and L for some of the surfaces where we have measured deposition: Whatman paper, Carbon stickers and glass slides using a contactless profilometer (Innowep TRACEiT). The results are displayed in Table 7.2:

Table 7.2: Measures of roughness as defined by [30] of the surfaces used for PM monitoring in our experiments.

	K (μm)	L (μm)	K/L
Carbon sticker	125.5±51.6	190.3±52.9	0.66±0.45
Whatman paper	59.39±17.4	522.5±156.0	0.11±0.07
Glass slide	35.5±0.7	428.5±198.2	0.083±0.04

The results displayed in Table 7.2 show that none of the surfaces used for monitoring falls within the range of roughness levels that affect deposition, because K/L is too large. According to [30], some of the materials with values of K and L that effect deposition significantly are smooth wallpaper ($K/L = 0.016$), rough wallpaper ($K/L = 0.064$) or wall plaster ($K/L = 0.045$). What we can conclude is that our validation experiments are not significantly altered by surface roughness. However, all the properties we have simulated contain many surfaces which may alter deposition. This affects the predictive capacity of our model, and the only possible solution is to measure all the roughness values and add them as boundary conditions.

Theoretical calculations of deposition on rough surfaces

In this Section we use the model of deposition on rough surfaces developed by [36]. It is a simpler model that can be solved analytically, and which describes deposition using a single

roughness parameter, k, which reflects the ,average height of the roughness irregularities. Their model states that the deposition velocity, u_d is calculated as:

$$u_d = 0.084\mathrm{Sc}^{-2/3} + \frac{1}{2}\left[\frac{\left(0.64k^+\frac{d_p^+}{2}\right)^2 + \frac{\tau^{+2}g^+L^+}{0.01085(1+\tau^{2+}L^+)}}{3.42 + \frac{\tau^{+2}g^+L^+}{0.01085(1+\tau^{2+}L^+)}}\right]^1 /1 + \tau^{2+}L^+ \times[1+8e^{-(\tau^+-10)^2/32}]\frac{0.037}{1-\tau^{+2}L^+(1+g^+/0.037)} \tag{7.24}$$

where tau^+ is the relaxation time, d_p the particle diameter, g the gravity, Sc is the Schmidt number and expressions for the constant L can be found in [36].

Figures 7.14 and 7.15 show a solution of Equation 7.24. We can observe that when roughness increases it eliminates the differences between particle diameters, flattening the characteristic shape of the curve of deposition velocities. Note that the effect of roughness is very similar to the effect of increased turbulence, as we have shown in Figure 4.10 in Chapter 4.

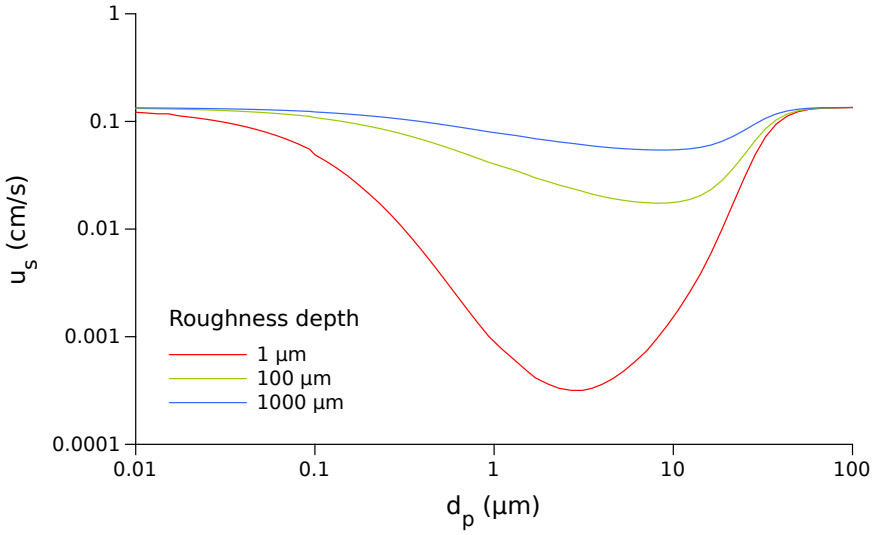

Figure 7.14: Deposition velocity vs. diameter for different values of roughness depth, k, calculated with Equation 7.24.

Figure 7.15 also shows that, when roughness is very high, all particles behave similarly. It also shows that the effects of roughness are particularly relevant in mid-sized particles, between 0.1 and 10 μm.

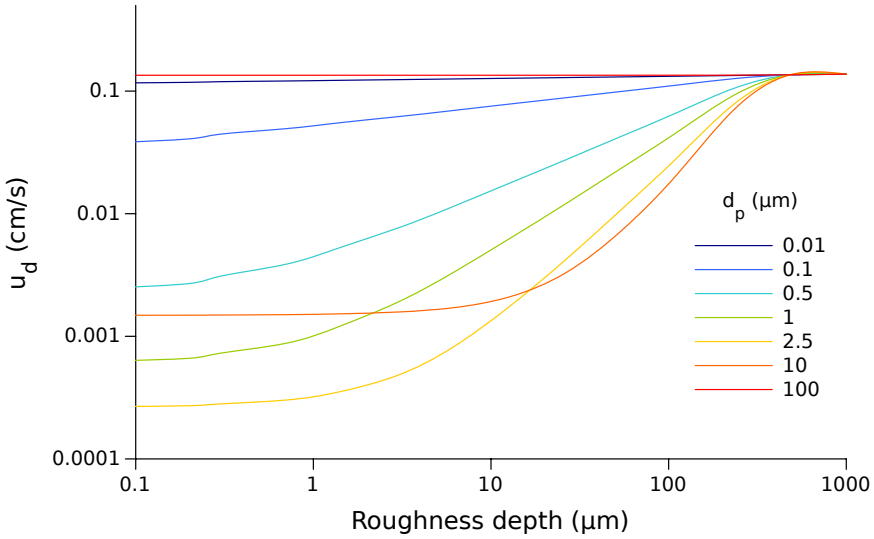

Figure 7.15: Deposition velocity vs. roughness depth for different values particle diameter, calculated with Equation 7.24.

References

[1] H. Moosmaller, R. Chakrabarty, and W. Arnott. “Aerosol light absorption and its measurement: A review”. *Journal of Quantitative Spectroscopy and Radiative Transfer* 110:11 (2009), pp. 844–878.

[2] J. Korsgaard. “House-Dust Mites and Absolute Indoor Humidity”. *Allergy* 38:2 (1983), pp. 85–92.

[3] K. K. Foarde, D. W. VanOsdell, and J. C. S. Chang. “Evaluation of Fungal Growth on Fiberglass Duct Materials for Various Moisture, Soil, Use, and Temperature Conditions”. *Indoor Air* 6:2 (1996), pp. 83–92.

[4] H. Harving et al. “House dust mite allergy and anti-mite measures in the indoor environment”. *Allergy* 46 (1991), pp. 33–38.

[5] N. B. F. Pinzari V. Cialei. “Measurement of the fungal deteriorating potential in the dust of indoor environments” (2010).

[6] R. M. Harrison et al. “A study of trace metals and polycyclic aromatic hydrocarbons in the roadside environment”. *Atmospheric Environment* 37:17 (2003), pp. 2391–2402.

[7] N. A. Janssen et al. “Mass concentration and elemental composition of airborne particulate matter at street and background locations”. *Atmospheric Environment* 31:8 (1997), pp. 1185–1193.

[8] M. Sharma, A. K. Agarwal, and K. Bharathi. “Characterization of exhaust particulates from diesel engine”. *Atmospheric Environment* 39:17 (2005), pp. 3023–3028.

[9] M. J. Kleeman, J. J. Schauer, and G. R. Cass. “Size and Composition Distribution of Fine Particulate Matter Emitted from Motor Vehicles”. *Environmental Science and Technology* 34:7 (2000), pp. 1132–1142.

[10] M. Strlič et al. “A comparative study of several transition metals in Fenton-like reaction systems at circum-neutral pH”. *Acta Chim Slov* 50:4 (2003), pp. 619–632.

[11] H. J. H. Fenton. “LXXIII.-Oxidation of tartaric acid in presence of iron”. *J. Chem. Soc., Trans.* 65 (1894), pp. 899–910.

[12] P. Brimblecombe, D. Thickett, and Y. H. Yoon. “The cementation of coarse dust to indoor surfaces”. *Journal of Cultural Heritage* 10:3 (2009), pp. 410–414.

[13] K. Kendall and C. Stainton. “Adhesion and aggregation of fine particles”. *Powder Technology* 121:2–3 (2001), pp. 223–229.

[14] A. P. D.A. Dillard. *Adhesion Science and Engineering: Surfaces, Chemistry and Applications*. Annals of Discrete Mathematics. Elsevier Science, 2002.

[15] W. Hinds. *Aerosol Technology: Properties, Behavior, and Measurement of Airborne Particles*. Wiley, 2012.

[16] K. Kendall, M. Kendall, and F. Rehfeldt. *Adhesion of Cells, Viruses and Nanoparticles*. Springer, 2010.

[17] R. Bradley. “The cohesive force between solid surfaces and the surface energy of solids”. *Philosophical Magazine Series 7* 13:86 (1932), pp. 853–862.

[18] H. Jung and D. B. Kittelson. “Measurement of Electrical Charge on Diesel Particles”. *Aerosol Science and Technology* 39:12 (2005), pp. 1129–1135.

[19] R. S. amd C. Hyland amd R. Blotyanskiy amd J.S. Wettlaufer amd E. R. Dufresne. “Surface tension and contact with soft elastic solids”. *Nature Communications* 4 (2013).

[20] J. Salvant, E. Barthel, and M. Menu. “Nanoindentation and the micromechanics of Van Gogh oil paints”. *Applied Physics A* 104:2 (2011), pp. 509–515.

[21] M. Guingo and J.-P. Minier. “A new model for the simulation of particle resuspension by turbulent flows based on a stochastic description of wall roughness and adhesion forces”. *Journal of Aerosol Science* 39:11 (2008), pp. 957–973.

[22] G. A. Loosmore. “Evaluation and development of models for resuspension of aerosols at short times after deposition”. *Atmospheric Environment* 37:1352 (2003), pp. 639–647.

[23] S. L. Goren. “The normal force exerted by creeping flow on a small sphere touching a plane”. *Journal of Fluid Mechanics* 41 (1970), pp. 619–625.

[24] G. Ziskind, M. Fichman, and C. Gutfinger. “Resuspension of particulates from surfaces to turbulent flows—Review and analysis”. *Journal of Aerosol Science* 26:4 (1995), pp. 613–644.

[25] L. Biasi et al. “Use of a simple model for the interpretation of experimental data on particle resuspension in turbulent flows”. *Journal of Aerosol Science* 32:10 (2001), pp. 1175–1200.

[26] A. Ibrahim, P. Dunn, and R. Brach. “Microparticle detachment from surfaces exposed to turbulent air flow: controlled experiments and modeling”. *Journal of Aerosol Science* 34:6 (2003), pp. 765–782.

[27] M. Soltani and G. Ahmadi. “On particle adhesion and removal mechanisms in turbulent flows”. *Journal of Adhesion Science and Technology* 8:7 (1994), pp. 763–785.

[28] M. Stempniewicz, E. Komen, and A. de With. “Model of particle resuspension in turbulent flows”. *Nuclear Engineering and Design* 238:11 (2008), pp. 2943–2959.

[29] H. Tennekes and J. Lumley. *A First Course in Turbulence*. MIT Press, 1972.

[30] T. Hussein et al. “Modeling Dry Deposition of Aerosol Particles onto Rough Surfaces”. *Aerosol Science and Technology* 46:1 (2012), pp. 44–59.

[31] V. Piskunov. “Parameterization of aerosol dry deposition velocities onto smooth and rough surfaces”. *Journal of Aerosol Science* 40:8 (2009), pp. 664–679.

[32] W. H. S. A. E. Perry and P. N. Joubert. “Rough wall turbulent boundary layers.” *Journal of Fluid Mechanics* 37 (1969), pp. 383–413.

[33] J. Nikuradse. “Stromungsgesetze in rauhen Rohren”. *Forschung auf dem Gebiete des Ingenieurwesen* (1933).

[34] J. Benson. “Boundary-layer response to a change in surface roughness.” PhD thesis. The University of Reading, 2005.

[35] W. P. Elliott. “The growth of the atmospheric internal boundary layer”. *Eos, Transactions American Geophysical Union* 39:6 (1958), pp. 1048–1054.

[36] F.-G. Fan and G. Ahmadi. “A sublayer model for turbulent deposition of particles in vertical ducts with smooth and rough surfaces”. *Journal of Aerosol Science* 24:1 (1993), pp. 45–64.

8
Conclusions

The main output of this Thesis is a working model of PM deposition indoors. This model has been extensively validated in many heritage buildings, and we are confident that it produces reliable results. This is innovative in many aspects: it is the first time a CFD deposition model has been validated against deposition data collected in real buildings, over such long experimental times, and displaying such complex structures and dynamic operation. Furthermore, we have used the model to investigate the behaviour of PM in indoor heritage spaces with unprecedented detail, allowing an almost complete understanding of the phenomena that brings particles to surfaces.

However, most of the work, and thus most of the conclusions, derive not from the model itself, but from the process of validating, interpreting and expressing its predictions. We have worked in many properties, where the model has faced many different challenges - different particle sizes, air flow properties, and room geometries. Behind each property there is an institution that maintains it, and our interaction with these institutions has also posed many challenges: they have different needs, different resources, different scientific approaches and ways of communicating.

Therefore, our conclusions refer not only to the facts of deposition, but to their significance for heritage institutions. We present the conclusions in four sections: Firstly, we describe how our approach contributes to the understanding of deposition. Secondly, how our results can contribute to a better protection of historical surfaces. The third Section describes what can we conclude about the simulation of particulate matter with CFD. Finally we report issues that require further research.

Understanding deposition

- Particulate matter concentration is typically homogeneous in rooms, but deposition is not. We can only refer to an indoor space as "well mixed" if we are concerned with the bulk concentration and its average decay rate. But deposition rates vary greatly, firstly due to the different inclination of surfaces, but also, crucially, due to differences in air flow regime. This is expressed clearly by the definition of the deposition flux;

$$J = u_d \, c \tag{8.1}$$

  All the possible effects of the air flow regime are contained in u_d. Its precise estimation is, therefore, the most important achievement of the model. u_d is increased by high turbulent diffusivity, by friction velocity and tangential stresses, and in a small degree by thermophoresis. Insofar as these parameters of the flow change in space, u_d will vary. These relationships are non-linear and often counter-intuitive.

- The definition of the deposition flux is a powerful tool to interpret a given indoor environment. We can classify every element that plays a role in deposition either as a source of particles (i.e. increases c) or a driver of deposition (i.e. increases u_d). This distinction lets us discern the real causes behind the observed deposition. We have seen many examples in our case-studies:

Sources of c	**Drivers of** u_d	**Combined effect**
Leakage	Filtered HVAC	Unfileterd HVAC
Candle	Open door	Open window
Cooking	Fan	Visitors
Clothing		

- This distinction also leads us to two ways of mitigating deposition. The first one is the classical mitigation approach: the reduction of c. It involves everything we would also do to reduce the concentration of gases (i.e. improving airtightness, implementing filters). In the case of PM we can count on another set of mitigation measures, based on reducing u_d. These strategies, which require a good understanding of the physical system, are based on the manipulation of the drivers of u_d in order to reduce the total deposition.

- We have investigated techniques of mitigation related to a reduction of u_d in some properties. We have seen, for example, that door wings in the Hampton Court Palace have the ability of reducing near-wall air movement, and therefore reduce deposition in the tapestries that surround doors. We have also seen that in many instances ventilation systems have a double effect: they tend to reduce the concentration of PM, but increase its ability to deposit. A careful placement of ventilation inlets and outlets may also reduce deposition. A good name to refer to the set of mitigation strategies focused on reducing u_d could be "turbulent mitigation".

- We have observed in many examples that high turbulence diminishes the differences between particle properties, particularly for $d_p < 10\ \mu\mathrm{m}$. In other words, the dependence on diameter due to the balance between Brownian diffusion and gravitational settling disappears, and the "V" shape of the deposition curve becomes flat:

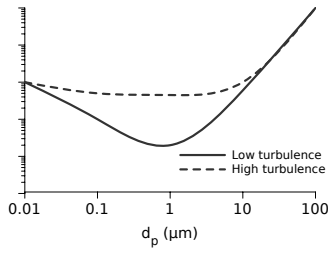

  In the absence of air motion, Brownian and gravitational settling become the main driving forces of deposition. In our experience, turbulence also overrides any effect of thermophoresis, and flows driven by mechanical ventilation or cross ventilation override buoyancy caused by temperature differences. Surface roughness has a similar effect on deposition rates, also eliminating the differences between particle sizes.

- The amount of particles in a surface is a balance between the particles that deposit and the particles that are resuspended. Resuspension requires fluctuating air flows, either produced by turbulence or some other kind of periodic movement. Humidity (which enhances capillarity) or static electricity are sometimes believed to increase deposition, but this is an illusion: in fact, they reduce resuspension. The final result, however, is just the same: adhesion forces increase the amount of particles on surfaces.

Protecting surfaces from deposition

- Our model can help heritage managers by providing new evidence. We have produced simulations with many purposes:
  - To predict deposition under different hypothetical scenarios (For example, in Apsley House, Section 6.4).
  - To interpret the measured deposition and find possible drivers of deposition (Hampton Court palaces, Section 6.3).
  - To provide evidence to support an intervention to reduce deposition (For example, in the Wellington Arch, Section 5.3).
  - To aid in the choice of sampling locations (Section 6.2).

  These cases demonstrate how CFD can fit into the preventive conservation process, by informing decisions and enabling risk assessment.

- Some further examples of potential uses of the model are: identification of representative locations for particle monitoring, identification of sources of particles and their relative importance, or identification of drivers of deposition. It can also quantify deposition, and thus help to plan cleaning schedules, or estimating the time to reach given levels of deposition.

- Due to the homogeneity of c, and the great variation of u_d, measurements of suspended PM concentration alone are useless for the purpose of risk assessment. The crucial parameter is J, the amount of particles per area and time, be it in mass, number, or area coverage. This may be self-evident, and would be of little significance if it wasn't the case that, often, concentration of PM, and not its deposition flux, is used to assess the risk to collections.

- We have explored alternative ways of expressing the outputs of the model. Deposition fluxes can be reported as area coverage in a certain time or, even better, as the time needed to reach a certain area coverage (which could be, for example, the threshold to visible deposition). These two metrics highlight the inhomogeneity of deposition profiles and are related directly to the language of preventive conservation and the daily practice of heritage institutions.

- We have identified four possible mechanisms related to PM deposition that lead cause a loss of value to surfaces: a loss of aesthetic value, chemical damage, biological growth, and physical damage during cleaning activities. All these mechanisms are related to area coverage, but our literature review suggests that they may depend on a range of other factors, such as environmental conditions and time. We have only explored experimentally the chemical effect of particles on paper.

- Our experiments indicate that the chemical effects of particles on organic materials do not depend only on the number of particles, but also on their composition. Specifically, we have found a positive correlation between the presence of Fe on soiled paper and its chemical stability. The role of Fe as a catalyst in oxidation of cellulose can explain this relationship.

  We have also found that visible soiling (about 5% area coverage) by chemically aggressive particles originated in road traffic causes only a $\sim 50\%$ increase in the rate of degradation. This implies that cleaning organic surfaces when PM becomes visible may be a good measure to protect them from chemical degradation due to PM.

- If a threshold or recommended limit of PM deposition has to be defined, to account for all materials and mechanisms of loss of value, it should involve composition, amount on the surface and time. For example: 5% area converge during one month. We have only demonstrated this for organic materials. Other materials such as metals and stone could react differently.

Simulating deposition

- We can recommend the use of an Eulerian drift-flux together with a RANS turbulence model such as $k - \epsilon$, coupled with near-wall corrections of the turbulent diffusivity, as those suggested by Lai and Nazaroff. This approach provides results that are significantly accurate when compared to real deposition data. The coincidence with the experiments is remarkable, especially given the number of factors affecting deposition, the time-scale of the simulations and the large uncertainties associated with many of our deposition measurements.

- Grid independence tests revealed that the drift-flux Eulerian approach does not require very fine meshes, and thus all the simulations of our case-studies can be solved in a personal computer. This is a promising result, because it implies that in the future, similar models could be implemented into simple 3D design software, or even in cloud-based applications, which could be used by users with minimum knowledge of CFD.

- The applicability of the model can be assessed with a set of non-dimensional numbers Φ, Sc, St, K_{pt}, Pe, and Re. Our model is a predictor of u_d, and therefore simulates turbulent flows. If in an indoor environment we have very small Re, i.e., no turbulence, the model becomes not only inaccurate (we would overestimate turbulent transport) but also unnecessary. u_d will be dominated by Brownian diffusion and gravity, deposition will be homogeneous and we will be in the realm of applicability of the well-mixed models.

- The simulation of coarse dust with low turbulence is a limiting case. One of the core assumptions of the mathematical model is that the diffusivity of the particles (ε) can be approximated with the turbulent diffusivity of the air (μ_t). This implicitly assumes that particles are inertia-less. But when they have significant inertia, the model will overestimate diffusivity (and thus deposition velocities). Future work must include a convincing solution for the diffusivity of high-inertia particles.

- That said, we can outline some an approximate guide of the cases that are covered by the model:

    1. The value of the five parameters listed in Table 4.1 of Section 4.4 should be within the safe ranges of applicability.
    2. The air regime should be turbulent (there must be a source of air flow).
    3. d_p can be approximately up to 100 $\mu\mathrm{m}$ (provided the air flow is such that K_p is vanishingly small).
    4. An outlet of air should be present (otherwise, only unsteady simulations are possible).
    5. Resuspension has to be negligible in comparison to deposition. To the five parameters mentioned in Point 1, we could add the resuspension criteria defined in Section 7.3.3:

$$X_r = \frac{\text{lift force}}{\text{adhesive forces}} \sim \frac{\rho\nu^2}{d_p}\left(\frac{d_p\, u^*}{\nu}\right)^3 \tag{8.2}$$

Which should be < 1 in order to ensure that resuspension can be ignored.

If these conditions are satisfied, any wall-bounded volume with any geometry can be simulated with our approach.

- We have suggested two methods to introduce an assessment of resuspension into the model. The simplest option is to evaluate the strength of the adhesion forces compared to the lift forces that cause resuspension. A more complex solution is to introduce a resuspension flux, which would only be valid for simulations that are averaged over long periods of time.

- Steady state simulations represent equilibrium situations. As long as an equilibrium situation is extended in time, we can simulate over this period. We have shown that in naturally ventilated buildings in which indoor concentration is controlled by infiltration, wind direction is the single most important factor differentiating deposition between different months. In other cases, this parameter might be visitors, the ventilation system, or a combination of these.

Future work

Many of the computational tools, theoretical oncepts and experimental methods that we have used in this thesis could be subject to improvement and further research. In this section we highlight some future research questions that are prioritary. They could be divided in two blocks: firstly, tweaks in the model that would improve its usability and its flexibility. In my opinion, it is only necessary to pursue these improvements if there is a clear future need to use this modelling approach in indoor applications. They can be part of any future research involving drift-flux simulations of dispersion and deposition. A second research strand is composed of all the issues that will contribute to our understanding of deposition and particulate matter: its chemical effects, the nature of deposits and the mechanisms that lead to loss of value. This block of future research should be of great interest for heritage institutions, and should be pursued without delay.

- Our model does not include surface properties such as roughness, which can be influential. Resuspension could also be implemented following our suggestions. A model with these changes should be validated with an appropriate case study (and the experimental data would also be a welcomed addition to the literature).

- Our model does not include the movement of visitors. This is crucial for many heritage applications, particularly for small buildings where air motion is influenced by visitor behaviour. The CFD technology is advanced enough to implement this feature.

- Some minor technical questions remain to be addressed. The assumption that $\varepsilon \sim \mu_t$ is not valid for large particles with significant inertia. A correction needs to be implemented that reduces the turbulent diffusivity of particles when they are too large to follow air flow. Perhaps this could be implemented using the parameter K_{pt}, but that is an aspect that requires further fundamental research. Coagulation is also a possible further extension of the model (and DQMOM would be an appropriate method.)

- The generation of fine particles from dust deposited in heat sources needs further research (both in general and in the case of indoor Heritage). Black stains of deposition above heating implements are a common sight. In Apsley House or the Wellington Arch, for example, they were present over lighting points and hot water pipes near radiators. However, the model wasn't able to predict a single one of these deposition events. Either the model severely under-predicts the effects of thermal events, or this deposition is caused by a source of c or driver of u_d not included in the model. As we found in the literature review, heating points might decompose coarse dust in fine particles and volatile compounds. Could that be the source of c that we are missing? More experiments would be needed to find an answer. The ubiquitous presence of this kind of deposition justifies further research.

- Regarding the investigation of the loss of value due to PM deposition and of possible thresholds, there is much to be done. Biological growth (both mould and pests) due to the accumulation of PM should be investigated. This research should look at particle size, particle composition, deposition time, temperature and RH. Research on the visual consequences of deposition should address the effects of fine and ultrafine particles. Research on cleaning should attempt to relate the amount of particles on surfaces of different materials with the damage caused by removing them.

- Our experiments on the chemical effects of PM on cellulose may serve as a first indication of its role on the degradation of organic materials, but they should be extended to other substrates, and perhaps repeated with more control on the nature of the deposited particles.

  In the future, this work can deliver two different outputs that will be of great practical use. The first and most desirable output would be a model wich is quick, simple, lightweight, possibly free and ideally user-friendly, which can be run directly by end-users in order to assess deposition in any typical scenario. The second output would be a better understanding of the dynamics of deposited particles, a full quantification of the loss of value that could motivate guidelines, help identify risks, and inform decisions. These two outputs can be researched independently, but the two final products will undoubtely benefit each other.

A closing thought

As we mentioned in the introduction, the process of testing and validating the model has also given rise, almost unintentionally, to a way of thinking and speaking about deposition. The concepts of concentration, velocity and flux are very useful to interpret PM deposition evidence,

and we have made an extensive use of them. The language required to define the model (e.g. tangential velocities, turbulent diffusion, near-wall phenomena) offers a consistent and logical vocabulary to describe indoor environments and approach new problems. If we had chosen another type of model (Lagrangian, or multi-compartment), perhaps our vocabulary would be slightly different. But what is really relevant is that we have established strong links between these concepts and experience. The model can provide new information, but it can also help extract valuable information from otherwise obscure evidence. This may be our main contribution. After all, the evidence we cannot interpret is not evidence for us. We can only find solutions to the problems we can describe. To that end, fluid dynamics is but another tool.

Appendix 1: Experimental methods

8.1 Introduction

This appendix describes the experimental methods used in this work. Many of these methods have been alluded to in the text, and will be explained in detail here. Cross-references are included to the sections where each method is used.

8.2 Environmental monitoring

8.2.1 Wind velocity and direction

We obtained the wind directions and velocities used in Sections 5.4.1 and 6.3.1 from the Meteorological office (MET). The closest weather station to Hampton Court palaces and Apsley House for which wind data are available is in Kew (which is equidistant to both places, approximately at 10 km). The second closest weather station is in Heathrow Airport, at 12 km from Kew. The daily average wind velocity and direction in Kew and in Heathrow are very similar. Figure 8.1 shows the correlation between wind velocity in both locations during 2012. Since Hampton and Apsley House are at comparable distances (between them and from these two weather stations), we can assume that the wind rose in these locations is very similar to that in any of the two weather stations. We have used the data from Kew.

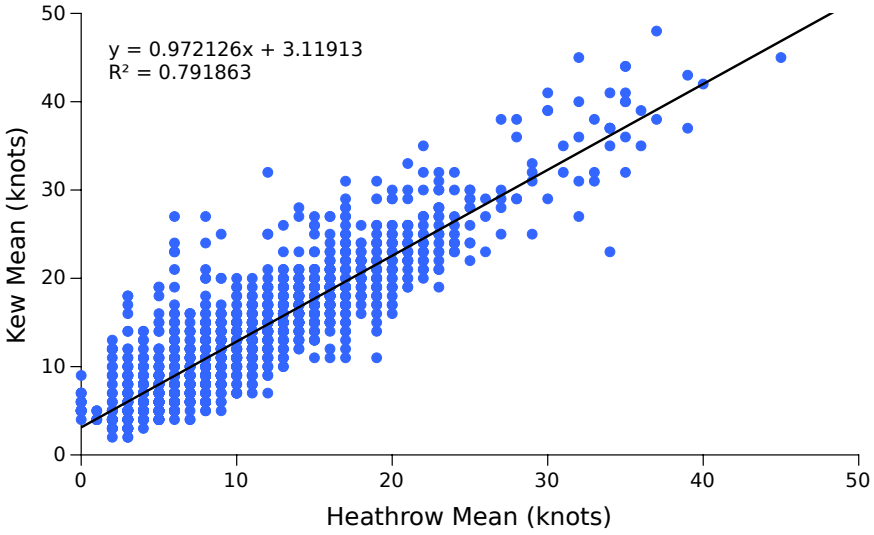

Figure 8.1: Comparison of wind velocities during 2012 in the Kew and Heathrow Airport weather stations.

8.2.2 Air speed monitoring indoors

We used several Ultrasonic Wind sensors (WindSonic M) to measure air velocities indoors. These sensors can measure velocities from 5 $\mathrm{cm/s}$. Each of the sensors measures air direction and velocity in a 2D plane. We combined several sensors to the velocity components in three dimensions (Figure 8.2). Some of the uses of these anemometers were the measurement of velocities in doors and gaps. They are used in the Wellington Arch (Section 5.3) and the Hampton Court Palace (Section 6.3.1), as well as in Apsley House in many instances (to detect leaks, find inlet velocities, find draft directions in doors and understand air motion).

Figure 8.2: Two of the ultrasonic anemometers used for various air speed measurements.

8.2.3 Suspended PM

We have used several instruments for particle counting:

TSI P-Trak Hand held condensation particle counter. Output in number per volume. Uses alcohol evaporation to increase particle diameter. Counts a single size bin between sizes 0.02 and 1 μm. Normal operation lasts 8 h but we modified it to measure during longer periods (See below). Used to count fine PM in all the case studies. P-Trak measurements can be seen in many Figures, for example, Figures 4.8 or 5.7.

Gradko DC1100 Table-top instruments set-up to measure two size modes each. Output in number per volume. We used 2 sets of three instruments which measure particles of the following sizes: >0.5 - >2.5, >2.5 - >5 and >5 - >10 μm. The smallest size mode includes all the larger sizes. Operating with these size counts we obtained three bounded size modes: $PM_{0.5-2.5}$, $PM_{2.5-10}$ and PM_{10-100}. The upper limit of 100 is only an indicative limit. The larger size mode, in reality, measures all the particles >10. We used these instruments to monitor suspended PM indoors and outdoors in Apsley House during the monitoring campaign (Section 5.4.1).

TSI Dustrak Hand held particle counter. Output in mass per volume, Calibrated at different sizes, we used it at its smallest size range $PM_{0.1-1}$ in order to investigate the relationship between mass concentration and number concentration.

The relationship between mass number concentrations measured with the Dustrak and the number concentrations measured with the P-Trak is not always direct. As Figure 8.3 illustrates, the differences on particle type and density result in different correlations between concentration measured in cm^{-3} and $\mathrm{mg/cm}^3$. The data shown in this plot corresponds to a 30 minute

experiment carried out outdoors near Apsley House. In the case illustrated in Figure 8.3 the instruments probably detected particles from two different origins (which could be, for example, resuspended dust and a smoke emission).

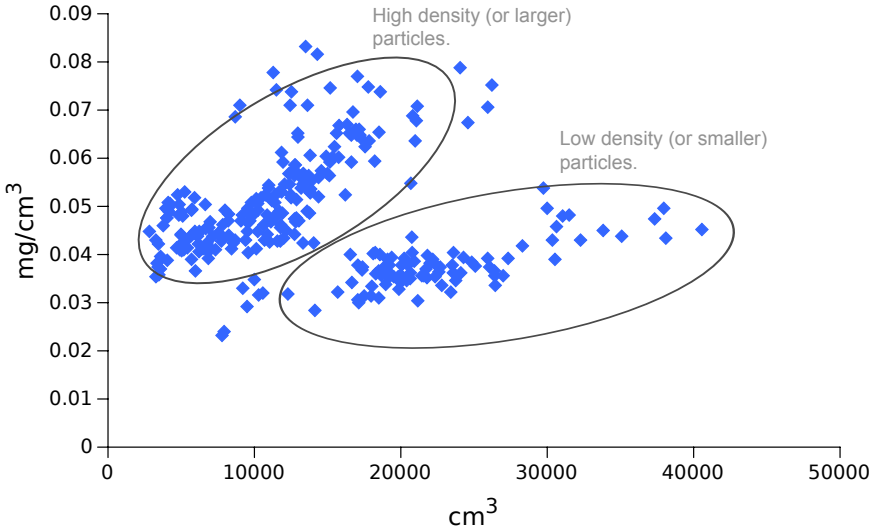

Figure 8.3: Comparison between suspended particulate mass and number in the same location during some minutes.

P-Trak extension module

The time of operation of the P-Trak particle counter is limited by its reservoir of isopropyl alcohol. The alcohol is stored in an annular wick with an external diameter of 1.5 cm and an internal diameter of 0.5 cm. When the caputred particles flow through the wick the alcohol condensates on them and their diameter increases. However, as alcohol evaporates and the wick becomes dry, the condensing capacity reduces and the number of counted particles decays, reaching zero in approximately eight hours (Figure 8.4).

We attached a 360 cm^3 tank to the instrument to serve as extra storage of alcohol. This tank transported alcohol to the wick by capillarity through a felt thread protected by a plastic tube. The felt thread was inserted in the wick through a small hole. In this set-up, the isopropyl alcohol was fed into the wick "on demand" to replace the evaporated alcohol. As seen in Figure 8.4 this resulted in a great improvement of the monitoring time, and was successfully used in cases such as the Wellington Arch (Section 5.3 or the tunnel experiment (Section 4.3.)

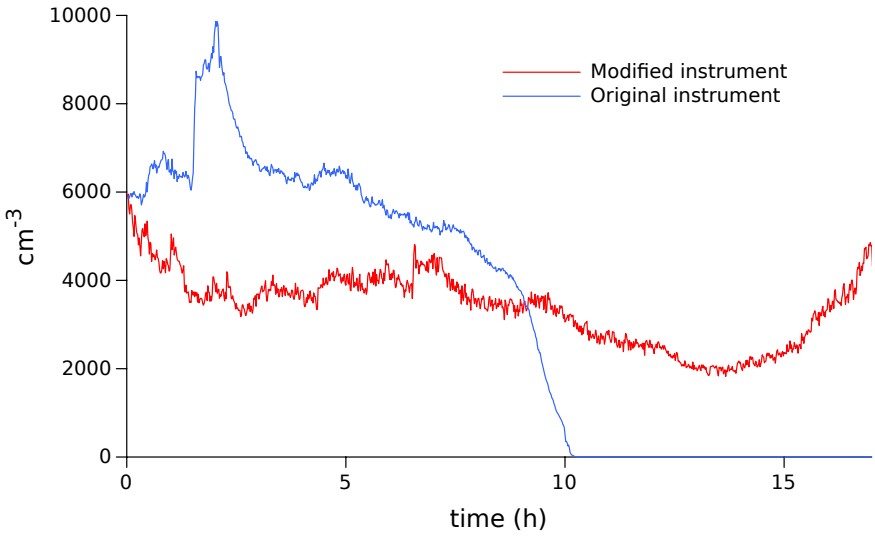

Figure 8.4: Comparison between the time of operation of a P-Trak before and after the addition of a reservoir of isopropyl alcohol.

However, this system has some limitations. Most importantly, if the felt becomes totally dry due to a long time out of operation, it needs to be extracted and soaked again in alcohol. This requires dismantling a part of the instrument every time it has to be used after prolonged rests. This situation could be improved using a material with higher capillarity, but we couldn't explore other materials in the framework of this project. Secondly, the instrument was never totally leak free, and even though isopropyl alcohol evaporates very quickly, this limited its unsupervised use indoors.

Particle size distributions

The combination of the P-Trak with the three Gradkos offers 5 size modes, which are enough to obtain a simple approximation to the particle size distribution. Figure 8.5 illustrates the measured distribution of suspended particles in different locations.

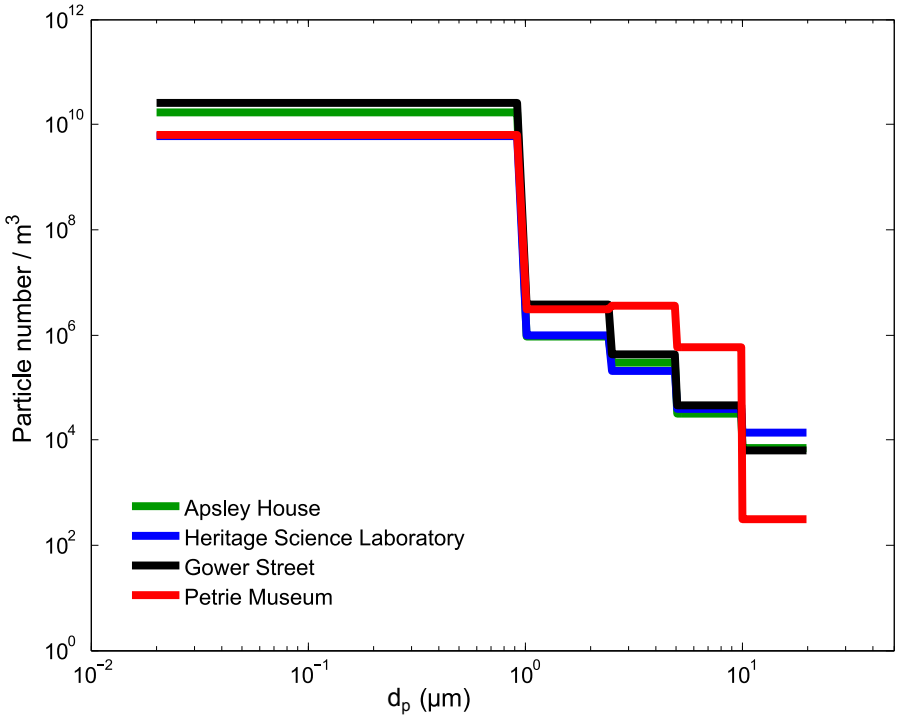

Figure 8.5: Measured size distributions in different locations using the Gradko particle counters in combination with a TSI-PTrak.

Long term monitoring set-up

Three of the Gradkos were used to monitor PM outdoors for more than 6 Months for the Apsley House campaign (Section 5.4.1) plus preparatory work for the experiment. The long monitoring time presented several problems, the first being the low capacity of data storage of the instruments (no more than 100 data points, either minute, hourly or daily averages). We decided to build our own data retrieving system. The instruments are programmed to send a signal every minute through their serial port. We used a serial-to-USB adaptor, connected to a USB hub and a 10 m USB extension to connect the three instruments to a computer located indoors. Due to the length of the USB extensions there was a significant loss of power that resulted in signal failures and sporadic losses of data. For this reason, both the USB cable and the USB hub were independently powered. The data were collected with specific software for serial data transmission. We did a weekly backup.

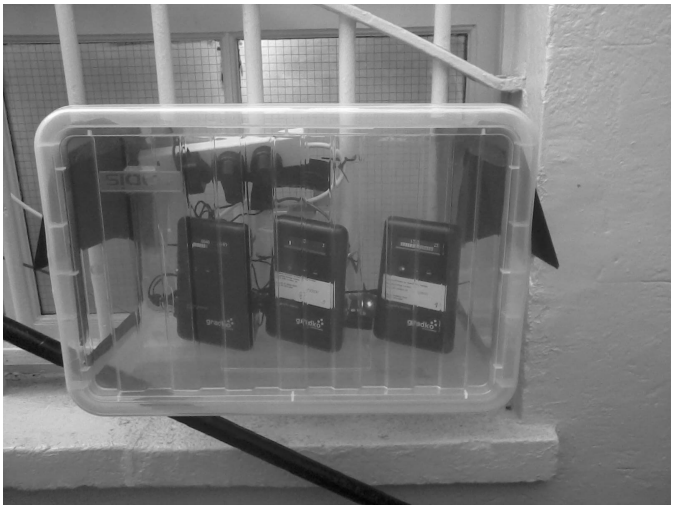

Figure 8.6: Protective case used to cover the particle counting instruments during extended monitoring periods.

We placed the Gradkos in a protective case in the service stairs in the main façade of Apsley House (Figure 8.6). The case was made of plastic and was conveniently adapted for monitoring with side holes that allowed air flow, and a transparent front wall which was useful to quickly check the display screens of the instruments.

8.3 Deposited PM

We counted deposited particles on glass slides (using an optical microscope) and on SEM carbon stubs (using a SEM microscope). The process of sample preparation differed, but we used the same particle counting algorithm in both cases.

8.3.1 Optical microscope

We used glass slides to collect and count particulate matter following an approach similar to [1]. After exposure, the glass slides were photographed with an optical microscope. Approximately ten images of every sample were taken. We used a magnification that provided a pixel size of $0.13\ \mu\mathrm{m}$. However, we didn't count particles smaller than four pixels, to avoid an overestimation of the amount of fine particles. With this set-up, the smallest particles that can be measured have a diameter of $\sim 0.3\ \mu\mathrm{m}$, which is close to the theoretical minimum detectable by the naked eye, which is given by the wavelength of the visible light ($390\ \mathrm{nm}$). The images were processed and the particles counted with an automated macro described below. Figure 8.7 shows an example of an image prepared for particle counting.

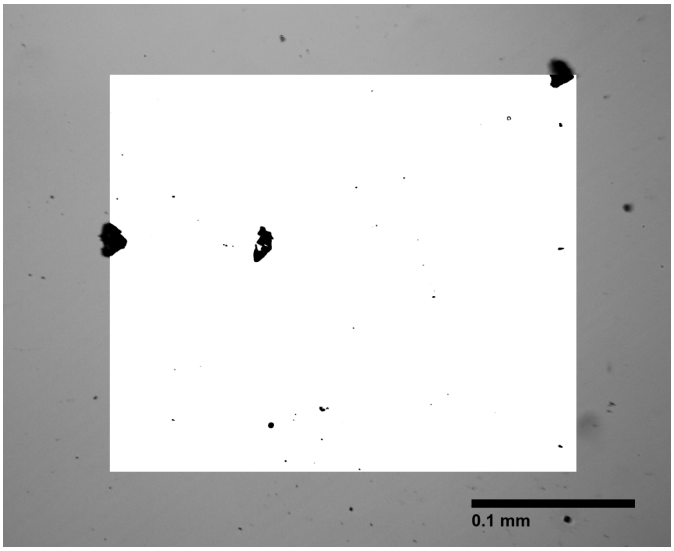

Figure 8.7: Example of an image of deposited particles on a glass slide taken with an optical microscope with a superimposed processed image.

8.3.2 Scanning Electron Microscope

Sample preparation

We collected particles on carbon Scanning Electron Microscope (SEM) stickers. We used SEM stubs to support the stickers in order to avoid direct contact with the surface where particles deposited. We designed a sample holder prepared to hold up to 14 SEM stubs, 7 vertically and 7 horizontally (Figure 8.8. The double-sided carbon stickers required some preparation before monitoring:

1. We removed the sticker of one of the sides of the double-sided SEM carbon sticker. We used isopropyl alcohol to dissolve the adhesive. This was necessary because some of the measured particles are smaller than the thickness of the adhesive layer, and could sink during the monitoring period.
2. We attached each sticker to a SEM stub, labelled it, and placed it on the sample holder.
3. We distributed the sample holders in Aplsey House in the locations marked in Section 5.4.1. Every month we retrieved a SEM stub and placed into a transportation box, which was prepared to fit the stubs with minimum movement, to avoid particle resuspension.

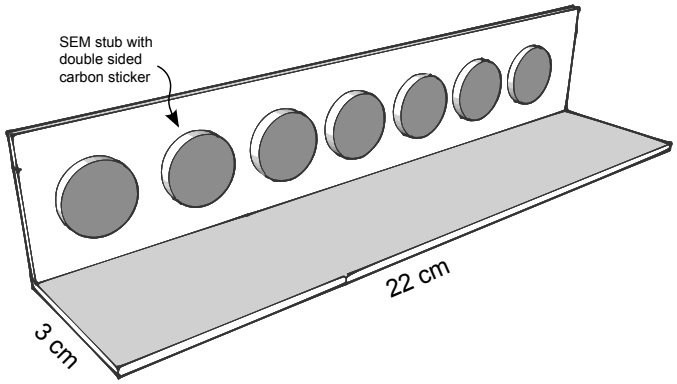

Figure 8.8: Design of the sample holder used for particle monitoring. This version has only vertical stickers, but we used horizontal stickers as well.

SEM counting

Every month we photographed the deposited samples using a Hitachi electron microscope (Hitachi S-3400N). We optimised the process largely by trial and error. Some guidelines for proper particle counting with a SEM microscope are:

1. A fixed magnification (and a fixed distance between beam and sample) should be used. The reason for this is that it is much easier to compare the samples afterwards if all the pictures have been obtained with the same magnification. Otherwise, a scale correction should be applied, both for the size of the particles (because the number of pixels that make up a particle will be different between days and samples) and to the measured area.

2. It might be tempting to increase the magnification for sparse populated areas. This is to be avoided for the reasons below, and for one added reason: particles are easy to find in any surface with sufficient magnification, but what is of interest is the homogeneous distribution of particles which can be related to deposition fluxes, not arbitrary deposition events. Therefore, if particles are not detected on a homogeneous scale, it is best to consider the sample to be below the detection level.

3. Also owing to the interest of homogeneous deposition, the screen captures should be taken without any user intervention. This is, either automatising the process in a grid-like system or by selecting the locations randomly.

4. There is a rule of thumb to find the right magnification of operation. It should be the maximum magnification in which an homogeneous pattern of deposition is found. And by homogeneous pattern we mean that the count of particles of a given size does not differ between scanned areas. Typically, we will always find an homogeneous distribution at the minimum magnification, because it will include a much larger area. But it is likely that the smallest particles of the system won't be detectable at such scale.

Our optimum set-up was to produce images with a magnification of x500, in which the size of a pixel in microns was in the vicinity of 0.05 μm. Even though we could provide images with a higher resolution, they did not provide a good assessment of the amount of larger particles. Furthermore, particles smaller than 0.1 μm were difficult to detect even at higher magnifications. With this set-up we easily detected particles larger than 0.05 μm. It was used to produce the size distributions displayed in Figure 5.17.

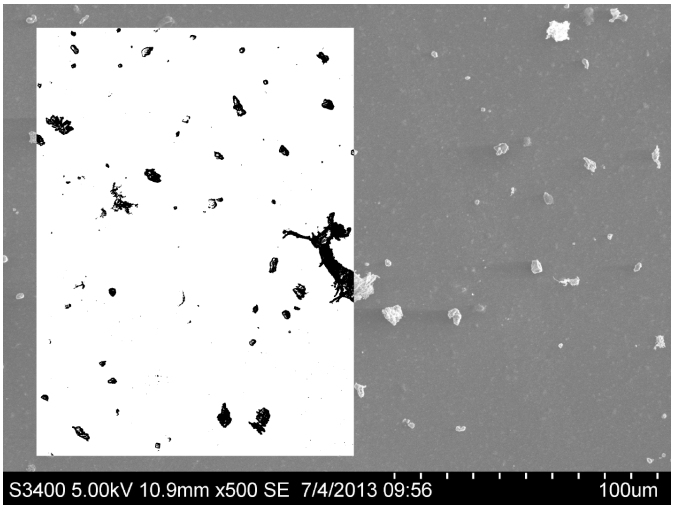

Figure 8.9: Example of an image of deposited particles on carbon sticker taken with a SEM microscope with a superimposed processed image. Note that, with the same magnification than Figure 8.7, much more detail can be appreciated.

Automation of the counting process

The open source application *imagemagick* was used to prepare the images for post-processing, firstly converting images from gray scale to binary black and white, with an adjustable threshold of luminosity. A square Section was cut in the centre of every image to avoid false readings from the peripheral areas out of focus (specially important for optical microscope images).

```
mogrify -threshold 30% -gravity Center
-crop 3000x3000+0+0 *.TIFF
```

Then an *ImageJ* macro was applied to the images. The macro smoothed the contours of the image, thus eliminating any image noise pixels that could be counted erroneously as particles. Then particles were analysed, leaving out any particle smaller than two pixels and accepting particles of any circularity.

```
dir = getDirectory("image");
 name=getTitle;
```

```
 path = dir+name;

run("Smooth");
run("Smooth");
run("Smooth");

run("Make Binary");
run("Analyze Particles...",
    "size=2-Infinity
     circularity=0.00-1.00
     show=Nothing
     display exclude
     clear include
     summarize record");
saveAs("Text", path);
```

The output of this macro is a list of particle sizes (measured in area) in text files that were later read and processed with R.

8.3.3 Chemical analysis with EDX

The chemical analysis of particles with Energy-dispersive X-ray spectroscopy (EDX) was useful to obtain chemical information of particles larger than 1 μm, but the instrument used did not provide any information on smaller particles (when we centred the analysis on particles smaller than 0.1 μm, only the carbon substrate was detected). Figure 8.10 shows the composition of two characteristic particles of 3 μm and 10 μm. The elements detected in particles of this size range, both indoor and outdoors, were: Na, Mg, Al, Si, S, Cl, Ca, Ti, Mn, Fe and Cu.

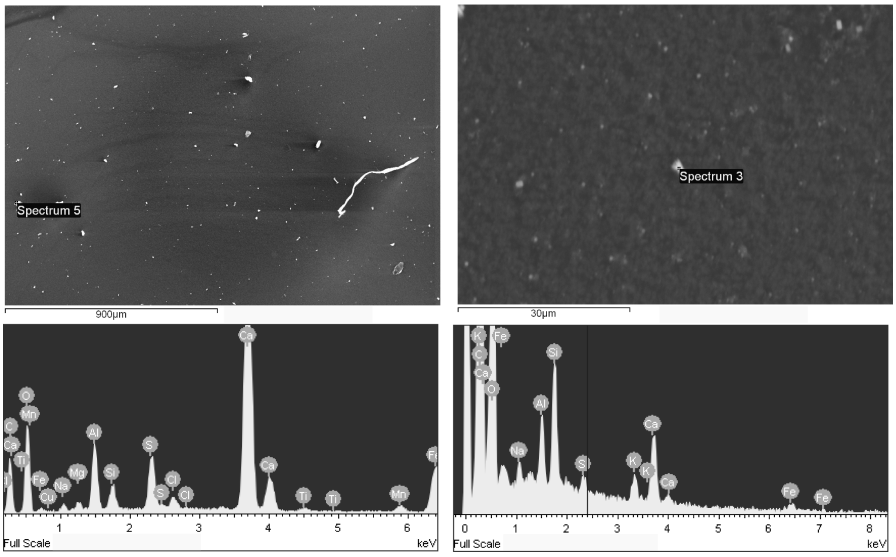

Figure 8.10: Examples of EDX spectra showing the particle composition of two particles.

8.3.4 Chemical analysis with ICP-MS

We analysed the chemical composition of the PM deposits on paper using Inductively Coupled Plasma Mass Spectrometry (ICP-MS) with the collaboration of Dr. Bojan Budič from the Kemijski Inštitut in Ljubljana, Slovenia. ICP-MS is a technique for elemental chemical characterization which can detect very small traces of metals and is capable if quantitatively measuring analytes down to a few nanograms [2]. This allowed us to obtain accurate measurements of the surface concentration of metals using a minimum amount of sample. These results are used in Section 7.2.3. We analysed a 1×1 cm square of paper for each month and from four different locations (the two indoor and the two outdoor locations of Apsley House.)

8.4 Viscometry

We used viscometry to determine the degree of polymerisation (DP) of cellulose in Section 7.2.3. The DP is defined as the number of monomers in a polymer. As the chains of cellulose break, they divide in smaller units, and thus the DP increases. The DP of cellulose can be estimated from the viscosity of a solution of the dissolved cellulose fibres.

As mentioned in Section 7.2.3 the degree of polymerisation was obtained with the procedure outlined in the standard BS ISO 5351:2010. This standard explains in detail the procedure to estimate the DP from viscometry measurements, as well as the experimental methods.

Experimental procedure

We refer the reader interested in specific details of the experimental method to the standard BS ISO 5351:2010. Only as a quick reference, we present here a summary of the main steps of the experimental procedure:

1. We cut and weighted paper samples of 20-25 mg each, and took note of the mass. The samples were brushed to remove any excess of coarse particles that could affect the measurement.
2. These samples were dissolved in 10 ml of distilled water with the help of small iron pieces and a sample shaker.
3. The resulting solution was mixed with 10 ml of a solution of Cupri-ethylenediamine, which dissolves cellulose, and shaken again.
4. The flask containing the resulting solution was placed in a water bath at 25 $^{\circ}\mathrm{C}$.
5. The viscosity was measured using a capillary tube viscometer. This type of viscometry requires the measurement of the time required for the solution to flow through a capillary tube, which was measured with a stop watch and recorded with a video camera.

Improvement with video analysis

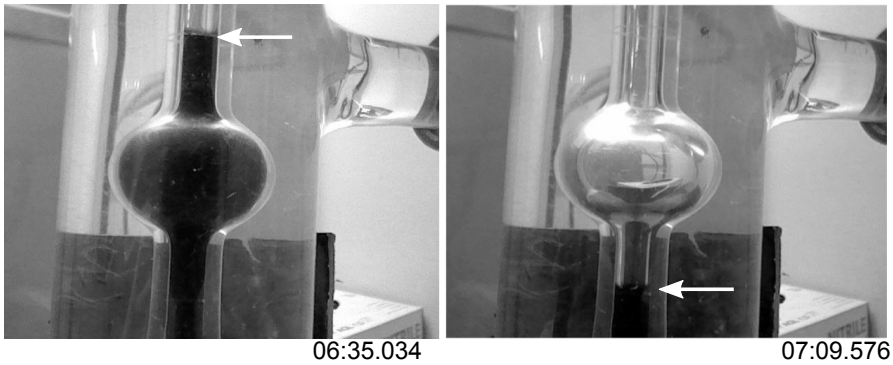

Figure 8.11: Example screen captures of a viscometry measurement carried out with the aid of a webcam. The time stamps indicate that the flow time can be measured with a precision of less than a tenth of a second.

The use of a video camera to record the movement of the liquid samples through the viscometer helped to improve the accuracy and repeatability of the measurements. Figure 8.11 illustrates the precision in which the speed of the flow can be measured. This precision is limited by the number of frames per second of the recording, and is much higher than the precision achieved with a manual stop-watch. However, the largest source of variation in our experiments was not in time measurements but in the inhomogeneity of the degradation of the samples.